CA125 Targeted Molecular Imaging of Epithelial Ovarian Cancer

by

Sai Kiran Sharma

A thesis submitted in partial fulfillment of the requirements for the degree of

Doctor of Philosophy

in

Pharmaceutical Sciences

Faculty of Pharmacy and Pharmaceutical Sciences

University of Alberta

ABSTRACT

Rationale: Ovarian cancer is the most lethal malignancy of the female reproductive system. ~80% of ovarian cancers are epithelial in origin and commonly classified as Epithelial Ovarian Cancer (EOC). This malignancy is characterized by an overexpression of Cancer Antigen-125 (CA125) – a cell surface mucinous glycoprotein that serves as a USFDA approved ovarian tumor associated antigen. However, the early detection of EOC is plagued by its asymptomatic nature of progression and the limitations of currently used front-line diagnostic tools such as immunoassays that are capable of detecting CA125 as a shed antigen in the serum of patients presenting in the clinic with pelvic masses suspected for ovarian cancer. At present, there is no technique available for the *in vivo* evaluation of CA125 expression in malignant tissues, which has been shown to be an early event in the recurrence of epithelial ovarian cancer.

Hypothesis: CA125 is a suitable target for the molecular imaging of epithelial ovarian cancer.

Methods: An immuno-PET strategy was devised to employ CA125-targeted monoclonal antibody (MAb B43.13) and its derivative single chain Fragment variable (scFv) as molecular probes for imaging *in vivo* expression of CA125 via positron emission tomography. Anti-CA125 MAb and scFv were prepared and functionally characterized for their targeting capabilities prior to and post radiolabeling them for use in immuno-PET imaging. In separate applications of this strategy, we employed three different PET-radionuclides – ^{18}F, ^{64}Cu and ^{89}Zr

with suitable versions of the antibody molecule as targeting vectors to carry out same-day, next day or later time point *in vivo* imaging of EOC in subcutaneously xenografted mice models.

Results: Biochemical methods of analysis including immunofluorescence, flow cytometry and immunoblotting revealed highly specific binding of the antibody vectors to CA125-positive NIH:OVCAR-3 cells with no binding to CA125-negative SKOV3 cells. Radiolabeled versions of the anti-CA125 MAb and scFv were obtained with high specific activity and both radioimmunoconjugate vectors demonstrated highly selective binding to NIH:OVCAR-3 cells and virtually no binding to SKOV3 cells. *In vivo* radiopharmacological evaluation of the anti-CA125 radioimmunoconjugate vectors in xenograft mice models provided consistently high absolute uptake values in NIH:OVCAR-3 tumors and minimal uptake in SKOV3 tumors. Results from small animal PET imaging were confirmed by *ex vivo* digital autoradiography, immunofluorescence and immunohistochemistry.

Conclusions: CA125 is a suitable target for non-invasive imaging of epithelial ovarian cancer. Radiolabeling of anti-CA125 MAb and scFv with positron emitting radionuclides did not compromise their immunoreactivity to the target antigen. Both the antibody-based radioimmunoconjugates presented targeted tumor accumulation and an expected *in vivo* biological clearance profile. This renders them as potential immuno-PET probes for targeted *in vivo* molecular imaging of CA125 in Epithelial Ovarioan Cancer.

PREFACE

This thesis is an original work done by Sai Kiran Sharma. The thesis is a part of a research project that received research ethics approval from the Animal Care Committee of the Cross Cancer Institute, Edmonton – *In vivo* chemistry for pretargeted molecular imaging and therapy of cancer, No. AC11191 approved on December 7, 2011.

The introduction in chapter 1 is my original compilation of existing literature on the subject. However, the highly inter-disciplinary nature of work for this thesis project necessitated chapters 2, 3, 4 and 6 to be executed in liaison with members from the Wuest lab and central facilities at the University of Alberta. I synthesized, engineered, functionally characterized and radiolabeled the antibody-based vectors used for targeting ovarian cancer cells and tumors in all projects presented in this thesis. Small animal imaging was performed and analyzed by Dr. Melinda Wuest. I have authored all the chapters of this thesis under the supervision of Dr. Frank Wuest.

Chapter 5 of this thesis is the result of collaboration between Dr. Frank Wuest at the University of Alberta, Canada and Dr. Jason Lewis at the Memorial Sloan-Kettering Cancer Center, (MSKCC) USA. I engineered and radiolabeled the antibody vector used for this project, while the animal studies were carried out with Dr. Brian Zeglis, Kuntal Kumar Sevak and Sean Carlin in the Lewis lab at MSKCC, who also contributed to the manuscript for this chapter.

Chapter 2 of this thesis has been published as Sharma SK, Suresh MR, Wuest FR, Improved soluble expression of a single-chain antibody fragment in *E.coli* for targeting CA125 in epithelial ovarian cancer. *Protein Expression and Purification*, 2014 July, Issue 102: 27-37.

Chapters 3 and 4 of this thesis have been submitted to the European Journal of Nuclear Medicine and Molecular Imaging Research; and are presently under peer review. Chapter 5 will be submitted for publication to the Journal of Nuclear Medicine. Chapter 6 is in the works and will be submitted to Molecular Imaging and Biology.

DEDICATION

I dedicate this thesis and my doctorate to the faith and inspiration of

my loving wife NEHA SHARMA,

to the memory of my beloved mother NEELAM SHARMA

&

to the strength and sacrifice of my dear father

AMAR DUTT SHARMA

ACKNOWLEDGEMENTS

I wish to express sincere gratitude to my supervisor, Dr. Frank Wuest, for his tremendous support that reflected in his enthusiasm and accessibility for discussions, collaborative intent, scientific flexibility and motivation for excellence that meant a lot to me throughout my Ph.D program. I thank Dr. Mavanur Suresh for inducting me into the University of Alberta as his graduate student. I wish him well through his retirement. Special thanks are extended to Dr. Lars-Oliver Klotz for agreeing to be my co-supervisor and supporting me through the rest of the program in absence of Dr. Suresh. Dr. Hoon Sunwoo is equally thanked for providing me with access to the facilities and resources in his lab to accomplish my research.

I sincerely thank the members of my graduate supervisory and candidacy committee – Dr. Michael Doschak, Dr. John Lewis and Dr. Yangxin Fu for their excellent insights and support through the program.

I acknowledge every member of the Wuest, Suresh and Klotz labs for their support in more ways than one. Some of them are central to the work presented in this thesis and I would like to extend a very special thanks to each of them – Dr. Melinda Wuest and Monica Wang for excellent work and terrific support with the animal studies; Dr. Vincent Bouvet and Jenilee Way for training me on several aspects related to radiochemistry; Dr. Batchu, Dr. Raghuwanshi, and Dr. Ganguly for helping me set myself up in Edmonton and the Suresh lab through the initial days of the program – I am deeply grateful to you guys.

There is a reason to be even more grateful when people outside of the defined research group help a fellow researcher tackle scientific problems. I am deeply grateful to the following people for helping me by going out of their way on many occasions and teaching me so much – Bonnie Andrais, Geraldine Barron, Jingzhou Huang, Darryl Glubrecht, Dr. Razmik Mirzayans, Dr. Jody Groenendyk, Biwen Xu, Dr. Jack Moore, Dr. Jitendra Kumar, Cheryl Nargang, Dr. Atul Bhardwaj, Dr. Matthew Hildebrandt and Dr. Hilmar Strickfaden. I am also grateful to Dr. Jason Lewis and Dr. Brian Zeglis for providing me an opportunity to work in collaboration and gain hands-on experience with ^{89}Zr-labeling in their laboratories at the Memorial Sloan-Kettering Cancer Center, NY, USA. Dr. John Wilson, Blake Lazurko and David Clendening are also thanked for their support with ^{18}F synthesis in the cyclotron facilities at the Cross Cancer Institute, Edmonton.

I wish to thank the Faculty of Graduate Studies, Faculty of Medicine and Dentistry and the Faculty of Pharmacy and Pharmaceutical Sciences at the University of Alberta for funding my graduate studies. Special thanks are extended to Natural Sciences Engineering and Research Council of Canada (NSERC) – CREATE program for funding my training as a radiochemist to develop molecular probes.

Finally, I am deeply grateful to my family and friends for all their love and support through this journey.

TABLE OF CONTENTS

LIST OF TABLES

LIST OF FIGURES

LIST OF ABBREVIATIONS AND SYMBOLS USED

aa	amino acid
A488	Alexa fluor-488
µm	micrometer
µL	microliter
µCi	microcurie
µg	micrograms
% ID/gm	percentage injected dose per gram
CA125	Cancer Antigen 125
CO_2	Carbon di-oxide
C-terminus	Carboxyl terminus of a protein
^{64}Cu	Copper-64
˚C	degree Celsius
DNA	Deoxyribose Nucleic Acid
DAPI	4', 6-Diamidino-2-phenylindole
DTT	Dithiothrietol
ELISA	Enzyme Linked Immunosorbent assay
EOC	Epithelial Ovarian Cancer
E.coli	*Escherichia coli*
EPR	Enhanced Permeability and Retention
EDTA	Ethylene Diamine Tetraacetic Acid

HPLC	High Performance Liquid Chromatography
[^{18}F]FDG	^{18}F-fluorodeoxyglucose
^{18}F	Fluorine-18
FITC	Fluorescein Isothiocyanate
γ	gamma
IPTG	Isopropyl β – D -1 thiogalactopyranoside
IgG	Immunoglobulin G
IMAC	Immobilized Metal Affinity Chromatography
immuno-PET	immune Positron Emission Tomography
Kb	Kilobases
KBq	KiloBequerels
K_D	Dissociation Constant
KDa	Kilo Daltons
L	Liter
M	Molar
Mol	moles
MAb	Monoclonal Antibody
MW	Molecular Weight
MALDI-ToF	Matrix Assisted Laser Desorption/Ionization – Time of Flight
mg/mL	milligrams per milliliter
MeV	Mega Electron Volts

MBq	MegaBequerels
Min	minutes
mCi	millicurie
OD	Optical Density
PAGE	Polyacrylamide Gel Electrophoresis
PCR	Polymerase Chain Reaction
p.i	post injection
rpm	revolutions per minute
ROI	Region of Interest
RCY	Radiochemical Yield
scFv	single chain Fragment variable
SDS	Sodium Dodecyl Sulphate
SEC	Size Exclusion Chromatography
SOE-PCR	Splice Overlap Extension PCR
SUV	Standardized Uptake Value
$t_{½}$	half-life
V_L	Variable Light Chain
V_L	Variable Heavy Chain
^{89}Zr	Zirconium-89

1

INTRODUCTION

1.1 HUMAN OVARIES: Structure and Function

The ovaries are a pair of primary female reproductive organs suspended by a mesentery on either side of the uterus and located in shallow depressions called the ovarian fossae within the lateral walls of the pelvic cavity. Described as ovoid shaped structures akin to the size of an almond measuring 3.5 cm in length, 2 cm wide and ~ 1 cm thick, with slight variations in these dimensions occurring as a function of age and physiological activity, each ovary is attached to the fimbriae of the fallopian tube that arches over its medial surface.[1]

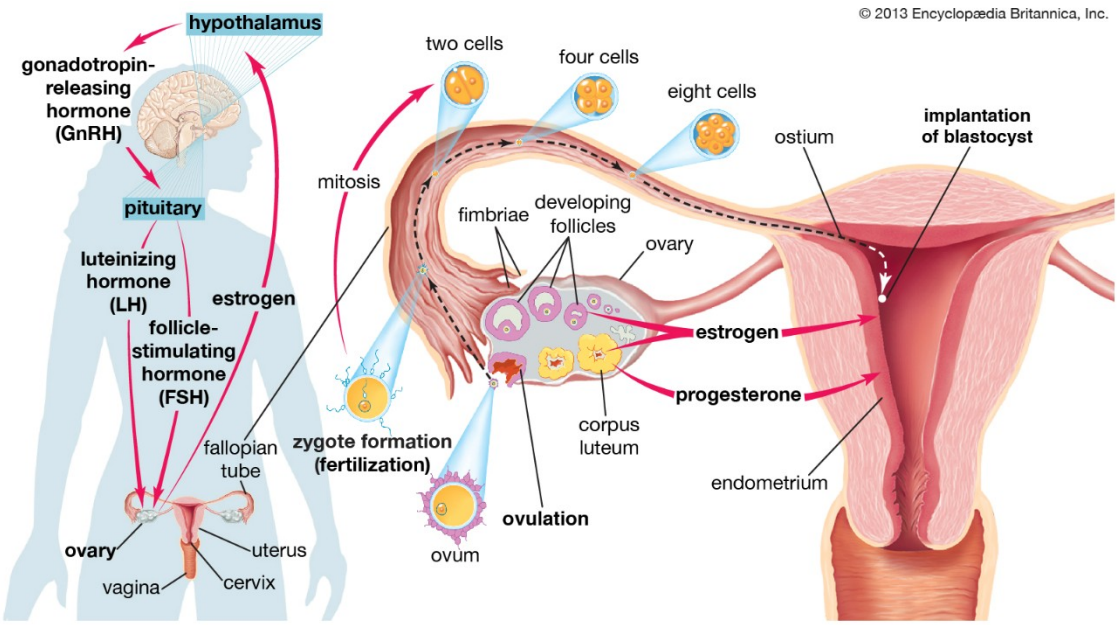

Figure 1.1: Major structures and hormones of the human female reproductive system. Image retrieved July 6, 2014 from Encyclopaedia Britannica *http://www.britannica.com/EBchecked/media/19648/Major-structures-and-hormones-involved-in-the-initiation-of-pregnancy*

The ovaries perform two major functions[2]:

a) Generation of a fertilizable oocyte with full potential for development
b) Secretion of female steroidal hormones required in preparation of the reproductive tract for fertilization and subsequent establishment of pregnancy

Anatomically, such a bifunctional unit necessitates a degree of compartmentalization in its structural organization. This is reflected by the fact that the ovary is derived from multiple embryonic structures including the coelomic epithelium, sub-coelomic mesoderm and primordial germ cells from the yolk sac endoderm. Consequently, it is comprised of several cell types to serve specified structural, reproductive and hormonal functions.[3] On their exterior, the ovaries are covered with a cuboidal single cell mesothelial layer of cells commonly referred to as the "Ovarian Surface Epithelium" (OSE). This layer is also called as the visceral peritoneum and is continuous with the serosa of the fallopian tube, peritoneal cavity and uterus. Deeper into their anatomy, the ovaries are divided into a dense granular outer cortex comprising of several ovarian follicles containing oocytes in different stages of development and an inner medulla comprised of blood vessels, lymphatics and nerve fibers.[1]

The functional activity of oogenesis in the ovaries begins early during fetal development with the formation of primary oocytes that remain suspended in prophase of meiosis I. On reaching puberty and under the influence of follicle stimulating hormone, the oocyte and associated follicle mature and get ready for ovulation that is further triggered by the luteinizing hormone. Each ovulatory

cycle releases secondary oocytes into the peritoneum that ultimately reach into the fallopian tube for potential fertilization.[1]

1.2 Cancer of the Ovary: One Name, Many Diseases?

In light of the aforementioned embryonic origins of the ovary that lead to its multi-compartmental organization as a functional apparatus, each cell type in its composition is thence capable of forming a different neoplasm in itself.[3] Therefore, emerging knowledge suggests that cancer of the ovary is a rather heterogeneous and complex group of diseases than just one entity.[4]

1.2.1 Disease Classification:

This section briefly illustrates the classification of ovarian cancer as per an evolving understanding of this complex disease.

Classification based on cell of origin:

Ovarian cancer has been noted to arise from 3 different cell types[5, 6]:

1) Malignant Epithelium – > 95 % of all ovarian cancers
2) Germ Cells – 2 - 3 % of all ovarian cancers
3) Gonadal or Sex Cord Stromal – 1 - 2 % of all ovarian cancers

Classification of Epithelial Ovarian Cancer based on Clinical Histopathology, Immunohistochemsitry and Molecular genetic analysis:

With epithelial ovarian cancers (EOC) being the most common type in the context of clinicopathologic and epidemiologic occurrence, this histotype has been more recently sub-classified into 5 sub-types on the basis of histopathology[5]:

1) High Grade Serous Ovarian Carcinomas (70 %)
2) Endometrioid Carcinomas (10 %)
3) Clear Cell Carcinomas (10 %)
4) Mucinous Carcinomas (3 %)
5) Low Grade Serous Carcinomas (< 5 %)

Classification based on Stage:

The International Federation of Gynecologic Oncology (FIGO) has provided a staging of ovarian cancer.[5] Ovarian cancer is a surgically staged disease. The stage of a cancer is reflective of its extent of spread in the body and is a good indicator to guide treatment of the disease.

Stage I: Tumor is confined to the ovaries or fallopian tube

Stage II: Tumor involves one or both ovaries or fallopian tubes with extension into the pelvis - uterus, tubes or other intraperitoneal tissues

Stage III: Tumor has spread beyond the pelvis – retroperitoneal or inguinal nodes

Stage IV: Tumor has spread to distant sites such as liver parenchyma and/or shows presence of pleural effusion

***Independent origin for each histotype*?**

Given a common embryonic origin of the ovarian surface epithelium and the lining of the peritoneal cavity from the coelomic epithelium, there tends to be a high degree of resemblance in the morphological appearance of neoplastic cells with their non-neoplastic counterparts in many parts of the female genital tract.[7] In more recent studies, this feature has linked specific subtypes of neoplastic cells to their more benign epithelial counterparts in these tissues as being potential sites of origin unlike previous assumptions whereby all subtypes of ovarian carcinomas were considered to be primarily ovarian in origin. For example: a benign structure such as endosalpingiosis in the fallopian tube bears resemblance with serous carcinomas, benign endometriosis bears resemblance to endometrioid and clear cell carcinomas, whereas endocervicosis has resemblance with mucinous carcinomas.[8] Despite such a revelation, it is ironic that current clinical treatment of epithelial ovarian cancer does not take into consideration these differences in histotypes to treat each of them as separate diseases.[7]

Classification based on underlying molecular fingerprint:

Furthermore, the objective to identify a common molecular fingerprint for ovarian cancer has inspired an investigation into the genetic and epigenetic landscape of neoplastic cells from different histotypes.[9] Although no common genetic alteration specific to ovarian cancer was identified by this approach, molecular and genetic fingerprints specific for certain ovarian histotypes were identified. In some cases, these were specific enough to enable distinguishing high grade from

low-grade carcinomas – particularly in the case of low grade versus high-grade carcinomas of the serous and endometrioid histotypes. These findings led to a proposal for reclassification of ovarian cancers in to two major categories:[7, 9]

Type I: Indolent tumors that are mostly restricted to the ovaries and constitute 25% of all ovarian carcinomas known to result in 10% of ovarian cancer related mortality.[10] These tumors are generally found to have mutations in *KRAS* (v-Ki-ras2 Kirsten rat sarcoma viral oncogene homology), *BRAF* (v-raf murine sarcoma viral oncogene homolog B1), *PTEN* (phosphatase and tensin homolog), *PIK3CA* (phoshatidylinositol 3-kinase catalytic subunit), *CTNNB1* (gene encoding β-catenin) *and HER2* (human epidermal growth factor receptor 2) and to develop in a stepwise fashion from well-recognized precursor lesions which are mostly borderline tumors. Overall, these tumors are genetically stable and thus resistant to platinum-based chemotherapy. The following histotypes and their corresponding mutated genes fall under this category:

A) Low Grade Serous Carcinoma (LGSC) - *KRAS*, *BRAF*
B) Low Grade Endometrioid Carcinoma (LGEC) – *CTNNB1, PTEN, PIK3CA*
C) Clear Cell Carcinoma – *PIK3CA, PTEN*
D) Mucinous Carcinoma – *KRAS*

Type II: Highly aggressive tumors that are usually metastasized by the time of diagnosis. This category comprises the most common form of serous ovarian

cancer that accounts for 75% of all epithelial ovarian cancers and causes 90% ovarian cancer related mortality.[10] These tumors are rarely diagnosed at early stages since their transition from occult lesions to malignant disease is rapid owing to their anatomical location on the surface of ovaries conducive for sloughing off and spreading of the malignant cells into the peritoneum. These tumors generally have mutations in the *TP53* gene and may also carry chromosomal gains/ amplifications of CCNE1 (Cyclin E1), which contributes to genetic instability in the presence of mutated *p53*. In fact, serous epithelial ovarian carcinomas are known to have the highest frequency of p53 mutations of any solid tumors.[11] These tumors are thus genetically unstable and highly susceptible to platinum-based chemotherapy. Nevertheless, they have a high rate of recurrence. The following histotypes fall under this category:

E) High Grade Serous Carcinoma (HGSC): 70% of epithelial ovarian cancers.
F) High Grade Endometrioid Carcinoma
G) Undifferentiated Carcinoma

Such a dual system of classification has led to the stratification of this disease inclusive of its epidemiology, molecular events, patterns of spread, premalignant origins, response to therapy and prognosis.

1.3 Pathogenesis of Epithelial Ovarian Cancer:

One of the most critical aspects to treat a malignancy is to know its cellular origins. While most cases of epithelial ovarian cancer are sporadic, 5 – 10% women may be genetically predisposed to the disease by virtue of carrying mutations in the BRCA gene.[12] Despite the aforementioned identification of the various subtypes of ovarian cancers and the elaborate classification based on histopathology and genetic alterations that lead to a malignant phenotype, there continues to be an incomplete understanding of the pathogenesis of epithelial ovarian cancers – especially that of high-grade serous carcinoma, which forms the epidemiologically most aggressive malignant subtype.

1.3.1 Incessant Ovulation Theory:

In 1971, Fathalla proposed the popular "Incessant Ovulation Theory" behind the origin of EOC, based on observations for high incidence of metastatic ovarian adenocarcinoma in hens that were forced to lay eggs through uninterrupted ovulation and consequently had extensive damage to their ovarian surface epithelium in this process.[13] The theory suggested an internalization of the damaged OSE leading to the formation of inclusion cysts that underwent metaplasia to differentiate into Mullerian-like epithelium. Such inclusion cysts were proposed to eventually become dysplastic and manifest as ovarian carcinoma. Furthermore, this theory resonated with epidemiologic evidence in human populations wherein risk of ovarian cancer was shown to increase as a function of the frequency of ovulation. This was evidenced by data that showed

women who had breaks in their ovulatory cycles as a consequence of pregnancy and/or intake of oral contraceptive pills (OCP) were at a reduced risk whereas nulliparous women were at an increased risk for ovarian cancer. However, this theory was in disagreement with other epidemiologic data such as evidence from women with polycystic ovarian syndrome (PCOS) who were at increased risk for EOC despite naturally infrequent ovulation. Furthermore, it was also shown that most OCPs functioned similar to progesterone – only formulations that do not preclude ovulation.[3]

1.3.2 Gonadotropin Hypothesis:

Alternatively, the gonadotropin hypothesis premised on the end result of an overstimulated OSE being at risk for malignant transformation under the effect of Follicle Stimulating Hormone (FSH) and luteinizing hormone (LH) was proposed to explain the insufficiencies of the incessant ovulation hypothesis. This theory accounted for the nulliparous women and those with PCOS as having high levels of gonadotropins and being at greater risk for ovarian cancer when compared to pregnant women and those taking OCPs, who had low levels of gonadotropins. Furthermore, it was able to account for perimenopausal women developing ovarian carcinomas due to an increased production of gonadotropins. However, there is no conclusive evidence to demonstrate malignant transformation of inclusion cysts or OSE as a result of gonadotropin exposure, even though few animal studies have shown that gonadotropin exposure promotes tumor growth.

In summary, both the aforementioned theories are based on the premise that ovulation by itself is an inflammatory process[14] involving repetitive disruption of the ovarian surface and its subsequent exposure to estrogen rich follicular fluid, release of cytokines and an influx of inflammatory cells in to the ovarian stroma. This is accompanied by increased oxidative stress via production of reactive oxygen (ROS) and reactive nitrogen species (RNS), cell damage, elevation of cytokines, proteases, prostaglandins and an onset of repair mechanisms with potential epithelial to mesencymal transition (EMT).[15] Taken together, all of these factors increase the susceptibility for occurrence of mutations augmented by the repetitive nature of this stress on a monthly basis throughout the reproductive age of women to potentiate oncogenesis.[16]

1.4 A New Paradigm in Ovarian Cancer: Role of the Fallopian Tube

Even though the anatomical and physiological features of the fallopian tube have been well documented in literature, it has only recently come to light in a manner that is challenging all previous understanding of epithelial ovarian cancer pathogenesis and etiology.[17]

As mentioned previously, the ovaries are derived from multiple embryonic structures and are covered by a cuboidal mesothelial layer called as the OSE. Therefore, the ovaries by themselves do not have a well-differentiated epithelium. All other organs of the female reproductive system – fallopian tubes, cervix, uterus and vagina are derivatives of the Mullerian duct. This distinction in developmental origins is further evidenced in patients with Mullerian agenesis

who have fully functional ovaries. Furthermore, the OSE is not reported to express CA125, which happens to be a marker of well-differentiated epithelium; rather it is known to express mesenchymal markers – vimentin and N-cadherin. This has strongly questioned the "ovarian origins" of EOCs in the absence of a real epithelial cell in the OSE. Instead, further clinicopathologic and genetic assessment of samples from epithelial ovarian cancers have revealed that most of these cells resemble the Mullerian – derived epithelium of the female genital tract. Further evidence was reported by Piek et al[18] in 2001, upon finding hyperplastic or dysplastic lesions with intraepithelial components located at the fimbriated ends of the fallopian tubal segments from women undergoing risk reduction bilateral salpingo-oophorectomies (BSO) either on account of harbouring a *BRCA* mutation or having breast cancer and/or a strong family history of ovarian cancer.

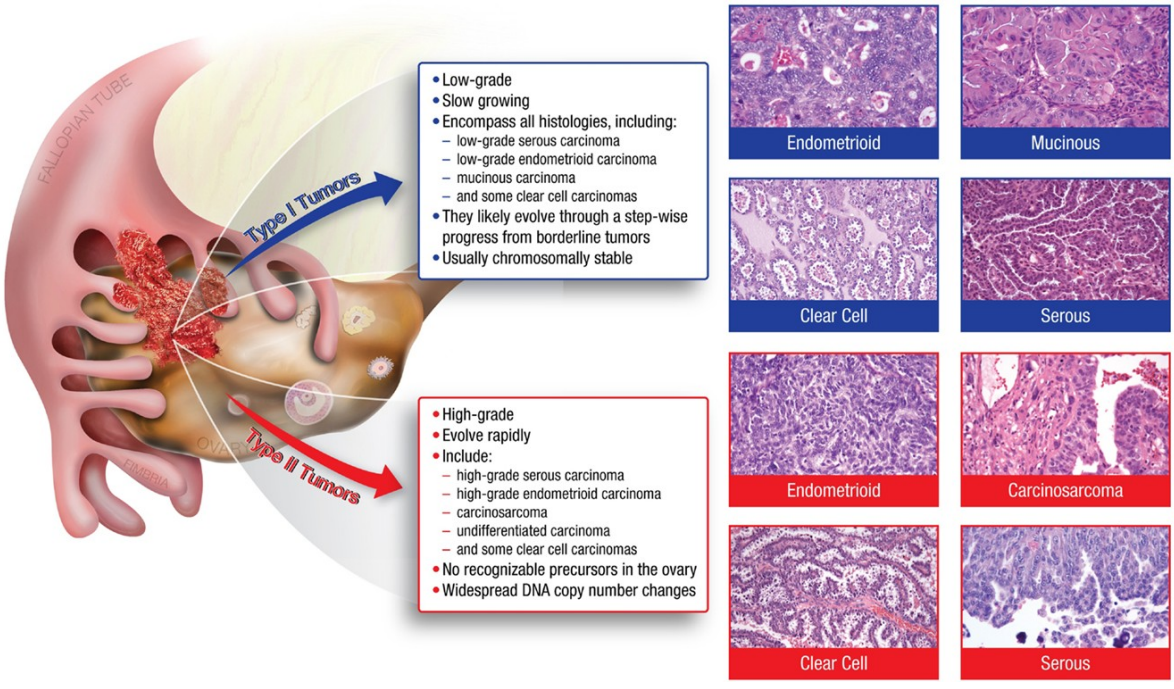

Figure 1.2: Ovarian cancer subtypes under the dual classification system. Image reproduced with permission from Jones PM and Drapkin R, *Front.Oncol.* 3:217 [8]

Such intraepithelial components came to be called as "Tubal Intraepithelial Carcinomas" (TIC) and have been characterized by strong cytoplasmic accumulation of mutated *TP53*, which has been previously mentioned as a hallmark of almost 100% Type II high-grade serous ovarian carcinomas. Furthermore, benign regions of the distal tubal epithelium that were found to express *TP53* have been termed as "p53 signatures" and are proposed to appear as precursor lesions earlier than TICs in the transformative process leading to high-grade serous carcinomas.[19] These observations held strong validity for the presence of TICs even with immunostaining and analysis of thin sections of distal tubal fimbriae from women outside the BRCA mutation cohorts.[20] This study also successfully established the clonality of metastatic ovarian cancer through identification of the same *TP53* mutation analyzed in the metastasized cells and the TIC.[21] Furthermore, TICs are a characteristic feature of HGSCs and are not found in endometrioid or mucinous subtypes of EOC.[22]

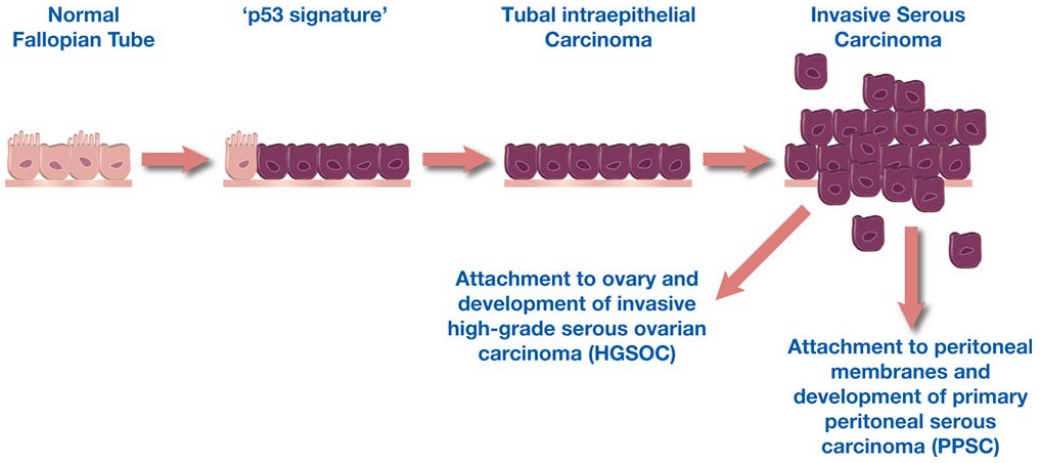

Figure 1.3: Stepwise development of High Grade Serous Carcinomas from the fallopian tube. Image reproduced with permission from Karst AM, Drapkin R, *F1000 Med Rep* 2011;**3**: 22.[24]

In addition, a comparative molecular analysis of p53 mutations from the distal fimbriae of fallopian tubes and ovarian inclusion cysts in $BRCA^{+}$ women undergoing risk reduction surgeries, revealed an absence of p53 mutations in the inclusion cysts but presence in the fallopian tubes of 38% of women in this study.[23]

Finally, this theory proposes that even though TICs may not be present in all HGSCs, most of them arise in the distal fallopian tubal epithelium as areas of dysplasia, which further transform into malignant cells. A convenient anatomical location of these malignant cells located at fimbriated ends, allows them to slough off and spread into the peritoneum or rub against the OSE of the neighbouring ovaries. However, in the absence of any ovarian involvement these metastasized cells may also form peritoneal carcinomas or tubal carcinomas.[3] Thus such a Tubal Intraepithelial Carcinoma theory based on the role of the fallopian tube explains an organized and logical manner in which HGSCs could potentially transition from benign to dysplastic lesions to form intraepithelial components (TICs) that ultimately transform into serous tubal intraepithelial carcinomas (STIC) prior to spreading peritoneally as disseminated serous carcinomas.[24]

More recently, the research group of Drapkin et al have developed an *ex vivo* model to recapitulate the human fallopian tube epithelium.[25] This has been used to demonstrate the transformation of secretory epithelial cells and their response to cellular stress such as genotoxic insult etc. They have also reported the

development of (hTERT) immortalized secretory fallopian epithelial cells and (c-myc) / (oncogenic Ras) transformed versions of these cells to recapitulate high-grade pelvic serous carcinomas (HGPSC) for *in vitro* and *in vivo* use with immunocompromised xenograft mice.[26]

The TIC theory and the aforementioned recent developments are having major implications to facilitate the search for new biomarkers, targeted therapies and imaging techniques directed in the right anatomical, molecular and physiological contexts respectively. Since most pre-malignant lesions including TICs for HGSC in women with $BRCA^{+}$ mutations have been found to exist in the distal tubal fimbriae, risk reduction surgery restricted to a salpingectomy would get rid of the fallopian tubes while preserving the ovaries. This bears great significance from an endocrine point of view as well as to avoid side effects such as cardiovascular risk, osteoporosis and cognitive impairment as a consequence of a complete hysterectomy or bilateral salpingo-oophorectomy.[3, 12]

In summary, it is now apparent that the disease previously considered "Ovarian Cancer" was grossly a misnomer. This is becoming clearer with an emerging understanding of the molecular basis for ovarian cancer as a very heterogeneous and complex set of independent diseases. Furthermore, provocative evidence to propose a tubal origin to HGSCs that were previously thought to arise from the OSE, is now challenging the field to delve deeper into the molecular pathogenesis of this disease. This inspires a new hope in the search for better diagnostic and

therapeutic approaches that may enable an early detection of the elusive malignancy!

1.5 TUMOR BIOMARKERS:

Simply put, tumor biomarkers are molecular signatures of neoplastic cells that help identify them within a complex cellular milieu. These inlcude genetic signatures characterized by DNA mutations, chromosomal alterations – gains or losses in segments, epigenetic changes, overexpressed and/or secreted proteins that are found in higher than normal amounts in the blood or other body fluids of individuals having a tumor. Tumor markers are not always limited to those that are produced by the neoplasms themselves, but could also be produced by the body in response to a neoplastic entity.

Furthermore, tumor biomarkers have been classified into two broad categories:[27]

A) Tumor Specific Antigens – molecules that contribute primarily to oncogenesis and are not expressed in normal cells of the body. For example: mutated p53 or Ras oncogenes, carcinoembryonic antigen (CEA) and alfafetoprotein (AFP).

B) Tumor Associated Antigens – molecules that are expressed differently between normal and neoplastic cells and are of utility in identifying cancerous cells from their healthy counterparts. For example: CA19-9, CA125

Some of the desirable features in a clinical biomarker are that it should be specific, reliable, measurable and predictive in nature. Given the relatively low

incidence for occurrence of ovarian cancer in the general population (12.3 per 100,000 in the United States between 2007 – 2011 [SEER, NCI, USA]), developing a tumor biomarker with relevance for screening faces a special challenge in that such a test needs to have a very high degree of specificity. Statistically, this demands a sensitivity of 75% and a specificity of 99.6% in order to achieve a positive predictive value of 10%.[28] CA125 – Cancer Antigen 125, as such is elevated in 80% of women with EOC and is reported to have a sensitivity of 50 – 62% for patients with early stage disease and 90% for patients with advanced stage disease.[29] Furthermore, with specificity > 95% for all advanced stage cases, CA125 is more suited as a biomarker for recurrence rather than general screening, wherein it tends to have a lower specificity. In recent years, several molecules such as HE4 (human epididymis 4), mesothelin, M-CSF (macrophage colony stimulating factor), Osteopontin, KLK6 (Human Kallikrein-6), CA72-4, CA19.9, CA15.3, MUC1, AFP and others have been assessed alone or in combination with CA125 in order to increase the sensitivity of a screening test for primary ovarian cancer.[30] Among these, the use of HE4 and CA125 together has demonstrated highest accuracy for the detection of malignancy. As of now, there is no single biomarker that outperforms CA125 to indicate an ovarian malignancy.

1.5.1 A Focus on CA125: Cancer Antigen 125

With a history of over three decades since its discovery by Bast and colleagues in 1981,[31] and despite its limitations for sensitivity and specificity, CA125 has long served as the most reliable tumor biomarker that has come to be a 'gold standard' of reference in the clinical assessment of epithelial ovarian cancer. CA125 is a mucinous glycoprotein expressed by fetal amniotic and coelomic epithelium.[32] Owing to its mucinous nature and a much later discovery of its being encoded by the MUC16 gene,[33] it is common to find literature interchangeably referring to this tumor biomarker as CA125 or MUC16. Under normal physiologic conditions, CA125 is expressed in adult tissues such as mesothelial cells of the pericardium, pleura and peritoneum that are embryonically derived from the coelomic epithelia and also in derivatives of the Mullerian epithelia such as fallopian tubes, endometrium and endocervix that constitute organs of the female genital tract. Other anatomical regions positive for the expression of CA125 include the ocular epithelium and the upper respiratory tract. CA125 can also be isolated from the peritoneal ascites of ovarian cancer patients.[34]

Subsequent to its molecular identification using a murine monocolonal antibody – OC125, several antibodies were developed for binding to CA125.[35-40] This led to their classification on the basis of three distinct epitopic regions / domains found in the CA125 antigen:[38]

Region A: binds OC125 like antibodies

Region B: binds M11 like antibodies

Region C: binds Ov197 like antibodies

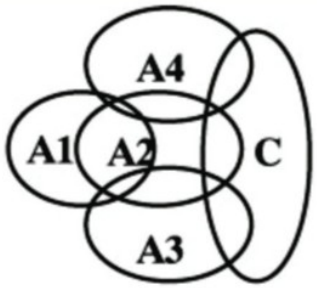

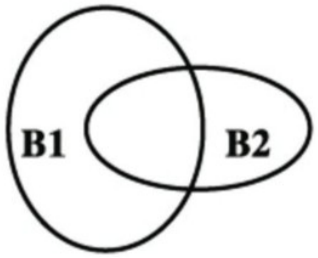

A = Oc125 -like

A1 = Oc125 and OvK95
A2 = OvK93
A3 = B43.13
A4 = ZS33, B27.1 and CCD247
A? = Ov198, K100

C = Ov197

B = M11 -like

B1 = M11, ZR45, MA602 -6
K91, Ov185, OvK101
K90, K94, K96, K102
CCD242, 145 -9, 130-22
B2 = ZR38
B? = MA602 -1

Figure 1.4: Representation of the 3 antibody binding domains (A-C) on the CA125 epitope. Image reproduced with permission from Nustad K et al, *Tumour Biol* 1996;**17**(6): 325-31.[37]

Biochemically, CA125 has been described as a repeating peptide epitope on a mucinous glycoprotein – MUC16, which is proposed to be 22,152 amino acids (aa) long with a molecular weight of 2.5 MDa (Mega Dalton), which potentially doubles in size as a result of glycosylation to produce a 3 -5 MDa glycoprotein.[41, 42] A conformation dependent peptidic nature of the CA125 epitope was revealed through the seminal works of Davis et al who conclusively demonstrated the sensitivity of CA125 to high temperature, low pH and treatment with proteases. This work also showed that there was a minimal effect from periodate treatment of the glycoprotein, thereby refuting previous claims of CA125 being a carbohydrate antigen.[43]

1.5.2 Structure of CA125:

Molecular cloning and analysis of MUC16 revealed its organizational similarity to other mucins that are known to have a tandem region sandwiched between N-terminal and C-terminal regions of the glycoprotein.[44] MUC16 has been described to have four distinct parts in its molecular structure:[45, 46]

1) A large N-terminal region – providing glycosylation sites
2) A tandem region – providing antibody binding sites
3) A transmembrane domain – providing an anchoring site
4) A cytoplasmic C-terminus – providing sites for phosphorylation

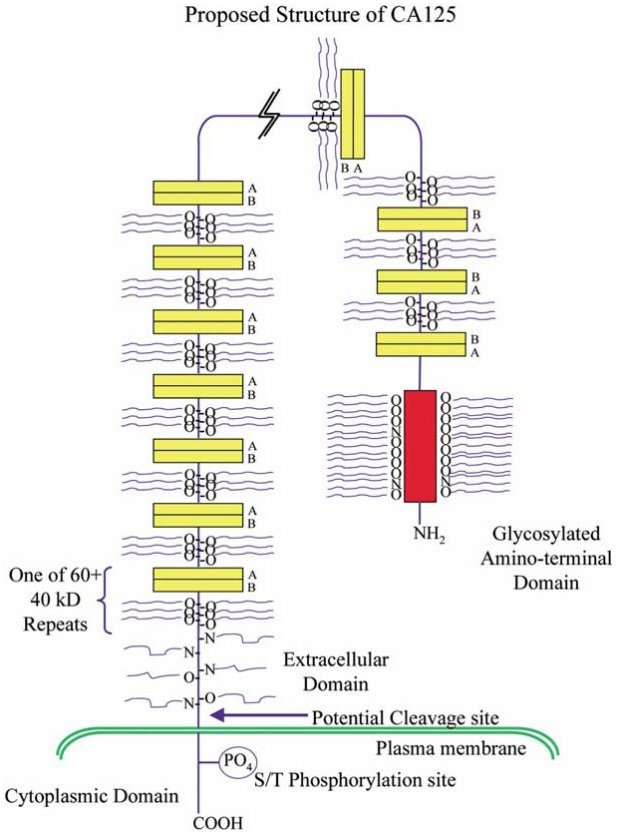

Figure 1.5: Proposed molecular structure of MUC16. Image reproduced with permission from O'Brien TJ et al, *Tumour Biol* 2001;**22**(6): 348-66.[45]

N-terminal region:

The extracellular N-terminus is reported to have 12,068 amino acids rich in serine and threonine residues acting as suitable sites for *O*-linked glycolsylation.

Tandem Repeat Region:

The tandem region has been described to have up to 60 repeats with each repeat being composed of 156 amino acids which are not identical but largely homologous per repeat. Two interesting aspects of the tandem regions are:

A) Presence of a highly conserved pair of cysteines at positions 59 and 79 that are potentially involved in the formation of intramolecular disulfide bonds that create loop-like structures within the MUC16 molecule. Alternatively, intermolecular disulfide bonds between the conserved cysteine residues have been proposed to promote the formation of an extracellular matrix.

The 21-mer-loop structure between Cys 59 and Cys 79 had previously been described as potential epitopic site on the CA125 peptide – called as the 'cysteine loop'. Some of the key characters of the cysteine loop as ideal sites for antibody binding included: a) an ability of the disulfide bond to push amino acids comprising the loop to move away from the protein core and thus become more available for antibody binding; b) the presence of hydrophilic amino acids at the center of the loop; c) the relative absence of nearby glycosylation.

Nevertheless, unlike previous experiments wherein protease digestion of this loop abrogated antibody binding with CA125, recent independent reports of Brennan et al using deletion constructs of the 156 aa repeat region and Berman et al.[47] using synthetic 21-mer peptide have challenged the cysteine loop theory to suggest that the cysteine loop by itself is insufficient as the target epitopic site. Taken together, their results questioned the accuracy of the cysteine-loop model to define a region on the CA125 epitope for antibody binding. Furthermore, studies with deletion constructs of the 156 aa tandem repeat regions have shown that deletion of the amino acids between position 129 through 156 did not impact antibody binding, but subsequent deletion of the first 30 amino acids at the N-terminus of such a construct abrogated binding to anti-CA125 antibodies from all three categories – OC125, M11 and Ov197. This has also led to a proposition for CA125 to be a discontinuous epitope within the 1 – 129 aa region of each tandem repeat.

B) Positively charged SEA (Sea Urchin Sperm Protein, Enterokinase and Agrin) domains in this region present a sandwich three-dimensional structure formed by two alpha helices, four antiparallel beta strands and a hydrophobic core. The presence of multiple SEA domains is a unique feature of MUC16 although their biological role has not yet been determined. SEA domains tend to have an autoproteolytic role, but it is uncertain if this directly contributes to the shedding of CA125 in the serum.

C-Terminal Region:

CA125 is tethered to the surface of neoplastic cells through the C-terminal domain of MUC16 comprised of 284 amino acids and has a potential site for phosphorylation that is proposed to play a role in cleavage of the mucin and release of the MUC16 ectodomain into the serum.

However, despite the recent progress made in deciphering the molecular structure and organization of the aforementioned regions of CA125 on this complex mucin, there is limited knowledge about the precise epitope sites for antibody binding/targeting, the role of multiple SEA domains, the effects of post-translational modifications and the factors that control the *in vivo* shedding of CA125.

1.5.3 Function of CA125:

Despite expression in the epithelia of normal tissues such as the pericardium, endometrium and cornea, a specific biological role for CA125 in health has not yet been understood.[44] Reports in the literature suggest an immunosuppressive role for this glycoprotein; particularly owing to its interaction with Natural Killer (NK) cells to reduce the expression of CD16 expression on their surface.[48] Such an NK-suppressive effect combined with its increased expression in pregnant women during the first trimester has also been suggestive of a role in preventing immunological rejection of the fetus.[49-52] Further, an interaction between MUC16 and galectin in the corneal epithelium has been proposed to provide a barrier to

bacterial and viral infections in the ocular epithelia.[53, 54] Additionally, owing to its expression in the pericardium, a rise in physiol.ogical CA125 levels has been implicated in congestive heart failure.[55, 56] However, MUC16 knock out mice have not shown any major physiological defects to warrant the mucin's indispensability in the health of these animals.[57]

In the context of ovarian cancer, MUC16 is reported to exercise an immunoprotective role to shield ovarian cancer cells from NK cells. This renders the tumor evasive to the immune system. Some of the mechanisms postulated to achieve this effect include steric hinderance of NK and ovarian cancer cell synapse formation[58] due to the macromolecular size of MUC16 and/or a consequence of binding between negatively charged terminal sialic acid residues of MUC16 with NK cell inhibitory receptors such as Siglec-9 that ultimately lead to an attenuation of natural killer cell activity against ovarian cancer cells.[59] This phenomenon has also been observed in MUC16 binding to monocytes, which are attracted to ovarian cancer cells and ultimately get attenuated in their downstream activity.[60] Additionally, NK cells within the ovarian tumor microenvironment have also been indicated in immune editing by virtue of attacking tumor cells with low levels of CA125 and thus indirectly enriching the tumor for cells with high levels of CA125 expression.[61]

Further, CA125 is also known to interact strongly with mesothelin expressed along the lining of the peritoneum.[62] This interaction is proposed to occur with a Kd of 5 nM between the N-glycans of MUC16 and super-helical ARM-type

repeats on mesothelin, that ultimately allows binding of ovarian tumor cells to the walls of the peritoneum to promote metastasis beyond the ovaries.[63, 64]

While knockdown of MUC16 in ovarian cancer cells has an anti-proliferative effect and negative impact on their metastatic potential, expression of its C-terminal domain in SKOV3 cells has been reported to increase their proliferation and *in vivo* tumor burden in xenograft mice.[65] These observations have been linked to downstream cell signaling interactions of MUC16 with components of the JAK-STAT pathway and/or Src-family kinases that induce E-cadherin mediated metastasis.[65]

1.5.4 CLINICAL UTILITY OF CA125:

As a consequence of neoplastic transformation in epithelial ovarian cells, CA125 is overexpressed and eventually shed into the blood pool of subjects. At present, the clinical usefulness of CA125 comes from its estimation in serum samples of individuals presenting in the clinic with pelvic masses suspected for ovarian cancer and in the follow-up of patients who have undergone cytoreductive surgery and/or chemotherapy. Typically, an immunoassay quantified serum CA125 level of $\leq$ 35 U/mL is considered normal while patients with advanced stages of the disease are known to have relatively higher serum CA125 levels.[66, 67] Nonetheless, CA125 levels can be elevated in premenopausal women during ovulatory cycles and also in the absence of neoplasia.[68]

Furthermore, CA125 has been employed as a screening biomarker in clinical trials. The most recent one is the United Kingdom Collaborative Trial of Ovarian

Cancer Screening (UKCTOCS), wherein > 200,000 post-menopausal women have been screened for ovarian cancer.[69] The interim results of this trial are promising and suggestive of > 47% women who tested positive in a combined assessment of CA125 levels with transvaginal ultrasound had stage I or stage II disease.[70] CA125 has also been used as a diagnostic marker for Epithelial Ovarian Cancer owing to the fact that elevation of CA125 levels have known to precede clinical detection of the disease at least by 3 months.[32, 71, 72] Also, the prognostic utility of CA125 has been highlighted by its ability to effect management of the disease through longitudinal monitoring of its levels in patients pre- and post-chemotherapy/surgery. This has been demonstrated by the fact that patients with elevated levels of CA125 post-treatment have a worse prognosis than those whose levels have normalized.[32, 67]

In addition to its diagnostic and prognostic utility, CA125 has also been a target for therapeutic approaches designed and attempted against EOC. Oregovomab (a MAb-B43.13 formulation), initially used as a radioimmunoscintigraphy agent[73] was later transformed into an immunotherapeutic[74] due to its ability for eliciting anti-idiotypic responses and T-cell stimulation against multiple epitopes on CA125 that resulted in an extended survival of patients treated with this agent.[75] After showing no significant effect as a monoimmunotherapy, Oregovomab (OvaRex-MAb-B43.13) is presently undergoing clinical trials in combination with routine adjuvant chemotherapeutic agents to treat ovarian cancer.[76] Abagovomab is an antibody that was used to generate specific anti-idiotypic

response to CA125.[77-80] Similarly, anti-mesothelin antibodies[81] and HN125 – an engineered version of the MUC16-binding epitope of mesothelin grafted onto the Fc portion of the human IgG1 antibody has been developed.[82] There have also been recent reports of antibody-drug conjugates (ADCs) using CA125-targeting antibodies – 3A5 and 11D10 conjugated with cytotoxic drug – monomethyl auristatin E (MMAE). These agents yielded promising results for high efficacy and minimal toxicity in Phase I clinical trials.[83, 84]

In summary, CA125 (MUC16) plays a vital role in the proliferation of EOC and its metastatis through an orchestration of intra- and inter-cellular interactions as described above. Simulatenously, the ability to clinically measure CA125 levels from the serum of EOC patients helps to monitor disease progression and to evaluate the response to therapy.

1.6 DIAGNOSIS OF OVARIAN CANCER:

This malady has metaphorically come to be known as the "whispering disease" and a "silent killer" owing to its synonymous description for asymptomatic progression. It is not only the fifth leading cause of cancer-related deaths in women, but also the most lethal gynecologic malignancy. This is exemplified by the National Cancer Institute's Surveillance Epidemiology and End Results (SEER) report for 2014, wherein 21,980 cases of ovarian cancer will be diagnosed in the United States alone, of which > 14,000 deaths are predicted as a result of this disease. Cancer Research UK has ranked ovarian cancer as eighteenth in

terms of worldwide incidences of cancer by virtue of its annual contribution to 1.7% of all cancers. The National Cancer Institute of Canada has predicted 2700 new cases of ovarian cancers that will be diagnosed in 2014, of which there will be an estimated 1750 deaths. Clearly, the disease has a high mortality rate that hasn't changed much over the last few decades.

As with any diseased condition, diagnosis plays a vital role in the treatment of ovarian cancer. Although recent knowledge suggests that the disease progresses with 23 known indications, most of these are abdominal or gastrointestinal in nature and rarely link directly to a gynecologic aspect. Most of these are mild indications such as bloating of the abdomen, constipation, early satiety, increased thirst and frequent urination that either get overlooked as non-specific signals or potentially mistaken for common disorders such as gastritis, irritable bowel syndrome, urinary tract infection etc. Consequently, most patients are diagnosed with the disease at late stages (III or IV). Less than 25% cases are detected at stage I. This is further hampered by the fact that CA125 is reported to be expressed in only 50% of stage I epithelial ovarian cancer. Nonetheless, there is a 90% cure rate for epithelial ovarian cancers diagnosed at stage I, whereas the cure rate plummets to 20 – 25% in patients diagnosed with late stage disease.[32] This raises a critical need for better diagnosis of epithelial ovarian cancer.

More recently, Goff et al introduced a symptom index (SI) for ovarian cancer with the intent to increase the possibilities for early detection.[85] The SI was considered positive if one or more of the symptoms were present over a period of 12 months and occurred more than twelve days a month. Independent investigations thus far

have clearly demonstrated that the severity, duration and frequency of the gastrointestinal and/or abdominal symptoms were significantly higher in women having ovarian cancer at all stages. The SI reported ovarian cancer in women with a sensitivity of 57% for early stage disease, 80% for advanced stage disease and a specificity of 90%. This was similar to CA125 serum tests, which are reported to have a sensitivity of 50 – 79% and specificity between 96 – 99% for advanced stage ovarian carcinomas. Furthermore, supplementing CA125 and HE4 values to the SI is reported to improve the detection of early stage EOC to raise the sensitivity to 84% with a specificity of 98.5%, if any two of the variables were positive.[86, 87] A conscious implementation of such a tool may be instrumental in triaging patients in a primary care setting.

1.6.1 Contemporary Diagnostics for Ovarian Cancer:

Nevertheless, patients presenting in the clinic with pelvic masses are routinely diagnosed for ovarian cancer via physical examination, careful analysis of the medical history, assessment of serum CA125 levels and adnexal imaging via trans-vaginal ultrasound (TVUS).

1.6.1.1 CA125 ELISA: (Enzyme Linked Immunosorbent Assay)

A two-site binding immunoassay such as CA125 II is currently used in the clinic to evaluate serum CA125 levels through a capture of the tumor associated antigen by an M11 antibody coated onto microtiter wells while an OC125 antibody is employed as a tracer.[65] Patients with elevated levels of CA125 at the time of presentation and post-treatment are known to have a worse prognosis than those

with low or normalized levels respectively at these stages. However, tumor markers such as CA125 have a major limitation in that their expression levels are often found to be elevated in many benign conditions. Furthermore, even if this information is specific, it does not indicate the precise location of the tumor in the body. This calls for an imaging technique that can provide a visual assessment to precisely assert the diagnosis of ovarian malignancies.

1.6.1.2 Ultrasound: (US)

Given the low cost of performing as well as undertaking an ultrasound examination combined with the convenience of bedside operation and widespread availability in almost every gynecologic clinic and the absence of ionizing radiations, have led to transvaginal ultrasound (TVUS) becoming the first-line pre-treatment triage imaging modality used in the clinical diagnosis of ovarian cancer.[88] This technique provides the capability to view adnexal masses and also differentiate them from unilocular ovarian cysts that are benign.[91] Though the addition of morphologic scoring systems and color Doppler have been introduced to enhance the clinical performance of US, the technique is mostly operator dependent unlike other tomographic methods and thus has not proven adequate diagnostic performance.[88] Even though an introduction of targeted microbubbles functionalized with antigen-binding ligands has been proposed to improve the specificity of US, the size of these agents practically limits them to eventually binding with epitopes expressed on the surface of endothelial cells in the tumor vasculature. In other words, such microbubbles are too large to extravasate through endothelial cells of blood vessels.

1.6.1.3 Computed Tomography: (CT)

This technique has been the most widely used imaging method in the surveillance of women who have already undergone primary treatment of ovarian cancer.[90, 91] While CT is capable of successfully identifying a hypodense region of pleural effusion in the thorax as an indicator of relapse, or pulmonary parenchyma as round solid nodules and calcifications in serous carcinoma, this technique is significantly limited in its ability to detect small recurrences due to low tissue contrast resolution. This is especially true for regions in the small bowel and mesentery. The other disadvantages of CT include exposure to ionizing radiation, and its inability to distinguish between recurrence, and post-operative or post-radiotherapy fibrosis.[90]

1.6.1.4 Magnetic Resonance Imaging: (MRI)

The combination of high-field magnets, phase arrayed body coils and fast impulse sequences has enabled magnetic resonance imaging to deliver high quality images with high tissue contrast and high resolution within a short scanning time. The introduction of diffusion weighted imaging (DWI) and perfusion imaging have enhanced the clinical utility of this modality by allowing visualization of macroscopic disease as well as providing information on the cellularity and vascularity of the tissue. Most importantly, MRI provides excellent soft-tissue contrast to reveal anatomical detail without the use of ionizing radiations and is fairly operator-independent. Nevertheless, some of its limitations include the costs associated with an MRI scan, a need for patient cooperation and the limited

window for regional scanning, unlike whole body scans that can be performed via CT. Furthermore, from an oncologic viewpoint, MRI is also limited in its capabilities for detecting micrometastasis in lymph nodes.[90]

1.7 MOLECULAR IMAGING:

An ability to image real time physiological events at the cellular and molecular level in disease and health has developed into a new field of medical imaging expertise commonly referred to as molecular imaging. Molecular imaging now plays an increasingly important role to equip physicians and oncologists with the extra pieces of information including the extent of spread of a disease, unique tumor-specific expression profiles of receptors and/or biomarkers for designing a targeted therapy, to evaluate response to therapy and monitor disease progression or recurrence – all of which can positively impact decision making to effect disease management in the larger scheme of patient care. Furthermore, this information may not be captured by conventional imaging techniques that deliver excellent anatomical details as opposed to biochemical information at a cellular level that can sometimes be obtained even prior to the development of symptoms.

1.7.1 Positron Emission Tomography: (PET)

Unlike the aforementioned conventional imaging techniques which are not originally designed to perform diagnosis at a molecular level, PET is a natively functional molecular imaging modality by virtue of its ability to generate real time information based on the differential *in vivo* physiological uptake or biochemical targeting and metabolic processing of a radiotracer/molecular probe between

neoplastic versus normal cells. Furthermore, PET is unique in its ability to render quantitative information in addition to functional imaging. PET relies on the use of 'tracers' formulated with radioisotopes that have an unstable nucleus and decay via emission of positrons, which travel a short distance in tissues prior to colliding with electrons to annihilate and produce two co-incident back-to-back 511 KeV gamma photons detectable by a PET scanner. A reconstruction of the lines of responses from a PET scan helps map the three-dimensional distribution of the radionuclide in the body.

The simplest and most widely used radiotracer in oncologic PET imaging is an analog of glucose – [^{18}F]FDG (^{18}F-fluoro-deoxyglucose) which functions as a radiotracer by virtue of its being taken up more avidly by neoplastic cells that inherently have a higher degree of glycolytic activity vis-à-vis normal healthy cells. The radiotracer gets phosphorylated by hexokinase upon entry into the neoplastic cells but, the lack of a 2'-hydroxyl group in this molecule precludes it from being further metabolized by such cells. Thus, the radiotracer gets trapped and continues to decay within the tumor cells that can be detected in a PET scan.

In the context of ovarian cancer, [^{18}F]FDG-PET is reported to have a low sensitivity (58 – 78%) and low specificity (76 – 87%) for the diagnosis of primary ovarian cancer, which may partly be attributed to the cystic nature of ovarian tumors.[88] However, a combination of [^{18}F]FDG-PET and CA125 evaluation yielded a sensitivity of 94 – 98%.[92] Furthermore, the evidence of recurrence on PET is reported to have preceded CT findings by 6 months.[93]

With surgery being the primary mode of treatment for epithelial ovarian cancers and an extremely high probability of recurrence of the disease combined with recent advances in the development of hybrid imaging technologies, there are several reports for the utility of PET/CT as a modality that delivers a high degree of accuracy for the detection of recurrent disease in the post-treatment surveillance of patients.[94-98] Such a combination has improved the sensitivity, specificity and accuracy for the diagnosis of malignant ovarian lesions.[97] Most importantly, PET/CT was reported to have found positive lesions in many instances where CT by itself was negative – especially metastatic lesions in the bowel wall whose detection was difficult with MRI or CT.[100-103] Furthermore, in one study, the addition of PET/CT information to conventional diagnosis was able to effect a change to the clinical management of the disease in up to 60% of the cases.[104, 105] Taken together, such reports are suggestive of PET/CT being most useful for the diagnosis of recurrent ovarian lesions in symptomatic patients that have a rising CA125 levels but negative or equivocal results from primary diagnosis using conventional imaging techniques. A meta-analysis by Gu et al illustrated the area under the receiver operator curve to be 0.92 for CA125, 0.93 for PET alone, 0.96 for PET/CT, 0.88 for CT and 0.80 for MRI for the detection of ovarian cancer.[106]

It is now apparent that active disease can be diagnosed via PET/CT despite low levels of CA125, and may have a potential for translation into an early diagnosis of recurrent ovarian cancer. This may help stratify patients suitable for site-specific treatment, radiation therapy and to choose optimal candidates for surgery.

[107, 108] Thus, [^{18}F]FDG-PET/CT can deliver increased lesion contrast along with delivering information on the anatomical localization and differentiation of neoplastic disease from post-treatment fibrosis.[109] However, some drawbacks for diagnosis with [^{18}F]FDG-PET/CT include a radiation burden to subjects and its physiological uptake in the bowel, kidneys and bladder. Furthermore, it is limited in its capability to diagnose small volume disease (5–7 mm) and lymphatic spread – especially into nodes surrounding the urinary bladder.

1.7.2 Targeted Positron Emission Tomography

In light of the aforementioned limitations and possibilities for non-specific uptake of generic radiotracers such as [^{18}F]FDG in cells under the effect of inflammation and other hypermetabolic benign or physiological conditions, it may be useful to adopt a more targeted approach to facilitate the *in vivo* imaging of ovarian carcinomas. This has been demonstrated through the synthesis and use of specific radiolabeled ligands as tracers for receptor molecules expressed in ovarian cancer. Overexpression of folate receptors (FR) on ovarian neoplasms forms an attractive target for tumor imaging and therapy.[110] Some recent efforts to carry out a folate receptor targeted molecular imaging in ovarian cancer include but are not limited to – the synthesis of several small molecule based ^{99m}Tc-labeled folate conjugates for SPECT imaging,[111-114] ^{99m}Tc-etarfolatide[115] and ^{111}In-DTPA folate;[116] ^{67}Ga/^{68}Ga-, ^{18}F- and ^{124}I-labeled folate conjugates for PET imaging;[117, 118] ^{18}F-labeled PET radiotracer targeting COX-1 in ovarian cancer;[119] fluorescein conjugated folate for intra-operative procedures;[120] a dual imaging affibody bioconjugate with capabilities for near infrared optical imaging and PET using

^{64}Cu;[121] development of a porphyrin-based multimodal PET-Optical probe for targeting folate receptors in ovarian cancer[122] and a smart probe developed from folate conjugated to a near infrared fluorescent dye by a linker that specifically gets cleaved by tumor-associated lysosomal cathepsin B enzyme upon FR mediated uptake into neoplastic ovarian cancer cells.[123]

Alternatively, radiolabeled antibodies against specific tumor associated antigens overexpressed by ovarian cancer cells – MoV 18 against Folate Receptor α,[124] OC125,[125, 126] MAb-B43.13,[73] MAb 3A5[84] against CA125 antigen, MAb MX35 against an unspecified ovarian cancer antigen and MAb MH99 against 17.1A antigen[127] have been described for use in *in vivo* applications.

1.7.2.1 Immuno-Positron Emission Tomography: (immuno-PET)

In recent years, the latter approach has sprung into a new branch of molecular imaging commonly referred to as immuno-PET.[128] This technology brings together the high specificity and affinity of antibody targeting vectors with the great sensitivity of detection rendered by positron emitting radionuclides.[129, 130] *In vivo* application of such a composite radiotracer is ultimately delivers real time information on its biochemical targeting capabilities and pharmacokinetics as analyzed via positron emission tomography. The use of this technology not only allows the development of a molecular probe that is highly specific for tumor targeting, but can also provide vital information about off-target effects and potential *in vivo* pharmacological profiles and fate of the targeting vector for therapeutic applications that may be intended in the future.

Within a short span of time, preclinical immuno-PET strategies have been developed against several oncologic targets ranging from applications suited for same to next–day imaging[131-143] and beyond[144-151] to image several solid and hematologic malignancies. This has mainly been facilitated by two factors:

a) Advances in recombinant technology that contributed to the synthesis of engineered antibodies, antibody fragments and nanobodies; [152-155]

Antibody Format	**Complete Antibody**	**F(ab')$_2$**	**Minibody**	**Diabody**	**Fab**	**scFv**	**Nanobody**
MW (KDa)	150	120	80	55	55	28	15
Source	Hybridoma or Engineered	Enzymatic	Engineered	Engineered	Enzymatic	Engineered	Camelids
Valency	Bivalent	Bivalent	Bivalent	Bivalent	Monovalent	Monovalent	Monovalent
Clearance Route	Hepatic	Hepatic / Renal	Hepatic	Renal	Renal	Renal	Renal

Table 1.1: Representation of different antibody formats employed for immuno-PET

b) An increasing awareness and availability of several positron emitting radionuclides that have provided a variety and choice to tailor molecular probes for use in immuno-PET strategies.

Radionuclide	T ½ (h)	Positron Yield (%)	β^+ max (MeV)
^{68}Ga	1.1	89	1.89
^{18}F	1.8	97	0.63
^{64}Cu	12.7	19	0.66
^{86}Y	14.7	33	3.15
^{76}Br	16.2	23	3.98
^{89}Zr	78.4	23	0.90
^{124}I	100.3	23	2.14

Table 1.2: List of PET-radionuclides and their salient properties suitable for immuno-PET

The aforementioned antibody constructs and radioisotopes thus form integral components in the armamentarium of a radiochemist to synthesize radiotracers for immuno-PET applications suited to the nature of the biological target and the *in vivo* pharmacokinetics of the targeting vector. This aspect is primarily governed by a cardinal principle of molecular imaging via PET that recommends a match between the biological (serum) half-life of the targeting vector with the physical (decay) half-life of the radioisotope used in conjunction with the biomolecule.[152]

Not to be missed, simultaneous advancements in the manufacture of PET scanners have been a great technological advance to support the progress in this field.

In summary, although serum CA125 levels serve as a diagnostic tool and prognostic indicator of disease burden resulting from ovarian carcinoma, it is considered clinically inadequate as an isolated value to decide further course of treatment in patients due to its limited specificity as a biomarker in the diagnosis of primary ovarian cancer. Trans-vaginal and/or trans-abdominal ultrasound is the current mainstay among imaging modalities used in the clinical diagnosis of primary ovarian cancer. In other words, serum CA125 and ultrasound form the major tests currently use to triage patients for further treatment. However, given the reliability of a rising CA125 level in high-risk group patients and those that have undergone primary cytoreductive surgery,[72] a combined application of [^{18}F]FDG-PET/CT has recently enabled relatively superior detection of recurrent disease even if these individuals were asymptomatic and had negative results from other conventional imaging modalities including CT and MRI. This may have potential implications for the preferential use of PET/CT towards an early detection of ovarian cancer in a recurrent setting, in order to positively impact disease management for the future.

1.8 THESIS OVERVIEW:

1.8.1 Rationale:

Despite the fact that 75% of women diagnosed with advanced stage ovarian cancer have a favourable clinical response as a result of optimal cytoreductive surgery and first-line platinum therapy, the mortality rate resulting from this cancer remains high with a 5 year survival rate of only 44.6%.[156] This illustrates the powerful impact of recurrence from this malignancy and the present-day limitations to effectively detect and treat the disease in this phase.

Recognizing the ongoing efforts to provide reliable and early detection of primary EOC through screening with novel biomarkers in combinatorial panels that incorporate risk stratification algorithms; the work presented in this thesis aims to develop a targeted non-invasive imaging strategy for the detection of epithelial ovarian cancer. The central idea is to overcome some limitations of present day methods used for ovarian cancer diagnosis and to prospectively result in an early detection of its recurrence to positively impact disease management.

The work in this thesis is premised on two facts:

a) CA125 is a reliable biomarker for recurrent epithelial ovarian cancer and bears a high diagnostic and prognostic value in this setting.[32, 71, 156, 157]
b) [^{18}F]FDG-PET has a high sensitivity and diagnostic accuracy in identifying recurrent epithelial ovarian cancer in asymptomatic patients having a rising CA125 level and negative results from conventional imaging modalities including CT and MRI.[90, 156, 159]

However, both these aspects have the following limitations:

a) Despite having a high prognostic and diagnostic significance in the recurrent setting, a rising CA125 level does not indicate the *in vivo* location of the malignancy.

b) Although CA125 ELISAs perform excellently well with a detection limit of 1.5 U/mL, these assays rely on the availability of CA125 antigen in circulation. There is a possibility that small volume recurrent disease may not shed as much antigen into the blood that can be detected by such ELISAs. Thus, patients may appear to have normal CA125 levels. This is further exemplified by a mathematical model proposed by Hori and Gambhir[157] wherein an ovarian tumor may take 10.6 years since its first neoplastic cell to grow up to a size of 10.52 mm^3, after which it sheds just enough CA125 antigen (1.5 U/mL) that is detectable by the existing high performance clinical ELISA kits.

c) [^{18}F]FDG-PET of ovarian cancer is sensitive yet suffers from relatively low [^{18}F]FDG uptake in these tumors partly due to their cystic nature.[88] This is compounded further by a limited ability to detect small volume residual disease resulting from very low differential glucose uptake in small lesions combined with the limitations of PET for spatial resolution.[90]

Considering these factors, we developed CA125-targeted vectors for non-invasive imaging of EOC with an aim to expand the diagnostic utility of CA125 and simultaneously overcome some limitations of present day ELISAs and [^{18}F]FDG-PET as diagnostic methods used in the context of ovarian cancer.

1.8.2 Hypothesis

Based on the aforementioned rationale, we hypothesized that CA125 is a suitable target for the molecular imaging of Epithelial Ovarian Cancer (EOC) to reflect *in vivo* tumor burden in subjects.

1.8.3 Aim:

To develop a CA125-targeted immuno-PET strategy for the molecular imaging of epithelial ovarian cancer.

1.8.4 Objectives:

- To develop a single-chain antibody fragment for targeting CA125 in epithelial ovarian cancer
- To synthesize an ^{18}F-labeled single-chain antibody fragment as a CA125-targeted radiotracer for same-day imaging of epithelial ovarian cancer
- To develop ^{64}Cu-labeled anti-CA125 antibody and single-chain antibody fragment for immuno-PET of epithelial ovarian cancer
- To maximize the potential of full-length antibody imaging through ^{89}Zr-immuno-PET of epithelial ovarian cancer
- To develop a CA125 targeted diabody for optimal antibody fragment-based same-day imaging of epithelial ovarian cancer

The forthcoming chapters 2-6 of this thesis illustrate how the aforementioned objectives were achieved and the findings thereof.

1.9 References:

1. National Cancer Institute, SEER Training Modules http://training.seer.cancer.gov/anatomy/reproductive/female/ovaries.html
2. Oktem O, Oktay K. The ovary: anatomy and function throughout human life. *Ann N Y Acad Sci* 2008;**1127**: 1-9.
3. Erickson BK, Conner MG, Landen CN, Jr. The role of the fallopian tube in the origin of ovarian cancer. *Am J Obstet Gynecol* 2013;**209**(5): 409-14.
4. Prat J. Ovarian carcinomas: five distinct diseases with different origins, genetic alterations, and clinicopathological features. *Virchows Arch* 2012;**460**(3): 237-49.
5. Mutch DG, Prat J. 2014 FIGO staging for ovarian, fallopian tube and peritoneal cancer. *Gynecol Oncol* 2014;**133**(3): 401-4.
6. Holschneider CH, Berek JS. Ovarian cancer: epidemiology, biology, and prognostic factors. *Semin Surg Oncol* 2000;**19**(1): 3-10.
7. Cho KR, Shih Ie M. Ovarian cancer. *Annu Rev Pathol* 2009;4: 287-313.
8. Jones PM, Drapkin R. Modeling High-Grade Serous Carcinoma: How Converging Insights into Pathogenesis and Genetics are Driving Better Experimental Platforms. *Front Oncol* 2013;**3**: 217.
9. Cho KR. Ovarian cancer update: lessons from morphology, molecules, and mice. *Arch Pathol Lab Med* 2009;**133**(11): 1775-81.
10. Rescigno P, Cerillo I, Ruocco R, Condello C, De Placido S, Pensabene M. New hypothesis on pathogenesis of ovarian cancer lead to future tailored approaches. *Biomed Res Int* 2013;**2013**: 852839.
11. Ahmed AA, Etemadmoghadam D, Temple J, et al. Driver mutations in TP53 are ubiquitous in high grade serous carcinoma of the ovary. *J Pathol* 2010;**221**(1): 49-56.

12. Gubbels JA, Claussen N, Kapur AK, Connor JP, Patankar MS. The detection, treatment, and biology of epithelial ovarian cancer. *J Ovarian Res* 2010;**3**: 8.

13. Fathalla MF. Incessant ovulation--a factor in ovarian neoplasia? *Lancet* 1971;**2**(7716): 163.

14. Espey LL. Ovulation as an inflammatory reaction--a hypothesis. *Biol Reprod* 1980;**22**(1): 73-106.

15. Zhu Y, Nilsson M, Sundfeldt K. Phenotypic plasticity of the ovarian surface epithelium: TGF-beta 1 induction of epithelial to mesenchymal transition (EMT) in vitro. *Endocrinology* 2010;**151**(11): 5497-505.

16. Murdoch WJ, Murphy CJ, Van Kirk EA, Shen Y. Mechanisms and pathobiology of ovulation. *Soc Reprod Fertil Suppl* 2010;**67**: 189-201.

17. Kurman RJ, Shih Ie M. The origin and pathogenesis of epithelial ovarian cancer: a proposed unifying theory. *Am J Surg Pathol* 2010;**34**(3): 433-43.

18. Piek JM, van Diest PJ, Zweemer RP, et al. Dysplastic changes in prophylactically removed Fallopian tubes of women predisposed to developing ovarian cancer. *J Pathol* 2001;**195**(4): 451-6.

19. Lee Y, Miron A, Drapkin R, et al. A candidate precursor to serous carcinoma that originates in the distal fallopian tube. *J Pathol* 2007;**211**(1): 26-35.

20. Kindelberger DW, Lee Y, Miron A, et al. Intraepithelial carcinoma of the fimbria and pelvic serous carcinoma: Evidence for a causal relationship. *Am J Surg Pathol* 2007;**31**(2): 161-9.

21. Soussi T, Ishioka C, Claustres M, Beroud C. Locus-specific mutation databases: pitfalls and good practice based on the p53 experience. *Nat Rev Cancer* 2006;**6**(1): 83-90.

22. Przybycin CG, Kurman RJ, Ronnett BM, Shih Ie M, Vang R. Are all pelvic (nonuterine) serous carcinomas of tubal origin? *Am J Surg Pathol* 2010;**34**(10): 1407-16.

23. Folkins AK, Jarboe EA, Saleemuddin A, et al. A candidate precursor to pelvic serous cancer (p53 signature) and its prevalence in ovaries and fallopian tubes from women with BRCA mutations. *Gynecol Oncol* 2008;**109**(2): 168-73.

24. Karst AM, Drapkin R. The new face of ovarian cancer modeling: better prospects for detection and treatment. *F1000 Med Rep* 2011;**3**: 22.

25. Levanon K, Ng V, Piao HY, et al. Primary ex vivo cultures of human fallopian tube epithelium as a model for serous ovarian carcinogenesis. *Oncogene* 2010;**29**(8): 1103-13.

26. Karst AM, Levanon K, Drapkin R. Modeling high-grade serous ovarian carcinogenesis from the fallopian tube. *Proc Natl Acad Sci U S A* 2011;**108**(18): 7547-52.

27. Graziano DF, Finn OJ. Tumor antigens and tumor antigen discovery. *Cancer Treat Res* 2005;**123**: 89-111.

28. Bast RC, Jr. Status of tumor markers in ovarian cancer screening. *J Clin Oncol* 2003;**21**(10 Suppl): 200s-05s.

29. Husseinzadeh N. Status of tumor markers in epithelial ovarian cancer has there been any progress? A review. *Gynecol Oncol* 2011;**120**(1): 152-7.

30. Su Z, Graybill WS, Zhu Y. Detection and monitoring of ovarian cancer. *Clin Chim Acta* 2013;**415**: 341-5.

31. Bast RC, Jr., Feeney M, Lazarus H, Nadler LM, Colvin RB, Knapp RC. Reactivity of a monoclonal antibody with human ovarian carcinoma. *J Clin Invest* 1981;**68**(5): 1331-7.

32. Gupta D, Lis CG. Role of CA125 in predicting ovarian cancer survival - a review of the epidemiological literature. *J Ovarian Res* 2009;**2:** 13.

33. Yin BW, Dnistrian A, Lloyd KO. Ovarian cancer antigen CA125 is encoded by the MUC16 mucin gene. *Int J Cancer* 2002;**98**(5): 737-40.

34. Madiyalakan R, Kuzma M, Noujaim AA, Suresh MR. An antibody-lectin sandwich assay for the determination of CA125 antigen in ovarian cancer patients. *Glycoconj J* 1996;**13**(4): 513-7.

35. O'Brien TJ, Raymond LM, Bannon GA, et al. New monoclonal antibodies identify the glycoprotein carrying the CA 125 epitope. *Am J Obstet Gynecol* 1991;**165**(6 Pt 1): 1857-64.

36. Lloyd KO, Yin BW, Kudryashov V. Isolation and characterization of ovarian cancer antigen CA 125 using a new monoclonal antibody (VK-8): identification as a mucin-type molecule. *Int J Cancer* 1997;**71**(5): 842-50.

37. Nap M, Vitali A, Nustad K, et al. Immunohistochemical characterization of 22 monoclonal antibodies against the CA125 antigen: 2nd report from the ISOBM TD-1 Workshop. *Tumour Biol* 1996;**17**(6): 325-31.

38. Nustad K, Bast RC, Jr., Brien TJ, et al. Specificity and affinity of 26 monoclonal antibodies against the CA 125 antigen: first report from the ISOBM TD-1 workshop. International Society for Oncodevelopmental Biology and Medicine. *Tumour Biol* 1996;**17**(4): 196-219.

39. Nustad K, Lebedin Y, Lloyd KO, et al. Epitopes on CA 125 from cervical mucus and ascites fluid and characterization of six new antibodies. Third report from the ISOBM TD-1 workshop. *Tumour Biol* 2002;**23**(5): 303-14.

40. Warren DJ, Nustad K, Beard JB, O'Brien TJ. Expression and epitope characterization of a recombinant CA 125 repeat: fourth report from the ISOBM TD-1 workshop. *Tumour Biol* 2009;**30**(2): 51-60.

41. Perez BH, Gipson IK. Focus on Molecules: human mucin MUC16. *Exp Eye Res* 2008;**87**(5): 400-1.

42. Bressan A, Bozzo F, Maggi CA, Binaschi M. OC125, M11 and OV197 epitopes are not uniformly distributed in the tandem-repeat region of CA125 and require the entire SEA domain. *Dis Markers* 2013;**34**(4): 257-67.

43. Davis HM, Zurawski VR, Jr., Bast RC, Jr., Klug TL. Characterization of the CA 125 antigen associated with human epithelial ovarian carcinomas. *Cancer Res* 1986;**46**(12 Pt 1): 6143-8.

44. Hattrup CL, Gendler SJ. Structure and function of the cell surface (tethered) mucins. *Annu Rev Physiol* 2008;**70**: 431-57.

45. O'Brien TJ, Beard JB, Underwood LJ, Dennis RA, Santin AD, York L. The CA 125 gene: an extracellular superstructure dominated by repeat sequences. *Tumour Biol* 2001;**22**(6): 348-66.

46. Weiland F, Martin K, Oehler MK, Hoffmann P. Deciphering the Molecular Nature of Ovarian Cancer Biomarker CA125. *Int J Mol Sci* 2012;**13**(8): 10568-82.

47. Berman ZT, Moore LJ, Knudson KE, Whelan RJ. Synthesis and structural characterization of the peptide epitope of the ovarian cancer biomarker CA125 (MUC16). *Tumour Biol* 2010;**31**(5): 495-502.

48. Patankar MS, Jing Y, Morrison JC, et al. Potent suppression of natural killer cell response mediated by the ovarian tumor marker CA125. *Gynecol Oncol* 2005;**99**(3): 704-13.

49. Baalbergen A, Janssen JW, van der Weiden RM. CA-125 levels are related to the likelihood of pregnancy after in vitro fertilization and embryo transfer. *Am J Reprod Immunol* 2000;**43**(1): 21-4.

50. Miller KA, Deaton JL, Pittaway DE. Evaluation of serum CA 125 concentrations as predictors of pregnancy with human in vitro fertilization. *Fertil Steril* 1996;**65**(6): 1184-9.

51. Mazor M, Bashiri A, Ghezzi F, et al. Maternal serum CA 125 is of prognostic value in patients with uterine bleeding in the detection of small-for-gestational-age neonates. *Eur J Obstet Gynecol Reprod Biol* 1996;**67**(2): 143-7.

52. Spitzer M, Kaushal N, Benjamin F. Maternal CA-125 levels in pregnancy and the puerperium. *J Reprod Med* 1998;**43**(4): 387-92.

53. Argueso P, Tisdale A, Spurr-Michaud S, Sumiyoshi M, Gipson IK. Mucin characteristics of human corneal-limbal epithelial cells that exclude the rose bengal anionic dye. *Invest Ophthalmol Vis Sci* 2006;**47**(1): 113-9.

54. Argueso P, Guzman-Aranguez A, Mantelli F, Cao Z, Ricciuto J, Panjwani N. Association of cell surface mucins with galectin-3 contributes to the ocular surface epithelial barrier. *J Biol Chem* 2009;**284**(34): 23037-45.

55. Durak-Nalbantic A, Resic N, Kulic M, et al. Serum level of tumor marker carbohydrate antigen-CA125 in heart failure. *Med Arh* 2013;**67**(4): 241-4.

56. Yilmaz MB, Nikolaou M, Cohen Solal A. Tumour biomarkers in heart failure: is there a role for CA-125? *Eur J Heart Fail* 2011;**13**(6): 579-83.

57. Cheon DJ, Wang Y, Deng JM, et al. CA125/MUC16 is dispensable for mouse development and reproduction. *PLoS One* 2009;**4**(3): e4675.

58. Gubbels JA, Felder M, Horibata S, et al. MUC16 provides immune protection by inhibiting synapse formation between NK and ovarian tumor cells. *Mol Cancer* 2010;**9**: 11.

59. Belisle JA, Horibata S, Jennifer GA, et al. Identification of Siglec-9 as the receptor for MUC16 on human NK cells, B cells, and monocytes. *Mol Cancer* 2010;**9**: 118.

60. Avril T, Floyd H, Lopez F, Vivier E, Crocker PR. The membrane-proximal immunoreceptor tyrosine-based inhibitory motif is critical for the inhibitory signaling mediated by Siglecs-7 and -9, CD33-related Siglecs expressed on human monocytes and NK cells. *J Immunol* 2004;**173**(11): 6841-9.

61. Dunn GP, Bruce AT, Ikeda H, Old LJ, Schreiber RD. Cancer immunoediting: from immunosurveillance to tumor escape. *Nat Immunol* 2002;**3**(11): 991-8.

62. Rump A, Morikawa Y, Tanaka M, et al. Binding of ovarian cancer antigen CA125/MUC16 to mesothelin mediates cell adhesion. *J Biol Chem* 2004;**279**(10): 9190-8.

63. Gubbels JA, Belisle J, Onda M, et al. Mesothelin-MUC16 binding is a high affinity, N-glycan dependent interaction that facilitates peritoneal metastasis of ovarian tumors. *Mol Cancer* 2006;**5**(1): 50.

64. Sathyanarayana BK, Hahn Y, Patankar MS, Pastan I, Lee B. Mesothelin, Stereocilin, and Otoancorin are predicted to have superhelical structures with ARM-type repeats. *BMC Struct Biol* 2009;**9**: 1.

65. Felder M, Kapur A, Gonzalez-Bosquet J, et al. MUC16 (CA125): tumor biomarker to cancer therapy, a work in progress. *Mol Cancer* 2014;**13**(1): 129.

66. van der Burg ME, Lammes FB, Verweij J. The role of CA 125 in the early diagnosis of progressive disease in ovarian cancer. *Ann Oncol* 1990;**1**(4): 301-2.

67. Niloff JM, Bast RC, Jr., Schaetzl EM, Knapp RC. Predictive value of CA 125 antigen levels in second-look procedures for ovarian cancer. *Am J Obstet Gynecol* 1985;**151**(7): 981-6.

68. Trape J, Filella X, Alsina-Donadeu M, Juan-Pereira L, Bosch-Ferrer A, Rigo-Bonnin R. Increased plasma concentrations of tumour markers in the absence of neoplasia. *Clin Chem Lab Med* 2011;**49**(10): 1605-20.

69. Menon U, Gentry-Maharaj A, Ryan A, et al. Recruitment to multicentre trials--lessons from UKCTOCS: descriptive study. *BMJ* 2008;**337**: a2079.

70. Menon U, Gentry-Maharaj A, Hallett R, et al. Sensitivity and specificity of multimodal and ultrasound screening for ovarian cancer, and stage distribution of detected cancers: results of the prevalence screen of the UK Collaborative Trial of Ovarian Cancer Screening (UKCTOCS). *Lancet Oncol* 2009;**10**(4): 327-40.

71. Gadducci A, Cosio S, Zola P, Landoni F, Maggino T, Sartori E. Surveillance procedures for patients treated for epithelial ovarian cancer: a review of the literature. *Int J Gynecol Cancer* 2007;**17**(1): 21-31.

72. Niloff JM, Knapp RC, Lavin PT, et al. The CA 125 assay as a predictor of clinical recurrence in epithelial ovarian cancer. *Am J Obstet Gynecol* 1986;**155**(1): 56-60.

73. McQuarrie SA, Baum RP, Niesen A, et al. Pharmacokinetics and radiation dosimetry of 99Tcm-labelled monoclonal antibody B43.13 in ovarian cancer patients. *Nucl Med Commun* 1997;**18**(9): 878-86.

74. Berek JS. Immunotherapy of ovarian cancer with antibodies: a focus on oregovomab. *Expert Opin Biol Ther* 2004;**4**(7): 1159-65.

75. Schultes BC, Baum RP, Niesen A, Noujaim AA, Madiyalakan R. Anti-idiotype induction therapy: anti-CA125 antibodies (Ab3) mediated tumor killing in patients treated with Ovarex mAb B43.13 (Ab1). *Cancer Immunol Immunother* 1998;**46**(4): 201-12.

76. Berek J, Taylor P, McGuire W, Smith LM, Schultes B, Nicodemus CF. Oregovomab maintenance monoimmunotherapy does not improve outcomes in advanced ovarian cancer. *J Clin Oncol* 2009;**27**(3): 418-25.

77. Reinartz S, Kohler S, Schlebusch H, et al. Vaccination of patients with advanced ovarian carcinoma with the anti-idiotype ACA125: immunological response and survival (phase Ib/II). *Clin Cancer Res* 2004;**10**(5): 1580-7.

78. Reinartz S, Hombach A, Kohler S, et al. Interleukin-6 fused to an anti-idiotype antibody in a vaccine increases the specific humoral immune response against CA125+ (MUC-16) ovarian cancer. *Cancer Res* 2003;**63**(12): 3234-40.

79. Sabbatini P, Dupont J, Aghajanian C, et al. Phase I study of abagovomab in patients with epithelial ovarian, fallopian tube, or primary peritoneal cancer. *Clin Cancer Res* 2006;**12**(18): 5503-10.

80. Pfisterer J, Harter P, Simonelli C, et al. Abagovomab for ovarian cancer. *Expert Opin Biol Ther* 2011;**11**(3): 395-403.

81. Hassan R, Ho M. Mesothelin targeted cancer immunotherapy. *Eur J Cancer* 2008;**44**(1): 46-53.

82. Xiang X, Feng M, Felder M, et al. HN125: A Novel Immunoadhesin Targeting MUC16 with Potential for Cancer Therapy. *J Cancer* 2011;**2**: 280-91.

83. Chen Y, Clark S, Wong T, et al. Armed antibodies targeting the mucin repeats of the ovarian cancer antigen, MUC16, are highly efficacious in animal tumor models. *Cancer Res* 2007;**67**(10): 4924-32.

84. Pastuskovas CV, Mallet W, Clark S, et al. Effect of immune complex formation on the distribution of a novel antibody to the ovarian tumor antigen CA125. *Drug Metab Dispos* 2010;**38**(12): 2309-19.

85. Goff BA, Mandel LS, Drescher CW, et al. Development of an ovarian cancer symptom index: possibilities for earlier detection. *Cancer* 2007;**109**(2): 221-7.

86. Andersen MR, Goff BA, Lowe KA, et al. Combining a symptoms index with CA 125 to improve detection of ovarian cancer. *Cancer* 2008;**113**(3): 484-9.

87. Andersen MR, Goff BA, Lowe KA, et al. Use of a Symptom Index, CA125, and HE4 to predict ovarian cancer. *Gynecol Oncol* 2010;**116**(3): 378-83.

88. Lutz AM, Willmann JK, Drescher CW, et al. Early diagnosis of ovarian carcinoma: is a solution in sight? *Radiology* 2011;**259**(2): 329-45.

89. McDonald JM, Doran S, DeSimone CP, et al. Predicting risk of malignancy in adnexal masses. *Obstet Gynecol* 2010;**115**(4): 687-94

90. Testa AC, Di Legge A, Virgilio B, et al. Which imaging technique should we use in the follow up of gynaecological cancer? *Best Pract Res Clin Obstet Gynaecol* 2014;**28**(5): 769-91.

91. Pannu HK, Bristow RE, Montz FJ, Fishman EK. Multidetector CT of peritoneal carcinomatosis from ovarian cancer. *Radiographics* 2003;**23**(3): 687-701.

92. Murakami M, Miyamoto T, Iida T, et al. Whole-body positron emission tomography and tumor marker CA125 for detection of recurrence in epithelial ovarian cancer. *Int J Gynecol Cancer* 2006;**16** Suppl 1: 99-107.

93. Zimny M, Siggelkow W, Schroder W, et al. 2-[Fluorine-18]-fluoro-2-deoxy-d-glucose positron emission tomography in the diagnosis of recurrent ovarian cancer. *Gynecol Oncol* 2001;**83**(2): 310-5.

94. Muramatsu T, Yamashita E, Takahashi K, et al. Usefulness of combined PET/CT for patient with epithelial ovarian cancer showing recurrence based on tumor marker CA125. *Tokai J Exp Clin Med* 2007;**32**(1): 23-7.

95. Soussan M, Wartski M, Cherel P, et al. Impact of FDG PET-CT imaging on the decision making in the biologic suspicion of ovarian carcinoma recurrence. *Gynecol Oncol* 2008;**108**(1): 160-5.

96. Risum S, Hogdall C, Loft A, et al. The diagnostic value of PET/CT for primary ovarian cancer--a prospective study. *Gynecol Oncol* 2007;**105**(1): 145-9.

97. Risum S, Loft A, Engelholm SA, et al. Positron emission tomography/computed tomography predictors of overall survival in stage IIIC/IV ovarian cancer. *Int J Gynecol Cancer* 2012;**22**(7): 1163-9.

98. Fuccio C, Castellucci P, Marzola MC, Al-Nahhas A, Fanti S, Rubello D. Noninvasive and invasive staging of ovarian cancer: review of the literature. *Clin Nucl Med* 2011;**36**(10): 889-93.

99. Antunovic L, Cimitan M, Borsatti E, et al. Revisiting the clinical value of 18F-FDG PET/CT in detection of recurrent epithelial ovarian carcinomas: correlation with histology, serum CA-125 assay, and conventional radiological modalities. *Clin Nucl Med* 2012;**37**(8): e184-8.

100. Bristow RE, del Carmen MG, Pannu HK, et al. Clinically occult recurrent ovarian cancer: patient selection for secondary cytoreductive surgery using combined PET/CT. *Gynecol Oncol* 2003;**90**(3): 519-28.

101. Makhija S, Howden N, Edwards R, Kelley J, Townsend DW, Meltzer CC. Positron emission tomography/computed tomography imaging for the detection of recurrent ovarian and fallopian tube carcinoma: a retrospective review. *Gynecol Oncol* 2002;**85**(1): 53-8.

102. Garcia Velloso MJ, Boan Garcia JF, Villar Luque LM, Aramendia Beitia JM, Lopez Garcia G, Richter Echeverria JA. [F-18-FDG positron emission tomography in the diagnosis of ovarian recurrence. Comparison with CT scan and CA 125]. *Rev Esp Med Nucl* 2003;**22**(4): 217-23.

103. Kurokawa T, Yoshida Y, Kawahara K, et al. Whole-body PET with FDG is useful for following up an ovarian cancer patient with only rising CA-125 levels within the normal range. *Ann Nucl Med* 2002;**16**(7): 491-3.

104. Simcock B, Neesham D, Quinn M, Drummond E, Milner A, Hicks RJ. The impact of PET/CT in the management of recurrent ovarian cancer. *Gynecol Oncol* 2006;**103**(1): 271-6.

105. Ebina Y, Watari H, Kaneuchi M, et al. Impact of FDG PET in optimizing patient selection for cytoreductive surgery in recurrent ovarian cancer. *Eur J Nucl Med Mol Imaging* 2014;**41**(3): 446-51.

106. Gu P, Pan LL, Wu SQ, Sun L, Huang G. CA 125, PET alone, PET-CT, CT and MRI in diagnosing recurrent ovarian carcinoma: a systematic review and meta-analysis. *Eur J Radiol* 2009;**71**(1): 164-74.

107. Thrall MM, DeLoia JA, Gallion H, Avril N. Clinical use of combined positron emission tomography and computed tomography (FDG-PET/CT) in recurrent ovarian cancer. *Gynecol Oncol* 2007;**105**(1): 17-22.

108. Iyer RB, Balachandran A, Devine CE. PET/CT and cross sectional imaging of gynecologic malignancy. *Cancer Imaging* 2007;**7** Spec No A: S130-8.

109. Lai CH, Yen TC, Chang TC. Positron emission tomography imaging for gynecologic malignancy. *Curr Opin Obstet Gynecol* 2007;**19**(1): 37-41.

110. Kalli KR, Oberg AL, Keeney GL, et al. Folate receptor alpha as a tumor target in epithelial ovarian cancer. *Gynecol Oncol* 2008;**108**(3): 619-26.

111. Guo W, Hinkle GH, Lee RJ. 99mTc-HYNIC-folate: a novel receptor-based targeted radiopharmaceutical for tumor imaging. *J Nucl Med* 1999;**40**(9): 1563-9.

112. Mathias CJ, Hubers D, Low PS, Green MA. Synthesis of [(99m)Tc]DTPA-folate and its evaluation as a folate-receptor-targeted radiopharmaceutical. *Bioconjug Chem* 2000;**11**(2): 253-7.

113. Leamon CP, Parker MA, Vlahov IR, et al. Synthesis and biological evaluation of EC20: a new folate-derived, (99m)Tc-based radiopharmaceutical. *Bioconjug Chem* 2002;**13**(6): 1200-10.

114. Okarvi SM, Jammaz IA. Preparation and in vitro and in vivo evaluation of technetium-99m-labeled folate and methotrexate conjugates as tumor imaging agents. *Cancer Biother Radiopharm* 2006;**21**(1): 49-60

115. Maurer AH, Elsinga P, Fanti S, Nguyen B, Oyen WJ, Weber WA. Imaging the folate receptor on cancer cells with 99mTc-etarfolatide: properties, clinical use, and future potential of folate receptor imaging. *J Nucl Med* 2014;**55**(5): 701-4.

116. Siegel BA, Dehdashti F, Mutch DG, et al. Evaluation of 111In-DTPA-folate as a receptor-targeted diagnostic agent for ovarian cancer: initial clinical results. *J Nucl Med* 2003;**44**(5): 700-7.

117. Muller C. Folate-based radiotracers for PET imaging--update and perspectives. *Molecules* 2013;**18**(5): 5005-31.

118. AlJammaz I, Al-Otaibi B, Al-Rumayan F, Al-Yanbawi S, Amer S, Okarvi SM. Development and preclinical evaluation of new (124)I-folate conjugates for PET imaging of folate receptor-positive tumors. *Nucl Med Biol* 2014;**41**(6): 457-63.

119. Perrone MG, Malerba P, Uddin MJ, et al. PET radiotracer [(18)F]-P6 selectively targeting COX-1 as a novel biomarker in ovarian cancer: Preliminary investigation. *Eur J Med Chem* 2014;**80**: 562-8.

120. van Dam GM, Themelis G, Crane LM, et al. Intraoperative tumor-specific fluorescence imaging in ovarian cancer by folate receptor-alpha targeting: first in-human results. *Nat Med* 2011;**17**(10): 1315-9.

121. Wang Y, Miao Z, Ren G, Xu Y, Cheng Z. A novel Affibody bioconjugate for dual-modality imaging of ovarian cancer. *Chem Commun* (Camb) 2014.

122. Liu TW, Stewart JM, Macdonald TD, et al. Biologically-targeted detection of primary and micro-metastatic ovarian cancer. *Theranostics* 2013;**3**(6): 420-7.

123. Lee H, Kim J, Kim H, Kim Y, Choi Y. A folate receptor-specific activatable probe for near-infrared fluorescence imaging of ovarian cancer. *Chem Commun* (Camb) 2014;**50**(56): 7507-10.

124. Buist MR, Kenemans P, den Hollander W, et al. Kinetics and tissue distribution of the radiolabeled chimeric monoclonal antibody MOv18 IgG and F(ab')2 fragments in ovarian carcinoma patients. *Cancer Res* 1993;**53**(22): 5413-8.

125. Zalutsky MR, Knapp RC, Bast RC, Jr. Influence of circulating antigen on blood pool activity of a radioiodinated monoclonal antibody. *Int J Rad Appl Instrum B* 1988;**15**(4): 431-7.

126. Chatal JF, Saccavini JC, Gestin JF, et al. Biodistribution of indium-111-labeled OC 125 monoclonal antibody intraperitoneally injected into patients operated on for ovarian carcinomas. *Cancer Res* 1989;**49**(11): 3087-94.

127. Rubin SC, Kairemo KJ, Brownell AL, et al. High-resolution positron emission tomography of human ovarian cancer in nude rats using 124I-labeled monoclonal antibodies. *Gynecol Oncol* 1993;**48**(1): 61-7.

128. van Dongen GA, Visser GW, Lub-de Hooge MN, de Vries EG, Perk LR. Immuno-PET: a navigator in monoclonal antibody development and applications. *Oncologist* 2007;**12**(12): 1379-89.

129. Wu AM. Antibodies and antimatter: the resurgence of immuno-PET. *J Nucl Med* 2009;**50**(1): 2-5.

130. McCabe KE, Wu AM. Positive progress in immunoPET--not just a coincidence. *Cancer Biother Radiopharm* 2010;**25**(3): 253-61.

131. Cai W, Olafsen T, Zhang X, et al. PET imaging of colorectal cancer in xenograft-bearing mice by use of an 18F-labeled T84.66 anti-carcinoembryonic antigen diabody. *J Nucl Med* 2007;**48**(2): 304-10.

132. Olafsen T, Sirk SJ, Olma S, Shen CK, Wu AM. ImmunoPET using engineered antibody fragments: fluorine-18 labeled diabodies for same-day imaging. *Tumour Biol* 2012;**33**(3): 669-77.

133. Hong H, Zhang Y, Orbay H, et al. Positron emission tomography imaging of tumor angiogenesis with a (61/64)Cu-labeled F(ab')(2) antibody fragment. *Mol Pharm* 2013;**10**(2): 709-16.

134. Zhang Y, Hong H, Orbay H, et al. PET imaging of CD105/endoglin expression with a (6)(1)/(6)(4)Cu-labeled Fab antibody fragment. *Eur J Nucl Med Mol Imaging* 2013;**40**(5): 759-67.

135. Lepin EJ, Leyton JV, Zhou Y, et al. An affinity matured minibody for PET imaging of prostate stem cell antigen (PSCA)-expressing tumors. *Eur J Nucl Med Mol Imaging* 2010;**37**(8): 1529-38.

136. Olafsen T, Sirk SJ, Betting DJ, et al. ImmunoPET imaging of B-cell lymphoma using 124I-anti-CD20 scFv dimers (diabodies). *Protein Eng Des Sel* 2010;**23**(4): 243-9.

137. Olafsen T, Betting D, Kenanova VE, et al. Recombinant anti-CD20 antibody fragments for small-animal PET imaging of B-cell lymphomas. *J Nucl Med* 2009;**50**(9): 1500-8.

138. Fu M, Brewer S, Olafsen T, et al. Positron emission tomography imaging of endometrial cancer using engineered anti-EMP2 antibody fragments. *Mol Imaging Biol* 2013;**15**(1): 68-78.

139. Lutje S, Franssen GM, Sharkey RM, et al. Anti-CEA antibody fragments labeled with [(18)F]AlF for PET imaging of CEA-expressing tumors. *Bioconjug Chem* 2014;**25**(2): 335-41.

140. Fonge H, Leyton JV. Positron emission tomographic imaging of iodine 124 anti-prostate stem cell antigen-engineered antibody fragments in LAPC-9 tumor-bearing severe combined immunodeficiency mice. *Mol Imaging* 2013;**12**(3): 191-202.

141. McCabe KE, Liu B, Marks JD, Tomlinson JS, Wu H, Wu AM. An engineered cysteine-modified diabody for imaging activated leukocyte cell adhesion molecule (ALCAM)-positive tumors. *Mol Imaging Biol* 2012;**14**(3): 336-47

142. Girgis MD, Kenanova V, Olafsen T, McCabe KE, Wu AM, Tomlinson JS. Anti-CA19-9 diabody as a PET imaging probe for pancreas cancer. *J Surg Res* 2011;**170**(2): 169-78.

143. Li L, Crow D, Turatti F, et al. Site-specific conjugation of monodispersed DOTA-PEGn to a thiolated diabody reveals the effect of increasing peg size on kidney clearance and tumor uptake with improved 64-copper PET imaging. *Bioconjug Chem* 2011;**22**(4): 709-16.

144. Natarajan A, Habte F, Gambhir SS. Development of a novel long-lived immunoPET tracer for monitoring lymphoma therapy in a humanized transgenic mouse model. *Bioconjug Chem* 2012;**23**(6): 1221-9.

145. Zhang Y, Hong H, Severin GW, et al. ImmunoPET and near-infrared fluorescence imaging of CD105 expression using a monoclonal antibody dual-labeled with (89)Zr and IRDye 800CW. *Am J Transl Res* 2012;**4**(3): 333-46.

146. Ogasawara A, Tinianow JN, Vanderbilt AN, et al. ImmunoPET imaging of phosphatidylserine in pro-apoptotic therapy treated tumor models. *Nucl Med Biol* 2013;**40**(1): 15-22

147. Viola-Villegas NT, Rice SL, Carlin S, et al. Applying PET to broaden the diagnostic utility of the clinically validated CA19.9 serum biomarker for oncology. *J Nucl Med* 2013;**54**(11): 1876-82.

148. Stillebroer AB, Franssen GM, Mulders PF, et al. ImmunoPET imaging of renal cell carcinoma with (124)I- and (89)Zr-labeled anti-CAIX monoclonal antibody cG250 in mice. *Cancer Biother Radiopharm* 2013;**28**(7): 510-5.

149. Ikotun OF, Marquez BV, Huang C, et al. Imaging the L-type amino acid transporter-1 (LAT1) with Zr-89 immunoPET. PLoS One 2013;**8**(10): e77476.

150. Holland JP, Divilov V, Bander NH, Smith-Jones PM, Larson SM, Lewis JS. 89Zr-DFO-J591 for immunoPET of prostate-specific membrane antigen expression in vivo. J Nucl Med 2010;**51**(8): 1293-300.

151. Sham JG, Kievit FM, Grierson JR, et al. Glypican-3-targeted 89Zr PET imaging of hepatocellular carcinoma. *J Nucl Med* 2014;**55**(5): 799-804.

152. Wu AM. Engineered antibodies for molecular imaging of cancer. *Methods* 2014;**65**(1): 139-47.

153. Knowles SM, Wu AM. Advances in immuno-positron emission tomography: antibodies for molecular imaging in oncology. *J Clin Oncol* 2012;**30**(31): 3884-92.

154. Wu AM, Olafsen T. Antibodies for molecular imaging of cancer. *Cancer* J 2008;**14**(3): 191-7.

155. Chakravarty R, Goel S, Cai W. Nanobody: the "magic bullet" for molecular imaging? *Theranostics* 2014;**4**(4): 386-98.

156. Marcus CS, Maxwell GL, Darcy KM, Hamilton CA, McGuire WP. Current approaches and challenges in managing and monitoring treatment response in ovarian cancer. J Cancer 2014;5(1): 25-30.

157. Gadducci A, Sartori E, Zola P, et al. Serum CA125 assay in the early diagnosis of recurrent epithelial ovarian cancer. Oncol Rep 1996;3(2): 301-3.

158. Hori SS, Gambhir SS. Mathematical model identifies blood biomarker-based early cancer detection strategies and limitations. Sci Transl Med 2011;3(109): 109ra16.

159. Torizuka T, Nobezawa S, Kanno T, et al. Ovarian cancer recurrence: role of whole-body positron emission tomography using 2-[fluorine-18]-fluoro-2-deoxy-D-glucose. Eur J Nucl Med Mol Imaging 2002;29(6): 797-803.

2

Improved soluble expression of a single-chain antibody fragment in *E.coli* for targeting CA125 in Epithelial Ovarian Cancer[1]

[1] *A version of this chapter has been published: Sharma SK, Suresh MR, Wuest FR. Improved soluble expression of a single-chain antibody fragment in E.coli for targeting CA125 in epithelial ovarian cancer. Protein Expression and Purification. 2014 July;102: 27-37*

2.1 Introduction

Recombinant technology has expanded the scope for engineering antibodies which have now evolved from being sentinels of the immune system to becoming key components in targeted diagnostic and therapeutic applications. One of the most popular formats of an engineered antibody is the single-chain fragment variable (scFv). Comprised of the heavy (V_H) and light (V_L) chain of an immunoglobulin's variable domains connected by a flexible peptide linker, this class of recombinant molecules are often referred to as the smallest yet complete active component of the immunoglobulin capable of binding to a target antigen.[1, 2] Some advantages of the scFv format over full-length antibodies are a) minimal immunogenicity due to the lack of F_c regions; b) faster *in vivo* clearance and better tissue penetration owing to a relatively smaller molecular size; c) cost effectiveness due to ease of production in simple host systems such as *E.coli* and d) their amenability to recombinant engineering.[3] Furthermore, the possibilities to screen immune libraries for isolation of high affinity scFv binders to practically any antigen by phage display,[4] ribosome display[5] and yeast display[6] technologies have expanded scientific capabilities and ease of discovery, synthesis and production of engineered antibodies. Nevertheless, having access to the parent hybridoma cell for a monoclonal antibody (MAb) can facilitate the isolation of its derivative scFv with retained immunoreactivity and specificity.[7, 8] This gains translational relevance when the scFv is sought from a clinically approved MAb.[9] However, there are challenges with the expression of murine antibody sequences

from a heterologous prokaryotic host such as *E.coli* in order to yield soluble and functional scFv.

Cancer Antigen 125 (CA125) is a mucinous glycoprotein that serves as a USFDA approved tumor biomarker for the diagnosis of epithelial ovarian cancer (EOC).[10, 11] CA125 can be detected in immunoassay techniques as an antigen shed in the serum of patients presenting in the clinic with pelvic masses.[12] The immunoassay formats and targeting applications have been greatly facilitated by the production of several antibodies against CA125.[13-16] Among those reported, MAb B43.13 has shown great translational benefit in the immunotherapy of EOC.[17] Interestingly, there are not as many scFv molecules developed against this tumor-associated antigen.[18-22] Prior literature indicates that the anti-CA125 B43.13 scFv was purified as a secreted protein from yeast,[18] as a secreted bi-specific scFv from murine myeloma NS0 cells,[20] and engineered to be produced as a bi-functional fusion construct in *E.*coli, albeit in low yields as a result of soluble expression.[21] Considering its previously demonstrated potential for biopharmaceutical application to target CA125,[20, 21, 23] the production of this scFv in multi-milligram amounts could be a starting point for further engineering and expansion of its utility as an EOC targeting vector for immunodiagnostics, drug delivery and potential immunotherapy.[24]

In the present work, we investigated the effects of variable domain orientation, different inter-domain linkers and codon optimization to increase the yields of soluble protein from heterologous expression of anti-CA125 B43.13 scFv in *E.coli*. The scFv was isolated from soluble fractions of recombinant cell lysates

with high purity using a single step purification via immobilized metal affinity chromatography and was found to be biochemically active for binding to target antigen CA125. Codon optimization was found to be the most important factor to positively impact soluble expression of anti-CA125 scFv resulting in up to 14-fold higher yields than all the other murine scFv variants examined in this study.

2.2 Materials

All chemicals including antibiotics used were purchased from Sigma Aldrich unless otherwise specified. Phusion high-fidelity DNA polymerase (Finnzymes, F-530S), and oligonucleotide primers (Integrated DNA Technologies) were used for PCR amplification of the scFv domains. *Nco* I (NEB, R0193S), *Not* I (NEB, R0189S) and T4 DNA Ligase (NEB, M0202S) were used for directional cloning of genes encoding the scFv domains. pET-22b(+) vector (Novagen, 69744) and *E.coli* Rosetta™ 2(DE3) (Novagen, 71400) were used for expression of the scFv. Bacto tryptone (BD, 212750), Yeast extract (BD, 211705) and sodium chloride (Fisher Scientific, 7647-14-5) were used to prepare the 2x YT medium. Isopropyl-β-D-thiogalactopyranoside (IPTG) (Fisher Scientific, BP1755-10) was used for induction of recombinant scFv expression. BugBuster Master Mix (Novagen, 71456) was used for cell lysis of harvested *E.coli* cultures. TALON® Superflow resin (Clontech, 635506) was used for immobilized metal affinity chromatography. Glycine (Bio-Rad, 161-0718) and Coomassie brilliant blue R-250 (Bio-Rad, 161-0400), Pre-stained SDS-PAGE standards – Low Range (Bio-Rad, 161-0305) were used for protein analysis by gel electrophoresis. Amicon Ultra-15, 10K MWCO filters (EMD Millipore, UFC901024) were used to concentrate the purified proteins. Fetal bovine serum (Life Technologies, 12483-020), penicillin-streptomycin (10,000 U/ml) (Life Technologies, 15140-122) and recombinant human insulin (SAFC Biosciences, 91077C) were used for culturing ovarian cancer cell lines. CelLytic™ M (Sigma, C2978) Trans-Blot nitrocellulose membrane (Bio-Rad, 162-0115), Amersham Hyperfilm ECL (GE Healthcare,

28906839), Amersham ECL Plus Western Blotting Detection Reagents (GE Healthcare, RPN2132), mouse anti-β actin IgG (Sigma, A1978), goat anti-mouse HRP conjugate (Sigma, A4416), 6X His MAb-HRP conjugate (Clontech, 631210) were used for immunoblotting. Alexa-fluor® 488 goat anti-mouse antibody (Life Technologies, A-11001) and Penta·His Alexa Fluor 488 conjugate (Qiagen, 35310) were used in immunofluoresce and flow cytometry studies. Anti-CA125 MAb was isolated from hybridoma B43.13 and anti-RANK receptor scFv was generously provided by Dr. Michael Doschak, University of Alberta, Canada.

2.3 Methods

2.3.1 Cloning of anti-CA125 scFv variants:

The genes encoding the variable domains of the anti-CA125 scFv were amplified by polymerase chain reaction (PCR) using a previously reported plasmid construct pWET8[20] as the template. Engineering of inter-domain linkers and production of different orientations of the single chain domains was performed by splice-overlap extension PCRs to create the following constructs viz. V_H-$(G_2S)_5$-V_L; V_L-$(G_2S)_5$-V_H; V_H-$(G_4S)_3$-V_L; V_L-$(G_4S)_3$-V_H; V_L-(218)-V_H, (Fig 1) with *Nco* I and *Not* I as unique 5' and 3' cloning sites respectively for ligation into pET-22b(+) expression vector.

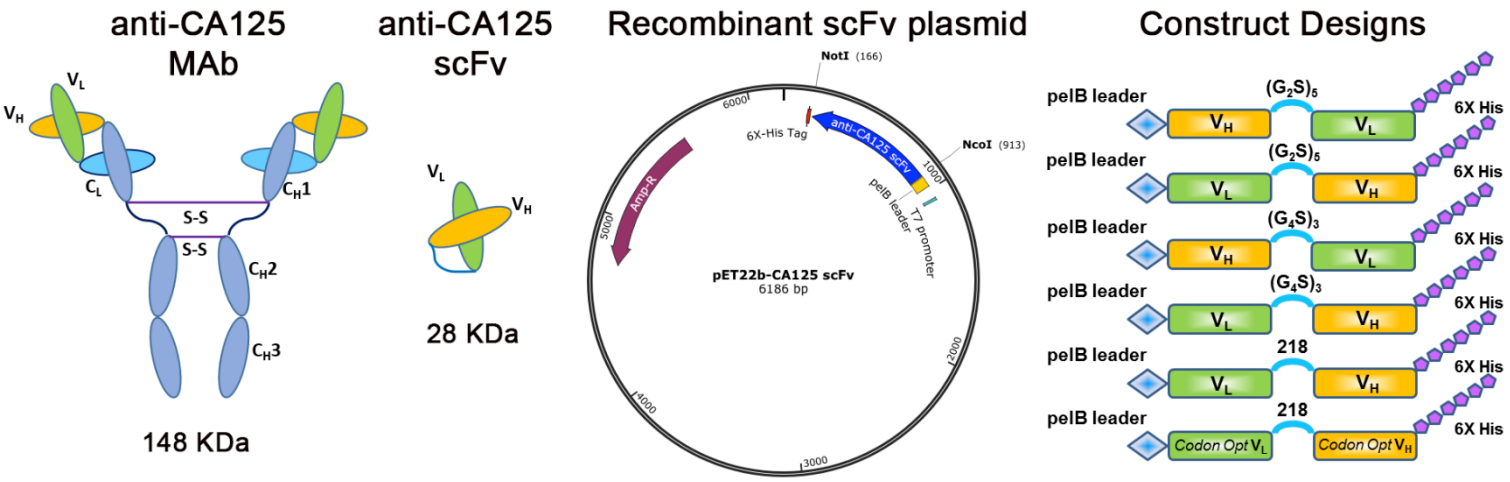

Figure 2.1: Schematic representation of the anti-CA125 MAb and its derivative scFv cloned into pET-22b(+) vector in different orientations for heterologous expression in *E.coli*.

Based on demonstrated outcomes for other scFv molecules suggested in prior reports,[25-27] the V_L-(218)-V_H scFv gene was codon-optimized for expression in *E.coli* and synthesized by GeneArt® (Life Technologies). The codon-optimized scFv gene was sub-cloned into pET-22b(+) vector between *Nco* I and *Not* I sites. This construct is hereafter designated as GA218 in this article, whereas the murine anti-CA125 scFv coding sequences will be referred to as the wild-type (WT) sequence. The scFv DNA cloned in each recombinant construct was verified by Sanger sequencing on a 3730 DNA analyzer (Applied Biosystems, Life Technologies) prior to transformation in the bacterial expression host.

2.3.2 Small scale expression analysis:

Each recombinant plasmid coding for different scFv constructs was transformed into chemically competent *E.coli* Rosetta 2(DE3) cells by heat-shock method and plated onto 1.5% 2x YT agar plates containing 100 µg/mL ampicillin and 34 µg/ml chloramphenicol. Single transformant colonies were picked and inoculated into 10 ml 2x YT medium (16 g/L tryptone, 10 g/L yeast extract and 5 g/L sodium chloride, pH 7.5) in the presence of antibiotics and cultured overnight by incubation at 37˚C with shaking at 200 rpm. 0.2 ml of the overnight grown culture was added to 20 ml of fresh 2x YT medium with the aforementioned concentration of antibiotics in a 125 mL shake flask and allowed to grow at 37˚C with shaking at 220 rpm until an OD_{600} of 0.6 – 0.8 was achieved. The shake flask cultures were briefly placed in ice cold water for 15 minutes prior to induction with a final concentration of 0.8 mM IPTG. The induced cultures were incubated

at 26˚C with shaking at 200 rpm overnight for 16 h. Spectrophotometric measurement of overnight grown cultures was performed to enable normalized loading (OD_{600} = 1) for a comparative evaluation of scFv expression from the different constructs. Samples representative of total cell protein samples were prepared by adding Laemmli sample buffer (50 mM Tris-HCl pH 6.8, 2% SDS, 10% glycerol, 5 mM 2-mercaptoethanol, 0.1% bromophenol blue) to the normalized cell pellets and heating them at 95˚C for 5 minutes prior to analysis on a 12% SDS-PAGE, followed by staining with Coomassie brilliant blue R-250 and immunoblotting with 6X His MAb-HRP conjugate.

2.3.3 Small scale batch binding:

To detect soluble scFv expressed and extractable at the small scale, pertinent volumes of the overnight grown bacterial cultures (volumes worth a total OD_{600} = 20) were processed further by cell lysis using BugBuster® Master Mix reagent to perform batch binding analyses with TALON® superflow metal affinity resin. 10 mM imidazole in 50 mM sodium di-hydrogen phosphate [$NaH_2PO_4.H_2O$] and 100 mM sodium chloride pH 7.0 was used as wash buffer and 150 mM imidazole in 50 mM sodium di-hydrogen phosphate and 100 mM sodium chloride pH 7.0 was used as the elution buffer. Supernatants harvested from cell lysates were allowed to incubate with 100 µL of TALON resin at 4˚C for 2 h. Unbound proteins were isolated by centrifugation of the mixture of lysate supernatant and resin at 500 g for 5 minutes. Two rinses were performed with 1 mL of wash buffer by adding it to the resin and allowing this to mix well for 10 minutes prior to centrifugation at

500 g for 5 minutes. The resulting supernatants were collected and designated as W_1 and W_2 samples. Finally, 2 x 10 minutes rinses were performed with the elution buffer prior to collection of eluate fractions upon centrifugation at 500 g for 5 minutes. The resulting fractions were designated as E_1 and E_2 samples. All fractions were analyzed by SDS-PAGE under reducing conditions followed by Coomasie staining and immunoblotting for hexa-histidine tagged scFv.

2.3.4 Medium scale expression and purification of anti-CA125 scFv variants:

To compare recombinant scFv yields from 1L cultures in shake flasks, single transformant colonies were picked for each construct and inoculated into 12.5 ml 2x YT medium with 100 µg/mL ampicillin, 34 µg/mL chloramphenicol and cultured overnight by incubation at 37˚C with shaking at 200 rpm. 5 ml of the overnight grown cultures was added to 500 ml fresh 2x YT medium in the presence of antibiotics in 2 liter flasks and incubated at 37˚C with shaking at 220 rpm until an OD_{600} of 0.6 – 0.8 was achieved. The shake flask cultures were briefly placed in ice cold water for 15 minutes prior to induction with a final concentration of 0.8 mM IPTG. The induced cultures were incubated at 26˚C with shaking at 200 rpm overnight for 16 h. The bacteria were harvested by centrifugation at 7000 rpm for 30 minutes and the pellet obtained thereof was frozen by storage at -20˚C. Soluble scFv variants were extracted from frozen cell pellets by lysis with BugBuster® Master Mix reagent as per the manufacturer's instructions. The cell lysate was cleared by centrifugation at 16,000 rpm for 30 minutes and the supernatant was collected for purification of soluble scFv. C-

terminal hexa-histidine tagged recombinant scFv was purified via immobilized metal affinity chromatography (IMAC) by passing the supernatant over TALON® superflow metal affinity resin packed in a column that was operated under gravity using a Masterflex HV-07520-00 peristaltic pump (Cole Parmer) to provide a flow rate of 1 mL/min. Non-specifically bound protein was washed using 15 column volumes of 10 mM imidazole in equilibration buffer (50 mM $NaH_2PO_4.H_2O$ and 100 mM NaCl pH 7.0). Soluble hexa-histidine tagged scFv bound to the affinity column was eluted by flowing a linear gradient of 10 mM – 150 mM imidazole in equilibration buffer prepared using a gradient maker GM-200 (CBS Scientific). 1 mL IMAC eluted fractions were collected and analyzed by 12% SDS-PAGE under reducing conditions, followed by Coomassie staining and immunoblotting with 6X His MAb-HRP conjugate. High purity eluate fractions were pooled together for dialysis into phosphate buffered saline (pH 7.4) and concentrated to a final volume of 1 mL using Amicon Ultra-15, 10K MWCO filters. Final concentrations of the purified scFv were quantified using a Pierce™ BCA protein assay kit (Thermo Scientific, 23227) according to the manufacturer's recommendations. Bovine serum albumin supplied with the kit was used to prepare a standard curve for protein estimation.

2.3.5 Molecular and functional characterization of anti-CA125 scFv constructs:

2.3.5.1 Protein ID: An in-gel tryptic digest of the purified scFv samples followed by LC-MS/MS analyses was performed to verify protein identity at the Institute of

Biomolecular Design, University of Alberta, Canada. Briefly, the excised SDS-PAGE bands were de-stained twice in 100 mM ammonium bicarbonate/acetonitrile (50:50). The samples were then reduced (10 mM β-ME in 100 mM bicarbonate) and alkylated (55 mM iodoacetamide in 100 mM bicarbonate). After dehydration enough trypsin (6 ng/μL) was added to just cover the gel piece and the digestion was allowed to proceed overnight (~16 hrs.) at room temperature. Tryptic peptides were first extracted from the gel using 97% water/2% acetonitrile/1% formic acid followed by a second extraction using 50% of the first extraction buffer and 50% acetonitrile.

Fractions containing tryptic peptides dissolved in aqueous 25% v/v ACN and 1% v/v formic acid were resolved and ionized by using nanoflow HPLC (Easy-nLC II, Thermo Scientific) coupled to the LTQ XL-Orbitrap hybrid mass spectrometer (Thermo Scientific). Nanoflow chromatography and electrospray ionization were accomplished by using a PicoFrit fused silica capillary column (ProteoPepII, C18) with 100 μm inner diameter (300 Å, 5 μm, New Objective). Peptide mixtures were injected onto the column at a flow rate of 3000 nL/min and resolved at 500 nL/min using 90 min linear gradients from 0 to 45% v/v aqueous ACN in 0.2% v/v formic acid. The mass spectrometer was operated in data-dependent acquisition mode, recording high-accuracy and high-resolution survey Orbitrap spectra using external mass calibration, with a resolution of 60 000 and *m*/*z* range of 400–2000. The ten most intense multiply charged ions were sequentially fragmented by using collision induced dissociation, and spectra of their fragments were recorded in the linear ion trap; after two fragmentations, all precursors

selected for dissociation were dynamically excluded for 60 s. Data was processed using Mascot (Matrix Science) and the NCBInr database was searched. Search parameters included a precursor mass tolerance of 0.8 Da and a fragment mass tolerance of 0.8Da. Peptides were searched with carbamidomethyl cysteine as a fixed modification and oxidized methionine as variable modification.

2.3.5.2 N-terminal Protein Sequencing: 12 μg each of scFv V_L-$(G_4S)_3$-V_H and GA218 were electrophoresed on a 4-15% Mini-PROTEAN® TGX™ precast gel (Bio-Rad) and electroblotted onto Hybond-P 0.45 μm PVDF membrane (GE Healthcare). The blot was stained with Coomassie brilliant blue R-250, destained with methanol and washed thoroughly with milli-Q water prior to excision of the scFv bands. N-terminal protein sequencing by Edman degradation was performed at the protein facility of the Iowa State University Office of Biotechnology, USA.

2.3.5.3 Cell lines and culture conditions: Ovarian cancer cells NIH:OVCAR-3 (ATCC® HTB-161™) that overexpress CA125 and SKOV3 (ATCC® HTB-77™) that do not express CA125 were used for *in vitro* functional characterization studies. Cells were cultured in DMEM-F12 medium supplemented with 10% v/v fetal bovine serum, 50 IU/mL penicillin, 50 μg/mL streptomycin. NIH:OVCAR-3 cells were additionally supplemented with 7 μg/mL recombinant human insulin. Cells were cultured using sterile techniques and grown in a 37°C incubator providing humidified atmosphere of 5% CO_2 in air.

2.3.5.4 Immunoblotting: 7.5 x 10^6 NIH:OVCAR-3 and SKOV3 cells were lysed with CelLytic™ M. Cell lysates were electrophoresed on a 4-15% Mini-PROTEAN® TGX™ precast gel (Bio-Rad) and transferred to a Trans-Blot nitrocellulose membrane (Bio-Rad). The membranes were probed separately to evaluate binding capabilities of the different anti-CA125 scFv constructs with target antigen in cell lysates. The blots were blocked for 45 min with 5% non-fat dry milk (Carnation) in PBS having 0.1% Tween-20 (PBST). Anti-CA125 MAb (3 mg/mL), mouse anti-β actin IgG and anti-CA125 scFv variants (~2 mg/mL) were used as primary antibodies (1: 5000 each) to probe the blots for 1 h at room temperature. Goat anti-mouse HRP conjugate (1: 5000) was used as secondary antibody to probe the blot against anti-CA125 MAb and mouse anti-β actin IgG for 1 h at room temperature. 6X His MAb-HRP conjugate (1:5000) was used as secondary antibody to probe against antigen-bound anti-CA125 scFv variants by incubating for 1 h at room temperature. Anti-CA125 targeting monoclonal antibody MAb B43.13[28] was used as a positive control. A hexa-histidine tagged anti-RANK receptor binding scFv[29] was used as an isotype control.

2.3.5.5 Flow Cytometry: 1.5 x 10^6 NIH:OVCAR-3 cells were harvested by trypsinization, rinsed twice with FACS buffer (PBS with 0.5% heat inactivated FBS, 2mM EDTA ,0.05% sodium azide) and resuspended by gentle tapping in ~100 µL FACS buffer. 10 µg of anti-CA125 MAb or scFv variants were incubated with the cell suspension for 30 min at room temperature. Cells were rinsed twice in FACS buffer and incubated for 30 min with 1.6 µg of Alexa-fluor®

488 goat anti-mouse antibody for the MAb sample and 2.4 µg of Penta·His Alexa Fluor 488 conjugate for scFv samples. Cells were rinsed twice with FACS buffer and analyzed by flow cytometry on a BD FACS Calibur with 10,000 events gated per sample. A hexa-histidine tagged anti-RANK receptor binding scFv was used as an isotype control. Negative controls included unstained NIH:OVCAR-3 cells and cells incubated with Alexa fluor 488 conjugated antibodies alone.

2.3.5.6 Immunofluorescence: NIH:OVCAR-3 cells were plated onto glass coverslips in 35-mm tissue culture dishes (100,000 cells/2 mL medium/dish) and incubated at 37°C for 48 h. The cells were rinsed with PBS and fixed in methanol for 30 min at -20°C. The fixed cells were incubated in 5% non-fat dry milk (Carnation) in PBS and immunostained separately for 1 h with anti-CA125 MAb and the purified scFv constructs. Corresponding Alexa fluor-488 labeled secondary antibodies were used as in the flow cytometry studies. Anti-CA125 MAb and scFv (2 mg/mL) (1:250) followed by secondary antibodies (2 mg/mL) (1:500) in PBS containing 5% non-fat dry milk. Appropriate blank and control samples were included in the experiments. All antibody incubations were followed by three rinses with PBST for 10 min each. Coverslips were mounted on microscopy slides (Fisherbrand) using Mowiol® mounting medium (Calbiochem, 475904) supplemented with DAPI (50 µg/ml). Immunofluorescence was observed through a Zeiss Plan Apochromat 40X/1.3 Oil DIC M27 lens on a confocal laser scanning microscope (Zeiss LSM 710). The images were analyzed using Zen 2011 software and processed further using Adobe Photoshop CS6.

2.4 Results:

2.4.1 scFv cloning and codon optimization:

Sanger sequencing of the recombinant plasmid constructs revealed high fidelity DNA amplification and successful directional cloning of all the scFv variants between *Nco*I and *Not*I restriction sites in pET22b (+) expression vector. Analysis of the nucleotide sequence for codons in the WT anti-CA125 scFv indicated that ~ 58.3%: 136 out of 233 codons (excluding the linker sequences) had to be modified for optimal expression in *E.coli*. This was further exemplified by more than 90% (32/35) of the original murine codons for serine (S) - the most abundant residue (15%) in the anti-CA125 scFv variable domain sequence had to be optimized for *E.coli* expression (Fig. 2.2). Similarly, among other abundant residues, 71.4% (15/21) codons for glycine (G), 73% (11/15) codons for leucine (L), 66.6% (10/15) codons for lysine (K) and 100% (6/6) codons for arginine (R) had to be modified (Fig. 2.2) to this end. The Codon Adaptation Index (CAI) for heterologous expression of WT anti-CA125 scFv nucleotide sequence in *E.coli* as calculated using an online rare codon analysis tool (http://www.genscript.com/cgi-bin/tools/rare_codon_analysis) improved from 0.64 to 0.93 after codon optimization. A CAI value between 0.8 -1.0 is considered ideal for recombinant expression in *E.coli*.

Anti-CA125 scFv: V_L sequence

```
WT atg gat gat atc gtg     tca     tct cca tcc tcc cta gct gtg tca gtt gga gag aag     act     agt
aa  M   D   D   I   V   -   S   -   S   P   S   S   L   A   V   S   V   G   E   K   -   T   -   S
Opt atg gat gat att gtt     agc     agc ccg agc agc ctg gca gtt agc gtt ggt gaa aaa     acc     agc

WT tgc aag tcc agt     agc ctt tta     agt tcc act caa aag     tac ttg gcc                 aaa cca
aa  C   K   S   S   -   S   L   L   -   S   S   T   Q   K   -   Y   L   A   -   -   -   -   K   P
Opt tgt aaa agc agc     agt ctg ctg     agc agc acc cag aaa     tat ctg gca                 aaa ccg

WT ggg     tct cct aaa ctg cta     tac         tcc act agg     tct ggg gtc cct     cgc ttc aca ggg
aa  G   -   S   P   K   L   L   -   Y   -   -   S   T   R   -   S   G   V   P   -   R   F   T   G
Opt ggt     agt ccg aaa ctg ctg     tat         agc acc cgt     agc ggt gtt ccg     cgt ttt acc ggt

WT agt gga tct ggg aca         act ctc     atc agc agt gtg aag gct gaa gac ctg     gtt     tac tgt
aa  S   G   S   G   T   -   -   T   L   -   I   S   S   V   K   A   E   D   L   -   V   -   Y   C
Opt agc ggt agc ggc acc         acc ctg     att agc agc gtt aaa gca gag gat ctg     gtg     tat tgc

WT caa caa         agc             acg ttc ggt gga ggc     aag ctc gag atc aaa
aa  Q   Q   -   -   S   -   -   -   T   F   G   G   G   -   K   L   E   I   K
Opt cag cag         agc             acc ttt ggt ggt ggc     aaa ctg gaa att aaa
```

Anti-CA125 scFv: V_H sequence

```
WT             cta         tct ggg gct gag ctg gtg agg cct ggg tcc tca     aag     tcc     aag gct
aa  -   -   -   L   -   -   S   G   A   E   L   V   R   P   G   S   S   -   K   -   S   -   K   A
Opt             ctg         agc ggt gca gaa ctg gtt cgt ccg ggt agc agc     aaa     agc     aaa gca

WT tct gac     gca     agt aac tac         aac     gtg aag     agg cct gga     ggt ctt gag
aa  S   D   -   A   -   S   N   Y   -   -   N   -   V   K   -   R   P   G   -   G   L   E   -   -
Opt agc gat     gcc     agc aat tat         aat     gtt aaa     cgt ccg ggt     ggt ctg gaa

WT gga             cct gga ggc ggt     cct aat     aat gga aag     aag ggt aaa gcc aca ctg act
aa  G   -   -   -   P   G   G   G   -   P   N   -   N   G   K   -   K   G   K   A   T   L   T   -
Opt ggt             ccg ggt ggt ggt     ccg aac     aat ggt aaa     aaa ggt aaa gca acc ctg acc

WT gac aaa tcc tcc agt aca     tac         ctc agc aga tta aca tct gag gac tct gcg gtc
aa  D   K   S   S   S   T   -   Y   -   -   L   S   R   L   T   S   E   D   S   A   V   -   -   -
Opt gat aaa agc agt agc acc     tat         ctg agc cgt ctg acc agc gaa gat agc gca gtt

WT     aga     gct     tcc     gct     gac tac     ggt caa gga     tca gtc     gtc tcc tcc
aa  -   R   -   A   -   S   -   A   -   D   Y   -   G   Q   G   -   S   V   -   V   S   S
Opt     cgt     gca     agt     gca     gat tat     ggt cag ggc     agc gtt     gtt agc agt
```

Figure 2.2: Sequence Information: Codon-optimized nucleotide sequences for amino acids in the variable light and heavy chains of anti-CA125 scFv. Single lettered amino acid residues are depicted sandwiched between the wild-type (WT) murine codons on top (typed in black) and the *E.coli*-optimized codons (Opt) for the same residue at the bottom (typed in color). All codons optimized for the following abundant amino acid residues in the scFv are coded in the following colors: serine (S) - red, glycine (G) – green, leucine (L) – orange, lysine (K) – purple, arginine (R) – light blue. Codons for these abundant residues that did not need optimization for *E.coli* expression are typed in black and the corresponding amino acid residue is underlined. All other optimized codons are typed in dark blue.

2.4.2 scFv expression analysis and purification yields:

Small scale analysis of total cell proteins from harvested cultures revealed successful recombinant expression of all scFv variants constructed in this study (Figs. 2.3A and 2.3B).

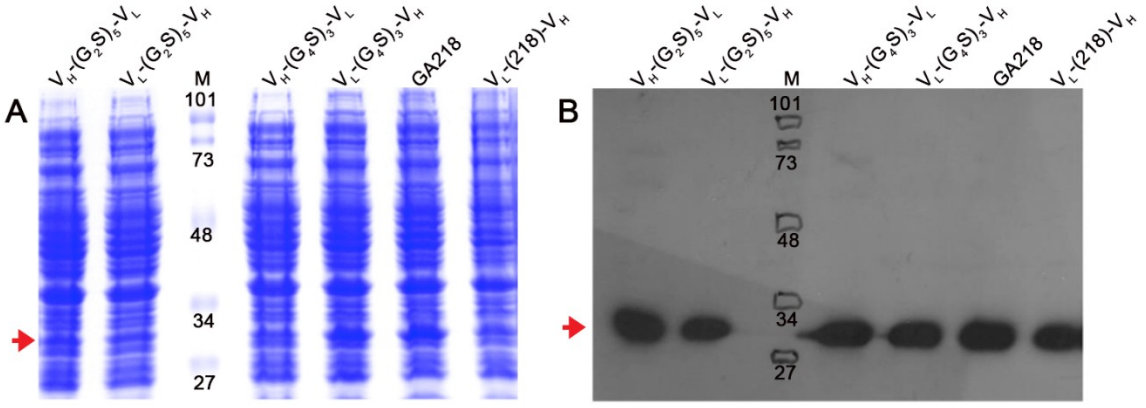

Figure 2.3: Anti-CA125 scFv expression analysis **A)** Coomassie-stained SDS-PAGE of total cell protein samples from the six anti-CA125 scFv constructs expressed in *E.coli*; **B)** A replica gel of the total cell protein samples immunoblotted for hexa-histidine tagged anti-CA125 scFv. Arrows indicate the position of migration corresponding to the molecular weight of the scFv ~28 KDa and is indicative of its presence in all samples. Lane M indicates the pre-stained SDS-PAGE low range molecular weight standard. All MWs are represented in KiloDaltons (KDa).

Most of the heterologously expressed scFvs were found in cell pellets as seen by Coomassie staining and immunoblotting (Figs. 2.4A and 2.4B). However, a distinct band of soluble scFv was seen in the cell lysate supernatant of the GA218 construct (Fig. 2.4B).

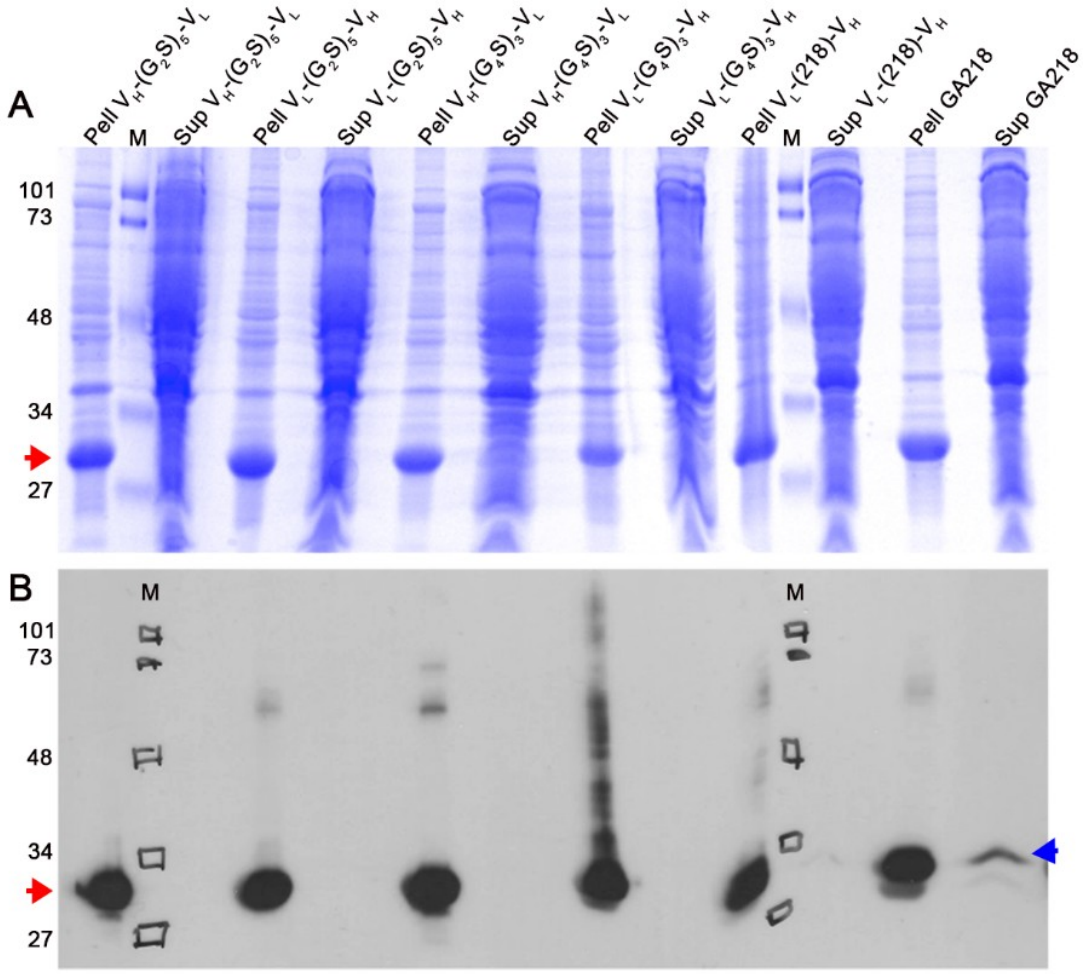

Figure 2.4: Small-scale expression anlaysis **A)** Coomassie-stained SDS-PAGE of samples containing the insoluble and soluble proteins obtained after processing of induced recombinant cultures using BugBuster master mix reagent for cell lysis. Insoluble fractions are labeled with a prefix Pell and corresponding soluble fractions for each construct are labeled with a prefix Sup. **B)** Replica gel of the same samples immunoblotted for the hexa-histidine tagged anti-CA125 scFv. Arrows indicate the position of migration of the scFv corresponding to ~28 KDa. All MWs are represented in KiloDaltons (KDa).

Batch binding analysis revealed maximum soluble expression and elution of scFv GA218 variant followed by scFv V_L-$(G_4S)_3$-V_H (Fig 2.5B).

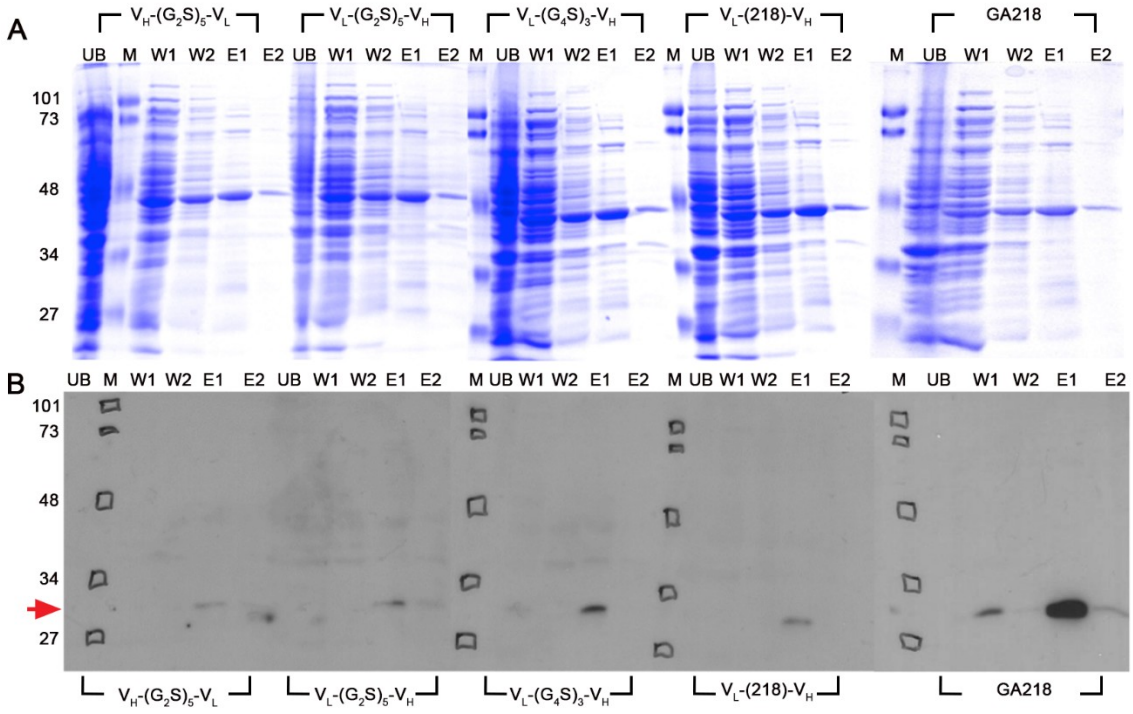

Figure 2.5: Batch Binding studies **A)** Representative Coomassie-stained SDS-PAGE of batch-binding experiments performed using lysates from various anti-CA125 scFv constructs. Each construct has 5 samples that have been analyzed with the following codes: UB – Unbound proteins, W1 – Wash 1, W2 – Wash 2, E1 – Eluate 1, E2 – Eluate 2; **B)** Replica gel of the same samples immunoblotted for the hexa-histidine tagged anti-CA125 scFv. Lane M represents prestained protein molecular weight standard. All MWs are represented in KiloDaltons (KDa). Arrow indicate the position and presence of the anti-CA125 scFv in the samples.

IMAC purification of 1L cultures for each scFv construct provided the following yields (averaged from n=5):

Construct	Culture Vol (L)	Wet cell weight (g)	scFv Yield (mg)	scFv yield (per liter)	scFv yield (per gram)
V_H-(G_2S)5-V_L	1	6.0	0.55	0.55	0.092
V_L-(G_2S)$_5$-V_H	1	5.5	0.35	0.35	0.064
V_H-(G_4S)$_3$-V_L	1	5.6	1.11	1.11	0.198
V_L-(G_4S)$_3$-V_H	1	7.5	1.05	1.05	0.140
V_L-(218)-V_H	1	7.3	0.4	0.4	0.055
GA218	1	**5.2**	**4.0**	4	**0.769**

Table 2.1: Representation of the various anti-CA125 scFv constructs and their recombinant soluble expression yields from *E.coli* Rosetta 2(DE3) strain using pET-22b(+) to facilitate C-terminal hexa-histidine tagged purification by immobilized metal affinity chromatography (IMAC).

The GA218 construct yielded ~ 3.8 fold higher amounts (mg/g) of soluble anti-CA125 scFv when compared to the next highest expressing construct V_H-(G_4S)$_3$-V_L. In comparison with the least expressing construct V_L-(218)-V_H, there was ~ 14-fold increase in mg/g yields of soluble anti-CA125 scFv. The difference in purified scFv yields between the listed constructs is represented in Fig 6, wherein equal volumes of the soluble scFv variants purified from 1L cultures and concentrated to a final volume of 1 mL were electrophoresed and analyzed by Coomassie staining and immunoblotting.

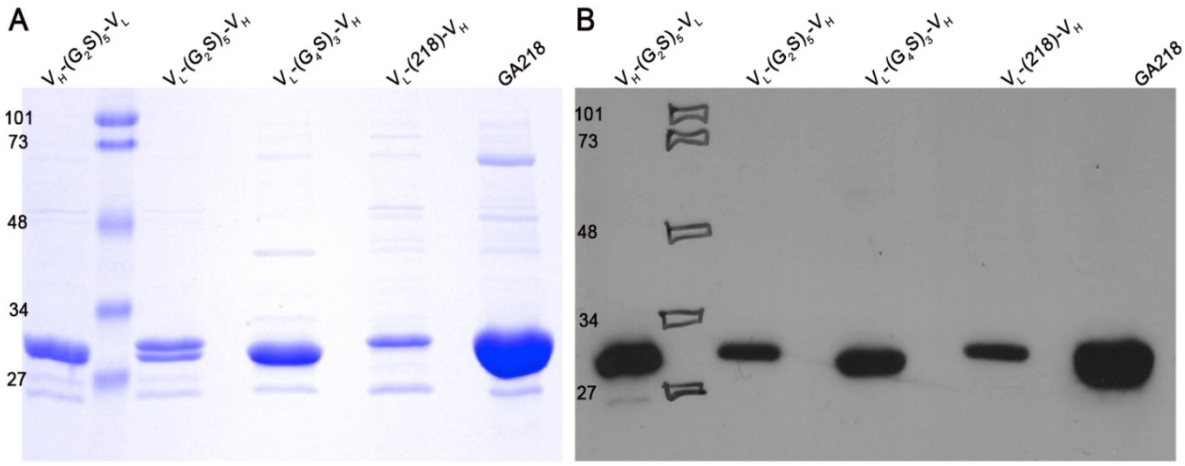

Figure 2.6: Anti-CA125 scFv expression and purification analysis **A)** Coomassie-stained SDS-PAGE of the IMAC purified scFv constructs expressed in *E.coli*. **B)** Replica gel of the same samples from A) immunoblotted for hexa-histidine tagged anti-CA125 scFv.

2.4.3 Characterization of scFv constructs:

LC-MS/MS analysis of peptides from the tryptic digests of purified scFv yielded high confidence score identities with mouse immunoglobulin variable light and heavy chain proteins upon performing a BLAST against the NCBInr database. The following 5 peptides obtained from the tryptic digests and LC-MS/MS analysis had 100% identities with amino acid sequences in the anti-CA125 scFv being examined. They also yielded high score identities with mouse immunoglobulin heavy and light chains from the NCBInr database:

1. **K·LLIYWASTR·E**
2. **K·NYLAWYQQK·P**
3. **M·SQSPSSLAVSVGEK·V**
4. **R·FTGSGSGTDFTLTISSVK·A**
5. **K·NYLAWYQQKPGQSPK·L**

N-terminal protein sequencing of the purified scFvs revealed absence of the pelB leader peptide upstream of the N-terminal scFv variable domain, thus indicating that the recombinant protein was processed in the bacterial periplasm and purified thereof. Functional characterization of the scFv variants by immunoblotting (Fig. 2.7A) revealed their highly specific binding to lysates of NIH:OVCAR-3 cells that overexpress CA125 and no binding to SKOV3 cell lysates. This experiment also demonstrated the migration of CA125 in a 4-15% gradient SDS-PAGE in good agreement with previously reported characterization studies for this antigen by Davis et al. [10] Furthermore, the use of MAb-B43.13 as a positive control and the anti-RANK receptor scFv as a negative control strengthens the demonstration for specificity of target binding by the various scFv constructs developed in this study. Results from flow cytometry (Fig. 2.7B) analyses indicated a shift in the forward scatter of fluorescence from samples of NIH:OVCAR-3 cells indirectly stained for CA125 using anti-CA125 MAb and scFv variants, while no shift of fluorescence was observed in the control samples. Immunofluorescence (Fig. 2.8) revealed membrane-specific binding of all scFv variants to target CA125 antigen expressed by NIH:OVCAR-3 cells and virtually no binding to CA125-negative SKOV3 cells. Control samples that included only Alexa fluor 488 conjugated secondary antibodies showed no membrane bound fluorescence, thus discounting any non-specific association observed in these cells.

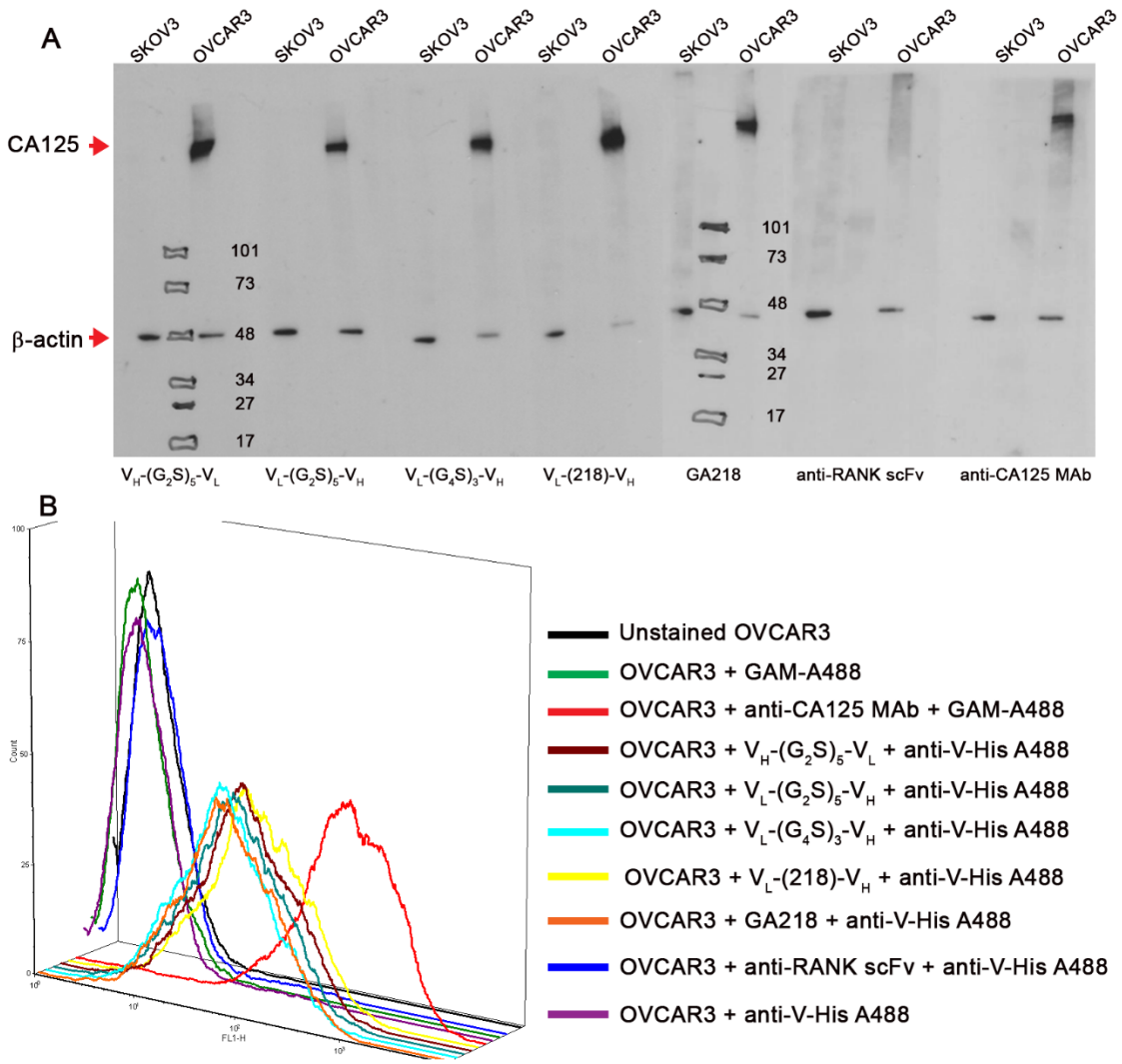

Figure 2.7: Functional characterization of purified anti-CA125 scFv constructs **A)** Immunoblots of SKOV3 and NIH:OVCAR-3 cell lysates probed for the presence of CA125 antigen using various anti-CA125 scFv constructs as represented at the bottom of the image. Arrows indicate the migratory positions and bands of CA125 antigen and β-actin in the cell lysates upon electrophoresis in a 4-15% gradient SDS-polyacrylamide gel; **B)** A 3-dimensional representation of histograms from flow cytometry analysis for the binding of various anti-CA125 scFv constructs and controls with NIH:OVCAR-3 cells. The X-axis represents forward scatter and Y-axis represents the cell counts.

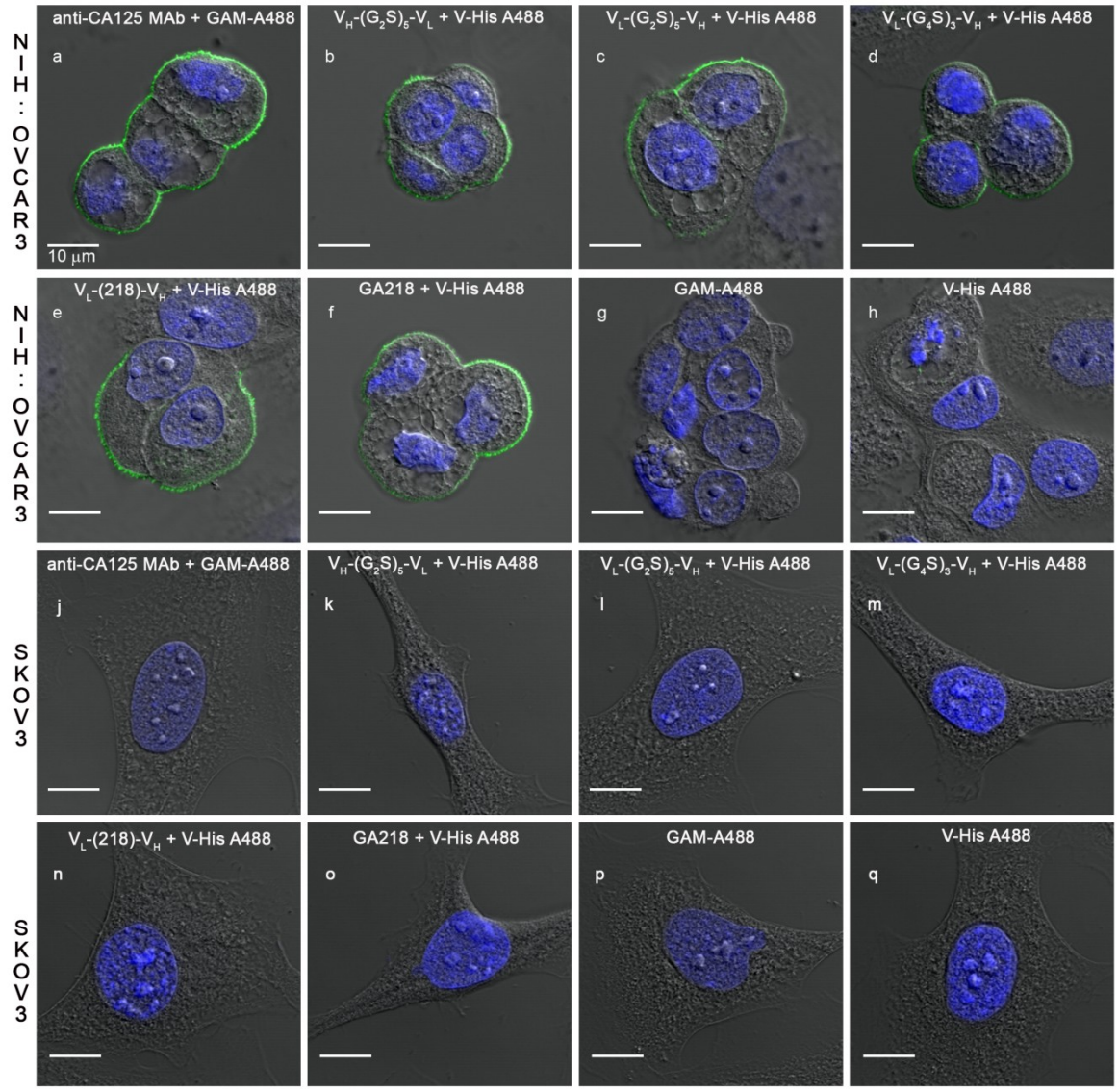

Figure 2.8: Immunostaining for biochemical binding activity of anti-CA125 scFv. Representative confocal images from immunofluorescence staining of CA125 using the various anti-CA125 scFv constructs on fixed NIH:OVCAR-3 and SKOV3 cells. GAM-A488 represents Alexa fluor 488 conjugated goat anti-mouse antibody. V-His A488 represents Alexa fluor conjugated anti-penta Histidine antibody.

2.5 Discussion:

Obtaining high yields of a functional recombinant protein is a prerequisite to its extensive characterization, molecular engineering and more importantly for eventual translation as a biopharmaceutical entity. Given the clinical potential of MAb B43.13 for immunotherapy of epithelial ovarian cancer (EOC)[30, 31] and the previously demonstrated *in vitro* targeting capabilities of its derivative scFv [20, 21, 23], we revisited the anti-CA125 MAb B43.13 scFv in order to extend its scope for application in molecular imaging of EOC. Previous reports for this scFv by Luo et al, had not mentioned purified yields of the scFv produced in *P. pastoris*[18], while Kriangkum et al, reported yields of ~ 0.2 mg/L for the scFv produced as a bi-specific scFv using NS0 myeloma cells [20] and Wang et al, reported 0.75 mg/L of the same scFv as a bi-functional fusion protein produced in *E.coli* [21]. Since all the previously reported yields were practically suboptimal for conducting extensive *in vitro* and *in vivo* studies, it was imperative to increase the soluble expression and yields of the anti-CA125 B43.13 scFv obtained per batch of recombinant *E.coli* culture.

Taking cues from the reported outcomes for other scFvs as cited further in this article, here we investigated the effect of 3 parameters on the yields of soluble anti-CA125 scFv expression in *E.coli*: a) variable domain orientation, b) inter-domain linkers and c) codon optimization. The $(G_4S)_3$ linker was included in this study as the most canonical flexible peptide linker used between scFv domains [32], while the $(G_2S)_5$ inter-domain linker was retained from the construct previously

reported by Wang et al.[21] The 218 linker was chosen for its reported ability to impart proteolytic stability and decreased aggregation of the scFv.[33]

Despite achieving successful expression of all the scFv constructs examined in this study, we observed a typically challenging phenomenon with heterologous protein expression using *E.coli*, wherein overexpressed recombinant proteins aggregate to form inclusion bodies.[34, 35] Furthermore, this feature is reported to be more pronounced in the case of antibody fragments such as scFvs, which tend to expose hydrophobic patches on the surfaces of their *in vivo* folding intermediates; that ultimately favors protein aggregation.[36, 37] Though it cannot be generalized, scFv molecules derived from hybridomas are more likely to be victims of this phenomenon over those selected from phage display libraries, which may have a higher propensity for soluble expression in *E.coli* owing to prior enrichment and selection as fusion proteins expressed from phagemids.

In our efforts to obviate scFv aggregation, other parameters such as lowering post-induction bacterial growth temperatures between 16˚C to 30˚C, using various concentrations of IPTG ranging from 0.01 mM to 1.0 mM for induction and the use of 0.4 M sucrose for protein expression were tested with no significant improvement in yields of soluble scFv. Purification of the anti-CA125 scFv V_L-$(G_4S)_3$-V_H from inclusion bodies provided highly pure scFv with yields up to 6 mg/L. Nonetheless, attempts to refold the denatured scFv in the presence of arginine and prescribed ratios of redox components repeatedly resulted in precipitation of > 95% of the protein during dialysis in phosphate buffered saline.

Consequently, we chose to express and purify the soluble, *in vivo* folded and biochemically active scFv instead of isolating it from inclusion bodies under denaturing conditions and performing *in vitro* refolding procedures. In the present work, small scale batch binding studies were instrumental in demonstrating the purified soluble scFv yields for all constructs. The intensity of chemiluminiscent signal corresponding to anti-CA125 scFv in the E1 fraction from GA218 was clearly indicative of higher amounts of soluble scFv produced from this construct in comparison to the others; especially since equal volumes of all eluates were used for such an analysis starting from normalized volumes of recombinant cell lysate supernatants used in the batch binding procedure.

Unlike reports for some scFv molecules [38, 39], we found very little difference in the yields for soluble anti-CA125 scFv (WT) expression in *E.coli* as a result of domain orientation. Nonetheless, our results indicated that the V_H-V_L orientation consistently provided ~ 1.4 fold higher yields (mg per gram wet cell weight) of the anti-CA125 scFv, for both the inter-domain linkers: $(G_2S)_5$ and $(G_4S)_3$. We also observed that the anti-CA125 scFv construct with $(G_4S)_3$ linker yielded more than twice the amounts of soluble WT scFv (mg/L and mg/g) over the $(G_2S)_5$ linker constructs in either domain orientation. This may be partially attributed to an increase of serine residues in the $(G_2S)_5$ linker and its corresponding non-optimized codons in the WT scFv sequence. Surprisingly, we found that the 218 linker-containing anti-CA125 scFv yielded much lower soluble scFv in contrast to its expected impact for decreased *in vivo* aggregation.

Going forward, we confined the scope of this study to the V_L-V_H orientation and found that codon optimization of the anti-CA125 scFv in this format had the maximum positive impact on its soluble expression in *E.coli*. This was evidenced by the poor codon adaptation index of 0.64 for the WT anti-CA125 scFv sequence and the fact that 58.3% of the WT codons were modified to suit the bias for heterologous expression in *E.coli*. Additionally, the challenge to *E.coli'*s translational machinery during heterologous overexpression of such proteins is briefly exemplified by the fact that while a native *E.coli* protein would comprise of ~ 5.7% serine residues [40], the anti-CA125 scFv constructs examined in this study were comprised of ~ 16% serine residues inclusive of those present in the inter-domain linkers. Furthermore, ~ 63% of these serine residues were encoded by rare codons such as TCA, AGT, TCG, TCC (arranged in the increasing order of their average frequency and abundance to code for serine) in *E.coli*.[40] Using *E.coli* Rosetta 2(DE3) as the expression host strain supplemented with tRNAs to provide the canonical rare codons for arginine (R), isoleucine (I), proline (P) and leucine (L) may have worked to our advantage by preventing truncated translation of the scFv during *in vivo* expression. However, the tendency of GA218 scFv to aggregate despite codon optimization and expression in a suitable host can be attributed to the primary protein sequence of the scFv itself and a plausible exposure of its hydrophobic patches in a folding intermediate that may result in off-pathway aggregation to form periplasmic inclusion bodies.[41] Nevertheless, in the present study, we were successfully able to demonstrate and achieve highest production of soluble anti-CA125 B43.13 scFv primarily as a result of codon

optimization. Further improvement of the soluble expression and corresponding purified yields relevant to the biopharmaceutical production of this scFv may be achieved via engineering of hydrophobic amino acid residues in the framework regions of this molecule without negatively affecting its immunoreactivity combined with the use of solubility enhancing tags and fermentation scale bioreactors.

In our hands, we found consistently higher yields of the scFv in soluble fractions from recombinant cell lysates upon using BugBuster master mix reagent when compared to the traditional osmotic shock method. Additionally, using the cobalt based metal affinity resin TALON® allowed single step purification of the hexa-histidine tagged scFv in high purity due to reduced non-specific binding of proteins from the cell lysate supernatant and convenient downstream processing on account of lower concentrations of imidazole used in elution buffers. N-terminal protein sequencing performed for two of the purified scFv variants V_L-$(G_4S)_3$-V_H and GA218 revealed the absence of pelB leader peptide; thus indicating that the scFv(s) were processed and successfully purified from the soluble periplasmic fractions. Successful translocation of the scFv into the oxidized environment of the periplasm increases the possibilities for intradomain disulfide bond formation, which eventually results in the molecule attaining a properly folded structure to be a functionally active scFv.

Finally, a set of qualitative assessments to evaluate the biochemical functionality by virtue of the purified scFv's antigen binding capability demonstrated that all constructs examined were able to bind the target antigen with high specificity as

observed from immunoblotting and flow cytometry experiments. The pattern of membrane bound fluorescence of CA125 observed upon immunostaining NIH:OVCAR-3 cells was in agreement with a previous report [42], which employed a FITC-labeled anti-CA125 targeting MAb B27.1. However, we were able to obtain higher resolution and superior quality images for immunostaining as compared to previous reports employing anti-CA125 targeting MAb [42] and scFv [21]. Furthermore, these studies also prompt the use of NIH:OVCAR-3 and SKOV3 cells to develop tumor xenograft models using mice for *in vivo* testing of targeting by anti-CA125 B43.13 scFv.

Conclusion:

In the present work, we improved the soluble expression of anti-CA125 B43.13 scFv in *E.coli* to obtain significantly higher yields of the epithelial ovarian cancer targeting vector. We found that codon optimization of the murine anti-CA125 scFv sequence and its expression in a tRNA supplemented host provided up to 14 fold higher yields of soluble anti-CA125 scFv when all other parameters for expression and purification were kept constant. This is a significant step forward in obtaining high yields of functionally active anti-CA125 scFv towards a greater scope for molecular characterization and engineering with extended applications for biomedical research.

2.7 References:

1. Holliger P, Hudson PJ. Engineered antibody fragments and the rise of single domains. *Nat Biotechnol* 2005;**23**(9): 1126-36.
2. Bird RE, Hardman KD, Jacobson JW, et al. Single-chain antigen-binding proteins. *Science* 1988;**242**(4877): 423-6.
3. Kipriyanov SM. High-level periplasmic expression and purification of scFvs. *Methods Mol Biol* 2009;**562**: 205-14.
4. Clackson T, Hoogenboom HR, Griffiths AD, Winter G. Making antibody fragments using phage display libraries. *Nature* 1991;**352**(6336): 624-8.
5. Schaffitzel C, Hanes J, Jermutus L, Pluckthun A. Ribosome display: an in vitro method for selection and evolution of antibodies from libraries. *J Immunol Methods* 1999;**231**(1-2): 119-35.
6. Feldhaus MJ, Siegel RW. Yeast display of antibody fragments: a discovery and characterization platform. *J Immunol Methods* 2004;**290**(1-2): 69-80.
7. J.V. Schaefer, A. Honneger, A. Pluckthun, Construction of scFv fragments from hybridoma or spleen cells by PCR assembly, in: R. Kontermann, S. Dubel (Eds.), Antibody Engineering, Vol 1, Springer-Verlag, Berlin, Heidelberg, 2010, pp. 21-44.
8. Toleikis L, Frenzel A. Cloning single-chain antibody fragments (ScFv) from hyrbidoma cells. *Methods Mol Biol* 2012;**907**: 59-71.
9. Fields C, O'Connell D, Xiao S, Lee GU, Billiald P, Muzard J. Creation of recombinant antigen-binding molecules derived from hybridomas secreting specific antibodies. *Nat Protoc* 2013;**8**(6): 1125-48.
10. Davis HM, Zurawski VR, Jr., Bast RC, Jr., Klug TL. Characterization of the CA 125 antigen associated with human epithelial ovarian carcinomas. *Cancer Res* 1986;**46**(12 Pt 1): 6143-8.

11. Scholler N, Urban N. CA125 in ovarian cancer. *Biomark Med* 2007;**1**(4): 513-23.

12. Capstick V, Maclean GD, Suresh MR, et al. Clinical evaluation of a new two-site assay for CA125 antigen. *Int J Biol Markers* 1991;**6**(2): 129-35.

13. Nustad K, Bast RC, Jr., Brien TJ, et al. Specificity and affinity of 26 monoclonal antibodies against the CA 125 antigen: first report from the ISOBM TD-1 workshop. International Society for Oncodevelopmental Biology and Medicine. *Tumour Biol* 1996;**17**(4): 196-219.

14. Nap M, Vitali A, Nustad K, et al. Immunohistochemical characterization of 22 monoclonal antibodies against the CA125 antigen: 2nd report from the ISOBM TD-1 Workshop. *Tumour Biol* 1996;**17**(6): 325-31.

15. Chen Y, Clark S, Wong T, et al. Armed antibodies targeting the mucin repeats of the ovarian cancer antigen, MUC16, are highly efficacious in animal tumor models. *Cancer Res* 2007;**67**(10): 4924-32.

16. Singleton J, Guillen DE, Scully MS, et al. Characterization of antibodies to CA 125 that bind preferentially to the cell-associated form of the antigen. *Tumour Biol* 2006;**27**(3): 122-32.

17. Berek JS. Immunotherapy of ovarian cancer with antibodies: a focus on oregovomab. *Expert Opin Biol Ther* 2004;**4**(7): 1159-65.

18. Luo D, Geng M, Schultes B, et al. Expression of a fusion protein of scFv-biotin mimetic peptide for immunoassay. *J Biotechnol* 1998;**65**(2-3): 225-8.

19. Hashimoto Y, Tanigawa K, Nakashima M, et al. Construction of the single-chain Fv from 196-14 antibody toward ovarian cancer-associated antigen CA125. *Biol Pharm Bull* 1999;**22**(10): 1068-72.

20. Kriangkum J, Xu B, Gervais C, et al. Development and characterization of a bispecific single-chain antibody directed against T cells and ovarian carcinoma. *Hybridoma* 2000;**19**(1): 33-41.

21. Wang WW, Das D, McQuarrie SA, Suresh MR. Design of a bifunctional fusion protein for ovarian cancer drug delivery: single-chain anti-CA125 core-streptavidin fusion protein. *Eur J Pharm Biopharm* 2007;**65**(3): 398-405.

22. Boivin M, Lane D, Piche A, Rancourt C. CA125 (MUC16) tumor antigen selectively modulates the sensitivity of ovarian cancer cells to genotoxic drug-induced apoptosis. *Gynecol Oncol* 2009;**115**(3): 407-13.

23. Ma J, Luo D, Kwon GS, Samuel J, Noujaim AA, Madiyalakan R. Use of encapsulated single chain antibodies for induction of anti-idiotypic humoral and cellular immune responses. *J Pharm Sci* 1998;**87**(11): 1375-8.

24. Accardi L, Di Bonito P. Antibodies in single-chain format against tumour-associated antigens: present and future applications. *Curr Med Chem* 2010;**17**(17): 1730-55.

25. Burgess-Brown NA, Sharma S, Sobott F, Loenarz C, Oppermann U, Gileadi O. Codon optimization can improve expression of human genes in Escherichia coli: A multi-gene study. *Protein Expr Purif* 2008;**59**(1): 94-102.

26. Tiwari A, Sankhyan A, Khanna N, Sinha S. Enhanced periplasmic expression of high affinity humanized scFv against Hepatitis B surface antigen by codon optimization. *Protein Expr Purif* 2010;**74**(2): 272-9.

27. Gustafsson C, Govindarajan S, Minshull J. Codon bias and heterologous protein expression. *Trends Biotechnol* 2004;**22**(7): 346-53.

28. Noujaim AA, Baum RP, Sykes TR, Sykes CJ, Hertel A, Niesen, A, et al. Monoclonal antibody B43.13 for immunoscintigraphy and immunotherapy of ovarian cancer, in: Klapdor, R. (Ed.), Current Tumor Diagnosis: Applications, Clinical Relevance, Trends. W Zuckschwerdt Verlag, Munich, 1994, pp. 823–829.

29. Newa M, Lam M, Bhandari KH, Xu B, Doschak MR. Expression, characterization, and evaluation of a RANK-binding single chain fraction variable: an osteoclast targeting drug delivery strategy. *Mol Pharm* 2014;**11**(1): 81-9.

30. Mobus VJ, Baum RP, Bolle M, et al. Immune responses to murine monoclonal antibody-B43.13 correlate with prolonged survival of women with recurrent ovarian cancer. *Am J Obstet Gynecol* 2003;**189**(1): 28-36.

31. Noujaim AA, Schultes BC, Baum RP, Madiyalakan R. Induction of CA125-specific B and T cell responses in patients injected with MAb-B43.13--evidence for antibody-mediated antigen-processing and presentation of CA125 in vivo. *Cancer Biother Radiopharm* 2001;**16**(3): 187-203.

32. Kortt AA, Dolezal O, Power BE, Hudson PJ. Dimeric and trimeric antibodies: high avidity scFvs for cancer targeting. *Biomol Eng* 2001;**18**(3): 95-108.

33. Whitlow M, Bell BA, Feng SL, et al. An improved linker for single-chain Fv with reduced aggregation and enhanced proteolytic stability. *Protein Eng* 1993;**6**(8): 989-95.

34. Palomares LA, Estrada-Mondaca S, Ramirez OT. Production of recombinant proteins: challenges and solutions. *Methods Mol Biol* 2004;**267**: 15-52.

35. Carrio MM, Villaverde A. Construction and deconstruction of bacterial inclusion bodies. *J Biotechnol* 2002;**96**(1): 3-12.

36. Nieba L, Honegger A, Krebber C, Pluckthun A. Disrupting the hydrophobic patches at the antibody variable/constant domain interface: improved in vivo folding and physical characterization of an engineered scFv fragment. *Protein Eng* 1997;**10**(4): 435-44.

37. Chowdhury PS, Vasmatzis G. Engineering scFvs for improved stability. *Methods Mol Biol* 2003;**207**: 237-54.

38. Tsumoto K, Nakaoki Y, Ueda Y, et al. Effect of the order of antibody variable regions on the expression of the single-chain HyHEL10 Fv fragment in E. coli and the thermodynamic analysis of its antigen-binding properties. *Biochem Biophys Res Commun* 1994;**201**(2): 546-51.

39. Hamilton S, Odili J, Gundogdu O, Wilson GD, Kupsch JM. Improved production by domain inversion of single-chain Fv antibody fragment against high molecular weight proteoglycan for the radioimmunotargeting of melanoma. *Hybrid Hybridomics* 2001;**20**(5-6): 351-60.

40. Kane JF. Effects of rare codon clusters on high-level expression of heterologous proteins in Escherichia coli. Curr Opin Biotechnol 1995;6(5): 494-500.

41. Knappik A, Pluckthun A. Engineered turns of a recombinant antibody improve its in vivo folding. *Protein Eng* 1995;**8**(1): 81-9.

42. Xiao Z, McQuarrie SA, Suresh MR, Mercer JR, Gupta S, Miller GG. A three-step strategy for targeting drug carriers to human ovarian carcinoma cells in vitro. *J Biotechnol* 2002;**94**(2): 171-84.

3

^{18}F-labeled single-chain antibody as a targeted radiotracer for same day imaging of Epithelial Ovarian Cancer[2]

[2]A version of this chapter will be submitted to the European Journal of Nuclear Medicine and Molecular Imaging Research: Sharma SK, Wuest M, Way JD, Bouvet VR, Wang M, Wuest F. ^{18}F-labeled single-chain antibody as a targeted radiotracer for same day imaging of Epithelial Ovarian Cancer.

3.1 Introduction:

Rapid advances in recombinant technology combined with an expanding scope to use a variety of radionulcides for positron emission tomography (PET) have empowered immuno-PET as a versatile tool that employs engineered antibody formats tailored for applications in the molecular imaging of cancer.[1, 2] A single-chain antibody fragment (scFv), comprised of the paratopic variable heavy and light chain domains of an immunoglobulin molecule is considered to be the smallest yet complete active component of the immunoglobulin capable of binding to a target antigen.[3] Therefore, it is not surprising that scFvs act as a good starting point and happen to be one of the most popular formats for further engineering of antibodies. In contrast to the molecular weight of ~150 KDa for a full-length antibody, the single-chain antibody fragments are one-fifth the size (~28 KDa) and propose to offer the following advantages: a) better tissue penetration – especially within the tumor's poorly vascularized environment; b) rapid systemic clearance – which can result in high tumor-to-background ratios to yield high contrast images at early time points and c) amenability to genetic engineering for various applications such as site-specific labeling; multimerization in order to improve avidity and affinity enhancement via site-directed mutagenesis etc. Bereft of an immunoglobulin's Fc portion and its associated downstream activation of immune modulators, scFv molecules and their engineered formats can potentially serve as non-immunogenic targeting vectors *in vivo*.[4] Such inherent properties of engineered antibody fragments can be particularly advantageous to oncologic imaging.

While the selection of an appropriate targeting vector for immuno-PET forms one side of the coin, the other facet involves the selection of an appropriate radionuclide for the preparation of a suitable radiotracer. This is largely governed by a cardinal principle of *in vivo* molecular imaging whereby maximum contrast and meaningful information from this application can be obtained as a result of an ideal match between the biological half-life of the targeting vector and the physical half-life of the radionuclide it is being labeled with.[5] Following this principle, it is only befitting that recombinant antibody formats such as single-chain variable fragments (scFv ~28 KDa) and diabodies (Db ~56 KDa), that possess a molecular weight below the cut-off for renal clearance and have relatively short biological half-lives (~ 0.5 h - 7 h) should be radiolabeled with fluorine-18 [^{18}F] or [^{68}Ga], having a physical half – life of 1.8 h (109.8 min) and 68 min respectively.[6]

More recently, the establishment of biomedical cyclotrons at several sites worldwide has contributed to the easy availability of ^{18}F and its routine use in [^{18}F]FDG scans to evaluate metabolic activity status of tumors and response to therapy in the clinic. This has concomitantly resulted in most clinical PET scanners being calibrated for use with this radioisotope. One other enticing feature to use ^{18}F is its 97% positron emission yield and lack of interfering radiations that ultimately provide high resolution images. Thus, there can be great potential for the clinical translation of a suitable radiotracer labeled with this isotope. These factors indicate a degree of ease and potential for the clinical translation of radiotracers labeled with this isotope. The greatest advantage however comes in

the form of a possibility to accomplish same-day imaging with a significant reduction of radioactivity burden to patients. In an immuno-PET setting, these objectives may be achieved by combining the short biological half-lives of antibody fragments with short-lived PET-radionuclides to formulate novel radiotracers. Conversely, full-length antibody radiotracers necessitate the use of relatively long-lived radioisotopes that continue to generate signals from tumor accretion while the radiotracer is systemically cleared from circulation over a period of days.

Epithelial ovarian cancer (EOC) is the most lethal gynecologic malignancy and is characterized by the overexpression of Cancer Antigen 125 (CA125) – a high molecular weight mucinous glycoprotein.[7] This antigen has also been found to express in breast cancer, mesothelioma, leiomyoma, leiomyosarcoma of gastrointestinal origin and some benign conditions such as endometriosis, ovulatory cycles, congestive heart failure, and liver disease.[8] A USFDA approved tumor biomarker that has served as a prognostic indicator of disease; it is currently assessed by immunoassays in serum samples of patients presenting in the clinic with pelvic masses and being diagnosed for ovarian cancers.[9] Most immunoassays have been developed using antibodies reported to bind with CA125.[10, 11] Among these, MAb B43.13 has been used for CA125-targeted immunotherapy of EOC.[12] Furthermore, apart from [^{18}F]FDG, which is used as a generic metabolic radiotracer for functional imaging of several cancers including ovarian tumors,[13] there is currently no targeted PET radiotracer available for same-day non-invasive imaging of EOC.

In the present work, we developed a single-chain antibody fragment to target CA125 and transformed it for use as a molecular imaging probe for same-day imaging of epithelial ovarian cancer via immuno-PET. To this end, an anti-CA125 scFv derived from murine monoclonal antibody MAb-B43.13 was produced and radiolabeled with ^{18}F ($t_{1/2}$ 109.8 min) using *N*-succinimidyl-4[^{18}F]fluorobenzoate ([^{18}F]SFB) as a prosthetic group in order to obtain [^{18}F]FBz-anti-CA125 scFv. The radiotracer was analyzed *in vitro* and *in vivo* using CA125 overexpressing NIH:OVCAR-3 cells and antigen negative SKOV3 cells in preclinical subcutaneously xenografted EOC mouse models.

3.2 Materials and Methods:

3.2.1 Production of CA125 targeting vectors:

The genes encoding for individual variable domains of the anti-CA125 scFv were amplified by polymerase chain reaction (PCR) from a previously reported plasmid construct pWET8.[14] The inter-domain peptide linker was changed to a canonical $(Gly_4Ser)_3$ linker by splice overlap extension PCR. The anti-CA125 scFv oriented as V_L-$(G_4S)_3$-V_H with the variable light chain domain at the N-terminus and variable heaving chain domain at the C-terminus. The construct was sub-cloned between *Nco* I and *Not* I restriction sites of pET-22b(+) vector (Novagen, 69744) for recombinant expression in *E.coli* Rosetta 2(DE3) (Novagen, 71400) . Single transformant colonies were grown in 2 litre bacterial cultures, induced with 0.8 mM Isopropyl-β-D-thiogalactopyranoside (IPTG) (Fisher Scientific, BP1755-10) and allowed to grow for 16 h at 26ºC prior to harvesting cells by centrifugation at 7000 rpm for 30 minutes. The cell pellet was treated with BugBuster Master Mix (Novagen, 71456) and soluble protein was extracted as per the manufacturer's instructions. The anti-CA125 scFv was purified by immobilized metal affinity chromatography using a cobalt-based TALON® Superflow resin (Clontech, 635506). The cell lysate supernatant was passed over the resin at a flow rate of 1 mL/min to allow binding of the hexa-histidine tagged scFv to the resin. The captured scFv was eluted from the column using a linear gradient of 10 mM – 150 mM imidazole as the eluant. 1 mL fractions were collected and analyzed by 12% SDS-PAGE stained with Coomassie brilliant blue R-250 and immunoblotted for the C-terminal hexa-histidine tag using 6X His MAb-HRP conjugate (Clontech,

631210). Eluted fractions containing high concentration of purified scFv were pooled together and dialyzed in phosphate buffered saline (pH 7.4) to remove excess imidazole and concentrated via centrifugation using Amicon Ultra-15, 10K MWCO filters (EMD Millipore, UFC901024). Anti-CA125 murine monoclonal antibody (MAb) was purified from MAb B43.13 hybridoma[15] cell culture supernatant by protein G affinity (Sigma, P-7700) on a BioLogic DuoFlow™ chromatography system (Bio-Rad, 760-0135). Final concentrations of the purified scFv and MAb were quantified using a Pierce™ BCA protein assay kit (Thermo Scientific, 23227) according to the manufacturer's recommendations.

3.2.2 Cell lines and culture conditions: Ovarian cancer cells NIH:OVCAR-3 (ATCC® HTB-161™) that overexpress CA125 and SKOV3 (ATCC® HTB-77™) that do not express CA125 were used for *in vitro* functional characterization studies. Cells were cultured in DMEM-F12 medium supplemented with 10% v/v fetal bovine serum (Life Technologies, 12483-020), 50 IU/mL penicillin, 50 µg/mL streptomycin (Life Technologies, 15140-122). NIH:OVCAR-3 cells were additionally supplemented with 7 µg/mL recombinant human insulin (SAFC Biosciences, 91077C). Cells were cultured using sterile techniques and grown in a 37°C incubator providing humidified atmosphere of 5% CO_2 in air.

3.2.3 Functional characterization of anti-CA125 scFv

Fluorescent labeling of 2 mg anti-CA125 MAb (4 mg/mL) and scFv (2 mg/mL) was carried out using the Pierce FITC antibody labeling kit (Thermo Scientific, 53027) as per the manufacturer's instructions.

3.2.3.1 Flow Cytometry: 1.5 x 10^6 NIH:OVCAR-3 cells were harvested by trypsinization, rinsed twice with FACS buffer (PBS with 0.5% heat inactivated FBS, 2mM EDTA, 0.05% sodium azide) and resuspended by gentle tapping in ~100 µL of this buffer. 10 µg of FITC-labeled anti-CA125 MAb or scFv, unmodified anti-CA125 scFv and a hexa-histidine tagged anti-RANK receptor binding scFv used as an isotype control in this experimental setup, were incubated with the NIH:OVCAR-3 cell suspension for 30 min at room temperature. Cells were rinsed twice in FACS buffer and incubated for another 30 min with 2.4 µg of Penta·His Alexa Fluor 488 conjugate (Life Technologies, A-11001) for samples previously incubated with unmodified scFv. Cells were rinsed twice with FACS buffer and analyzed by flow cytometry on a BD FACS Calibur with 10,000 events gated per sample. Negative controls included unstained NIH:OVCAR-3 cells and cells incubated with Penta·His Alexa fluor 488 – conjugated antibody alone.

3.2.3.2 Immunofluorescence: NIH:OVCAR-3 and SKOV3 cells were plated onto glass coverslips in 35-mm tissue culture dishes (100,000 cells/2 mL medium/dish) and incubated at 37°C for 48 h. The cells were rinsed with PBS and fixed in methanol for 30 min at -20°C. The fixed cells were incubated in 5% non-

fat dry milk (Carnation) in PBS and immunostained separately for 1 h with FITC-labeled versions of the anti-CA125 MAb and scFv, unmodified anti-CA125 scFv and anti-RANK receptor scFv used (isotype control). Penta·His Alexa Fluor 488 conjugate was used as a secondary antibody in the case of unmodified anti-CA125 scFv and anti-RANK receptor scFvs. FITC-labeled anti-CA125 MAb and scFv (1 mg/mL each) were used at 1:250 dilution Un-modified anti-CA125 scFv and anti-RANK receptor scFv were further incubated with Penta·His Alexa Fluor 488 conjugate (1:500) in PBS containing 5% non-fat dry milk. Appropriate blank and control samples were included in the experiments. All antibody incubations were followed by three rinses with PBST for 10 min each. Coverslips were mounted on microscopy slides (Fisherbrand) using Mowiol® mounting medium (Calbiochem, 475904) supplemented with DAPI (50 μg/mL). Immunofluorescence was observed through a Zeiss Plan Apochromat 40X/1.3 Oil DIC M27 lens on a confocal laser scanning microscope (Zeiss LSM 710). The images were analyzed using Zen 2011 software and processed further using Adobe Photoshop CS6.

3.2.4 Synthesis of [^{18}F]SFB: [^{18}F]SFB was synthesized on an automated synthesis unit as per a previously reported method.[16] Non carrier added [^{18}F]fluoride was produced via an $^{18}O(p,n)^{18}F$ nuclear reaction from [^{18}O]H_2O (Rotem Industries Ltd, Hyox oxygen-18 enriched water, min. 98%) on an ACSI TR19/9 Cyclotron (Advanced Cyclotron Systems Inc., Richmond, Canada). Radiosynthesis of N-succinimidyl-4-[^{18}F]fluorobenzoate was performed on a GE TRACERlab™ FX (General Electric Company, Fairfield, Connecticut, United

States.) This ASU was modified for the program and hardware as shown in Fig 3.1. The synthesis was initiated by the elution of resin-bound cyclotron-produced [^{18}F]fluoride from a Waters Sep-Pak®light QMA anion exchange column into Reactor 1 (R1) of the GE TRACERlab™ FX using a solution of 86% K2.2.2./K_2CO_3 (1.5 mL). [^{18}F]Fluoride was dried azeotropically (V2, CH_3CN, 1.5 mL) under vacuum and a steady stream of nitrogen at 50°C and 95°C. To dried [^{18}F]fluoride, (4-Iodophenyl) diphenylsulfoniumtriflate (V3) in CH_3CN (1 mL) was added and reacted at 80°C for 10 minutes. Once the reaction was completed and cooled, 1 N HCl (V4,1.0 mL) was added and allowed to react for an additional 5 minutes at 100°C. After de-protection the mixture was diluted with water (V5, 12 mL) and passed through a Macherey-Nagel Chromabond® HR-P M (330 mg, Purification Column 1). 4-[^{18}F]fluorobenzoic acid ([^{18}F]FB) was eluted off in CH_3CN (V6, 3mL) into Reactor 2 (R2), which pre-contains 25 wt% tetramethylammonium hydroxide in methanol (35 μL) in CH_3CN (0.5 mL). [^{18}F]FB was additionally dried azeotropically (V8, CH_3CN, 1.5 mL) under vacuum and a steady stream of nitrogen at 50°C and 95°C to reduce the volume from 3 mL to 0.5 mL. To volume reduced [^{18}F]FB, N,N,N,N-Tetramethyl-O-(N-succinimidyl) uronium tetrafluoroborate (V9, 40 mg) in CH_3CN (1 mL) was added and reacted for 90°C for 2 minutes. Once completed, the mixture was diluted with 5 % acetic acid (V10, 12 mL) and passed through a Macherey-Nagel Chromabond® HR-P M (330 mg, purification column 2). The purification column 2 was additionally washed with water (V11, 10 mL) and the final product was

eluted in CH_3CN (4 mL) through a Waters SepPak Silica Plus column in to a 10 mL sealed collection vial with a vent needle.

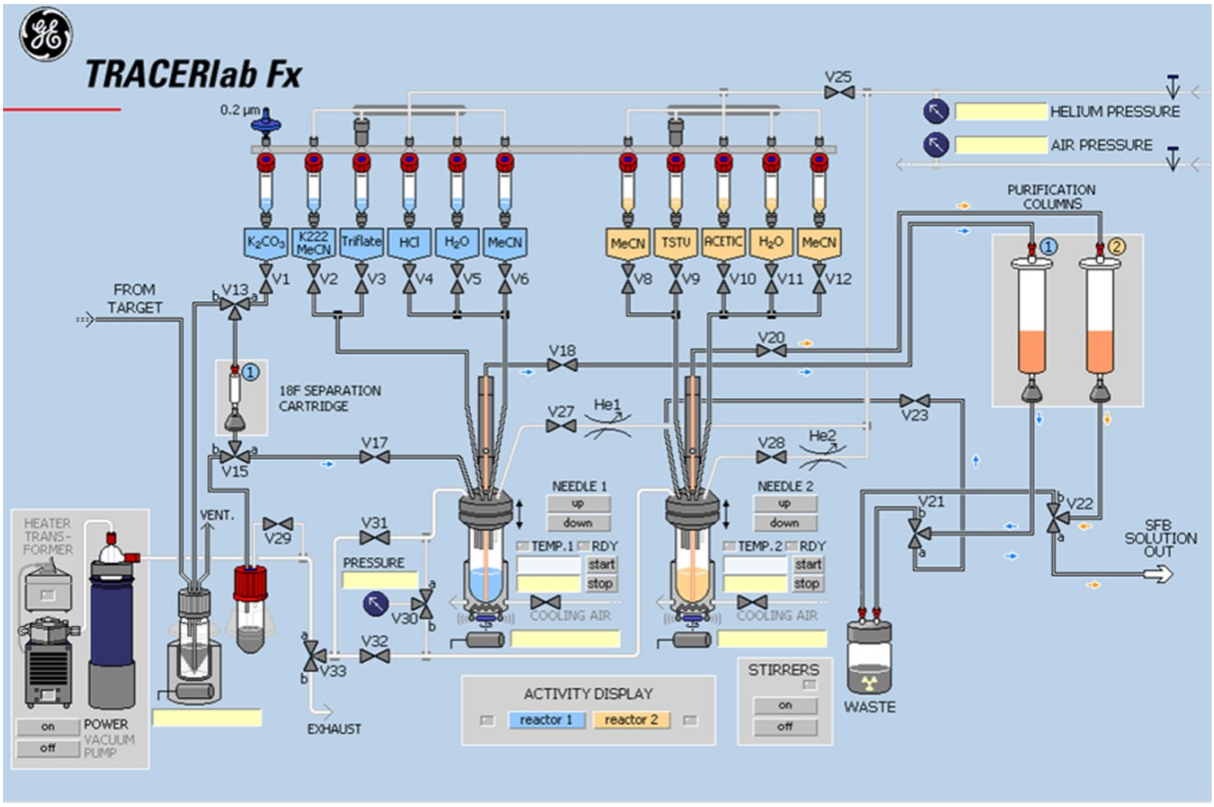

Figure 3.1: Scheme of the automated synthesis unit for the synthesis of *N*-succinimidyl-4-[^{18}F]fluorobenzoate [^{18}F]SFB

3.2.5 ^{18}F labeling of anti-CA125 scFv:

The [^{18}F]SFB was further purified by HPLC on a semi-preparative Luna C18 column (100 Å, 10 µm, 250 x 10 mm) using a gradient elution of acetonitrile – water at a flow rate of 3 mL/min with monitored UV detection at 254 nm and a HERM detection of the radiotrace. 1 GBq of the ASU – synthesized [^{18}F]SFB was injected into the semi-preparative HPLC column and the purification was initiated with an acetonitrile – water elution gradient from 15/85 to 50/50 (v/v) for 12 min, which was then allowed to stay at 50/50 (v/v) for a minute followed by a 6 min gradient elution from 50/50 to 70/30 (v/v), continued as a final eluent ratio of acetonitrile – water for an additional 11 min in a programmed run time of 30 min. [^{18}F]SFB corresponding to the area under the curve from the HPLC radiotrace was collected in a 50 ml pear shaped flask (Ace glass, 9477-27). The HPLC-purified [^{18}F]SFB was concentrated to dryness on a rotary evaporator set at 35˚C. 100 µg of anti-CA125 scFv (2 mg/mL) in borate buffer pH 8.3 was added to the dried [^{18}F]SFB and mixed well to dissolve the two reactants prior to transferring the reaction mixture into a Protein LoBind 1.5 mL tube (Eppendorf, 13698794). The reaction was allowed to proceed in a thermal shaker set at 37˚C, 550 rpm for 45 minutes. ^{18}F-labeled scFv was further purified by passing the reaction mixture over an Econo-Pac® 10DG desalting column (Bio-Rad, 732-2010) pre-equilibrated with 0.9% saline (Becton Dickinson, 306572) which was also used as the eluent for this purification. 350 µL elution fractions were collected from the desalting column and associated radioactivity was measured on an Atomlab 400 dose calibrator (Biodex). 15 µL of each elution fraction was electrophoresed in a

12% SDS-PAGE gel under reducing conditions and evaluated by autoradiography on a BAS-5000 phoshorimager (Fujifilm). Radiochemical yields and purity were determined by thin layer chromatography on TLC Silica Gel 60 F_{254} (Merck KGaA, Germany) using a 5:1 (v/v) mixture of ethyl acetate – hexane as the eluent. Fractions containing high specific activity [^{18}F]FBz-anti-CA125 scFv were further used for *in vitro* and *in vivo* radiopharmacological experiments. The same procedure was also applied for ^{18}F-labeling of the anti-CA125 MAb-B43.13, which was used as a positive control for *in vitro* binding and cell uptake studies.

3.2.6 *In vitro* binding analysis:

3.2.6.1 Cell Uptake Studies: NIH:OVCAR-3 and SKOV3 cells were grown to obtain 250,000 cells per well in 12-well tissue culture plates. Prior to the uptake experiment, growth media was removed and cells were rinsed twice with PBS and incubated in Krebs buffer at 37°C for 1 h. In separate experiments, the ^{18}F-labeled anti-CA125 MAb and scFv (100 KBq) were added to each well except those assigned for measuring background activity alone. Cell uptake was terminated at 5, 10, 15, 30, 60, 90, 120 min by adding ice cold Krebs buffer and rinsing the wells twice to wash away any un-bound [^{18}F]FBz-MAb/scFv prior to cell lysis with RIPA buffer. The cell lysates were transferred to scintillation vials and measured for radioactivity using a γ-counter (Wizard$^{2®}$ 2480 Automatic Gamma Counter, Perkin-Elmer, Canada). Protein levels were quantified using a Pierce™ BCA protein assay kit according to the manufacturer's recommendations. Cell uptake levels were normalized to percent of the total amount of radioactivity per

milligram of protein (% radioactivity/mg protein) and plotted as a function of time. All experiments were performed in triplicates.

3.2.6.2 Determination of EC_{50} values: Using a similar setup as that used for the cell uptake experiments, blocking studies were performed using NIH:OVCAR-3 cells in two sets of 12-well tissue culture plates containing ~250,000 cells per well. One set was used to evaluate cell uptake of ^{18}F-labeled MAb from 5 -120 min as mentioned previously. In the other set, a competition was allowed to occur over the same periods of time by co-incubation of 1 mg unmodified anti – CA125 MAb B43.13 with 100 KBq of ^{18}F-labeled MAb per well. The uptake was terminated by addition of ice-cold Krebs buffer and the cells were further processed for the measurement of radioactivity and quantitative evaluation of cell uptake as outlined above. Furthermore, EC_{50} values for anti-CA125 MAb B43.13 were determined via titration of the cell uptake using 100 KBq ^{18}F-labeled MAb or scFv with the co-incubated concentrations of un-labeled MAb B43.13 ranging from 1×10^{-5} through 1×10^{-12} over a fixed time period of 90 min at 37˚C.

3.2.7 *In vivo* experiments:

3.2.7.1 Xenograft models: All experiments were carried out according to guidelines of the Canadian Council on Animal Care (CCAC) and approved by the local animal care committee of the Cross Cancer Institute, Edmonton. Six weeks old BALB/c and NIH-III female mice were obtained from Charles River labs (Quebec, Canada). The animals were housed in ventilated cages and provided

food and water *ad libitum*. NIH:OVCAR-3 tumors were induced on the left shoulder by two subsequent subcutaneous injections of 15 x 10^6 and 10 x 10^6 cells in a 300 µL suspension of 1:1 mixture of PBS and matrigel (BD Biosciences). The second injection of cells was administered at the same site within 7-10 days. NIH:OVCAR-3 tumors grew for 6-8 weeks before reaching suitable tumor sizes of 150 – 200 mm^3. In separate animals, SKOV3 tumors were induced on the left shoulder by a single subcutaneous injection of 5 x 10^6 cells in PBS and were grown for about 2-3 weeks before achieving similar tumor sizes.

3.2.7.2 Small animal PET imaging:

Positron emission tomography (PET) experiments were performed with SKOV3 or NIH:OVCAR-3 tumor-bearing BALB/c nude or NIH-III mice after injecting [^{18}F]FBz-anti-CA125 scFv and analyzing its tumor uptake *in vivo*. For radiotracer injection, a catheter was placed into the tail vein of the mouse. Under anesthesia, mice were placed in prone position into the centre of field of view of the microPET® R4 or Inveon® PET scanner (Siemens Preclinical Solutions, Knoxville, TN, USA). A transmission scan for attenuation correction was not acquired. 2-7 MBq of [^{18}F]FBz-anti-CA125 scFv or [^{18}F]FDG in 100-150 µL saline was injected intravenously through the catheter into the tail vein. PET acquisition continued for 60 min in 3D list mode. The dynamic list mode data were sorted into sinograms with 53 time frames (10x2, 8x5, 6x10, 6x20, 8x60, 10x120, 5x300 s). The frames were reconstructed using Ordered Subset Expectation Maximization (OSEM) or maximum a posteriori (MAP)

reconstruction modes. Correction for partial volume effects was not performed. The image files were further processed using the ROVER v2.0.51 software (ABX GmbH, Radeberg, Germany). Masks defining 3D regions of interest (ROI) were set and the ROIs were defined by thresholding. Mean standardized uptake values [SUV_{mean} = (activity/mL tissue) / (injected activity/body weight), mL/g] were calculated for each ROI. Time-activity curves (TAC) were generated and the semi-quantified PET data are presented as means ± SEM.

3.3 Results:

3.3.1 Anti-CA125 scFv production and characterization:

Anti-CA125 scFv was purified in yields of 1 milligram per liter of recombinant bacterial culture using immobilized metal affinity chromatography (Fig 3.2). The anti-CA125 MAb (used as a positive control for binding to CA125) was purified by protein G affinity chromatography from the cell culture supernatant of B43.13 hybridoma. We were able to conjugate two moles of FITC per mole of MAb and scFv.

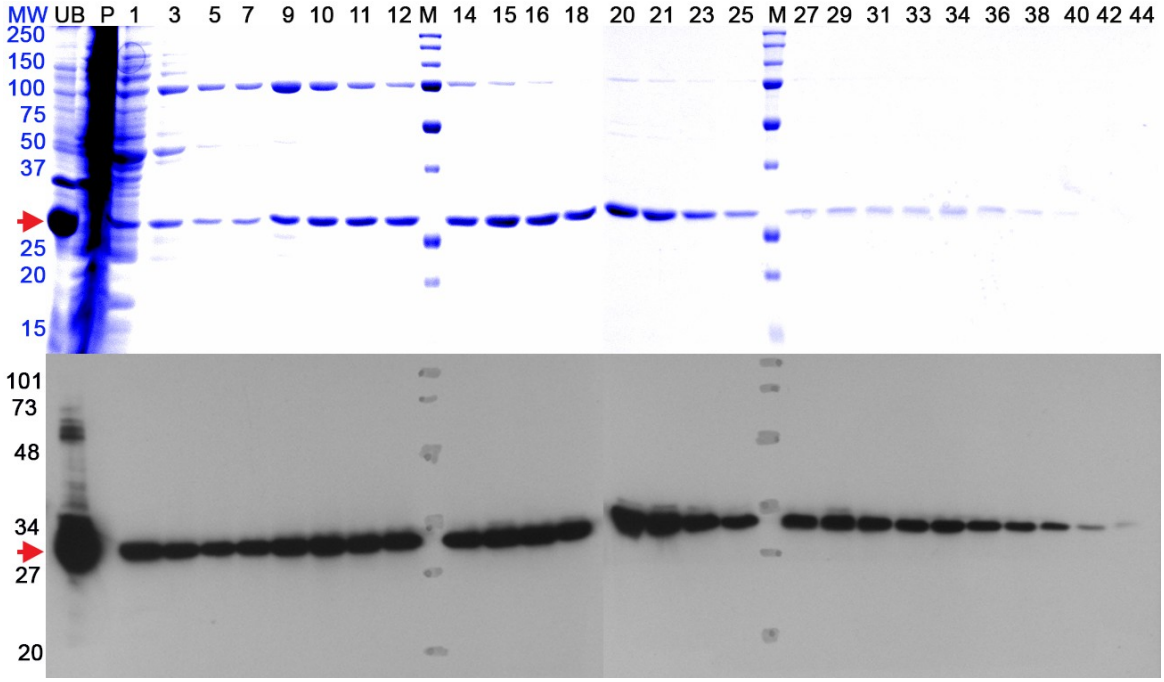

Figure 3.2: Purification of anti-CA125 scFv. Immobilized metal affinity chromatography (IMAC) purification profile of the anti-CA125 scFv. **A)** Coomassie-stained SDS PAGE gel; **B)** corresponding immunoblot of a replica gel probed for hexa-histidine tag. UB: Unbound fraction; P: Insoluble – Pellet fraction; M: Protein Molecular Weight Standard; lanes numbered 1-44 indicate the IMAC fractions. Molecular weights (represented in KiloDaltons – Kda) corresponding to the protein standards used are mentioned on the left

hand side of the images. Red arrows indicate the migration position of the anti-CA125 scFv (~ 28KDa).

Immunoreactivity of the FITC-labeled vectors for binding to CA125 as assessed by flow cytometry revealed a shift in forward scatter of fluorescence indicative of binding to NIH:OVCAR-3 cells only in samples incubated with anti-CA125 targeting vectors whereas the control samples had no shift of forward scatter as seen in the histogram (Fig 3.3).

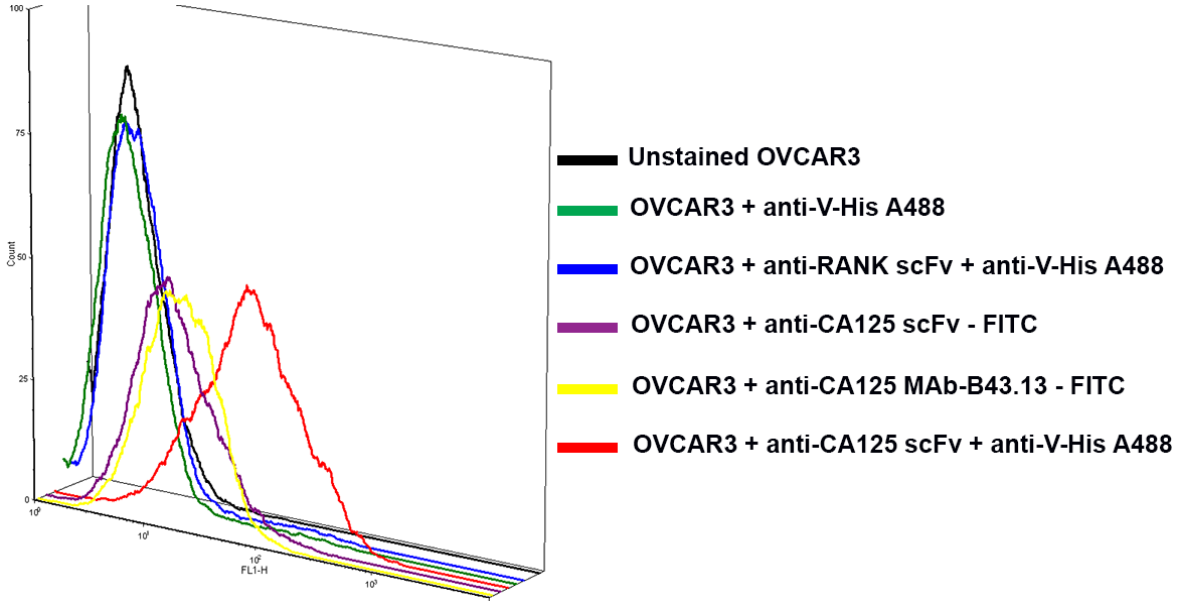

Figure 3.3: Functional characterization of anti-CA125 scFv. A three dimensional histogram from flow cytometry analyses of anti-CA125 scFv and control samples using NIH:OVCAR-3 cells. X axis represents forward scatter of fluorescence and Y axis represents the cell counts.

Immunofluorescence revealed membrane bound fluorescence in NIH:OVCAR-3 cells incubated with anti-CA125 MAb and scFv but, no binding to CA125-negative SKOV3 cells with these targeting vectors as seen in Fig 3.4.

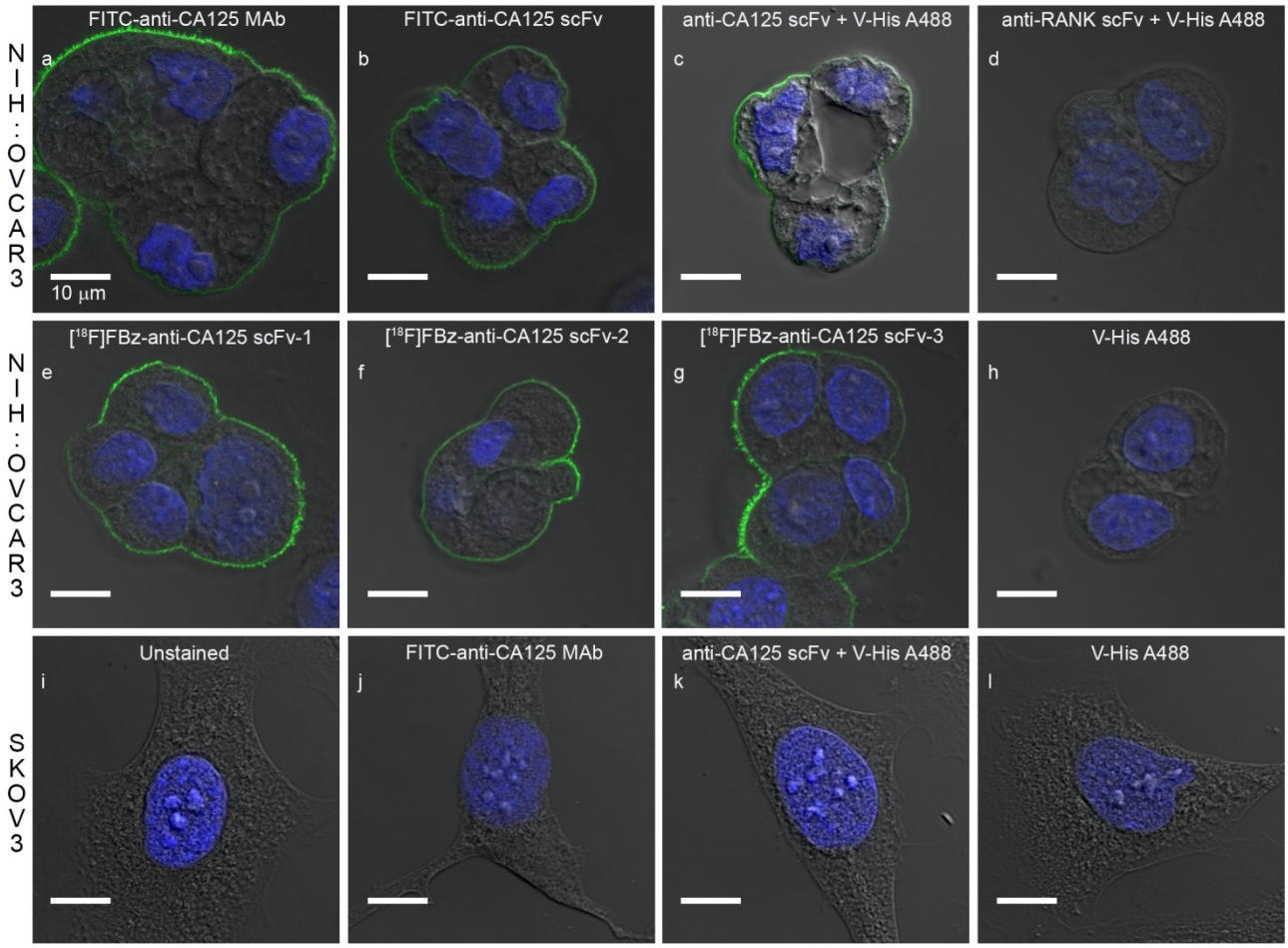

Figure 3.4: Representative confocal images from immunofluorescence of CA125 expressed on NIH:OVCAR-3 cells using a) FITC-labeled anti-CA125 MAb B43.13; **b)** FITC-labeled anti-CA125 scFv; The following samples were indirectly immunostained with **c)** anti-CA125 scFv; **d)** anti-RANK receptor scFv used as isotype control; **e)** ^{18}F-labeled anti-CA125 scFv from experiment – 1; **f)** ^{18}F-labeled anti-CA125 scFv from experiment – 2; **g)** ^{18}F-labeled anti-CA125 scFv from experiment – 3; Negative Control – **h)** Alexa fluor 488 conjugated anti-penta histidine (V-His A488) used as a secondary antibody control. **i – l)** representative images of CA125 negative SKOV3 cells immunostained to validate specific binding of anti-CA125 targeting vectors (MAb/scFv) and Alexa fluor 488 – conjugated secondary antibodies.

3.3.2 [^{18}F]SFB synthesis and radiolabeling of anti-CA125 scFv:

Automated synthesis of N-succinimidyl-4-[^{18}F]fluorobenzoate [^{18}F]SFB afforded 67 ± 19% radiochemical yield, (decay corrected) over a total synthesis time of 58 ± 4 min with >95 % radiochemical purity (n = 186). The maximum activity achieved was 9.77 GBq from 17.0 GBq of starting [^{18}F]Fluoride (Fig. 3.5)

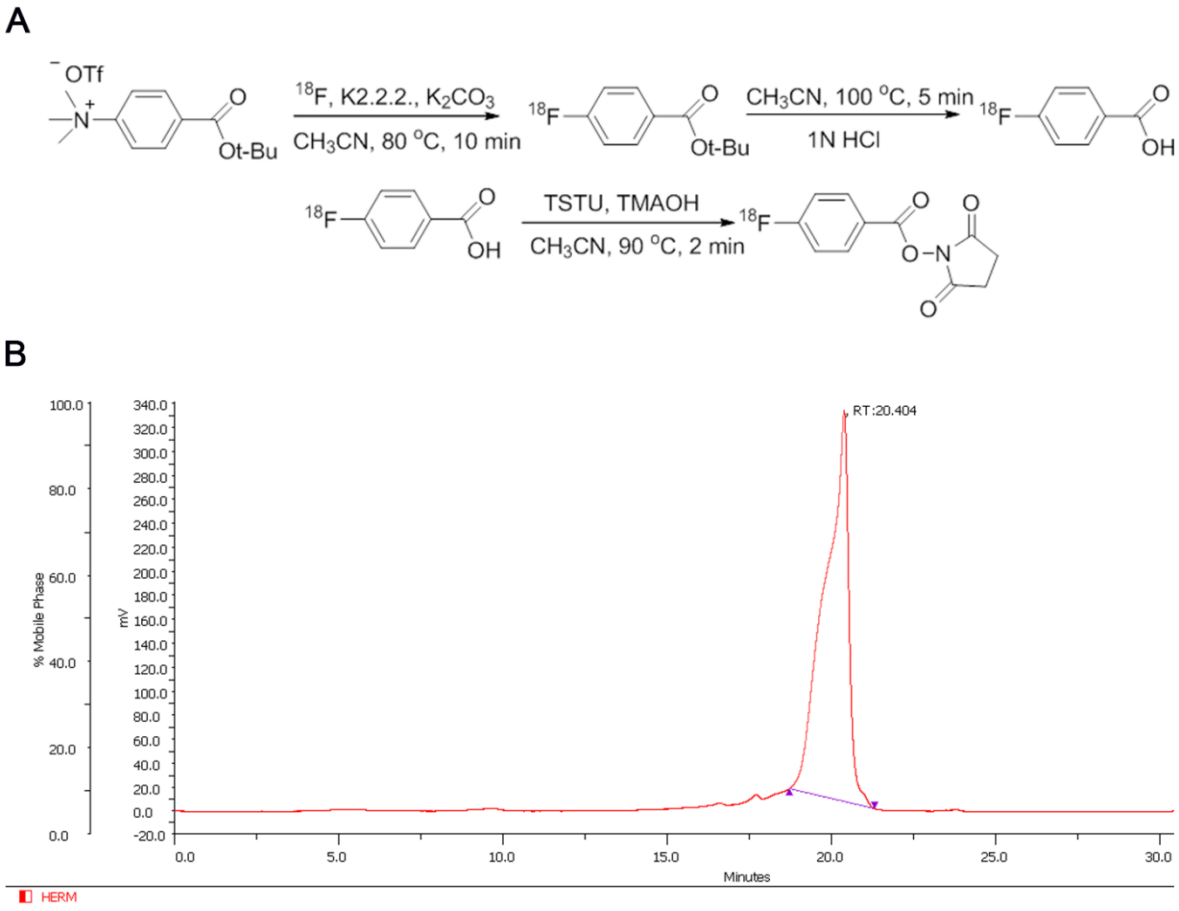

Figure 3.5: [^{18}F]SFB synthesis and purification. **A**) Chemical reaction scheme for the synthesis of *N*-succinimidyl-4-[^{18}F]fluorobenzoate; **B**) Radioactive HPLC trace of purified [^{18}F]SFB for radiolabeling the anti – CA125 scFv. The retention time of [^{18}F]SFB is indicated at 20.404 min.

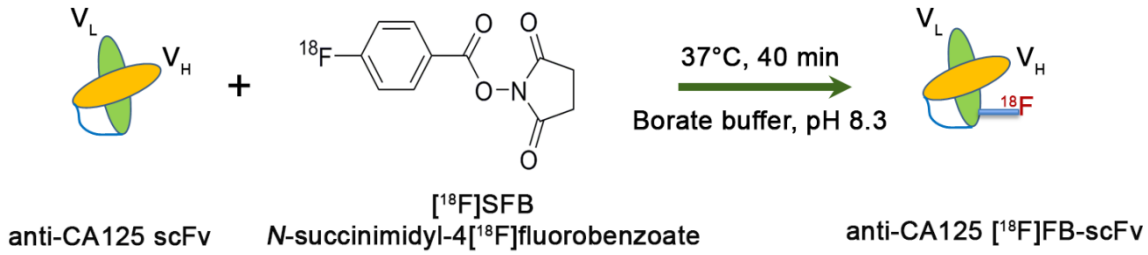

Figure 3.6: Schematic representation for the ^{18}F-labeling of anti-CA125 scFv

[^{18}F]FBz- anti-CA125 scFv was obtained in radiochemical yields of 3.68 ± 1.81% (n=17) and specific activity of 3.88 ± 0.76 GBq/µmol (n=5). Further purification of the [^{18}F]FBz-anti-CA125 scFv from unreacted [^{18}F]SFB and its degradation intermediate in borate buffer pH 8.3 by size exclusion chromatography on an EconoPac® 10DG desalting column, provided ^{18}F-labeled scFv in > 97% purity as analyzed from phosphorimages of eluted samples electrophoresed in a 12% SDS-polyacrylamide gel (Fig 3.7) and radio-TLCs (Fig 3.8).

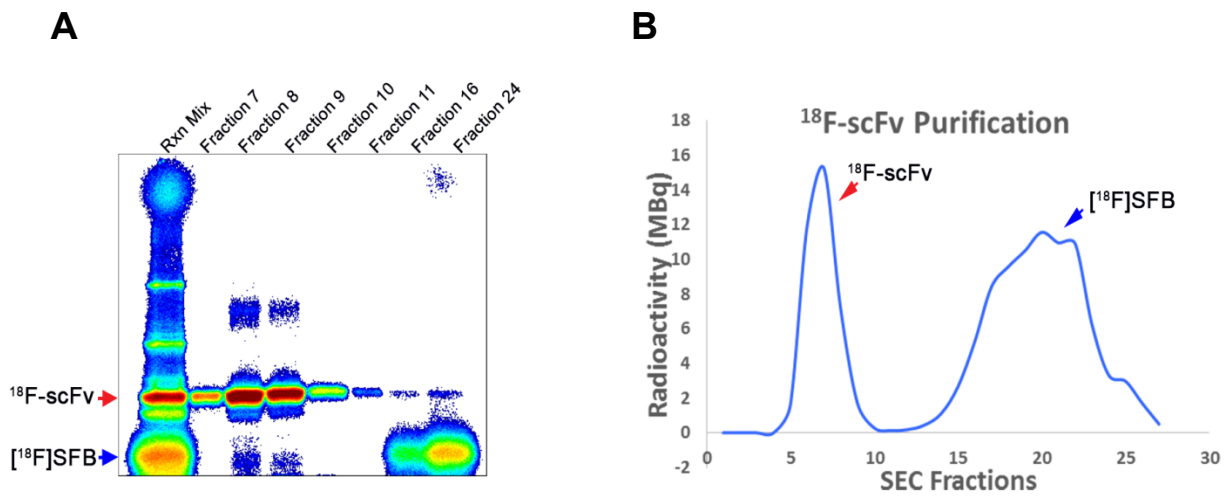

Figure 3.7: Quality control for purification of [^{18}F]FBz-anti-CA125 scFv. **A)** Phosphorimage of the size exclusion chromatography (SEC) purified ^{18}F-labeled anti-CA125 scFv fractions electrophoresed in a 12% SDS-polyacrylamide gel; **B)** A representative plot of the corresponding elution profile as a result of size based exclusion of radioactive samples from the ^{18}F-labeling reaction mixture.

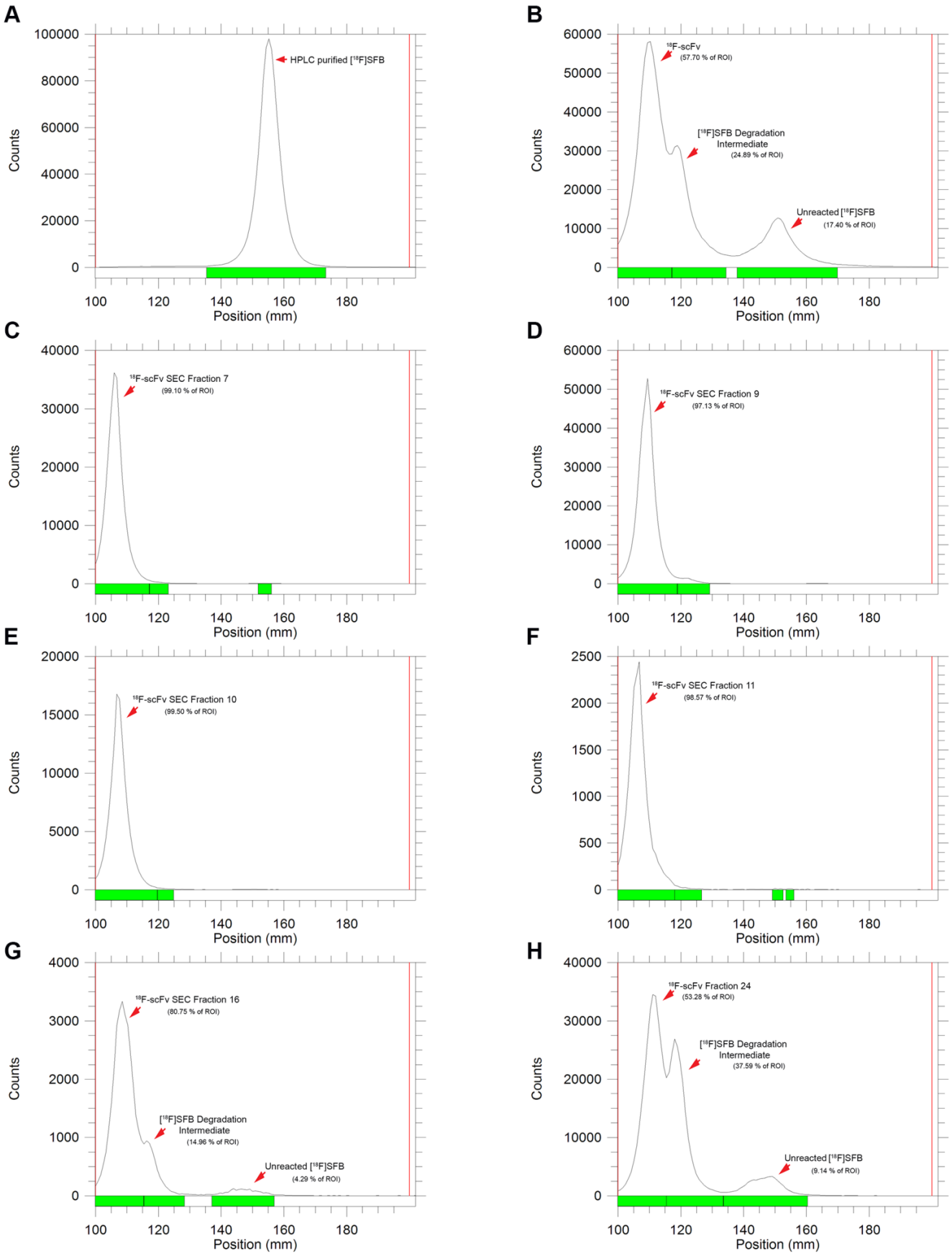
A
HPLC purified [18F]SFB
Counts
Position (mm)
B
18F-scFv
(57.70 % of ROI)
[18F]SFB Degradation Intermediate
(24.89 % of ROI)
Unreacted [18F]SFB
(17.40 % of ROI)
C
18F-scFv SEC Fraction 7
(99.10 % of ROI)
D
18F-scFv SEC Fraction 9
(97.13 % of ROI)
E
18F-scFv SEC Fraction 10
(99.50 % of ROI)
F
18F-scFv SEC Fraction 11
(98.57 % of ROI)
G
18F-scFv SEC Fraction 16
(80.75 % of ROI)
[18F]SFB Degradation Intermediate
(14.96 % of ROI)
Unreacted [18F]SFB
(4.29 % of ROI)
H
18F-scFv Fraction 24
(53.28 % of ROI)
[18F]SFB Degradation Intermediate
(37.59 % of ROI)
Unreacted [18F]SFB
(9.14 % of ROI)

Figure 3.8: Quality control Radio-TLCs: **A)** HPLC-purified [^{18}F]SFB; **B)** ^{18}F- labeling reaction mixture at end of radiotracer synthesis [45 min]; **C)** size exclusion column (SEC)-purified fraction 7; **D)** SEC-fraction 9; **E)** SEC-fraction 10; **F)** SEC-fraction 11; **G)** SEC-fraction 16; **H)** SEC-fraction 24.

3.3.3 *In vitro* functional characterization of anti-CA125 [^{18}F]FBz-scFv:

The purified [^{18}F]FBz-anti-CA125 scFv showed highly specific binding to NIH:OVCAR-3 and virtually no binding to SKOV3 cells used for *in vitro* cell uptake studies (Fig 3.9B). This was also observed for the ^{18}F-labeled anti-CA125 MAb (Fig. 3.9A). Inhibition studies carried out using ^{18}F-labeled anti-CA125 MAb and scFv provided *in vitro* EC_{50} values of 48 nM for the [^{18}F]FBz-anti-CA125 MAb and 40 nM for the [^{18}F]FBz-anti-CA125 scFv . These values were within a comparable range for both the radiotracers co-incubated with different concentrations of un-labeled anti-CA125 MAb (Fig. 3.9C).

Further, immunofluorescence experiments performed after complete decay of the purified [^{18}F]FBz-anti-CA125 scFvc also revealed retention of immunoreactivity of the labeled antibody fragment (Fig. 3.4 e – g).

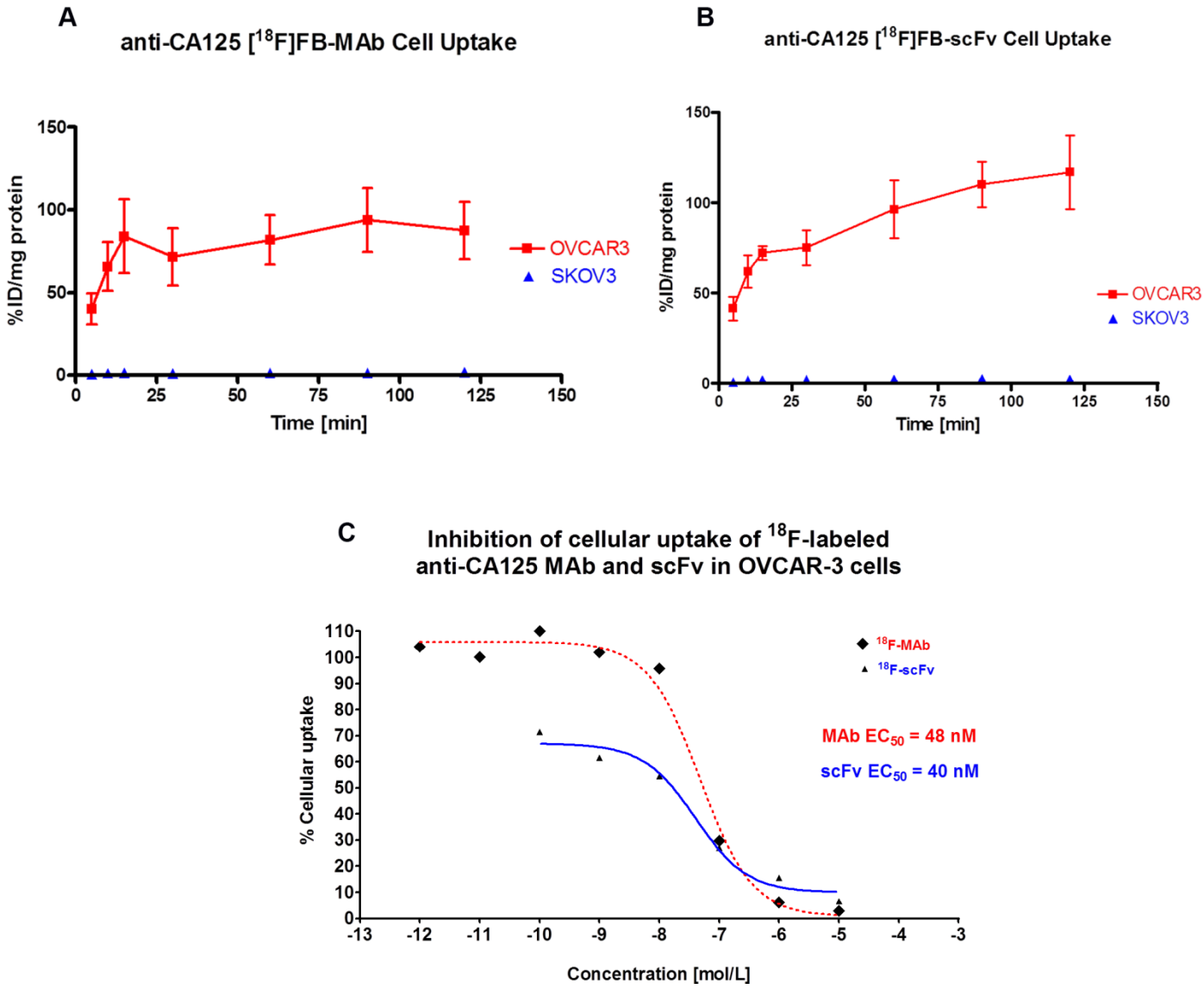

Figure 3.9: *In vitro* analysis of anti-CA125 scFv binding: **A)** ^{18}F-labelled MAb; **B)** ^{18}F-labeled scFv; **C)** Non-linear regression analysis of ^{18}F-labeled MAb versus scFv binding in competition with various concentrations of un-labeled MAb B43.13 for EC_{50} calculation.

3.3.4 Small animal imaging:

In vivo analysis of [^{18}F]FBz-anti-CA125 scFv in NIH-III mice bearing NIH:OVCAR-3 and SKOV3 xenografts as documented in micro-PET scans revealed most of the radioactivity present as either circulating in the bloodstream or in the organs of clearance such as kidney and liver (Fig. 3.10C and D). Overall, within the first hour post-injection of the radiotracer, there was significantly higher amounts of radioactivity present in the blood pool of NIH:OVCAR-3 xenograft mice, while the tumor itself revealed an SUV_{mean} of 0.5 (n=3). SKOV3 tumor had a SUV_{mean} of 0.3 (n=2). In comparison, a metabolic radiotracer - [^{18}F]FDG provided an SUV_{mean} of 0.3 for SKOV3 tumors xenografted in NIH-III mice and an SUV_{mean} of 0.6 in NIH:OVCAR-3 tumors xenografted in BALB/c nude mice (Fig. 3.10A and B)

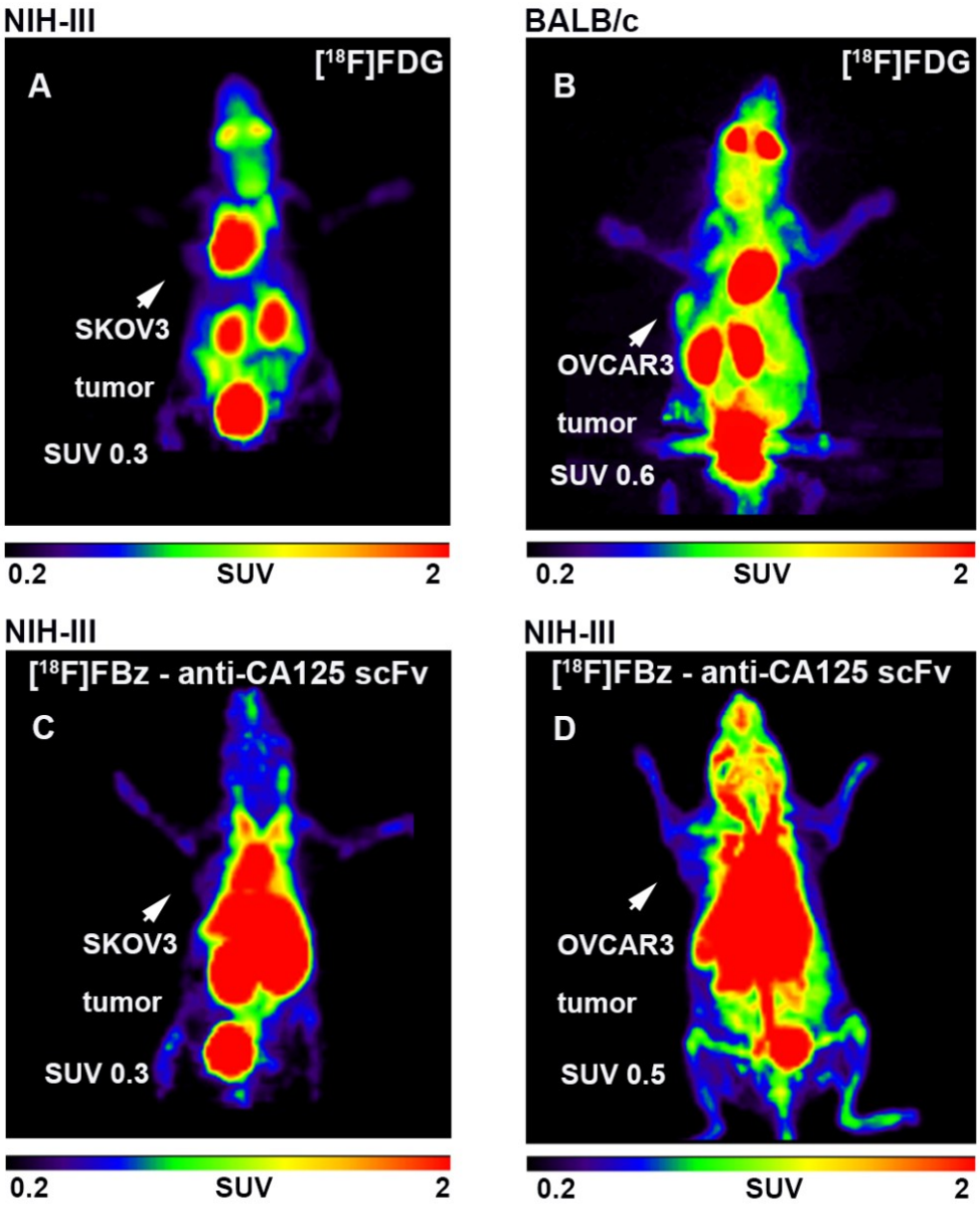

Figure 3.10: *In vivo* analysis of radiotracer: Comparative micro-PET images of NIH:OVCAR-3 and SKOV3 xenograft mice injected with [^{18}F]FBz-anti-CA125 scFv and standard clinical PET radiotracer [^{18}F]FDG.

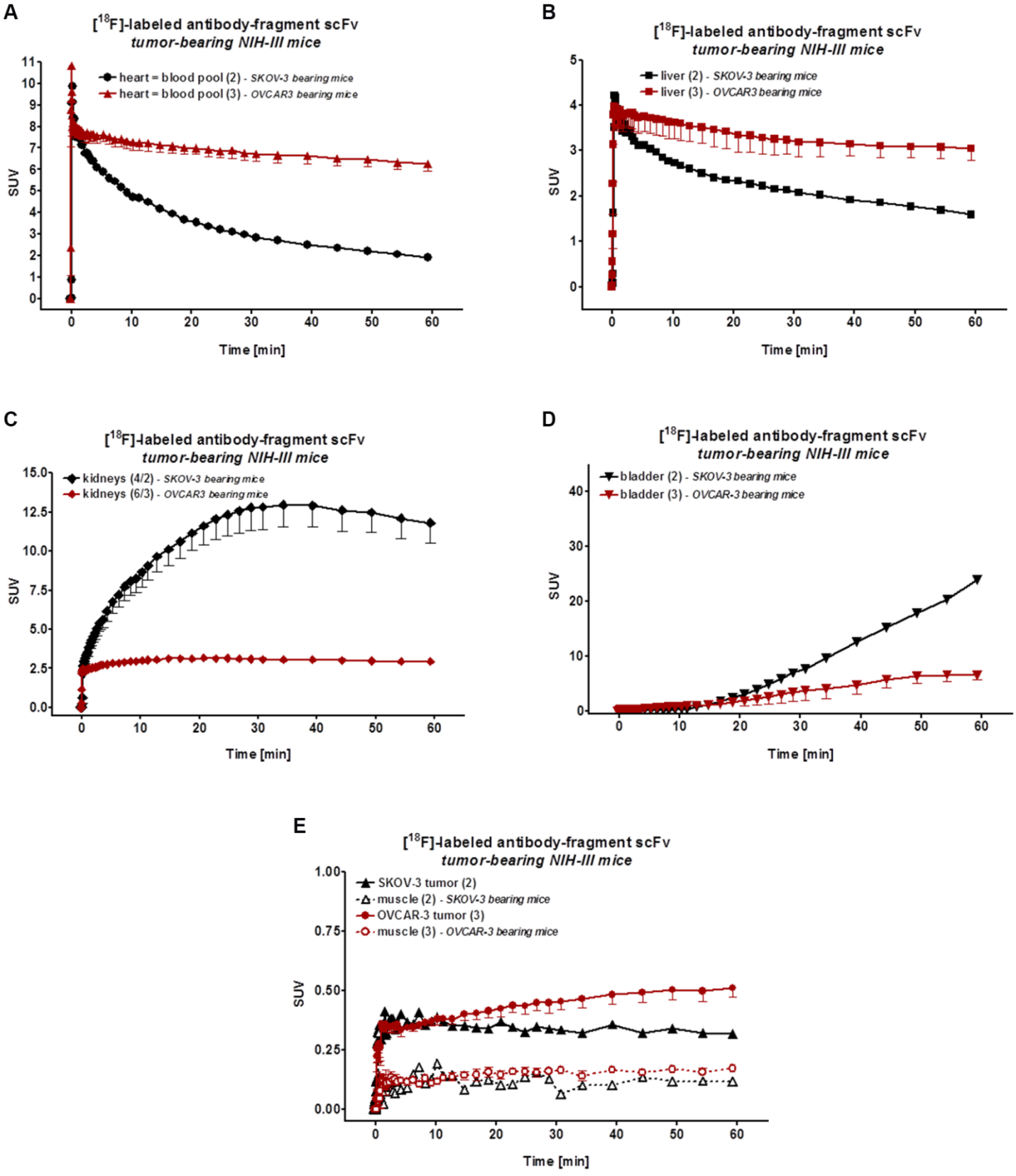
A
[18F]-labeled antibody-fragment scFv
tumor-bearing NIH-III mice
heart = blood pool (2) - SKOV-3 bearing mice
heart = blood pool (3) - OVCAR3 bearing mice
SUV
Time [min]
B
[18F]-labeled antibody-fragment scFv
tumor-bearing NIH-III mice
liver (2) - SKOV-3 bearing mice
liver (3) - OVCAR3 bearing mice
SUV
Time [min]
C
[18F]-labeled antibody-fragment scFv
tumor-bearing NIH-III mice
kidneys (4/2) - SKOV-3 bearing mice
kidneys (6/3) - OVCAR3 bearing mice
SUV
Time [min]
D
[18F]-labeled antibody-fragment scFv
tumor-bearing NIH-III mice
bladder (2) - SKOV-3 bearing mice
bladder (3) - OVCAR-3 bearing mice
SUV
Time [min]
E
[18F]-labeled antibody-fragment scFv
tumor-bearing NIH-III mice
SKOV-3 tumor (2)
muscle (2) - SKOV-3 bearing mice
OVCAR-3 tumor (3)
muscle (3) - OVCAR-3 bearing mice
SUV
Time [min]

Figure 3.11: *In vivo* analysis of radiotracer: Analyzed radioactive time activity curves obtained from dynamic micro-PET scans for [^{18}F]FBz-anti-CA125 scFv in NIH:OVCAR-3 versus SKOV3 tumor-bearing NIH-III mice.

An analysis of the radioactivity time activity curves from 1 h dynamic micro – PET scans revealed a concurrence with the aforementioned observation for considerably higher amounts of [^{18}F]FBz-anti-CA125 scFv in the blood pool of NIH:OVCAR-3 xenograft mice than in SKOV3 mice injected with the same amount of radiotracer (Fig 3.11A). Although [^{18}F]FBz-anti-CA125 scFv is expected to be renally cleared (via kidneys and bladder), the radiotracer seems to conform with this clearance pathway only in SKOV3 xenograft animals (Fig. 3.11 C and 3.11D), wherein most of it is being processed by the kidneys (Fig. 3.11C) or is present in the bladder for excretion (Fig. 3.11D). In contrast, there appears to be a tendency for [^{18}F]FBz-anti-CA125 scFv to be cleared hepatically in NIH:OVCAR-3 bearing xenograft mice (Fig. 3.11B) rather than the expected renal route.

3.4 Discussion:

As a dimension of functional imaging, immuno-PET fundamentally relies on the ability of an antibody-based targeting vector to specifically bind to its target antigen *in vivo*. Since most antibody derived fragments employed in this approach are engineered molecules produced by recombinant methods,[17] it is vital that they are prepared with high purity and attain the most appropriate structure that retains biochemical affinity for functional binding to the target antigen. In the present work, this was achieved by the expression and *in vivo* folding of the CA125 targeting scFv in an oxidizing environment provided by the periplasm of recombinant *E.coli* and purified by immobilized metal affinity chromatography. Furthermore, the utility of these biomolecular targeting vectors for immuno-PET involves conjugation with a positron-emitting radionuclide, without compromising their immunoreactivity to the target antigen. As a preliminary assessment of the functional activity upon labeling, the anti-CA125 scFv and MAb were conjugated with fluorescein isothiocyanate owing to its ability for stable thiourea bond formation with primary amines on biomolecules under slightly basic pH conditions. Our observation of membrane bound fluorescence; indicative of CA125 expression upon immunostaining NIH:OVCAR-3 cells was in agreement with a previous report,[18] which employed a FITC-labeled anti-CA125 targeting MAb B27.1.

Having demonstrated the functional viability of fluorescently labeled CA125 targeting vectors, we embarked upon the task of radiolabeling anti-CA125 scFv with ^{18}F, with an aim to develop a suitable molecular probe for same-day imaging

of EOC. Since direct radiofluorination procedures could affect the function of biomolecules such as antibody fragments, we chose to employ *N*-succinimidyl-4-[^{18}F]fluorobenzoate ([^{18}F]SFB) as a prosthetic group to perform this function in a rather mild fashion.[19] Being an activated ester with a succinimidyl nucleus, [^{18}F]SFB reacts rapidly via acylation with aliphatic amines on biomolecules such as anti-CA125 scFv to form stable amide bonds generating an ^{18}F-fluorobenzoylated version of the targeting agent – [^{18}F]FBz-anti-CA125 scFv. Furthermore, in accordance with early reports,[20, 21] and our own experience, we purified the ASU-provided [^{18}F]SFB by HPLC in order to obtain higher coupling yields and preserved immunoreactivity, even though this step added an extra 23 minutes to the synthesis of ^{18}F-labeled anti-CA125 scFv. The [^{18}F]FBz-anti-CA125 scFv not only demonstrated highly specific binding to NIH:OVCAR-3 cells, but also yielded EC_{50} values that were comparable to that obtained for the full-length MAb. This indicated retention of immunoreactivity and comparable *in vitro* targeting capabilities of the antibody fragment being employed as a vector.

Since the radiopharmacological profile of [^{18}F]FBz-anti-CA125 MAb would be incompatible for the purpose of same day imaging, only [^{18}F]FBz-anti-CA125 scFv was employed for small animal imaging studies by micro-PET. [^{18}F]FDG was included in the study to serve as a current gold standard ^{18}F-based radiotracer for direct evaluation of the utility of a targeted radiotracer such as [^{18}F]FBz-anti-CA125 scFv in the same preclinical tumor models. [^{18}F]FDG demonstrated a typical radiopharmacological profile with most of it found in regions of high metabolism (heart) and organs of clearance (kidneys and bladder). Taking into

consideration the data from micro-PET images and the analyzed time activity curves, [^{18}F]FBz-anti-CA125 scFv clearly revealed a higher persistence in the systemic circulation of both the tumor xenograft models used in this study; with the effect being more pronounced in NIH:OVCAR-3 tumor-bearing mice. Furthermore, a major proportion of the [^{18}F]FBz-anti-CA125 scFv tends to be cleared hepatically in stark contrast with the expected *in vivo* radiopharmacologically preferred renal route of clearance for radiotracers below MW ~ 60 KDa as conformed to by the same radiotracer in SKOV3 tumor-bearing animals. This unique observation may be attributed to the potential formation of immunocomplexes between trace amounts of both [^{18}F]FBz-anti-CA125 scFv and CA125 molecules that may be present as shed antigen in the bloodstream of corresponding NIH:OVCAR-3 tumor-bearing animals. A similar observation of potential immunocomplex formation with shed antigen within the first 90 minutes of the radiotracer injection and subsequent clearance via the liver has been previously reported by McQuarrie et al, dealing with the administration of the parental anti-CA125 MAb-B43.13 formulated as a radiotracer using ^{99m}Tc for radioimmunoscintigraphy in human patients.[22] However, in that report an excess dose of radioimmunoconjugate employed (2 mg of ^{99}mTc-MAb B43.13 per patient) ensured tumor bioavailability of the tracer for use in radioimmunoscintigraphy, despite immunocomplex formation.[22, 23]

Additionally, despite having good immunoreactivity and promising *in vitro* binding capabilities, the scFv format appears to be greatly limited by its molecular weight / size, which was initially proposed as its prime advantage for enhanced

tumor penetration and rapid systemic clearance in order to translate into optimal tumor-to-background ratios to deliver high contrast images within a shorter period of time. This has also been demonstrated in previous reports,[25, 26 27] wherein the monomeric scFv format becomes a victim of first pass clearance via the renal route. An evaluation of the ideal size for tumor targeting agents by Wittrup et al,[28] described scFv molecules as residing in the death-valley of their evaluation curve. This has been attributed to the plausible explanation that scFv molecules are too small to escape renal clearance and too big for rapid extravasation from blood vessels carrying them to the tumor. Furthermore, a lack of sufficient avidity also contributes to a loss of *in vivo* binding efficacy for the monomeric scFv. Therefore, diabodies have been proposed and demonstrated to yield relatively better *in vivo* tumor uptake of antibody fragments which are below the renal cut-off for clearance.[21, 29, 30] It is also noteworthy that although the scFv seemed to follow its expected route for pharmacological clearance, the presence of a polar hexa-histidine tag at its C-terminus and the overall positive charge of the molecule owing to its amino acid composition may also be factors that contribute to its re-absorption and retention in the kidneys.[30, 31] Pre-dosing the animal subjects with positively-charged amino acids such as poly-L-lysine (1.2 g/kg) as a competitive strategy routinely practiced in the clinic for administration of peptide-receptor radionuclide therapy (PRRT) or co-infusion of succinylated gelatin (150 mg/kg) reported for preclinical immuno-PET applications using nanobodies may be options to help circumvent excessive renal trapping of the radiotracer and concomitantly improve its tumor bioavailability.[31] Nevertheless, these approaches

manifest side effects related to nausea and vomiting. Finally, despite similar tumor-to-muscle ratios for the radiotracer used in both xenograft bearing mice, there was a slightly higher and differential absolute uptake value of [^{18}F]FBz-anti-CA125 scFv in NIH:OVCAR-3 tumors when compared with SKOV3 tumors. This feature highlights the tumor targeting specificity of the scFv radiotracer despite its aforementioned limitations for *in vivo* functioning.

Further engineering of the anti-CA125 scFv into a diabody is warranted in order to improve avidity so that better tumor binding and favourable *in vivo* radiopharmacological profiles for same-day imaging can be achieved. Nonetheless, the anti-CA125 scFv can be employed as an analytical reagent for *in vitro* and *ex vivo* analysis of samples being investigated for the presence of CA125. It may also be applied to develop immunoaffinity resins for the isolation of CA125 antigen for biomedical research applications.

3.5 Conclusions:

An scFv derived from MAb-B43.13 was produced by recombinant methods and purified as a biochemically active protein capable of binding to target antigen – CA125. The scFv was radiolabeled using [^{18}F]SFB as a prosthetic group to yield [^{18}F]FBz-anti-CA125 scFv with retained immunoreactivity. *In vivo* application of the [^{18}F]FBz-anti-CA125 scFv as a radiotracer in preclinical ovarian cancer xenograft mice revealed a modest absolute tumor uptake in NIH:OVCAR-3 xenograft mice. [^{18}F]FBz-anti-CA125 scFv demonstrated remarkably different *in vivo* biodistribution and radiopharmacological profiles between the test and control tumors and also in comparison with [^{18}F]FDG. In summary, the present work demonstrates the development of a CA125-targeted antibody-fragment based molecular probe for same-day imaging of epithelial ovarian cancer via immuno-PET. This study demonstrates the feasibility of prosthetic group mediated radiofluorination of biomolecules such as antibody fragments and its subsequent use for molecular imaging of EOC. Moreover, the limitations of using such a vector in a setting that involves circulating shed antigens, which may be easier targets for antibody fragment binding at early time points in PET imaging, are exemplified through this work. Clearly, a monomeric scFv is not a suitable molecule of choice as a radiotracer for oncologic imaging of solid tumors.

3.6 References:

1. Knowles SM, Wu AM: Advances in immuno-positron emission tomography: antibodies for molecular imaging in oncology. *J Clinical Oncol* 2012, **30**:3884-3892.
2. Wu AM: Engineered antibodies for molecular imaging of cancer. *Methods* 2014, **65**:139-147.
3. Holliger P, Hudson PJ: Engineered antibody fragments and the rise of single domains. *Nat Biotechnol* 2005, **23**:1126-1136.
4. Wu AM, Yazaki PJ: Designer genes: recombinant antibody fragments for biological imaging. *Q J Nucl Med* 2000, **44**:268-283.
5. Wu AM: Antibodies and antimatter: the resurgence of immuno-PET. *J Nucl Med* 2009, **50**(1):2-5.
6. Wu AM, Olafsen T: Antibodies for molecular imaging of cancer. *Cancer J* 2008, **14**: 191-197.
7. Davis HM, Zurawski VR, Jr., Bast RC, Jr., Klug TL: Characterization of the CA 125 antigen associated with human epithelial ovarian carcinomas. *Cancer Res* 1986, **46**:6143-6148.
8. Scholler N, Urban N: CA125 in ovarian cancer. *Biomark Med* 2007, **1**:513-523.
9. Capstick V, Maclean GD, Suresh MR, Bodnar D, Lloyd S, Shepert L, Longenecker BM, Krantz M: Clinical evaluation of a new two-site assay for CA125 antigen. *Int J Biol Markers* 1991, **6**:129-135.
10. Nustad K, Bast RC, Jr., Brien TJ, Nilsson O, Seguin P, Suresh MR, Saga T, Nozawa S, Bormer OP, de Bruijn HW *et al*: Specificity and affinity of 26 monoclonal antibodies against the CA 125 antigen: first report from the ISOBM TD-1 workshop. International Society for Oncodevelopmental Biology and Medicine. *Tumour Biol* 1996, **17**:196-219.

11. Nap M, Vitali A, Nustad K, Bast RC, Jr., O'Brien TJ, Nilsson O, Seguin P, Suresh MR, Bormer OP, Saga T *et al*: Immunohistochemical characterization of 22 monoclonal antibodies against the CA125 antigen: 2nd report from the ISOBM TD-1 Workshop. *Tumour Biol* 1996, **17**:325-331.

12. Berek JS: Immunotherapy of ovarian cancer with antibodies: a focus on oregovomab. *Expert Opin Biol Ther* 2004, **4**:1159-1165.

13. Iagaru AH, Mittra ES, McDougall IR, Quon A, Gambhir SS: 18F-FDG PET/CT evaluation of patients with ovarian carcinoma. *Nucl Med Commun* 2008, **29**:1046-1051.

14. Wang WW, Das D, McQuarrie SA, Suresh MR: Design of a bifunctional fusion protein for ovarian cancer drug delivery: single-chain anti-CA125 core-streptavidin fusion protein. *Eur J Pharm Biopharm* 2007, **65**:398-405.

15. Noujaim AA, Baum RP, Sykes TR, Sykes CJ, Hertel A, Niesen, A, et al. Monoclonal antibody B43.13 for immunoscintigraphy and immunotherapy of ovarian cancer. In Current Tumor Diagnosis: Applications, Clinical Relevance, Trends. Edited by Klapdor, R. Munich: W Zuckschwerdt Verlag; 1994; 823–829.

16. Mading P, Fuchtner F, Wust F: Module-assisted synthesis of the bifunctional labelling agent N-succinimidyl 4-[(18)F]fluorobenzoate ([(18)F]SFB). *Appl Radiat Isot* 2005, **63**:329-332.

17. Olafsen T, Wu AM: Antibody vectors for imaging. *Seminars in nuclear medicine* 2010, **40**:167-181.

18. Xiao Z, McQuarrie SA, Suresh MR, Mercer JR, Gupta S, Miller GG: A three-step strategy for targeting drug carriers to human ovarian carcinoma cells in vitro. *J Biotechnol* 2002, **94**:171-184.

19. Wester HJ, Hamacher K, Stocklin G: A comparative study of N.C.A. fluorine-18 labeling of proteins via acylation and photochemical conjugation. *Nucl Med Biol* 1996, **23**:365-372.

20. Vaidyanathan G, Zalutsky MR: Improved synthesis of *N*-succinimidyl 4-[^{18}F]fluorobenzoate and its application to the labeling of a monoclonal antibody fragment. *Bioconjug Chem* 1994, **5**:352-356.

21. Garg PK, Garg S, Zalutsky MR: Fluorine-18 labeling of monoclonal antibodies and fragments with preservation of immunoreactivity. *Bioconjug Chem* 1991, **2**:44-49.

22. McQuarrie SA, Riauka T, Baum RP, Sykes TR, Noujaim AA, Boniface G, MacLean GD, McEwan AJ: The effects of circulating antigen on the pharmacokinetics and radioimmunoscintigraphic properties of ^{99m}Tc labelled monoclonal antibodies in cancer patients. *J Pharm Pharm Sci* 1998, **1**:115-125.

23. McQuarrie SA, Baum RP, Niesen A, Madiyalakan R, Korz W, Sykes TR, Sykes CJ, Hor G, McEwan AJB, Noujaim AA: Pharmacokinetics and radiation dosimtery of ^{99}Tc^{m} – labelled monoclonal antibody B43.13 in ovarian cancer patients. *Nucl Med Commun* 1997, **18**:878-886.

24. Williams LE, Wu AM, Yazaki PJ, et al. Numerical selection of optimal tumor imaging agents with application to engineered antibodies. *Cancer Biother Radiopharm* 2001;**16**(1): 25-35.

25. Cai W, Olafsen T, Zhang X, Cao Q, Gambhir SS, Williams LE, Wu AM, Chen X: PET imaging of colorectal cancer in xenograft-bearing mice by use of an 18F-labeled T84.66 anti-carcinoembryonic antigen diabody. *J Nucl Med* 2007, **48**:304-310.

26. Olafsen T, Sirk SJ, Olma S, Shen CK, Wu AM: ImmunoPET using engineered antibody fragments: fluorine-18 labeled diabodies for same-day imaging. *Tumour Biol* 2012, **33**:669-677.

27. Wittrup KD, Thurber GM, Schmidt MM, Rhoden JJ: Practical theoretic guidance for the design of tumor-targeting agents. *Methods enzymol* 2012, **503**:255-268.

28. Schneider DW, Heitner T, Alicke B, Light DR, McLean K, Satozawa N, Parry G, Yoo J, Lewis JS, Parry R: In vivo biodistribution, PET imaging, and tumor accumulation of 86Y- and 111In-antimindin/RG-1, engineered antibody fragments in LNCaP tumor-bearing nude mice. *J Nucl Med* 2009, **50**:435-443.

29. Eder M, Knackmuss S, Le Gall F, et al. 68Ga-labelled recombinant antibody variants for immuno-PET imaging of solid tumours. *Eur J Nucl Med Mol Imaging* 2010;**37**(7): 1397-407.

30. Vegt E, de Jong M, Wetzels JF, Masereeuw R, Melis M, Oyen WJ, Gotthardt M, Boerman OC: Renal toxicity of radiolabeled peptides and antibody fragments: mechanisms, impact on radionuclide therapy, and strategies for prevention. *J Nucl Med* 2010, **51**:1049-1058.

31. D'Huyvetter M, Vincke C, Xavier C, Aerts A, Impens N, Baatout S, De Raeve H, Muyldermans S, Caveliers V, Devoogdt N *et al*: Targeted Radionuclide Therapy with a ^{177}Lu-labeled Anti-HER2 Nanobody. *Theranostics* 2014, **4**:708-720.

4

Immuno-PET of Epithelial Ovarian Cancer: Harnessing the potential of CA125 for non-invasive imaging[3]

[3]A version of this chapter will be submitted to the European Journal of Nuclear Medicine and Molecular Imaging Research: Sharma SK, Wuest M, Wang M, Glubrecht D, Andrais B, Lapi SE, Suresh MR, Wuest F. Immuno-PET of Epithelial Ovarian Cancer: Harnessing the potential of CA125 for non-invasive imaging

4.1 Introduction

Despite its relative rarity in the general population and the availability of standard treatment through surgical intervention and platinum chemotherapy, epithelial ovarian cancer (EOC) continues to be the most insidious and lethal gynecologic malignancy in the western world. The Surveillance Epidemiology and End Results (SEER) program estimated 22,240 new cases of ovarian cancer in 2014 alongside 14,270 deaths resulting from this disease in the United States alone.[1] A combination of the asymptomatic nature of this malignancy and high incidence of recurrence results in a low 5-year survival rate of 44%.[1]

Cancer Antigen 125 (CA125) is a high molecular weight mucinous glycoprotein overexpressed on the membrane of EOC cells.[2-4] It has long served as a standard of care serum biomarker for ovarian cancer surveillance although its presence is also reported in some non-gynecologic malignancies and benign conditions such as pregnancy, menstruation, endometriosis, liver disease and congestive heart failure.[3, 4] Post-treatment elevation of serum CA125 level in EOC patients serves as an indicator of progressive disease and finds greatest use in the management of patients with documented evidence of ovarian cancer.[3-5] However, a normal CA125 serum titer does not always imply an absence of the disease. An estimated 50% of patients with normal levels of CA125 post-chemotherapy have small volumes of active disease at second-look surgery, and a large portion of this population succumbs to recurrence from the disease.[6] Presently, serial CA125 levels in patients are tested using ELISA-based immunoassays. Despite their indicative advantage, such assays can be far from delivering a true representation

of the *in vivo* pathophysiological pattern, and may be limited in their capabilities for early detection of ovarian neoplasms.

From a diagnostic standpoint, it is known that radiological progression precedes clinical progression by 2-3 months and when combined with CA125, it can be preceded by 5 months.[5] Among contemporary imaging modalities, [^{18}F]FDG-PET (^{18}F-Fluorodeoxyglucose positron emission tomography) has shown highest sensitivity and accuracy in detecting recurrent ovarian cancer whilst simultaneous investigations with CT, MRI and ultrasound yielded negative or equivocal results.[7-9]

Over the years, several antibodies have been developed to target CA125.[10-13] Among those reported, MAb-B43.13 has seen the most progress towards clinical translation for the immunotherapy of EOC.[14-16] More recently, immuno-PET has emerged as a strategy that unifies the specificity of antibody-based targeting with the sensitivity for detection by positron emitting radionuclides via PET in order to render a superlative diagnostic potential.[17]

We hypothesized that *in vivo* imaging of CA125 expression while it is present on the surface of ovarian carcinomas, could lead to a much earlier detection of recurrent disease.

The goal of this study was to develop a targeted non-invasive method for the *in vivo* detection of CA125 present on ovarian carcinomas. This would allow the use of CA125 as a biomarker for early detection of ovarian cancer by providing a more accurate *in vivo* evaluation of tumor load and residual disease for effective disease management. Previous research with MAb B43.13 and the recent reports

of antibody-based radiotracers targeting biomarkers of similar pathophysiological nature in other cancers,[18, 19] prompted us to develop an immuno-PET strategy for the *in vivo* imaging of EOC. Towards this goal, anti-CA125 MAb (MAb-B43.13) and its derivative single chain Fragment variable (scFv-B43.13) were radio-labeled with positron emitter ^{64}Cu ($t_{1/2}$ 12.7 h) and analyzed *in vitro* and *in vivo* using CA125 overexpressing NIH:OVCAR-3 cells and antigen negative SKOV3 cells in preclinical EOC xenograft mouse models.

4.2 Materials and Methods

4.2.1 Expression and purification of MAb-B43.13 and its derivative scFv:

Anti-CA125 murine monoclonal antibody was purified from B43.13 hybridoma[15] by protein G affinity chromatography (Sigma, P-7700). Anti-CA125 scFv was produced after deletion of the core-streptavidin from previously described fusion constructs.[20] The scFv was expressed as a C-terminal hexa-histidine tagged protein in *E.coli* Rosetta 2(DE3) (Novagen, 71400) and purified by immobilized metal affinity chromatography using a TALON® superflow resin (Clontech, 635506).

4.2.2 Cell lines and culture conditions: Ovarian cancer cell lines NIH:OVCAR-3 and SKOV3 were obtained from ATCC and used for *in vitro* and *in vivo* studies. Cells were cultured in DMEM-F12 medium supplemented with 10% v/v fetal bovine serum (Life Technologies, 12483-020), 50 IU/mL penicillin, 50 μg/mL streptomycin (Life Technologies, 15140-122). NIH:OVCAR-3 cells were additionally supplemented with 7 μg/mL recombinant human insulin (SAFC Biosciences, 91077C). Cells were cultured using sterile techniques and grown in a 37°C incubator providing humidified atmosphere of 5% CO_2 in air.

4.2.3 Characterization of CA125 targeting vectors:

MAb-B43.13 and scFv-B43.13 were characterized for binding to the target antigen by immunoblotting, immunofluorescence and flow cytometry. FITC-labeled MAb-B43.13 was also tested for uptake in live cells over a period of 48 h.

4.2.3.1 Western blotting: 7.5 x 10^6 NIH:OVCAR-3 and SKOV3 cells were lysed with CelLytic™M (Sigma, C2978). Cell lysates were electrophoresed on a 4-15% Mini-PROTEAN® TGX™ precast gel (Bio-Rad, #456-1086) and transferred to a Trans-Blot nitrocellulose membrane (Bio-Rad, 162-0115). The membranes were probed separately to evaluate MAb versus scFv binding with target antigen – CA125 in cell lysates. The blots were blocked for 45 min with 5% non-fat dry milk (Carnation) in PBS having 0.1% Tween-20 (PBST). MAb-B43.13 (3 mg/mL), mouse anti-β actin IgG (Sigma) and scFv-B43.13 (2 mg/mL) were used as primary antibodies (1: 5000) to probe the blots for 1 h at room temperature. Goat anti-mouse HRP conjugate (Sigma, A4416) was used as secondary antibody (1: 5000) to probe the blot against anti-CA125 MAb and mouse anti-β actin IgG (Sigma, A1978) for 1 h at room temperature. 6X His MAb-HRP conjugate (Clontech, 631210) was used as secondary antibody (1:5000) to probe against scFv-B43.13 for 1 h at room temperature. The blots were washed with PBST and developed on Amersham Hyperfilm ECL (GE Healthcare, 28906839) using Amersham ECL Plus Western Blotting Detection Reagents (GE Healthcare, RPN2132).

4.2.3.2 Fluorescent labeling of anti-CA125 MAb/scFv: 1 mg each of MAb-B43.13 and scFv-B43.13 (2 mg/mL) were fluorescently labeled using the Pierce® FITC antibody labeling kit (Thermo Scientific, 53027) according to the manufacturer's instructions.

4.2.3.3 Flow Cytometry: 1.5 x 10^6 NIH:OVCAR-3 cells were harvested by trypsinization, rinsed twice with FACS buffer (PBS with 0.5% heat inactivated FBS, 2mM EDTA, 0.05% sodium azide) and resuspended by gentle tapping in ~100 µL FACS buffer. 10 µg of MAb-B43.13 or scFv-B43.13 was incubated with the cell suspension for 30 min at room temperature. Cells were rinsed twice in FACS buffer and incubated for 30 min with 4 µg of Alexa-fluor® 488 goat anti-mouse antibody (Life Technologies, A-11001) for the MAb samples and 4 µg of Penta·His Alexa Fluor 488 conjugate (Qiagen, 35310) for scFv samples. Cells were rinsed twice with FACS buffer and analyzed by flow cytometry on a BD FACS Calibur with 10,000 events gated per sample. A dengue virus targeting IgG (12A1) and a hexa-histidine tagged anti-RANK receptor scFv were used as isotype controls for the experiments. Negative controls included unstained NIH:OVCAR-3 cells and cells incubated with Alexa fluor 488 conjugated antibodies alone.

4.2.3.4 Immunofluorescence: NIH:OVCAR-3 and SKOV3 cells were plated onto glass coverslips in 35-mm tissue culture dishes (100,000 cells/2 mL medium/dish) and incubated at 37°C for 48 h. The cells were rinsed with PBS and fixed in methanol for 30 min at -20°C. The fixed cells were incubated in 5% non-fat dry milk (Carnation) in PBS for 30 min and immunostained separately for 1 h with FITC-labeled versus un-labeled MAb-B43.13 and scFv-B43.13. The un-labeled MAb and scFv samples were indirectly stained with corresponding Alexa fluor 488 labeled secondary antibodies as used in flow cytometry experiments.

MAb-B43.13 and scFv-B43.13 (2 mg/mL) were used at 1:250 dilution followed by 1:500 dilutions of secondary antibodies (2 mg/mL) in PBS containing 5% non-fat dry milk. Appropriate blank and control samples were included in the experiments. Antibody incubations were followed by three rinses with PBST for 10 min each. Coverslips were mounted on microscopy slides (Fisherbrand) using Mowiol® mounting medium (Calbiochem, 475904) supplemented with DAPI (50 µg/mL). Immunofluorescence was observed through a Zeiss Plan Apochromat 40X/1.3 Oil DIC M27 lens on a confocal laser scanning microscope (Zeiss LSM 710) and images were analyzed using Zen 2011 software. Separately, 30 µg of FITC-labeled anti-CA125 MAb was added to NIH:OVCAR-3 cells grown on coverslips and allowed to incubate under standard cell culture conditions over a period of 48 h to study uptake in live cells. Coverslips were washed and mounted on glass slides for analysis by confocal microscopy at 0.5, 1, 4, 12, 24 and 48 h time points.

4.2.4 NOTA Functionalization: p-SCN-Bn-NOTA [S-2-(4-Isothiocyanatobenzyl)-1,4,7-triazacyclononane-1,4,7-triacetic acid] (Macrocyclics Inc, B-605) was conjugated to MAb-B43.13 and scFv-B43.13 as a bi-functional chelator for ^{64}Cu radiolabeling. Briefly, a 6 molar excess of p-SCN-Bn-NOTA in DMSO was added to MAb/scFv-B43.13 in 0.1 M sodium bi-carbonate buffer pH 8.5 and allowed to react for 1 h at 37°C. NOTA-functionalized MAb/scFv-B43.13 was purified from un-conjugated NOTA while simultaneously achieving buffer exchange into 0.25 M sodium acetate pH 5.5 by using an Econo-Pac® 10DG

desalting column (Bio-Rad, 732-2010). The number of NOTA molecules conjugated per MAb and scFv was determined by MALDI-ToF MS analysis and according to the method described by Cooper et al.[21]

4.2.5 Determination of Bi-functional Chelates per MAb/scFv:

NOTA conjugated anti-CA125 MAb and scFv were analyzed by MALDI-ToF-MS at the Institute for Biomolecular Design, University of Alberta, to determine the number of bi-functional chelate molecules per targeting vector. 1 μL of each sample was mixed with 1 μL of sinapic acid (10 mg/mL in 50% acetonitrile:water and 0.1% trifluoroacetic acid). 1 μL of the sample/matrix solution was then spotted onto a stainless steel target plate and allowed to air dry. All mass spectra were obtained using a Bruker Ultraflex MALDI-ToF/ToF (Bruker Daltonic GmbH). Ions were analyzed in positive mode and external calibration was performed by use of a standard protein mixture.

An isotopic dilution assay as per the method of Cooper et al [21] was also performed to verify data obtained from MALDI-ToF analysis of immunoconjugates. Percentage radiolabeling efficiency was plotted as a function of different moles of copper added to a fixed concentration (moles) of MAb/scFv in order to determine the average number of bi-functional chelate molecules conjugated per targeting vector.

4.2.6 Preparation of CA125 targeting radioimmunoconjugates:

4.2.6.1 General*:* All glassware was rinsed with ultra-pure HCl (Fisherbrand, A508-P500). Trace metals basis ultra-pure chemicals for buffer preparations were

purchased from Sigma Aldrich. All buffer solutions were treated with biotechnology grade Chelex 100 (Bio-Rad, 143-2832).

4.2.6.2 ^{64}Cu labeling of NOTA-functionalized MAb/scFv: ^{64}Cu was produced via a ^{64}Ni(p,n)^{64}Cu nuclear reaction on a CS-15 biomedical cyclotron at Washington University, St. Louis, USA as previously described.[22] 85 MBq of ^{64}Cu-acetate was added to 100 µg NOTA-functionalized MAb/scFv-B43.13 and allowed to react at 30°C, 550 rpm for 1 h in a thermomixer. 1 mM EDTA was added to quench the reaction over 10 min. ^{64}Cu-NOTA-MAb-B43.13 and ^{64}Cu-NOTA-scFv-B43.13 radioimmunoconjugates were purified using an Econo-Pac® 10DG desalting column pre-equilibrated with 0.25 M sodium acetate, pH 5.5 used as the eluent. 350 µL elution fractions were collected from the column and radioactivity was measured on an Atomlab 400 dose calibrator (Biodex Inc). High specific activity radioimmunoconjugates were used for *in vitro* and *in vivo* radiopharmacological experiments. ^{64}Cu-labeled 12A1 MAb was used as an isotype control for *in vivo* experiments.

4.2.7 Functional characterization of CA125 targeting radioimmunoconjugates:

^{64}Cu-labeled anti-CA125 MAb and scFv were evaluated for target vs non-target cell uptake over a period of 2 h in an *in vitro* assay. Briefly, NIH:OVCAR-3 and SKOV3 cells were allowed to incubate for various time intervals with a fixed amount (100 KBq) of the aforementioned radioimmunoconjugates, then rinsed

and counted for cell-bound radioactivity. Immunoreactivity of the radioimmunoconjugates was assessed as per the method of Lindmo et al.[23] Direct binding studies were performed to determine the dissociation constant (K_D) and maximum number of binding sites (B_{max}) on target cells.

4.2.7.1 Quality control of purified radioimmunoconjugates:

^{64}Cu-NOTA-MAb-B43.13 and ^{64}Cu-NOTA-scFv-B43.13 were purified by size exclusion chromatography using a pre-packed desalting column. The radioimmunoconjugates eluted out in the earlier fractions owing to their molecular size compared with the EDTA chelated ^{64}Cu from the reaction mixture. 1 μL of the quenched radiolabeling reaction mixtures and selected fractions from size exclusion purification were spotted on ITLC-SG strips, allowed to dry and separate using 10mM EDTA pH 5.5 as the eluent and analyzed on a radio-TLC scanner (Bioscan AR-2000). As per previously established results in such experiments for quality control, ^{64}Cu-labeled anti-CA125 MAb and scFv remained at the baseline and any un-conjugated or EDTA-chelated ^{64}Cu moved with the solvent front on ITLC strips. Additionally, 15 μL of each elution fraction was electrophoresed in a 12% SDS-PAGE gel under non-reducing conditions and evaluated by autoradiography on a BAS-5000 phoshorimager (Fujifilm).

4.2.7.2 Stability of radioimmunoconjugates:

^{64}Cu-labeled MAb and scFv was analyzed by incubating 5 MBq of purified radioimmunoconjugates in 500 μL human AB type serum at 37°C for 48 h.

Samples were analyzed by size exclusion HPLC at 0, 24 and 48 h on a Biosep SEC-S2000 column (Phenomenex, 00F-2145-B0), using an isocratic mobile phase of 0.1 M phosphate buffer at a flow rate of 1 mL/min and by ITLC using 10 mM EDTA pH 5.5 as the eluent or via ITLC.

4.2.7.3 SOD Challenge experiments:

^{64}Cu-labeled MAb (5MBq) was challenged with a 1000 fold excess of Superoxide dismutase (Sigma, S8160) and allowed to incubate at 37°C over a period of 48 h. Samples were analyzed for trans-chelation by size exclusion chromatography on a Shimadzu analytical HPLC using the conditions mentioned above.

4.2.7.4 Cell Uptake Studies: NIH:OVCAR-3 and SKOV3 cells were seeded to obtain 250,000 cells per well in 12-well tissue culture plates. Prior to the uptake experiment, growth media was removed and cells were rinsed twice with PBS and incubated in Krebs buffer at 37°C for 1 h. The radioimmunoconjugate (100 KBq) was added to each well except those assigned to measure background activity alone. Cell uptake was terminated at 5, 10, 15, 30, 60, 90, 120 min by adding ice cold Krebs buffer and rinsing the wells twice to wash away any un-bound radioimmunoconjugates prior to lysing cells with RIPA buffer. The cell lysates were transferred to scintillation vials and measured for radioactivity using a γ-counter (Wizard$^{2®}$ 2480 Automatic Gamma Counter, Perkin-Elmer, Canada). Protein levels were quantified using a Pierce™ BCA protein assay kit according to the manufacturer's recommendations. Cell uptake levels were normalized to

percent of the total amount of radioactivity per milligram of protein (% radioactivity / mg protein) and plotted as a function of time. All experiments were performed in triplicates.

4.2.7.5 Lindmo assay for determination of immunoreactive fraction:

NIH:OVCAR-3 cells were aliquoted into microcentrifuge tubes at concentrations of 5, 4, 3, 2.5, 2, 1.5 and 0.5 x 10^6 cells in 500 μL PBS (pH 7.4). A stock solution of the radioimmunoconjugate was prepared in PBS (pH 7.4) supplemented with 1% BSA such that 50 μL of this solution contained 20,000 cpm which was then uniformly aliquoted into individual tubes. This setup was allowed to incubate for 1 h at room temperature on a platform mixer. Thereafter, cells were pelleted by centrifugation (5,000 rpm for 3 mins), rinsed twice with ice cold PBS and the supernatant was aspirated prior to measuring cell-bound radioactivity on a γ-counter (Wizard$^{2®}$ 2480 Automatic Gamma Counter, Perkin-Elmer, Canada). Radioactivity data obtained thereof was background corrected and compared with counts from the total activity control samples from the experiment. The immunoreactive fraction was determined by performing a linear regression analysis on a double-inverse plot of (total/bound) activity versus normalized cell concentration. All data was obtained in triplicates and no weighting was applied.

4.2.7.6 Direct binding studies were performed to determine the dissociation constant (K_D) and maximum number of binding sites (B_{max}) by incubating 0.5 x 10^6 cells with increasing concentrations (0.2 nM – 19.2 nM) of ^{64}Cu-labeled anti-

CA125 MAb in 250 µl PBS supplemented with 0.2% bovine serum albumin. To evaluate non-specific binding, a corresponding experimental set was prepared with 100 nM of un-labeled immunoconjugate added to the reaction in order to provide this reagent in 5–500 fold molar excess to the radioimmunoconjugate concentrations used. This setup was allowed to incubate at room temperature for 1 h with gentle shaking. Cells were pelleted by centrifugation at 1200 rpm for 5 min followed by 2 rounds of rinsing with ice cold PBS. Cell-bound radioactivity was measured using a γ-counter. Data was plotted using a non-linear regression fit analysis on GraphPad Prism6.

4.2.8 Animal Imaging: Small animal PET experiments were performed on a MicroPET® R4 or INVEON PET scanner (Siemens Preclinical Solutions). Mice were anesthetized by inhalation of isoflurane (Baxter Healthcare) in 40% oxygen/60% nitrogen, 1 L/min, while maintaining body temperature at 37°C throughout the experiment. 6–10 MBq of high specific activity radioimmunoconjugate (~30-40 µg) in 150 – 200 µL of 0.25M sodium acetate (pH 5.5) was administered intravenously via a tail vein catheter. For blocking experiments, 1 mg of unmodified anti-CA125 MAb was administered intraperitoneally 24 h prior to injection of the ^{64}Cu-labeled radioimmunoconjugates. In separate animals, 8-10 MBq of ^{64}Cu-labeled 12A1 IgG was administered via tail injection to evaluate non-specific uptake. Whole body PET data was acquired by performing static scans for each animal at 24 h p.i and 48 h p.i. Data acquisition continued for 60 min in 3D list mode. All PET

image files were reconstructed using the maximum a posteriori (MAP) algorithm. The image files were further processed using the ROVER v 2.0.51 software (ABX GmbH, Radeberg, Germany). Masks for defining 3D regions of interest (ROI) were set and the ROIs were defined by thresholding. Standardized uptake values [SUV = (activity/ml tissue) / (injected activity/body weight), mlg^{-1}] were calculated for each ROI. Data are expressed as means ± SEM from n investigated animals.

4.2.9 Animal Imaging: All experiments were carried out according to guidelines of the Canadian Council on Animal Care (CCAC) and approved by the local animal care committee of the Cross Cancer Institute, Edmonton. Six weeks old BALB/c nude female mice were obtained from Charles River labs (Quebec, Canada). The animals were housed in ventilated cages and provided food and water *ad libitum*. NIH:OVCAR-3 tumors were induced on the left shoulder by two subsequent subcutaneous injections of 15 x 10^6 and 10 x 10^6 cells in a 300 μL suspension of 1:1 mixture of PBS and matrigel (BD Biosciences). The second injection of cells was administered at the same site within 7-10 days. NIH:OVCAR-3 tumors grew for 6-8 weeks before reaching suitable tumor sizes of 150 – 200 mm^3. SKOV3 tumors were induced on the left shoulder by a single subcutaneous injection of 5 x 10^6 cells in PBS and were grown for about 2-3 weeks before achieving similar tumor sizes.

4.2.10 *Ex vivo* analyses:

NIH:OVCAR-3 tumor-bearing animal was injected with 4.55 MBq of ^{64}Cu-labeled anti-CA125 MAb via tail vein. At 24 h p.i the animal was euthanized by cervical dislocation. The tumor was submerged into O.C.T (Optimum Cutting Temperature) medium and flash frozen using a bath of dry ice cooled methanol. 7 micron slices were cut on a Leica CM 1850 cryostat. The tissue sections were further analyzed by autoradiography, immunofluorescence and immunohistochemistry.

4.2.10.1 Autoradiography: Tissue sections were placed into a BAS-Cassette (Fujifilm) and exposed to a phosphorimaging plate (Fujifilm) for 15 h at room temperature. The images were developed on a BAS-5000 reader (Fuji Photo Film) and analyzed with Adaptive Image Deconvolution Algorithm (AIDA) Image Analyzer v.450 software.

4.2.10.2 Immunofluorescence: Upon thawing, tissue sections were fixed with formalin for 30 min. The fixed sections were blocked overnight at 4°C using 0.12 mg/mL unconjugated goat anti-mouse Fab fragment (Jackson Immunoresearch) in 0.5% fish skin gelatin (Sigma) pH 7.4, supplemented with 0.1% triton X-100. The sections were rinsed 3x with Tris-buffered saline supplemented with 0.5% Tween 20 (TBST) for 5 min each. B43.13 MAb was used as primary antibody (1: 6000) in Dako antibody diluent and allowed to incubate overnight at 4°C. The sections were rinsed 3x with TBST and incubated with Alexa-fluor® 488 goat anti-mouse

antibody (Life Technologies) used as secondary antibody (1:400) in Dako antibody diluent for 2 h at room temperature. After three washes with TBST, the sections were rinsed with water and counterstained using Hoechst H33342 (2 μg/mL) for 5 min. The sections were rinsed and mounted under a coverslip using FluorSave (Calbiochem). The slides were analyzed with a Zeiss Plan Apochromat 10X/0.45 na lens on a confocal laser scanning microscope (Zeiss LSM 710) using Z-stack for image acquisition. The images were registered using Zen 2011 software (ZEISS) and further processed with Adobe Photoshop CS6.

4.2.10.3 Immunohistochemistry: To analyze the samples for immunohistochemistry, the same procedures for treatment, fixation, blocking and probing of tissue with primary antibody were followed. Dako EnVision™+ HRP conjugated anti-mouse antibody was used as a secondary antibody and no counterstain was employed. The sections were observed with a Zeiss Fluar 2.5X/0.12 na lens on an Axioskop 2 Plus microscope. Images were processed and analyzed on AxioVision 4.7 (ZEISS) and further processed with Adobe Photoshop CS6.

4.2.11 CA125 serum levels: A CA125 (Human) ELISA kit (Abnova, KA0205) was used to analyze CA125 levels in xenograft mouse serum. The kit is based on the principle of solid-phase enzyme-linked immunosorbent assay. Analysis was performed according to the manufacturer's instructions.

4.2.12 Statistical Analysis:

All data are expressed as means ± SEM. Graphs were constructed using GraphPad Prism 4.0 (GraphPad Software). Where applicable, statistical differences were tested by un-paired Student's t-test and were considered significant for $p < 0.05$.

4.3 Results

4.3.1 Isolation, characterization and modification of CA125 targeting vectors:

CA125 targeting vectors were purified in yields of 6 mg/L for MAb-B43.13 and 0.7 mg/L for the scFv (Fig. 4.1A). Analysis by western blot (Fig. 4.1B) and immunofluorescence staining (Fig. 4.2) ascertained the following: a) expression of CA125 in NIH:OVCAR-3 cells; b) absence of CA125 expression in SKOV3 cells; c) binding of MAb and scFv to target antigen CA125. Isothiocyanate-based labeling of anti-CA125 MAb and scFv with fluorescein yielded 2 moles of FITC per mole of MAb and scFv. Flow cytometry analysis with FITC-labeled MAb-B43.13 and scFv-B43.13 demonstrated preserved immunoreactivity by binding to CA125 antigen expressed on the membrane of NIH:OVCAR-3 cells (Fig. 4.3). FITC-labeled anti-CA125 MAb remained membrane bound over a period of 48 h with minimal cellular internalization observed upon incubation with NIH:OVCAR-3 cells maintained in culture over the period of analysis (Fig. 4.4).

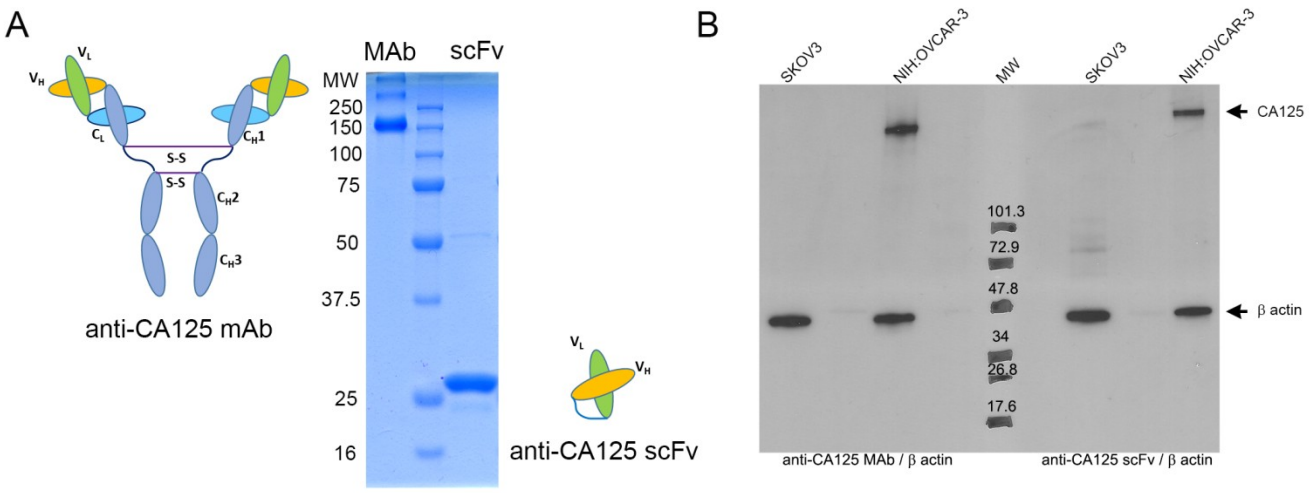

Figure 4.1: Purification and biochemical characterization of anti-CA125 MAb and scFv. **A)** Representative images of purified anti-CA125 MAb (148 KDa) and scFv (28 KDa) upon SDS-PAGE under non-reducing conditions. **B)** Western blots of SKOV3 (CA125-negative) and NIH:OVCAR-3 (CA125-positive) cells with anti-CA125 MAb, and anti-β actin antibody (*left half of blot*); anti-CA125 scFv and anti-β actin antibody (*right half of blot*).

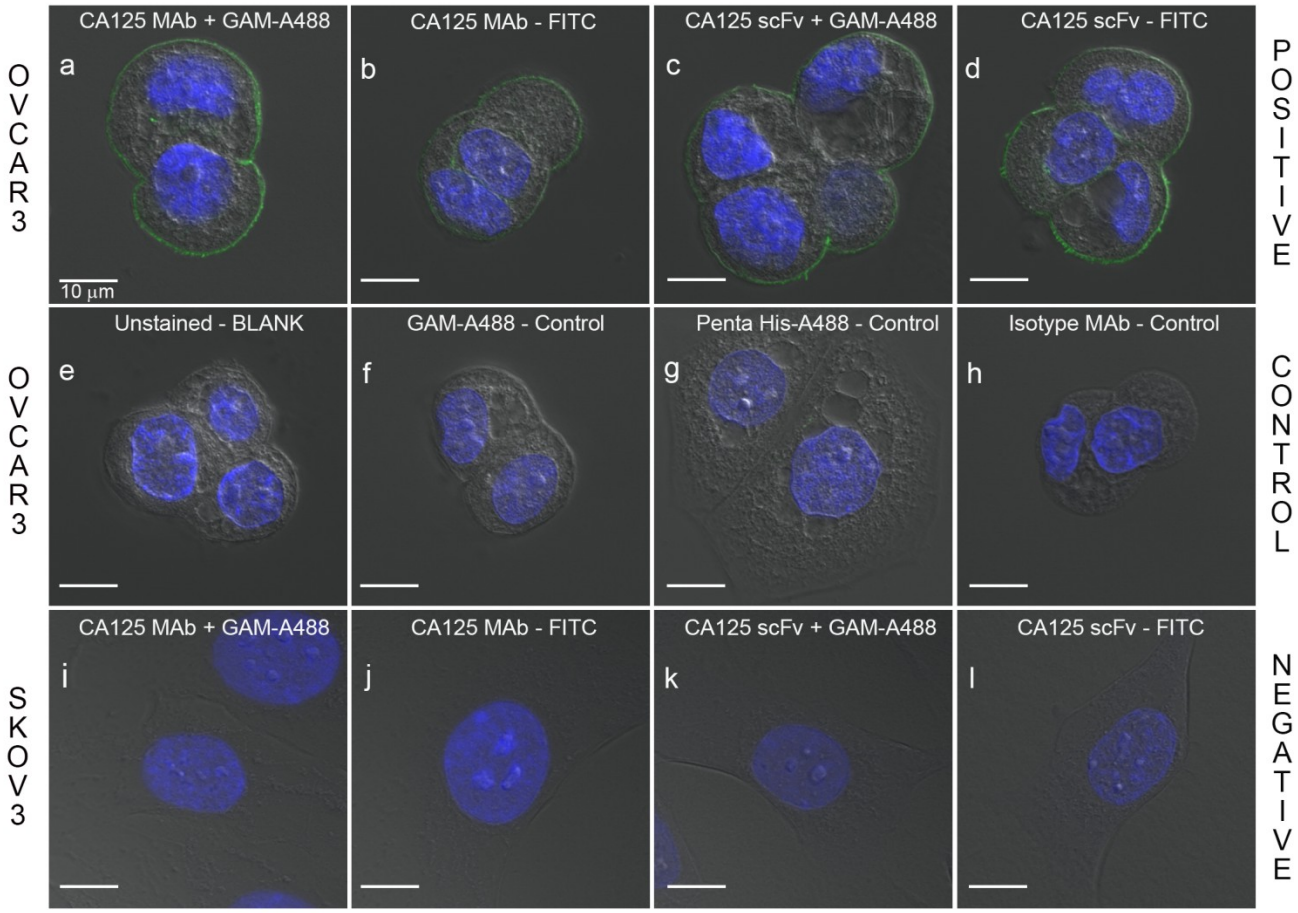

Figure 4.2: Functional characterization of anti-CA125 vectors. Confocal microscopy images of immunofluorescence studies; **a-b**) NIH:OVCAR-3 cells stained with unlabeled versus FITC-labeled anti-CA125 MAb. Goat anti-mouse Alexa fluor 488 IgG (GAM-A488) was used as secondary antibody; **c-d**) NIH:OVCAR-3 cells stained with unlabeled versus FITC-labeled anti-CA125 scFv. Penta-His Alexa fluor 488 antibody was used as secondary antibody; **e**) Unstained NIH:OVCAR-3 cells (Blank); **f**) NIH:OVCAR-3 cells stained with GAM-A488 antibody (Negative control); **g**) NIH:OVCAR-3 cells stained with Penta-His Alexa fluor 488 antibody (Negative control); **h**) NIH:OVCAR-3 cells stained with MAb 12A1 and GAM-A488 antibody (Isotype control); **i-j**) SKOV3 cells stained with unlabeled versus FITC-labeled anti-CA125 MAb; **k-l**) SKOV3 cells stained with unlabeled versus FITC-labeled anti-CA125 scFv. Scale bar represents 10 μm.

A

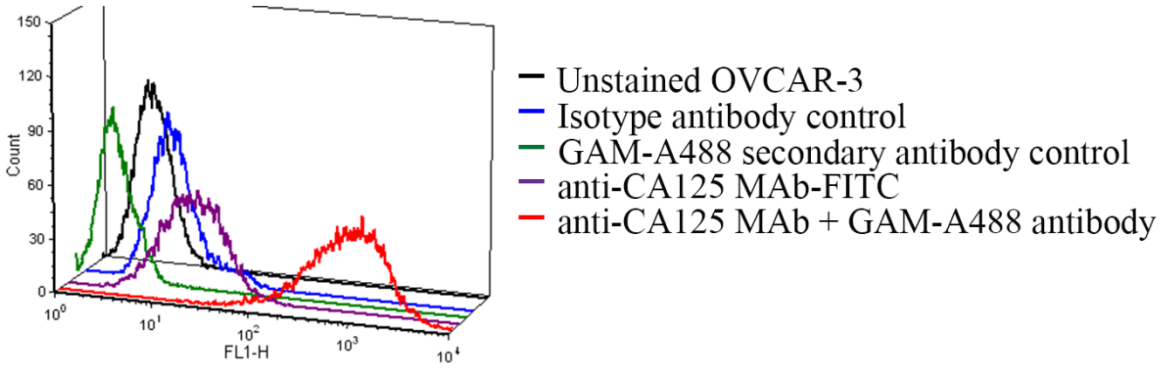

B

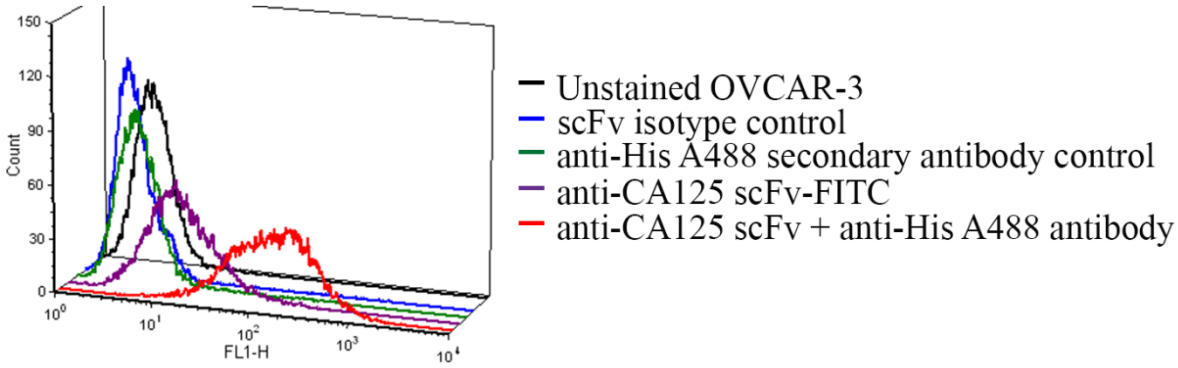

Figure 4.3: Functional characterization of anti-CA125 MAb and scFv. Flow cytometry analysis of **A)** anti-CA125 MAb; **B)** anti-CA125 scFv with NIH:OVCAR-3 cells.

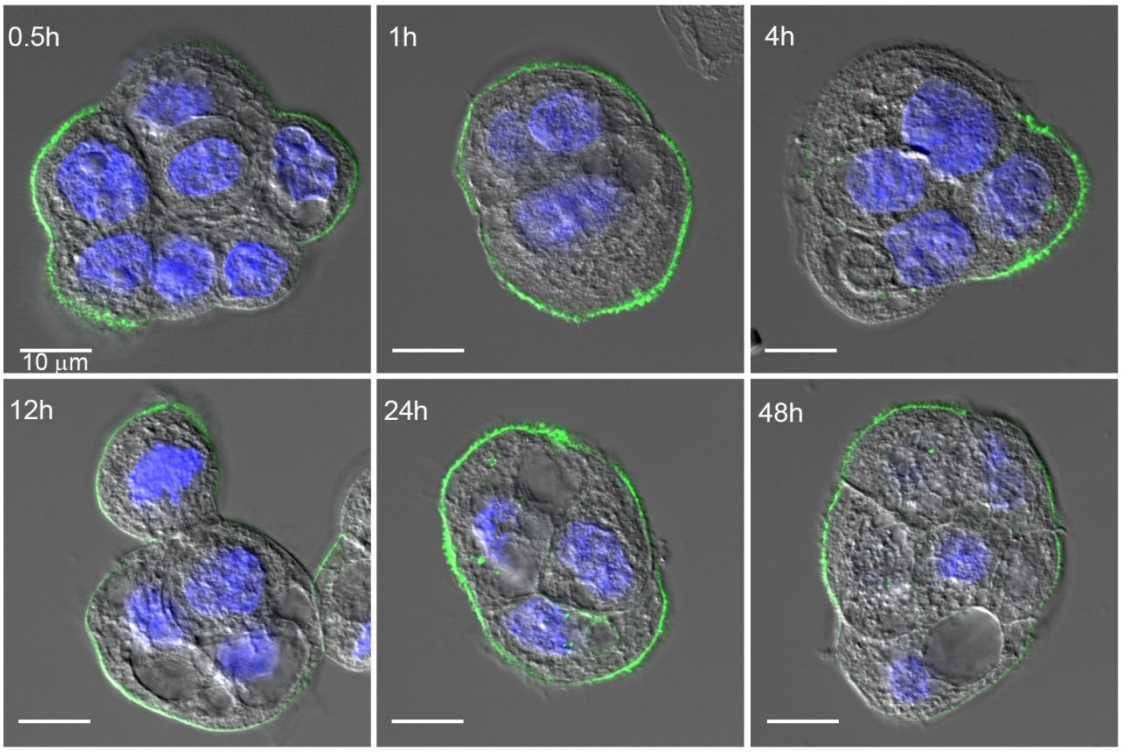

Figure 4.4: Antibody internalization assay: Confocal microscopy images of NIH:OVCAR-3 cells stained with FITC-labeled MAb-B43.13. Minimal internalization of anti-CA125 antibody was observed over a period of 48 h.

4.3.2 Development and functional assessment of CA125 targeting radioimmunoconjugates:

MALDI-ToF analyses and isotopic dilution assays revealed an average of 2.4 NOTA molecules conjugated per MAb and 1.9 NOTA molecules conjugated per scFv (Figs. 4.5 and 4.6). ^{64}Cu-labeling and purification of radioimmunoconjugates provided isolated radiochemical yields of 65 ± 8 % (n= 14) with specific activity of 296 ± 37 MBq/mg for ^{64}Cu-NOTA-MAb-B43.13 and 56 ± 14 % (n= 9) with specific activity of 122 ± 44 MBq/mg for ^{64}Cu-NOTA-scFv-B43.13. Radiochemical purity of the isolated radioimmunoconjugates was > 99% as analyzed from phosphorimages of electrophoresed fractions (Figs. 4.8) and ITLC (Fig. 4.9). SEC-purified ^{64}Cu-NOTA-MAb-B43.13 was > 95% stable in human AB type serum over 48 h (Fig 4.10) and demonstrated highly specific binding to CA125 expressed on NIH:OVCAR-3 cells with virtually no binding to SKOV3 cells as evaluated by cell uptake studies (Figs 4.11A and 4.11B). Immunoreactivity of ^{64}Cu-NOTA-MAb-B43.13 and ^{64}Cu-NOTA-scFv-B43.13 preparations was found to be > 90% as obtained from the inverse of the intercept of plots (Figs. 4.12A and 4.12B respectively). ^{64}Cu-NOTA-MAb-B43.13 displayed negligible trans-chelation of the radiometal from the radioimmunoconjugate (Fig. 4.13).

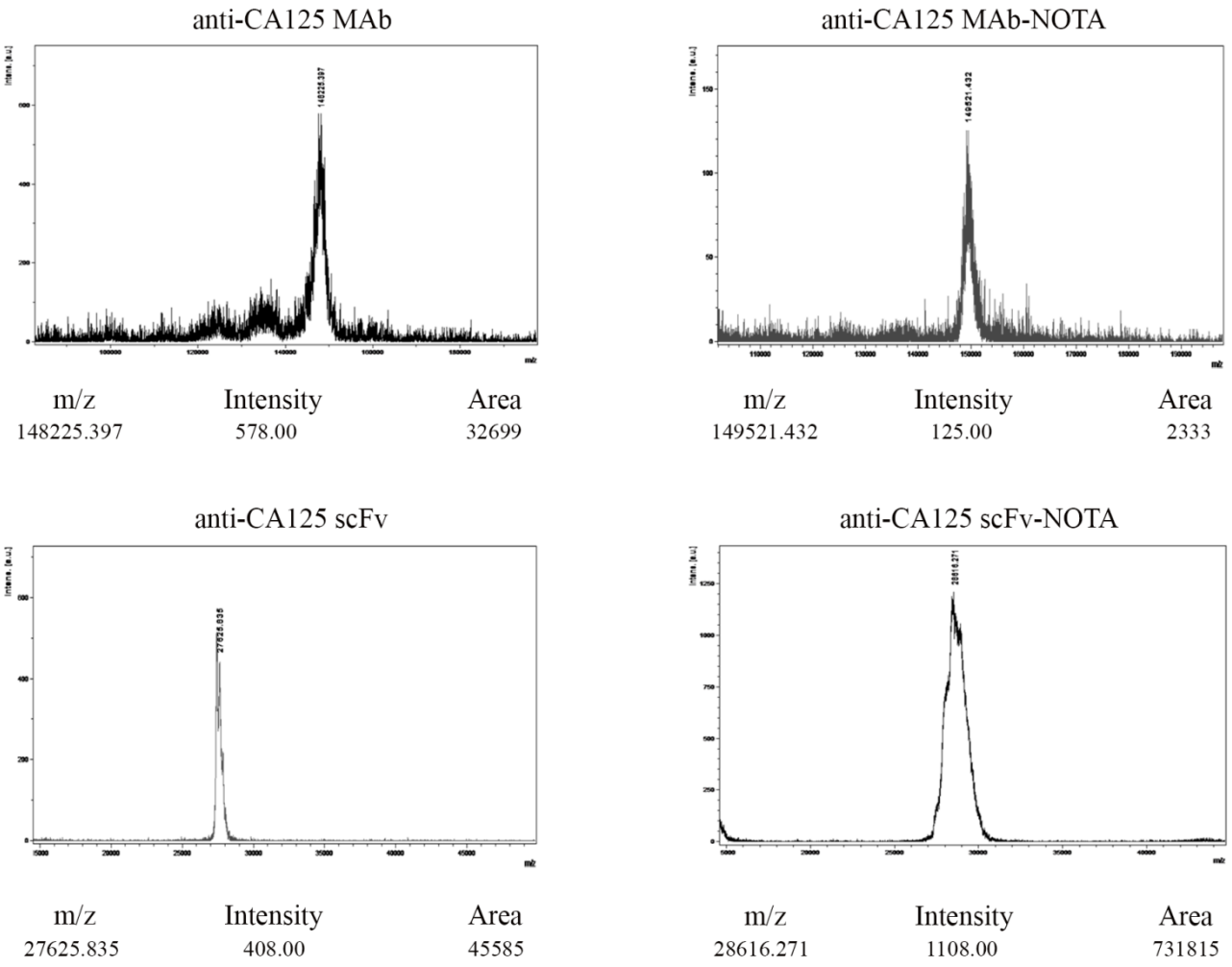

Figure 4.5: Determination of number of bi-functional chelators per anti-CA125 vector. Chromatograms from MALDI-ToF analysis of MAb-B43.13 and scFv-B43.13 (left) versus their NOTA conjugated counterparts (right). The number of NOTA molecules conjugated per MAb/scFv was calculated by dividing the difference between the masses of the NOTA-conjugated version and plain MAb or scFv by the molecular weight of NOTA (559.9 Da).

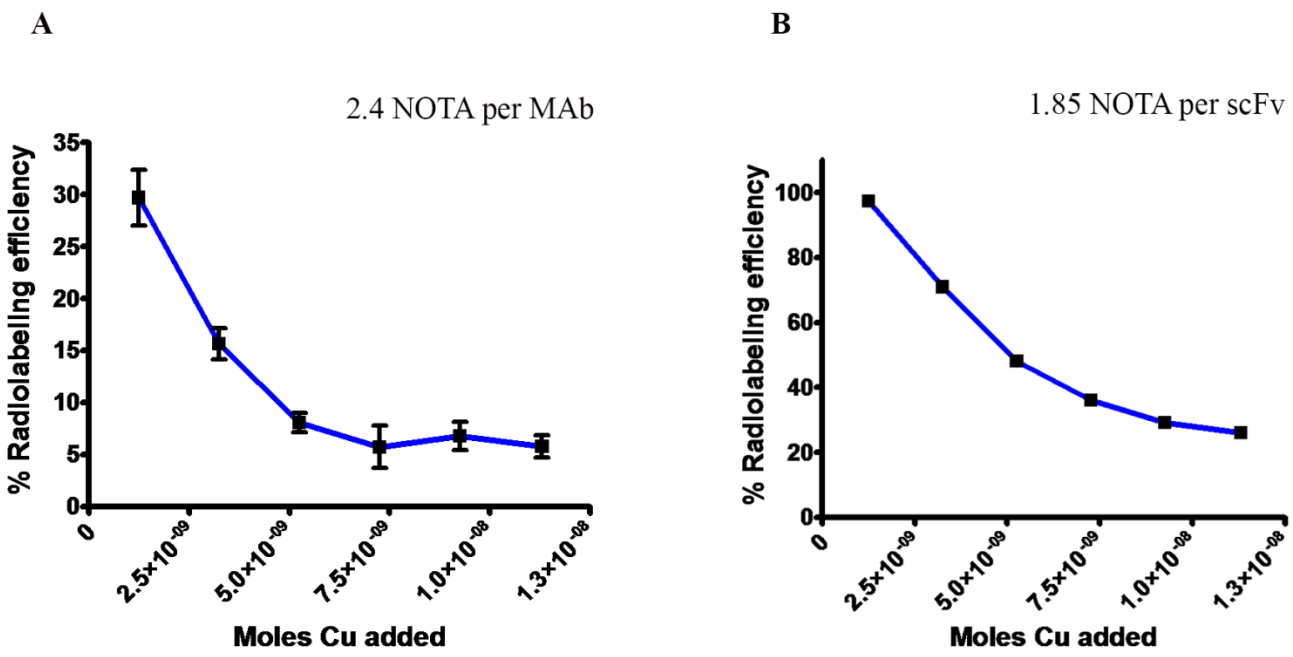

Figure 4.6: Determination of the number of bi-functional chelators (BFCs) per **A)** MAb-B43.13 and **B)** scFv-B43.13 by radiometric isotopic dilution method. This was determined by plotting the radiolabeling efficiencies obtained using different concentrations of ^{64}Cu and immunoconjugate. The percentage (%) radiolabeling efficiency was used to indirectly derive the number of moles of ^{64}Cu chelated to the immunoconjugate by knowing the number of moles of ^{64}Cu added initially. The moles of ^{64}Cu chelated are divided by the (fixed) moles of MAb-B43.13 (0.25 nmols) or scFv-B43.13 (1.285 nmols) added per radiolabeling reaction. Finally, the average ratio across different concentrations is considered as the number of BFCs conjugated per MAb-B43.13 or scFv-B43.13 molecule.

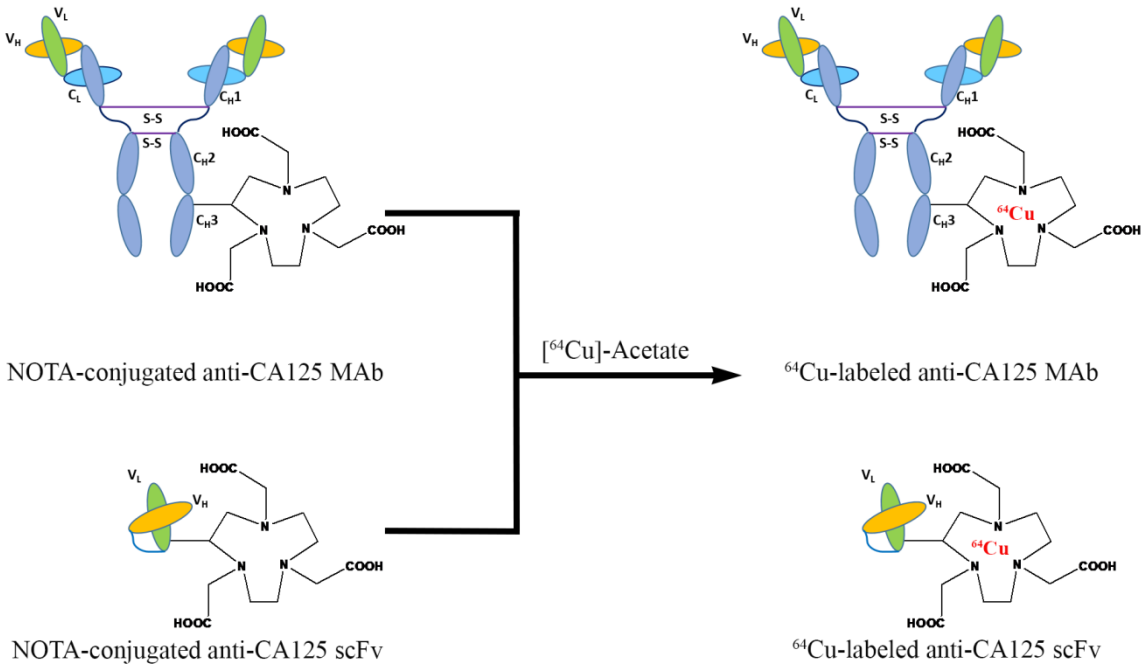

Figure 4.7: Diagrammatic representation for ^{64}Cu-labeling of NOTA-MAb-B43.13 and NOTA-scFv-B43.13

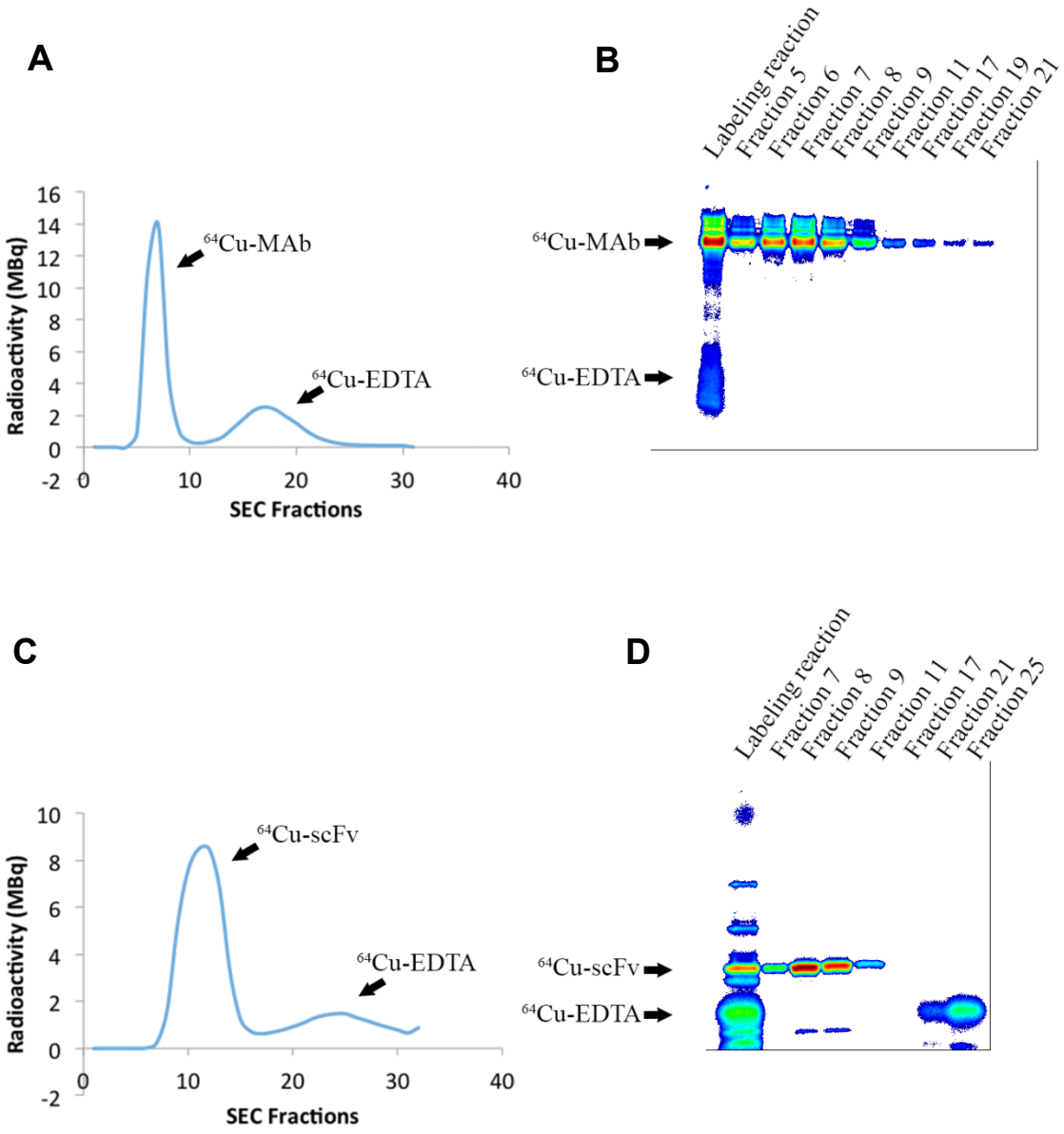

Figure 4.8: Quality control for purification of ^{64}Cu-radioimmunoconjugates. **A)** Histograms for size exclusion purification of ^{64}Cu-NOTA-MAb-B43.13; **B)** Phosphorimage of SEC-purified ^{64}Cu-NOTA-MAb-B43.13 fractions upon SDS-PAGE; **C)** Histograms for size exclusion purification of ^{64}Cu-NOTA-scFv-B43.13; **D)** Phosphorimage of SEC-purified ^{64}Cu-NOTA-MAb-B43.13 fractions upon SDS-PAGE**.**

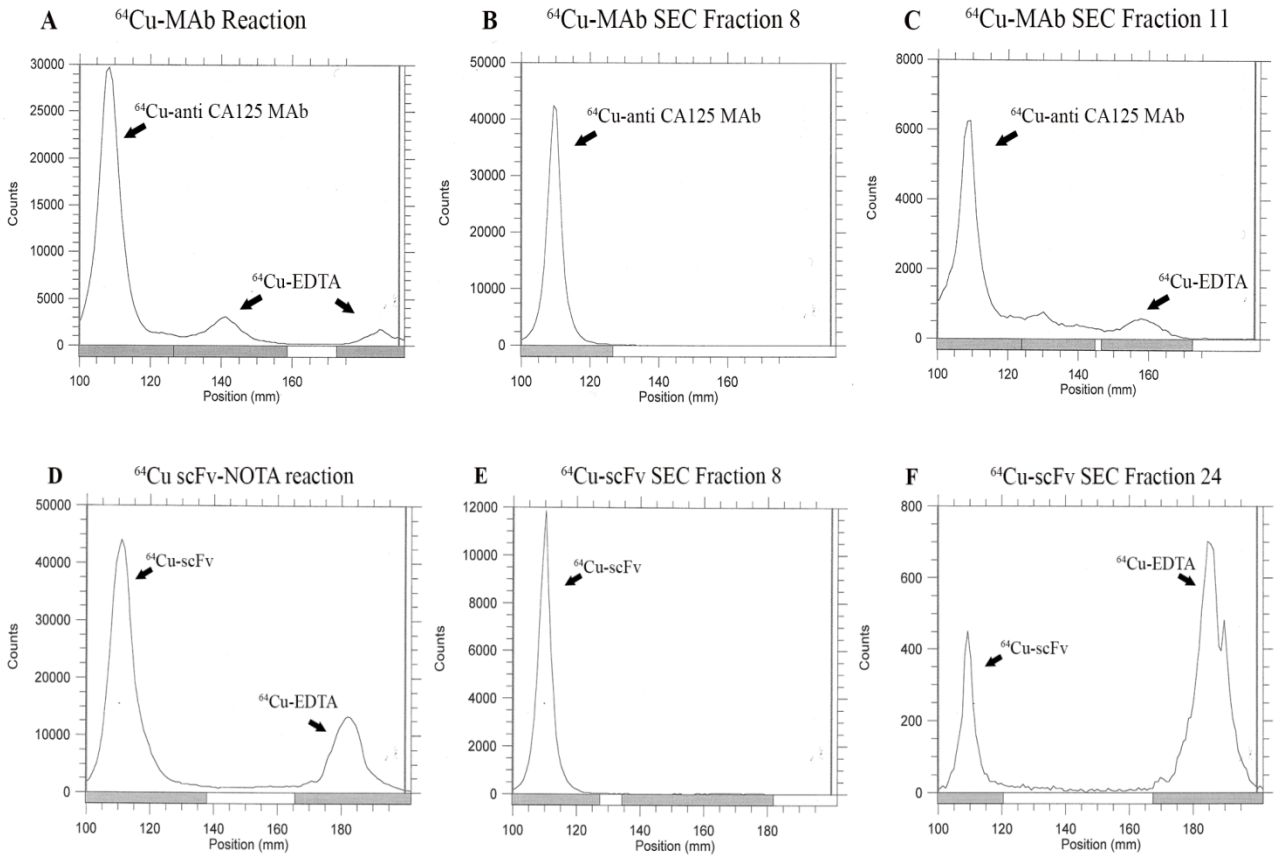

Figure 4.9: Quality control Radio-TLCs of **A)** crude reaction mixture from ^{64}Cu-labeling of NOTA-MAb-B43.13; **B)** Fraction 8 from SEC-purified ^{64}Cu-NOTA-MAb-B43.13; **C)** Fraction 11 from SEC-purified ^{64}Cu-NOTA-MAb-B43.13; **D)** crude reaction mixture from ^{64}Cu-labeling of NOTA-scFv-B43.13; **E)** Fraction 8 from SEC-purified ^{64}Cu-NOTA-scFv-B43.13; **F)** Fraction 24 from SEC-purified ^{64}Cu-NOTA-scFv-B43.13. The antibody-based radioimmunoconjugate construct remains at the baseline (extreme left of the TLC plate), while ^{64}Cu ions and [^{64}Cu]-EDTA elute with the solvent front (far right side of each TLC plate).

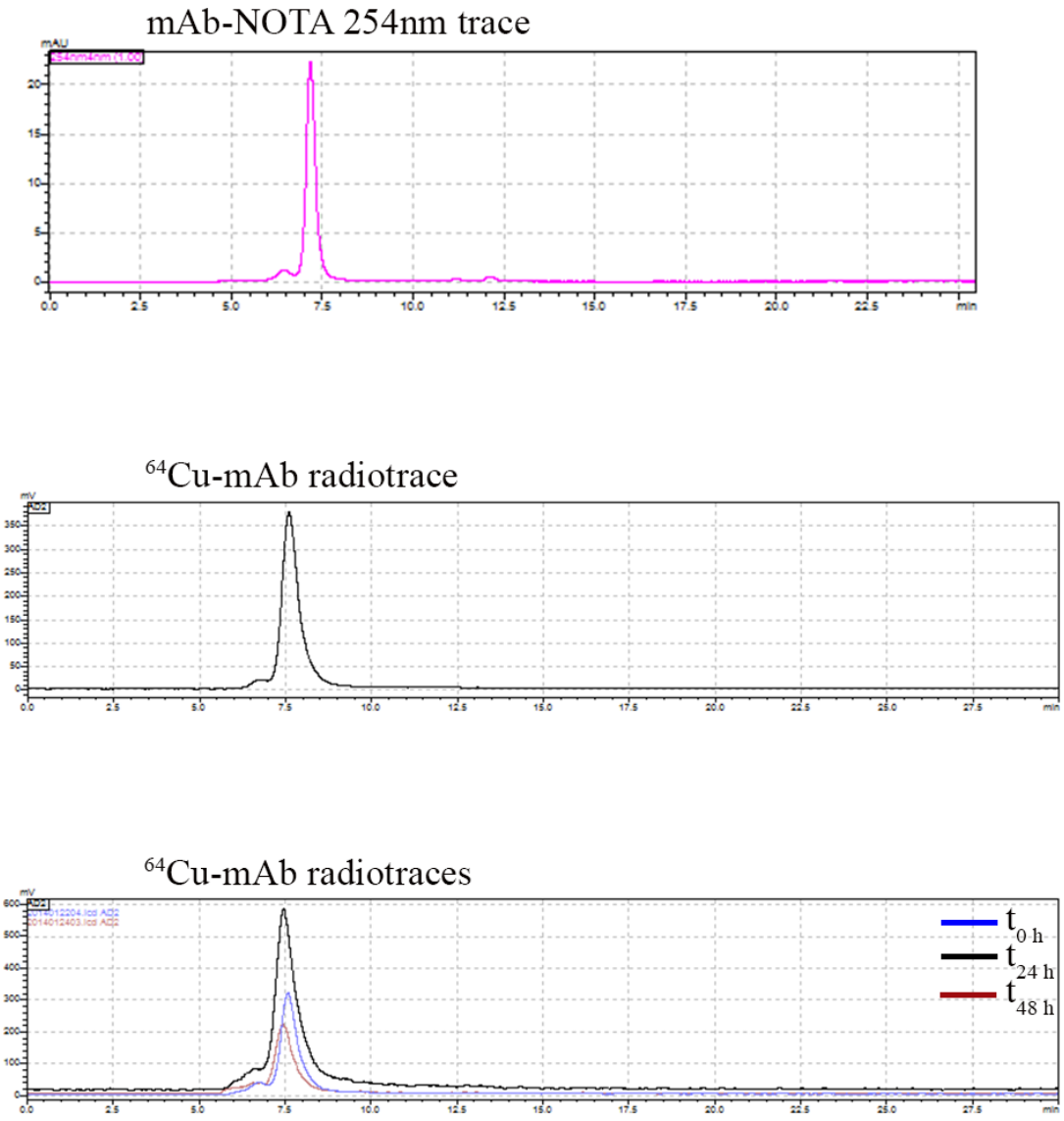

Figure 4.10: Quality control and stability study of purified ^{64}Cu-NOTA- MAb B43.13 radioimmunoconjugate. **A)** Analytical HPLC UV-trace of NOTA-MAb-B43.13; **B)** Radio-HPLC trace of ^{64}Cu-NOTA-MAb-B43.13 at t=0 h; **C)** Overlay of radio-HPLC traces of ^{64}Cu-NOTA-MAb-B43.13 at t=0 h, 24 h and 48 h to analyze any degradation or loss of ^{64}Cu from the radioimmunoconjugate upon incubation in serum for the indicated periods of analysis.

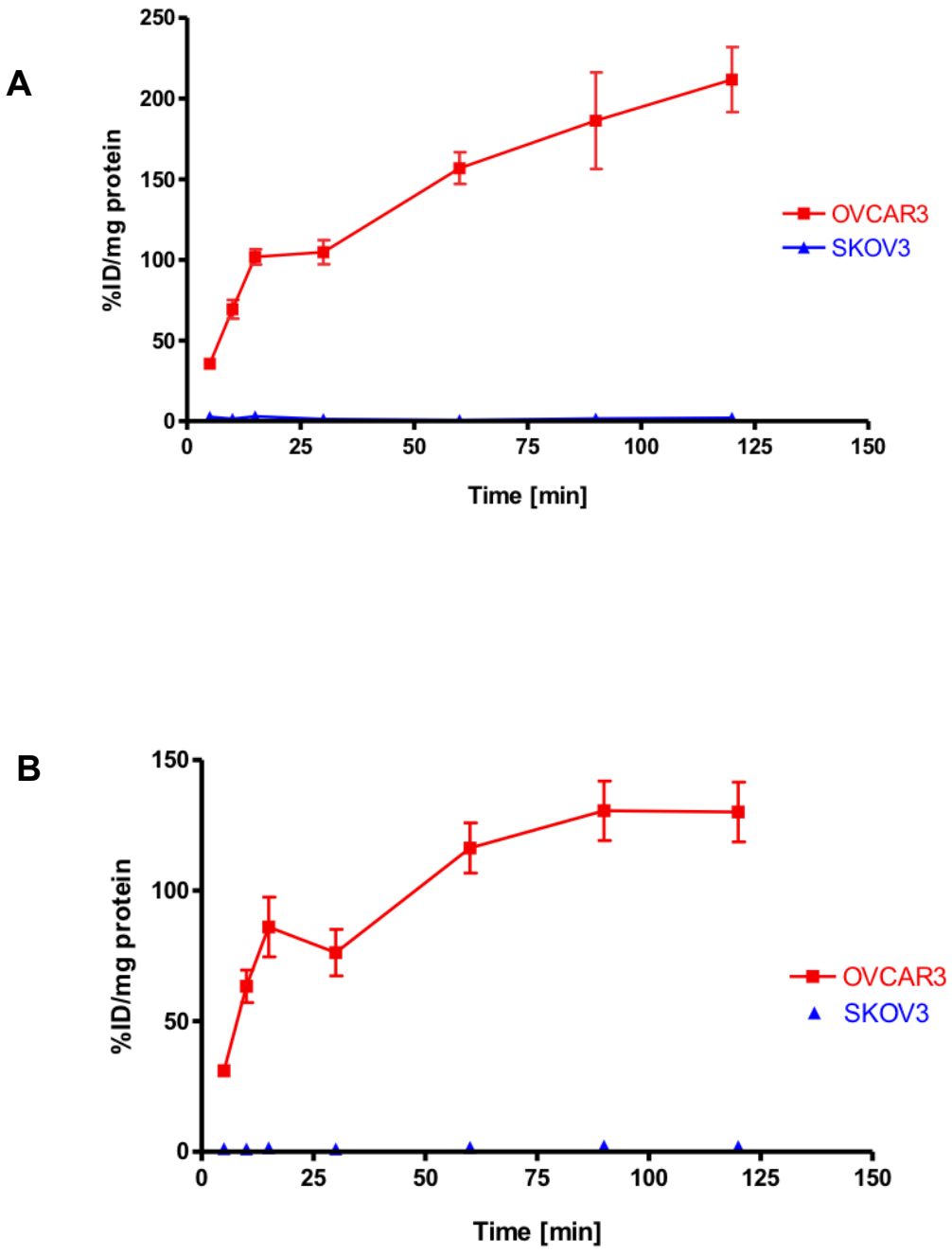

Figure 4.11: *In vitro* analysis of purified ^{64}Cu-radioimmunoconjugates. Representative graphs for cell uptake of **A)** ^{64}Cu-NOTA- MAb B43.13 and **B)** ^{64}Cu-NOTA-scFv-B43.13 in NIH:OVCAR-3 and SKOV3 cells.

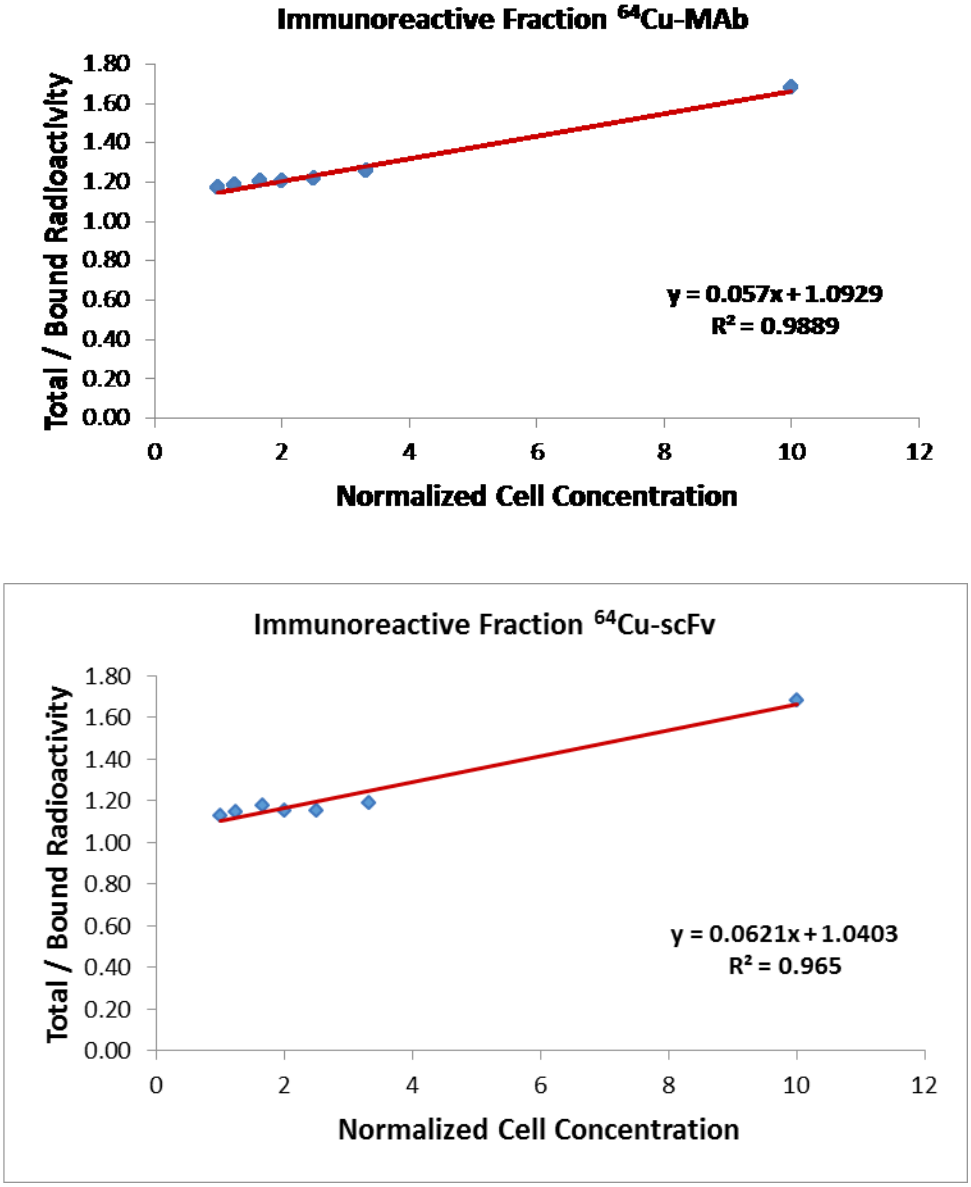

Figure 4.12: Immunoreactivity Test. **A)** Representative double inverse plots from Lindmo assays performed with ^{64}Cu-NOTA-MAb-B43.13 and **B)** ^{64}Cu-NOTA-scFv-B43.13 in NIH:OVCAR-3 cells. The immunoreactive fraction is calculated by multiplying the inverse of the intercept on these plots with 100. (Eg: ^{64}Cu-NOTA-MAb-B43.13 IR% = (1/1.0929) x 100 = 91.5%)

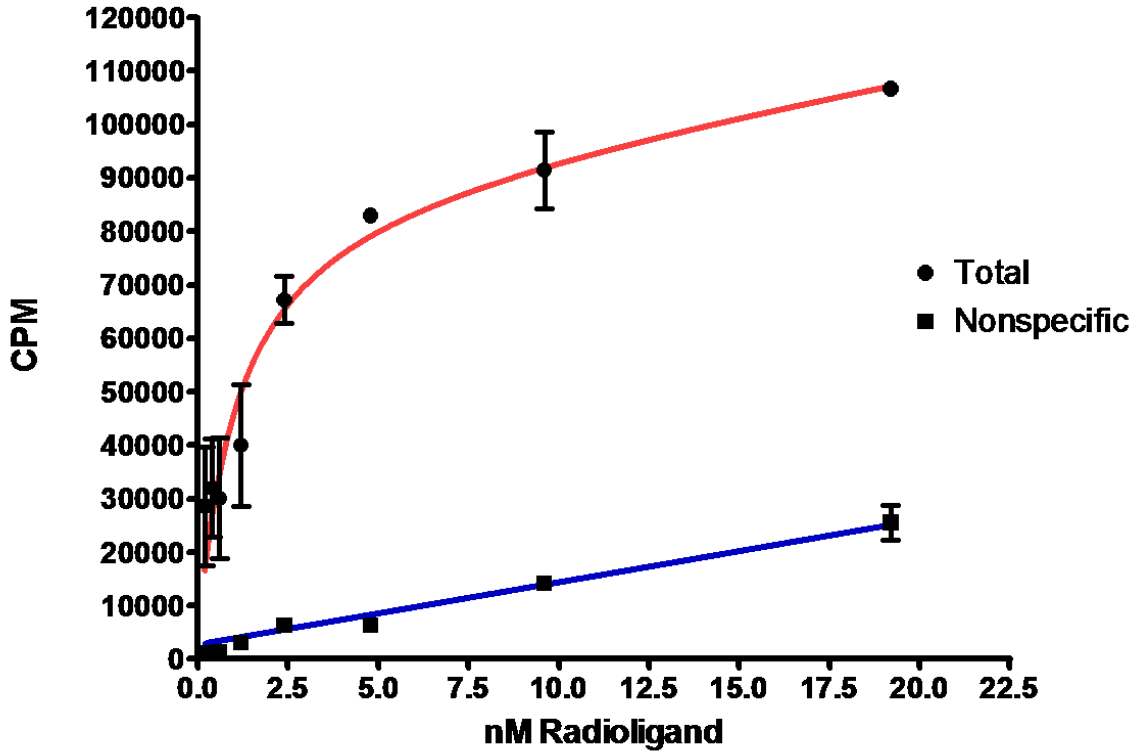

Figure 4.13: Biochemical characterization of CA125 binding sites and the binding affinity of anti-CA125 MAb. Graph of non-linear regression fit analysis of data from saturation binding study to determine affinity constant (K_D) of ^{64}Cu-NOTA-MAb-B43.13 and maximum number of antigen sites (B_{max}) on NIH:OVCAR-3 cells. The K_D was calculated to be 1.066 x 10^{-9} M and the B_{max} was 86,591.

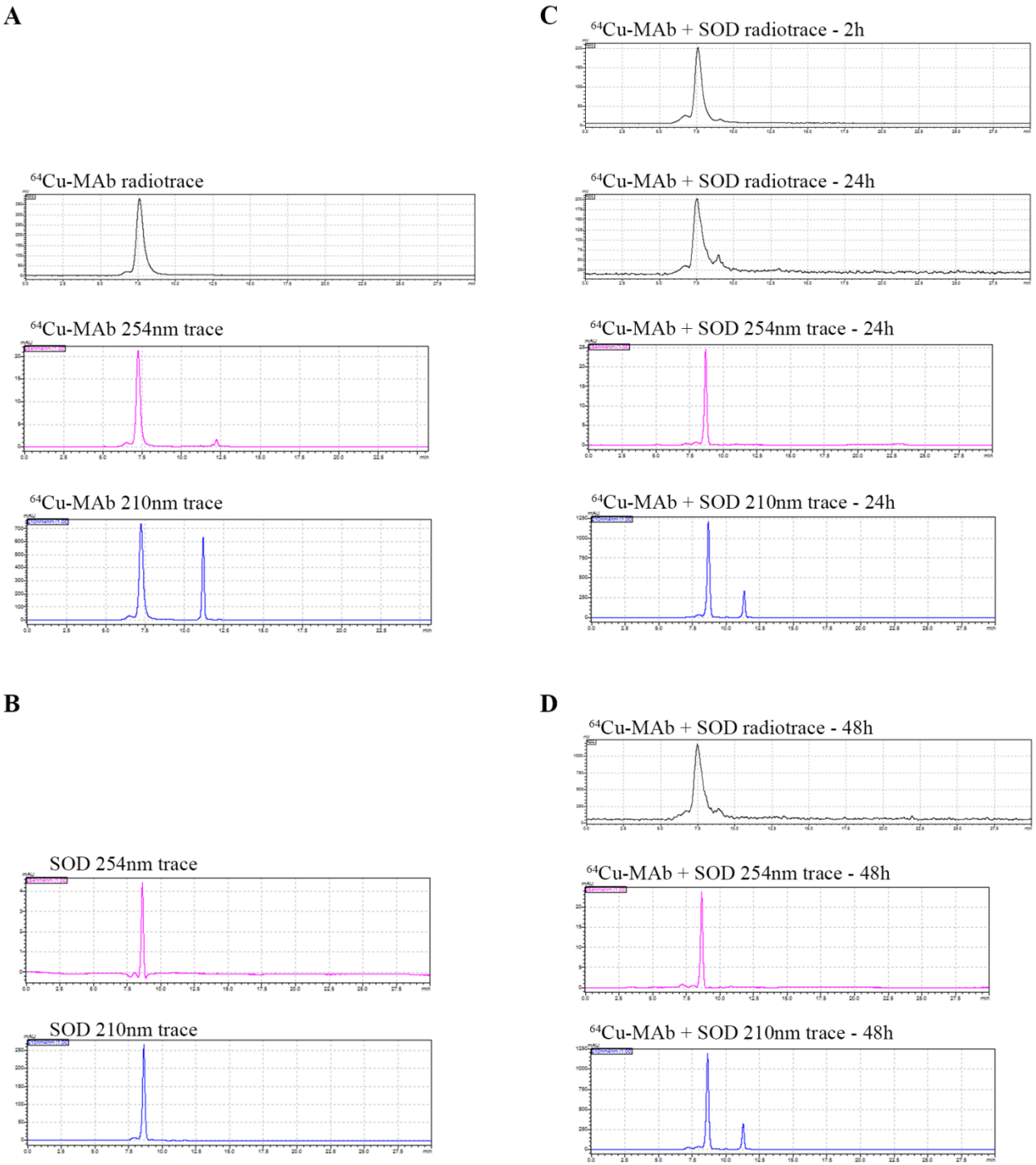

Figure 4.14: Quality control and trans-chelation analysis of ^{64}Cu-NOTA-MAb-B43.13. Analytical Radio and UV-traces from size exclusion HPLC showing elution profile and retention times for **A)** ^{64}Cu-NOTA-MAb-B43.13; **B)** UV-traces for Superoxide

Dismutase (SOD); **C)** ^{64}Cu-NOTA-MAb-B43.13 challenged with excess SOD to evaluate trans-chelation of ^{64}Cu after incubation in 0.25M sodium acetate for 24 h; **D)** ^{64}Cu-NOTA-MAb-B43.13 challenged with excess SOD to evaluate trans-chelation of ^{64}Cu after incubation in 0.25M sodium acetate for 48 h.

4.3.3 *In vivo* experiments and radiopharmacological evaluation:

PET imaging studies performed using ^{64}Cu-NOTA-MAb-B43.13 and using ^{64}Cu-NOTA-scFv-B43.13 in NIH:OVCAR-3 and SKOV3 tumor-bearing mice as well as experiments with ^{64}Cu-labeled isotype IgG and [^{18}F]FDG are summarized in Fig. 4.15. In NIH:OVCAR-3 tumors, ^{64}Cu-NOTA-MAb-B43.13 reached maximum SUV_{mean} of 5.76 ± 0.85 at 24 h post injection (p.i), which rose to 7.06 ± 0.67 at 48 h p.i (n=4). NIH:OVCAR-3 xenograft mice pre-dosed with unlabeled MAb revealed a SUV_{mean} of 2.90 ± 0.45 at 24 h p.i (n=4, $p<0.05$) and 3.96 ± 0.76 at 48 h p.i (n=4, $p<0.05$). Non-specific tumor uptake using ^{64}Cu-labeled isotype IgG was found to have SUV_{mean} of 1.77 ± 0.44, at 24 h p.i (n=3, $p<0.05$) with no further change at 48 h p.i. A SUV_{mean} of 1.80 ± 0.69, 24 h p.i (n=5, $p<0.01$ vs. uptake in OVCAR3 24 h p.i) was observed in SKOV3 tumors. In contrast, PET studies using ^{64}Cu-labeled anti-CA125 scFv in xenograft mice revealed SUV_{mean} of 0.64 ± 0.04, 24 h p.i (n=3) in NIH:OVCAR-3 tumors and 0.25 ± 0.11 (n=3, $p<0.05$) in SKOV3 tumors.

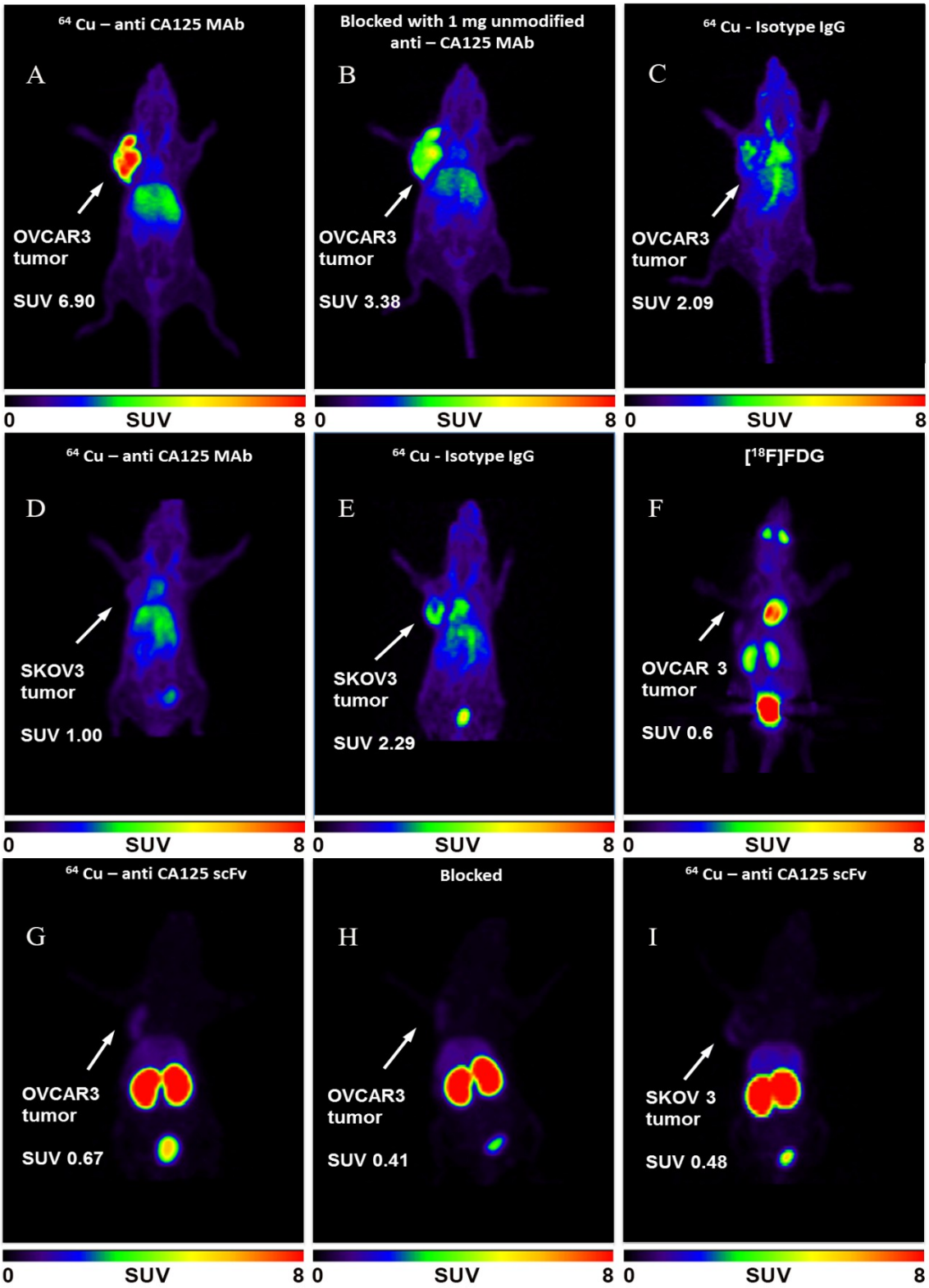
64 Cu – anti CA125 MAb
A
OVCAR3 tumor
SUV 6.90
Blocked with 1 mg unmodified anti – CA125 MAb
B
OVCAR3 tumor
SUV 3.38
64 Cu - Isotype IgG
C
OVCAR3 tumor
SUV 2.09
0 SUV 8
64 Cu – anti CA125 MAb
D
SKOV3 tumor
SUV 1.00
64 Cu - Isotype IgG
E
SKOV3 tumor
SUV 2.29
[18F]FDG
F
OVCAR 3 tumor
SUV 0.6
0 SUV 8
64 Cu – anti CA125 scFv
G
OVCAR3 tumor
SUV 0.67
Blocked
H
OVCAR3 tumor
SUV 0.41
64 Cu – anti CA125 scFv
I
SKOV 3 tumor
SUV 0.48
0 SUV 8

Figure 4.15: *In vivo* small animal PET analysis of radioimmunoconjugates. **A-E** and **G-I)** Representative 24 h post injection (p.i) small animal-PET images of xenograft mice injected with anti-CA125 radioimmunoconjugates. **F)** 1 h p.i PET image of NIH:OVCAR-3 xenograft mouse injected with ^{18}F-FDG. Color intensity scale bars represent Standardized Uptake Value (SUV) of radiotracer in animals. Standardized uptake values [SUV = (activity/mL tissue) / (injected activity/body weight), mLg^{-1}]

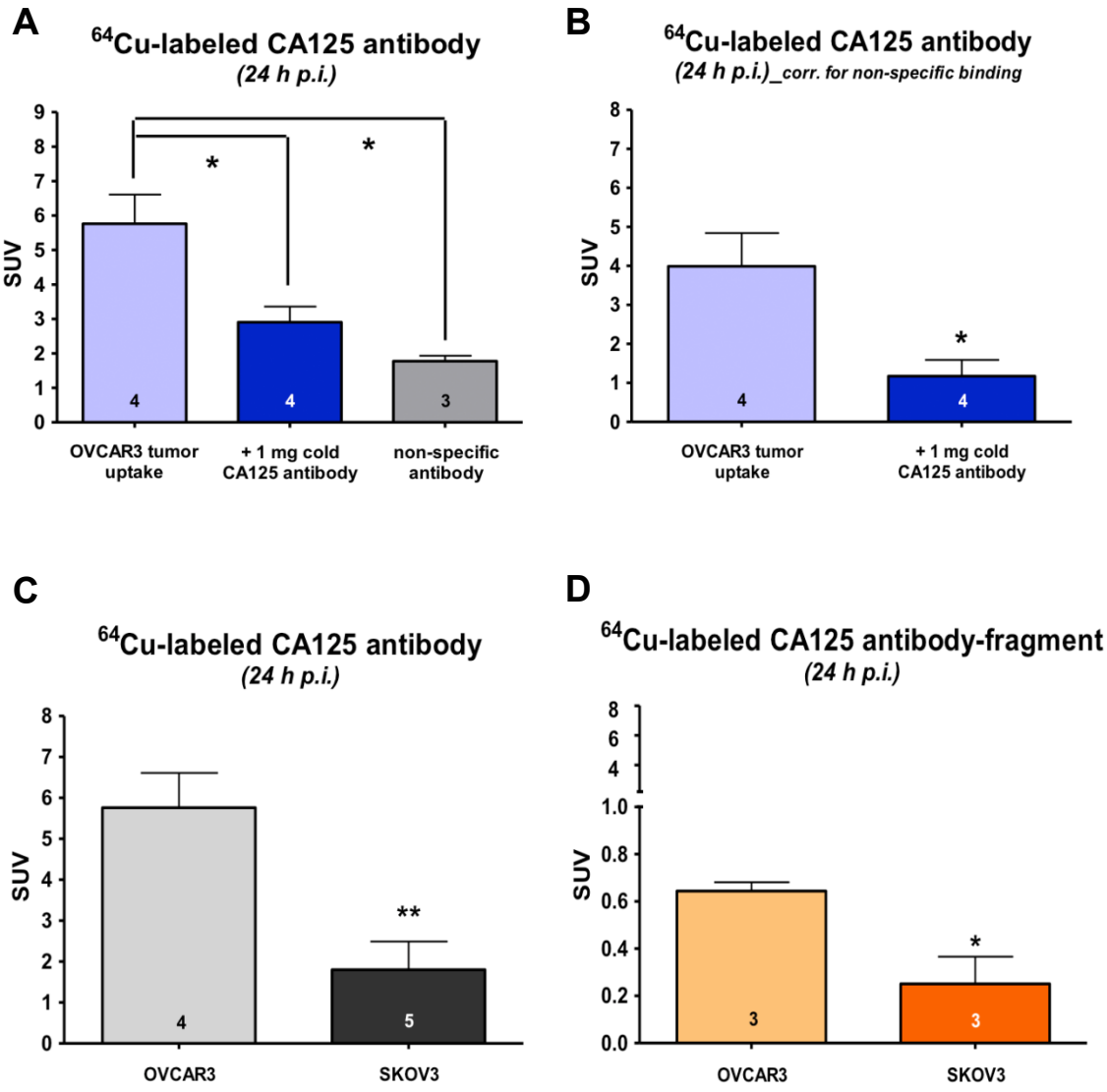

Figure 4.16: *In vivo* analysis for uptake of radioimmunoconjugates. Bar diagram representation of **A)** SUV of ^{64}Cu-NOTA-MAb-B43.13 in NIH:OVCAR-3 tumors of experimental and control animals. **B)** SUV ^{64}Cu-NOTA-MAb-B43.13 in NIH:OVCAR-3 tumors after correction for non-specific uptake. **C)** Comparative tumor SUV of ^{64}Cu-NOTA-MAb-B43.13 in NIH:OVCAR-3 versus SKOV3 xenograft mice. **D)** SUV of ^{64}Cu-NOTA-scFv-B43.13 in NIH:OVCAR-3 versus SKOV3 xenograft mice. The number of animals (n) per analysis are indicated at the bottom of each bar.

Overall, *in vivo* clearance of the radioimmunoconjugates was evaluated from the heart (representing blood pool content), liver and kidneys (Fig 4.17). After 24 h, SUV_{mean} in the heart and liver of xenograft animals imaged with ^{64}Cu-labeled anti-CA125 MAb was found to be 2.40 ± 0.20 and 2.59 ± 0.20 (n=4) respectively. SUV_{mean} in the kidneys of these animals was 1.64 ± 0.09. In contrast, injection of ^{64}Cu-labeled anti-CA125 scFv led to SUV_{mean} (n=3) of 0.31 ± 0.06 in the heart, 0.98 ± 0.11 in the liver and 13.2 ± 1.2 in the kidneys after 24 h. This information demonstrated the different clearance profiles between the full-length antibody and the fragment. Muscle SUV_{mean} at 24 h p.i were comparable between injections of ^{64}Cu-labeled anti-CA125 MAb (0.46 ± 0.07; n=4), in blocked experiments (0.45 ± 0.05; n=4) and non-specific ^{64}Cu-isotype IgG (0.44 ± 0.04; n=3), respectively.

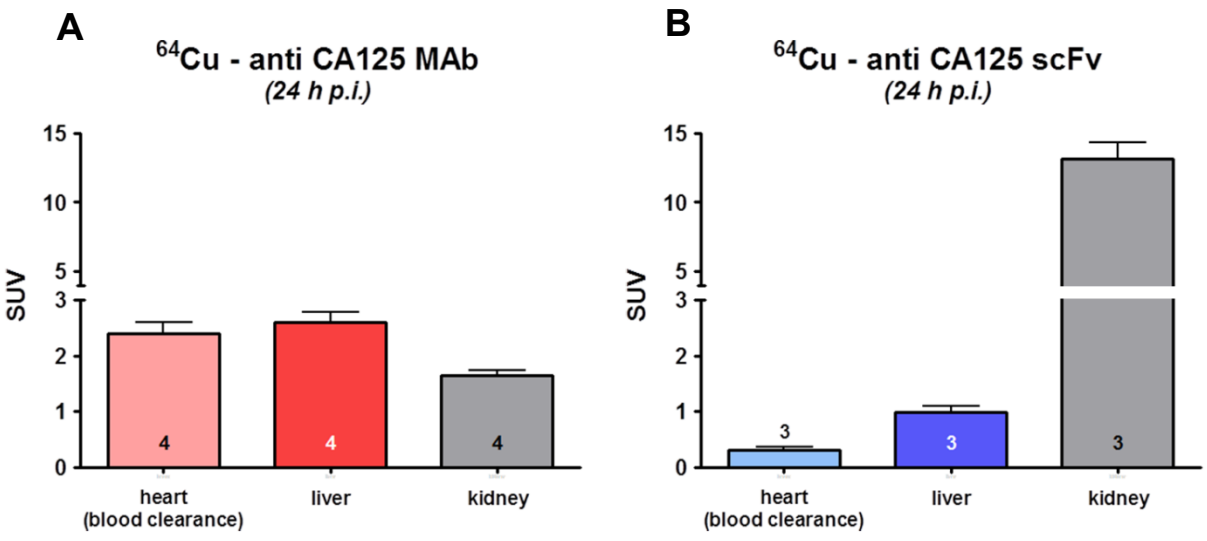

Figure 4.17: Uptake of radioimmunoconjugates in organs of clearance. Bar diagram representation of **A)** ^{64}Cu-NOTA-MAb-B43.13-associated radioactivity measured in vital organs – the heart, liver and kidneys at 24 h p.i; **B)** ^{64}Cu-NOTA-scFv-B43.13-associated radioactivity measured in vital organs – the heart, liver and kidneys at 24 h p.i.

Tumor-to-muscle ratios calculated at 24 h p.i for ^{64}Cu-labeled anti-CA125 MAb was found to be 13.07 ± 1.72 (n=4); 6.85 ± 1.73 (n=4) in animals used for blocking experiments and 4.12 ± 0.49 (n=3) in animals injected with isotype radioimmunoconjugate. (Fig. 4.18) Tumor-to-muscle ratios calculated at 24 h p.i for ^{64}Cu-labeled anti-CA125 scFv were found to be 5.03 ± 0.77 (n=3) and 4.41 (n=1) in the test and blocking experiments respectively.

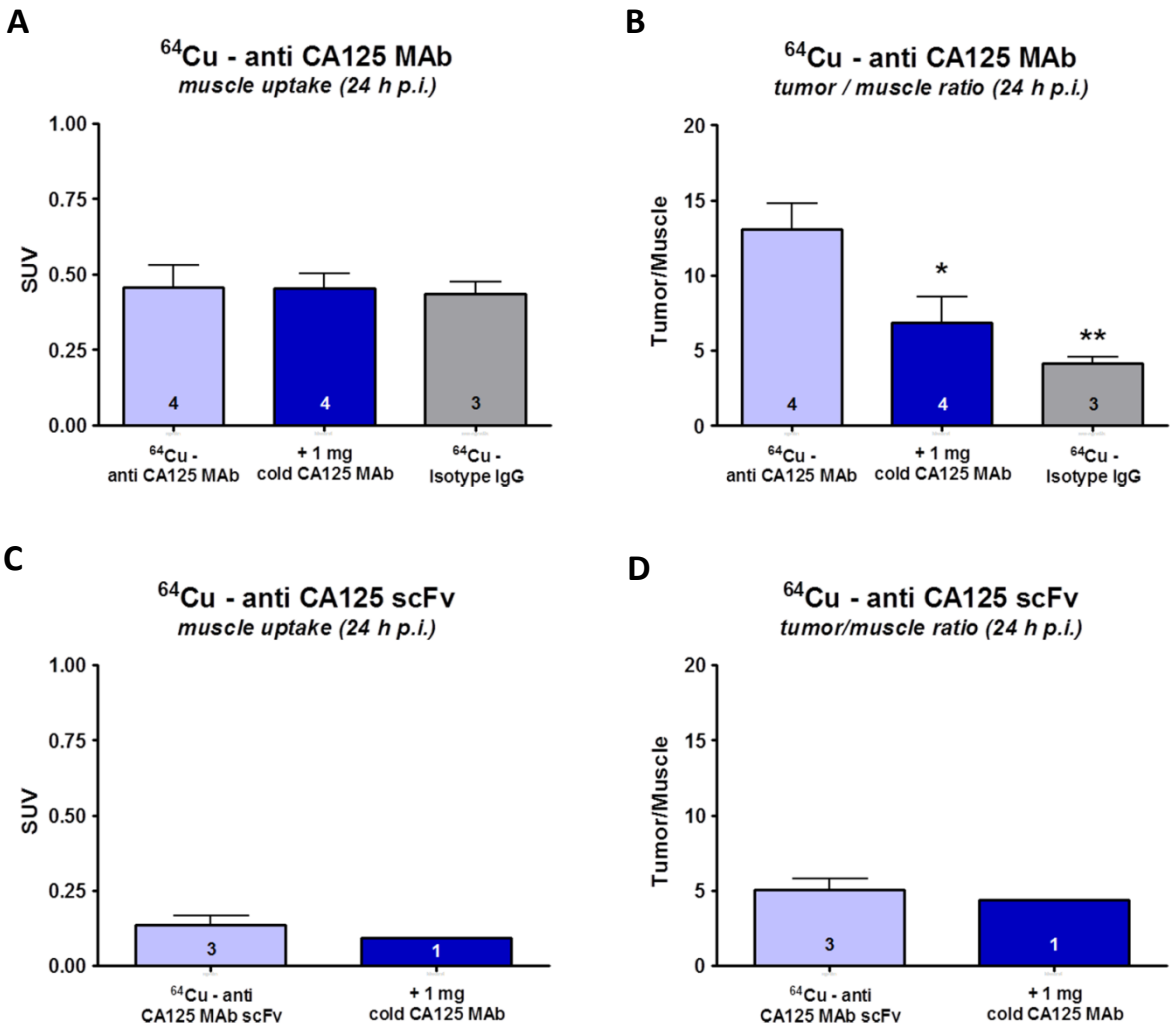

Figure 4.18: *In vivo* tumor-to-background ratios for ^{64}Cu-labeled anti-CA125 radioimmunoconjugates. Bar diagram representation for **A)** Muscle uptake of radioactivity in different NIH:OVCAR-3 bearing xenograft animal groups injected with ^{64}Cu-NOTA-MAb-B43.13 or ^{64}Cu-NOTA-isotype IgG; **B)** Corresponding tumor-to-muscle ratios obtained in the experimental and control groups shown in A); **C)** Muscle uptake of radioactivity in NIH:OVCAR-3 bearing xenograft animals injected with ^{64}Cu-NOTA-scFv-B43.13; **D)** Corresponding tumor-to-muscle ratios obtained in the experimental and control groups shown in C). The numbers of animals (n) per analysis are indicated at the bottom of each bar.

4.3.4 *Ex vivo* analysis:

The NIH:OVCAR-3 tumor tested positive for CA125 expression as seen from immunofluorescence and immunohistochemistry of tissue sections (Figs. 4.19A-F). Immunohistochemistry revealed necrotic and apoptotic regions spanned by connective tissue in the tumor's upper half. Overall, the lower half had more radioactive hot-spots, stained stronger for CA125 expression and had more vasculature surrounded by positively staining tumor foci, which collectively formed pockets of high signals. CA125 staining was observed on the surface of neoplastic cells in the tumor. Hot-spots representative of *in vivo* targeting by the radiotracer as seen in autoradiography of tumor slices correlated well with signals from the other two techniques. A good correlation of all three types of signals was observed in regions of tumor foci interspersed with blood vessels and/or supported by mouse connective tissue.

No CA125 was detected as circulating antigen in the serum of NIH:OVCAR-3 xenograft animals although cell culture supernatants of NIH:OVCAR-3 tested positive for presence of CA125 (Fig. 4.20).

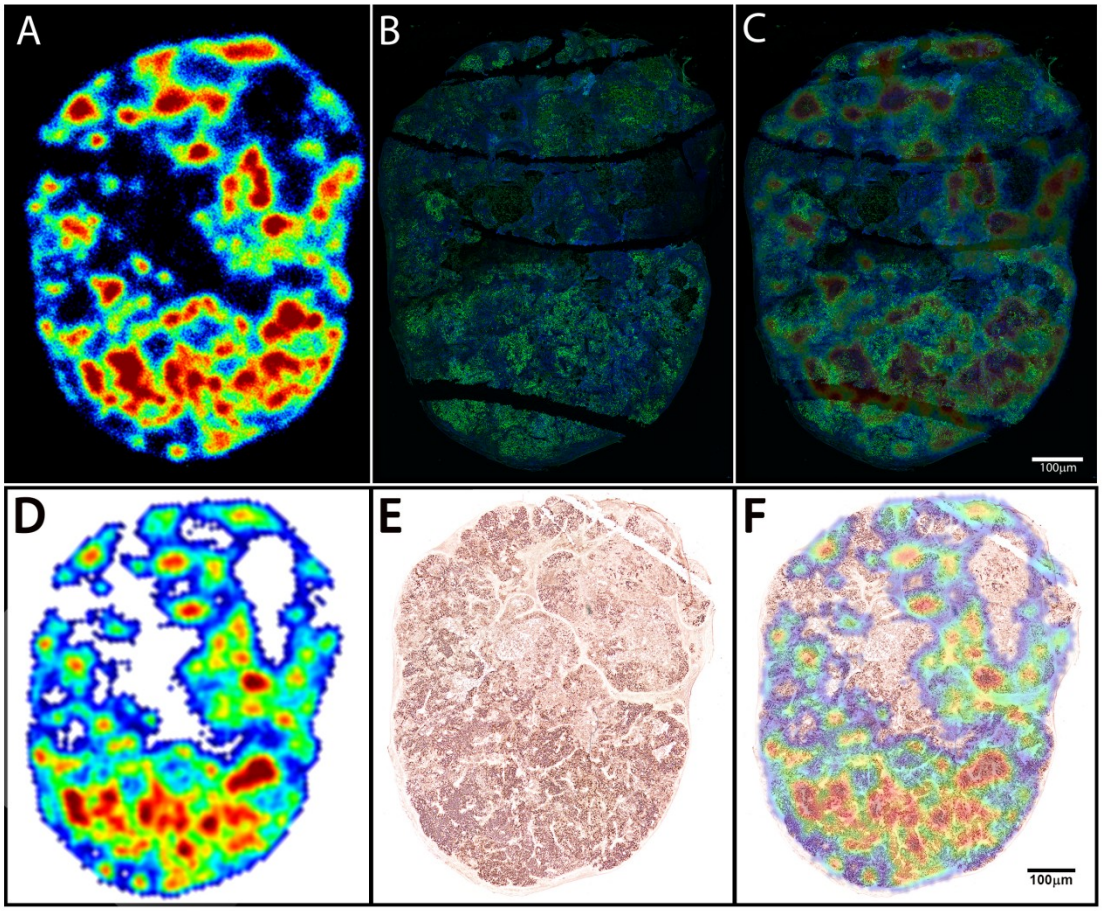

Figure 4.19: *Ex vivo* analysis. **A)** Autoradiography image from a section of NIH:OVCAR-3 tumor indicating hot spots of *in vivo* targeting by ^{64}Cu-NOTA-MAb-B43.13. **B)** Immunofluorescence image of the same section staining green in regions of CA125 expression (Alexa fluor 488) and counterstained blue (Hoechst 33342) for nuclei. **C)** Overlay of images A and B to establish concurrence between signals from independent methods of *ex vivo* analysis to indicate CA125 expression and targeting. **D)** Autoradiography image from a separate section of NIH:OVCAR-3 tumor indicating hot spots of *in vivo* targeting by ^{64}Cu-NOTA-MAb-B43.13. **E)** Immunohistochemistry image of corresponding tissue section. Intensity of staining is indicative of CA125 expression in the sample. **F)** Overlay of images D and E to establish concurrence between signals from independent methods of *ex vivo* analysis to indicate CA125 expression and targeting.

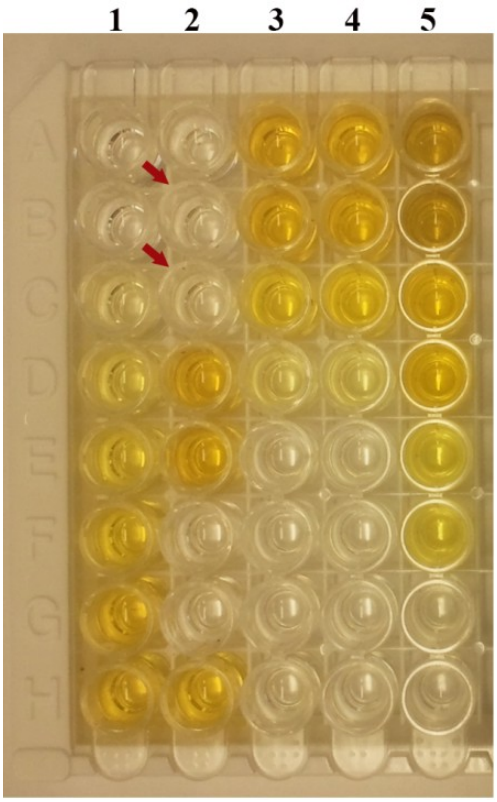

Fig 4.20: CA125 ELISA

A1, A2: PBS Blank

B1: Kit CA125 Standard 0 U/ml

C1: Kit CA125 Standard 15 U/ml

D1: Kit CA125 Standard 50 U/ml

E1: Kit CA125 Standard 100 U/ml

F1: Kit CA125 Standard 200 U/ml

G1: Kit CA125 Standard 400 U/ml

B2: Mouse serum BALB/c OVCAR3 xenograft-1

C2: Mouse serum BALB/c OVCAR3 xenograft-2

D2, E2: OVCAR3 spent cell culture media (100%)

F2, G2: OVCAR3 unused cell culture media (100%)

H1, H2: OVCAR3 spent cell culture media concentrate (Conc)

A3, A4: OVCAR3 spent cell culture media (1:5 of Conc)

B3, B4: OVCAR3 spent cell culture media (1:10 of Conc)

C3, C4: OVCAR3 spent cell culture media (1:100 of Conc)

D3, D4: OVCAR3 spent cell culture media (1:1000 of Conc)

E3, E4: OVCAR3 unused cell culture media (1:5 of Conc)

F3, F4: OVCAR3 unused cell culture media (1:10 of Conc)

G3, G4: OVCAR3 unused cell culture media (1:100 of Conc)

H3, H4: OVCAR3 unused cell culture media (1:1000 of Conc)

A5, B5: OVCAR3 Cell lysate (1:10)

C5, D5: OVCAR3 Cell lysate (1:100)

E5, F5: OVCAR3 Cell lysate (1:1000)

G5: SKOV3 Cell lysate (1:10)

H5: SKOV3 Cell lysate (1:100)

4.4 Discussion

Epithelial ovarian cancer (EOC) accounts for more than 90% of all ovarian carcinomas presented in the clinic. 70% of these cases are High Grade Serous Cancers (HGSC) overexpressing CA125.[24] This offers a premise to target CA125 for *in vivo* diagnosis of ovarian neoplasms. For the present study, NIH:OVCAR-3 human adenocarcinoma cells representative of HGSCs and SKOV3 cells representative of human clear cell ovarian carcinoma that do not express CA125 were utilized in order to develop a robust preclinical testing platform to validate CA125 antigen expression and targeting. Both cell lines displayed consistent biochemical characteristics across *in vitro*, *in vivo* and *ex vivo* analyses. Compared with previous reports,[25] MAb-B43.13 was engineered using a universal bioconjugation strategy to enable radiolabeling using ^{64}Cu to exploit its specific targeting capabilities as a radiotracer for immuno-PET.

In contrast with NIH:OVCAR-3 cells in culture,[26] *in vivo* uptake of [^{18}F]FDG in OVCAR3 tumors was found to be relatively low (Fig. 4.15F). Utility of a targeted radiotracer may thus be more sensitive and efficient in delineating EOC tumors over a metabolic radiotracer. Isothiocyanate based bioconjugation of a fluorescent tag or macrocyclic chelator within prescribed molar ratios to the MAb/scFv and subsequent radiolabeling yielded consistent results without compromising the immunoreactivity of CA125 targeting vectors. This widens the scope for labeling with different radionuclides, fluorophores, and functional groups for use in diverse imaging and therapeutic applications. Based on indications from a previous report[27] and our observations for non-internalization of surface antigen-

bound MAb-B43.13 over 48 h; pre-targeting applications via conjugating click components to MAb-B43.13 are presently being explored.

Our studies with MAb-B43.13 and scFv-B43.13 in preclinical ovarian cancer models found higher targeted tumor uptake of ^{64}Cu-NOTA-MAb-B43.13. Specificity of the observed *in vivo* tumor uptake was validated by pre-dosing OVCAR3 xenograft animals with 1 mg of un-modified MAb-B43.13 24 h prior to injection of ^{64}Cu-labeled anti-CA125 MAb/scFv. Non-specific tumor uptake was determined to be arising from enhanced permeability and retention effect,[28] whose numerical value fell in range with ^{64}Cu-MAb B43.13 uptake observed in antigen negative SKOV3 tumors. Thus, a correction factor was used to evaluate all final tumor uptake values obtained with this radiotracer.

Background radiation in all PET imaging studies using ^{64}Cu-NOTA-MAb B43.13 could be accounted by: a) its longer residency time in systemic circulation; b) consistent non-specific muscle uptake of radiotracer in all experimental animals; c) hepatobiliary clearance of radiotracer and/or immunocomplexes; d) potential trans-chelation of ^{64}Cu from NOTA by hepatic enzymes such as Superoxide dismutase (SOD). However, NOTA has demonstrated high *in vivo* kinetic stability as a chelator for $^{64}Cu^{2+}$ ions[29] and *in vitro* challenge experiments of ^{64}Cu-MAb B43.13 with an excess of purified SOD showed negligible trans-chelation (Fig. 4.14).

In contrast with its favourable *in vitro* targeting properties and proposed advantages for better tumor penetration and pharmacokinetics attributed to molecular size, the ^{64}Cu-labeled antibody fragment was less efficient in its role as

a radiotracer for *in vivo* targeting of CA125. These observations are supported by other reports from *in vivo* use of such monomeric antibody fragments.[30, 31] Although the scFv is expected to be renally cleared, we observed maximum trapping of the radioimmunoconjugate in kidneys as early as 1 h p.i. This phenomenon precludes the scFv's bioavailability to the tumor for any substantial accumulation, thus accounting for the lower tumor SUV observed with this vector. Further molecular engineering of the scFv into a diabody in order to provide competitive avidity and better *in vivo* performance is currently underway.

While autoradiography revealed successful *in vivo* targeting of the tumor by ^{64}Cu-labeled anti-CA125 MAb, immunohistochemistry provided a panoramic view of CA125 expression in tumor slices to indicate regions of high vascularity and other constituents of the tumor mass. Lower half of the tumor had more vascular perfusion, thus forming suitable sites for neoplastic cell growth appearing as densely stained tumor foci in this area. The vasculature also serves as a route of entry for targeted radioimmunoconjugates such as antibodies into the tumor. Most of the correlating signals from results between the three *ex vivo* techniques seem to go hand in glove with strong CA125 staining in the neighbourhood of dense vascular perfusion. This can be explained by a combinatorial effect of the aberrant tumor vasculature and limited penetration capability of antibody radioimmunoconjugates for extravasation across blood vessels to further reach the tumor cells. The shedding properties of CA125 antigen and diffuse lymphatics in the tumor may create reservoirs of shed antigen in regions of high CA125 expression surrounding tumor vasculature. Thus most of the antibody tracer

coming into the tumor would form immunocomplexes (IC) with shed antigen at such junctions, only to be cleared via lymphatics in due course of time. Subcutaneous tumor xenograft models were used in this preclinical study to allow for easy assessment of tumor burden and to evaluate the extent of tumor targeting. However, this strategy warrants testing in alternative xenograft or transgenic animal models that more closely represent human epithelial ovarian cancer in its natural setting of the peritoneum.

The concurrence of *in vitro*, *in vivo* and *ex vivo* data taken from this preclinical study represents an initial step in fulfillment of the goal to investigate CA125 as a suitable target for *in vivo* imaging of epithelial ovarian cancer. Drawing information from the present findings and prior literature reports,[32-35] it can be speculated that along the course of EOC progression, there may be a pathophysiological time interval between the overexpression of CA125 antigen on surface of ovarian neoplasms and its subsequent shedding into the bloodstream of subjects at high risk for epithelial ovarian cancer and during recurrence. This time interval could be a gap between active small volume disease brewing to relapse and the limitations of present day methods for detection of CA125. Molecular imaging by immuno-PET may possibly bridge this gap to achieve early detection of EOC.

4.5 Conclusion

In the work at hand, we have described the synthesis and preclinical radiopharmacological evaluation of ^{64}Cu-labeled MAb-B43.13 and its derivative scFv for the PET imaging of CA125 in EOC. This approach offers both an opportunity for early detection of EOC in patients at high risk and a method to monitor patients for recurrence, by providing a non-invasive *in vivo* assessment of CA125 status. A robust model system was developed for preclinical testing, and antibody-based CA125 targeting radioimmunoconjugates were successfully produced with excellent immunoreactivity. Overall, the more efficient tumor targeting capabilities and favourable radiopharmacological profiles of the full-length antibody make it a suitable radiotracer for non-invasive *in vivo* evaluation of CA125 in EOC.

4.6 References:

1. Howlader N, Noone AM, Krapcho M, et al. SEER Cancer Statistics Review, 1975-2010, National Cancer Institute. Bethesda, MD, http://seer.cancer.gov/csr/1975_2010/, based on November 2012 SEER data submission, posted to the SEER web site, April 2013.
2. Davis HM, Zurawski VR, Jr., Bast RC, Jr., Klug TL. Characterization of the CA 125 antigen associated with human epithelial ovarian carcinomas. *Cancer Res* 1986;**46**(12 Pt 1): 6143-8.
3. Bast RC, Jr., Xu FJ, Yu YH, Barnhill S, Zhang Z, Mills GB. CA 125: the past and the future. *Int J Biol Markers* 1998;**13**(4): 179-87.
4. Scholler N, Urban N. CA125 in ovarian cancer. *Biomark Med* 2007;**1**(4): 513-23.
5. Pignata S, Cannella L, Leopardo D, Bruni GS, Facchini G, Pisano C. Follow-up with CA125 after primary therapy of advanced ovarian cancer: in favor of continuing to prescribe CA125 during follow-up. *Ann Oncol* 2011;**22** Suppl 8: viii40-viii44.
6. Son H, Khan SM, Rahaman J, et al. Role of FDG PET/CT in staging of recurrent ovarian cancer. *Radiographics* 2011;**31**(2): 569-83.
7. Murakami M, Miyamoto T, Iida T, et al. Whole-body positron emission tomography and tumor marker CA125 for detection of recurrence in epithelial ovarian cancer. *Int J Gynecol Cancer* 2006;**16** Suppl 1: 99-107.
8. Zimny M, Siggelkow W, Schroder W, et al. 2-[Fluorine-18]-fluoro-2-deoxy-d-glucose positron emission tomography in the diagnosis of recurrent ovarian cancer. *Gynecol Oncol* 2001;**83**(2): 310-5.
9. Gadducci A, Cosio S. Surveillance of patients after initial treatment of ovarian cancer. *Crit Rev Oncol Hematol* 2009;**71**(1): 43-52.

10. Capstick V, Maclean GD, Suresh MR, et al. Clinical evaluation of a new two-site assay for CA125 antigen. *Int J Biol Markers* 1991;**6**(2): 129-35.

11. Nustad K, Bast RC, Jr., Brien TJ, et al. Specificity and affinity of 26 monoclonal antibodies against the CA 125 antigen: first report from the ISOBM TD-1 workshop. International Society for Oncodevelopmental Biology and Medicine. *Tumour Biol* 1996;**17**(4): 196-219.

12. Nap M, Vitali A, Nustad K, et al. Immunohistochemical characterization of 22 monoclonal antibodies against the CA125 antigen: 2nd report from the ISOBM TD-1 Workshop. *Tumour Biol* 1996;**17**(6): 325-31

13. Chen Y, Clark S, Wong T, et al. Armed antibodies targeting the mucin repeats of the ovarian cancer antigen, MUC16, are highly efficacious in animal tumor models. *Cancer Res* 2007;**67**(10): 4924-32.

14. Baum RP, Noujaim AA, Nanci A, et al. Clinical course of ovarian cancer patients under repeated stimulation of HAMA using MAb OC125 and B43.13. *Hybridoma* 1993;**12**(5): 583-9.

15. Schultes BC, Zhang C, Xue LY, Noujaim AA, Madiyalakan R. Immunotherapy of human ovarian carcinoma with OvaRex MAb-B43.13 in a human-PBL-SCID/BG mouse model. *Hybridoma* 1999;**18**(1): 47-55.

16. Berek JS. Immunotherapy of ovarian cancer with antibodies: a focus on oregovomab. *Expert Opin Biol Ther* 2004;**4**(7): 1159-65.

17. Wu AM. Antibodies and antimatter: the resurgence of immuno-PET. *J Nucl Med* 2009;**50**(1): 2-5.

18. Holland JP, Divilov V, Bander NH, Smith-Jones PM, Larson SM, Lewis JS. 89Zr-DFO-J591 for immunoPET of prostate-specific membrane antigen expression in vivo. *J Nucl Med* 2010;**51**(8): 1293-300.

19. Viola-Villegas NT, Rice SL, Carlin S, et al. Applying PET to broaden the diagnostic utility of the clinically validated CA19.9 serum biomarker for oncology. *J Nucl Med* 2013;**54**(11): 1876-82.

20. Wang WW, Das D, McQuarrie SA, Suresh MR. Design of a bifunctional fusion protein for ovarian cancer drug delivery: single-chain anti-CA125 core-streptavidin fusion protein. *Eur J Pharm Biopharm* 2007;**65**(3): 398-405.

21. Cooper MS, Ma MT, Sunassee K, et al. Comparison of (64)Cu-complexing bifunctional chelators for radioimmunoconjugation: labeling efficiency, specific activity, and in vitro/in vivo stability. *Bioconjug Chem* 2012;**23**(5): 1029-39.

22. Kume M, Carey PC, Gaehle G, et al. A semi-automated system for the routine production of copper-64. *Appl Radiat Isot* 2012;**70**(8): 1803-6.

23. Lindmo T, Boven E, Cuttitta F, Fedorko J, Bunn PA, Jr. Determination of the immunoreactive fraction of radiolabeled monoclonal antibodies by linear extrapolation to binding at infinite antigen excess. *J Immunol Methods* 1984;**72**(1): 77-89.

24. Prat J. New insights into ovarian cancer pathology. *Ann Oncol* 2012;**23** Suppl 10: x111-7.

25. McQuarrie SA, Baum RP, Niesen A, et al. Pharmacokinetics and radiation dosimetry of 99Tcm-labelled monoclonal antibody B43.13 in ovarian cancer patients. *Nucl Med Commun* 1997;**18**(9): 878-86.

26. Lutz AM, Ray P, Willmann JK, Drescher C, Gambhir SS. 2-deoxy-2-[F-18]fluoro-D-glucose accumulation in ovarian carcinoma cell lines. *Mol Imaging Biol* 2007;**9**(5): 260-6.

27. Xiao Z, McQuarrie SA, Suresh MR, Mercer JR, Gupta S, Miller GG. A three-step strategy for targeting drug carriers to human ovarian carcinoma cells in vitro. *J Biotechnol* 2002;**94**(2): 171-84.

28. Fang J, Nakamura H, Maeda H. The EPR effect: Unique features of tumor blood vessels for drug delivery, factors involved, and limitations and augmentation of the effect. *Adv Drug Deliv Rev* 2011;**63**(3): 136-51.

29. Dearling JL, Voss SD, Dunning P, et al. Imaging cancer using PET--the effect of the bifunctional chelator on the biodistribution of a (64)Cu-labeled antibody. *Nucl Med Biol* 2011;**38**(1): 29-38.

30. Wittrup KD, Thurber GM, Schmidt MM, Rhoden JJ. Practical theoretic guidance for the design of tumor-targeting agents. *Methods Enzymol* 2012;**503**: 255-68.

31. Schneider DW, Heitner T, Alicke B, et al. In vivo biodistribution, PET imaging, and tumor accumulation of 86Y- and 111In-antimindin/RG-1, engineered antibody fragments in LNCaP tumor-bearing nude mice. *J Nucl Med* 2009;**50**(3): 435-43.

32. Hori SS, Gambhir SS. Mathematical model identifies blood biomarker-based early cancer detection strategies and limitations. *Sci Transl* Med 2011;**3**(109): 109ra16.

33. McQuarrie SA, Riauka T, Baum RP, et al. The effects of circulating antigen on the pharmacokinetics and radioimmunoscintigraphic properties of 99m Tc labelled monoclonal antibodies in cancer patients. *J Pharm Pharm Sci* 1998;**1**(3): 115-25.

34. Masuho Y, Zalutsky M, Knapp RC, Bast RC, Jr. Interaction of monoclonal antibodies with cell surface antigens of human ovarian carcinomas. *Cancer Res* 1984;**44**(7): 2813-9.

35. Marth C, Zeimet AG, Widschwendter M, Daxenbichler G. Regulation of CA 125 expression in cultured human carcinoma cells. *Int J Biol Markers* 1998;**13**(4): 207-9.

5

^{89}Zr immuno-PET of Epithelial Ovarian Cancer[4]

[4]This work has been carried out in collaboration with Dr. Jason Lewis at the Memorial Sloan Kettering Cancer Center, New York.

A version of this chapter will be submitted to the Journal of Nuclear Medicine: Sharma SK, Zeglis BM, Sevak KK, Carlin S, Wuest M, Knight JK, Lewis JS, Wuest F. ^{89}Zr immuno-PET of Epithelial Ovarian Cancer

5.1 Introduction:

Nuclear medicine has benefitted greatly from the high specificity and affinity of antibodies used in conjunction with radioisotopes to function as molecular agents for applications in diagnostic imaging and therapy.[1] The maximum potential of this combination is usually achieved when the radioisotope used in such a composite targeting entity has a physical half-life comparable to the *in vivo* biological/pharmacokinetic half-life of the antibody. This is especially true from the perspective of molecular imaging strategies such as positron emission tomography (PET), wherein a radiotracer is developed as a concerted function of the targeting vector (antibody) and corresponding effector molecule (radionuclide) brought together into a single unit. In other words, PET-radionuclides such as Gallium-68 ($t_{1/2}$ = 1.1 h) and Fluorine-18 ($t_{1/2}$ = 1.8 h) would have insufficient physical half-lives to match the pharmacokinetics of full-length antibodies while Copper-64 ($t_{1/2}$ = 12.7 h) and Yttrium-86 ($t_{1/2}$ = 14.7 h) may be more suitable, yet imperfect to harness the full potential of antibodies as radiotracers for human use.

On the other hand, Iodine-124 ($t_{1/2}$ = 100.2 h, 4.18 d) has been a radionuclide of choice for immuno-PET strategies using full-length antibodies and has shown success in preclinical and clinical applications.[2, 3, 4] However, this isotope suffers from limitations due to its cost of production, low positron yield (23%) and *in vivo* dehalogenation that results in uptake of free radioiodine in the thyroid and gut at later time points. More importantly, it renders poor resolution due to higher

positron energy and long range positrons emitted in coincidence with γ-rays that potentially contributes to radiation burden in patients.

More recently, there has been a widespread interest and greater clinical acceptance of Zirconium-89 (^{89}Zr: $t_{1/2}$ 78.4 h or 3.2 d) for diagnostic imaging via immuno-PET with full-length antibodies.[5, 6, 7] Some attractive features of this radioisotope include a favourable physical half that is well matched with the biological half-life of full-length antibodies, its relative ease and cost of production,[8] *in vivo* stability, low energy positron emissions that contribute to higher resolution images.[9, 10] Furthermore, immuno-PET imaging with ^{89}Zr-MAbs can potentially serve as a scout for potential immunotherapy using ^{177}Lu versions of the same tumor targeting antibody.[11] This aspect renders a translational benefit to using ^{89}Zr for preclinical testing of radiotracers. In addition, better *in vivo* residualizing properties combined with an ongoing development of ligands[12, 13] for efficient chelation of this radionuclide are proving advantageous for its application in preclinical and clinical cancer research

In this chapter, we utilized ^{89}Zr in order to maximize the previously demonstrated diagnostic potential of anti-CA125 MAb-B43.13 and deliver a translational benefit to the immuno-PET strategy for *in vivo* evaluation of CA125 expression in epithelial ovarian cancer. This was achieved by functionalizing the anti-CA125 MAb-B43.13 via conjugation with desferrioxamine (DFO), used as a ligand for chelation of $^{89}Zr^{+4}$. The resultant radioimmunoconjugate – ^{89}Zr-DFO-MAb-B43.13 was subsequently tested in a preclinical setting for its *in vitro*

functionality using CA125-positive NIH:OVCAR-3 and CA125-negative SKOV3 cells. Immunocompromised mice were xenografted with these cell lines to develop corresponding subcutaneous tumor models for evaluation of the *in vivo* tumor targeting capabilities and associated pharmacokinetics of the radioimmunoconjugate as an immuno-PET tracer. Here, we show successful *in vivo* tumor targeting properties of ^{89}Zr-DFO-MAb-B43.13 by virtue of its ability to dileneate ovarian tumors within 24 h p.i and furthermore provide an opportunity to track the *in vivo* radiopharmacological profile of the radiotracer up to 120 h p.i

5.2 Materials and Methods:

5.2.1 Preparation of anti-CA125 immunoconjugate:

Murine monoclonal anti-CA125 antibody was produced from B43.13 hybridoma[14] and purified from its cell culture supernatant by protein G affinity (Sigma, P-7700) on a BioLogic DuoFlow™ chromatography system (Bio-Rad, 760-0135). The concentration of purified MAb-B43.13 was quantified using a Pierce™ BCA protein assay kit (Thermo Scientific, 23227) according to the manufacturer's recommendations. IgG from mouse serum (Sigma, I5381) was used as an isotype control for the experiments involved in this study and also to generate a standard curve for protein estimation of MAb-B43.13. p-SCN-DFO; *p*-isothiocyanatobenzoyl-desferrioxamine (Macrocyclics, B-705) was conjugated to MAb-B43.13 and mouse IgG (isotype) as a bi-functional chelator for ^{89}Zr radiolabeling. Briefly, a 10 molar excess of p-SCN-DFO dissolved in DMSO was added to MAb-B43.13 in 0.1 M sodium bi-carbonate buffer pH 9.0 and allowed to react for 1 h at 37°C. DFO-functionalized MAb-B43.13 was purified from un-conjugated DFO whilst simultaneously achieving buffer exchange into phosphate buffered saline (PBS) pH 7.4 by using an Econo-Pac® 10DG desalting column (Bio-Rad, 732-2010). The number of DFO molecules conjugated per MAb was determined by MALDI-ToF MS analysis.

5.2.2 Determination of bi-functional chelates per MAb-B43.13:

To determine the average number of bi-functional chelate molecules conjugated per molecule of MAb-B43.13, MALDI-ToF-MS analysis was performed at the Institute for Biomolecular Design, University of Alberta. 1 µL of the DFO-MAb-B43.13 samples was mixed with 1 µL of sinapic acid (10 mg/ml in 50% acetonitrile:water and 0.1% trifluoroacetic acid). 1 µL of the sample/matrix solution was then spotted onto a stainless steel target plate and allowed to air dry. All mass spectra were obtained using a Bruker Ultraflex MALDI-ToF/ToF (Bruker Daltonic GmbH). Ions were analyzed in positive mode and external calibration was performed by use of a standard protein mixture. The average number of DFOs conjugated per MAb-B43.13 molecule was derived by calculating the difference of masses between the DFO-conjugated versus un-modified MAb-B43.13 and dividing this difference by the molecular weight of DFO (752.9 Da).

5.2.3 Functional characterization of MAb –B43.13 immunoconjugates:

5.2.3.1 Cell lines and culture conditions: Ovarian cancer cells NIH:OVCAR-3 (ATCC® HTB-161™) that overexpress CA125 were used for *in vitro* functional characterization studies. Cells were cultured in DMEM-F12 medium supplemented with 10% v/v fetal bovine serum (Life Technologies, 12483-020), 50 IU/mL penicillin, 50 µg/mL streptomycin (Life Technologies, 15140-122) and were additionally supplemented with 7 µg/mL recombinant human insulin (SAFC

Biosciences, 91077C). Cells were cultured using sterile techniques and grown in a 37°C incubator providing humidified atmosphere of 5% CO_2 in air.

5.2.3.2 Immunofluorescence: NIH:OVCAR-3 cells were plated onto glass coverslips in 35-mm tissue culture dishes (100,000 cells/2 mL medium/dish) and incubated at 37°C for 48 h. The cells were rinsed with PBS and fixed in methanol for 30 min at -20°C. The fixed cells were incubated in 5% non-fat dry milk (Carnation) in PBS and immunostained separately for 1 h with 1:250 dilution of 2 mg/mL anti-CA125 MAb-B43.13, DFO-MAb-B43.13 and anti-dengue MAb12A1 (isotype control). Alexa-fluor® 488 conjugated goat anti-mouse antibody (1 mg/mL) (Life Technologies, A-11001) was used as a secondary antibody (1:500) in PBS containing 5% non-fat dry milk. Appropriate control samples were included in the experiments. All antibody incubations were followed by three rinses with PBST for 10 min each. Coverslips were mounted on microscopy slides (Fisherbrand) using Mowiol® mounting medium (Calbiochem, 475904) supplemented with DAPI (50 µg/ml). Immunofluorescence was observed through a Zeiss Plan Apochromat 40X/1.3 Oil DIC M27 lens on a confocal laser scanning microscope (Zeiss LSM 710). The images were analyzed using Zen 2011 software and processed further using Adobe Photoshop CS6.

5.2.3.3 Flow Cytometry: 1.5 x 10^6 NIH:OVCAR-3 cells were harvested by trypsinization, rinsed twice with FACS buffer (PBS with 0.5% heat inactivated FBS, 2mM EDTA, 0.05% sodium azide) and resuspended by gentle tapping in ~100 µL of this buffer. 10 µg of MAb B43.13, FITC-conjugated MAb-B43.13,

DFO-conjugated MAb-B43.13 and MAb12A1 (isotype control), were incubated with the NIH:OVCAR-3 cell suspension for 30 min at room temperature. Cells were rinsed twice in FACS buffer and incubated for another 30 min with 1.6 μg of Alexa-fluor® 488 conjugated goat anti-mouse IgG (Life Technologies, A-11001) used as a secondary antibody. Cells were rinsed twice with FACS buffer and analyzed by flow cytometry on a BD FACS Calibur. Ten thousand events were gated. Negative controls included unstained NIH:OVCAR-3 cells and coverslips of cells incubated separately with MAb-B43.13 only and secondary antibody alone.

5.2.4 Preparation of radioimmunoconjugates: (*Performed at MSKCC, NYC*)

To prepare an isotype mouse IgG immunonjugate for ^{89}Zr-labeling, a 5 molar excess of p-SCN-DFO was added to mouse IgG in 0.1 M sodium bi-carbonate buffer pH 9.0 and processed similarly as DFO-MAb-B43.13. To radiolabel the immunoconjugate constructs, 300-400 μg of the DFO-conjugated antibody was first added to 200 μL buffer (PBS, pH 7.4). [^{89}Zr]Zr-oxalate (2000-2500 μCi, 74 – 95 MBq) in 1.0 M oxalic acid was then adjusted to pH 7.0-7.5 with 1.0 M Na_2CO_3. After adjustment of the pH, ^{89}Zr was added to the antibody solution, and the resultant mixture was incubated at room temperature for 1 h. The reaction progress was assayed using radio-TLC with an eluent of 50 mM EDTA, pH 5, and the reaction was quenched with 50 μL of the same EDTA solution. The antibody construct was purified using size-exclusion chromatography (Sephadex G-25 M, PD-10 column, GE Healthcare; dead volume = 2.5 mL, eluted with 500 μL

fractions of PBS, pH 7.4) and concentrated, if necessary, with centrifugal filtration. The radiochemical purity of the crude and final radioimmunoconjugate was assayed by radio-TLC. In the ITLC experiments, the antibody construct remains at the baseline, while $^{89}Zr^{4+}$ ions and [^{89}Zr]-EDTA elute with the solvent front.

5.2.5 Cell lines and Culture:

Human ovarian adenocarcinoma NIH:OVCAR-3 and SKOV3 cells were obtained from American Type Culture Collection (ATCC, Manassas, VA). The cells were grown as adherent mono layers according to recommendations of ATCC in a 37°C incubator providing humidified atmosphere of 5% CO_2 in air. The NIH:OVCAR-3 cells were cultured using RPMI 1640 medium supplemented with heat inactivated fetal bovine serum (20% v/v, GIBCO, Life Technologies, Carlsbad, CA), 2 mM L-glutamine, 10 mM HEPES, 1 mM sodium pyruvate, 4.5 g/L glucose, 1.5 g/L sodium bicarbonate, bovine insulin (0.01 mg/mL, Gemini Bioproducts), 100 units/mL penicillin and 100 µg/mL streptomycin. The SKOV3 cells were cultured using McCoy's 5A medium supplemented with heat inactivated fetal bovine serum (10% v/v, GIBCO, Life Technologies, Carlsbad, CA), 1.5 mM L-glutamine, 2.2 g/L sodium bicarbonate, 100 units/mL penicillin and 100 µg/mL streptomycin. Adherent cells were harvested with 0.25% trypsin and 0.53 mM EDTA in Hank's Buffered Salt Solution (HBSS) without any traces of calcium or magnesium. The cells were passaged regularly at 70-80%

confluence in a ratio of 1:2 to 1:4 (NIH:OVCAR-3) and 1:3 to 1:6 (SKOV3) for sub-cultivation.

5.2.6 Immunoreactivity measurements:

5.2.6.1 Lindmo assay[15] for determination of immunoreactive fraction: NIH:OVCAR-3 cells were aliquoted into microcentrifuge tubes at concentrations of 5, 4, 3, 2.5, 2, 1.5 and 0.5 x 10^6 cells in 500 μL PBS (pH 7.4). A stock solution of the ^{89}Zr-DFO-MAb-B43.13 radioimmunoconjugate was prepared in PBS (pH 7.4) supplemented with 1% BSA such that 50 μL of this solution contained 20,000 cpm, which was then uniformly aliquoted into individual tubes. This setup was allowed to incubate for 1 hr at room temperature on a platform mixer. Thereafter, NIH:OVCAR-3 cells were pelleted by centrifugation (5,000 rpm for 3 mins), followed by two rinses with ice cold PBS before aspirating out the supernatant prior to measuring cell-bound radioactivity on a γ-counter (Wizard$^{2®}$ 2480 Automatic Gamma Counter, Perkin-Elmer, Canada). Radioactivity data obtained thereof was background corrected and compared with counts from the total activity control samples in the experiments. A similar set up was organized to conduct experiments with CA125-negative SKOV3 cells as well. The immunoreactive fraction was determined by performing a linear regression analysis on a double-inverse plot of (total/bound) activity versus normalized cell concentration. This value is obtained from the inverse of the intercept on the plot. All data was obtained in triplicates and no weighting was applied.

5.2.6.2 Antigen Saturation Binding Assay: Additionally, the *in vitro* immunoreactivity of ^{89}Zr-DFO-MAb-B43.13 radioimmunoconjugate was determined using an antigen saturation binding assay. To this end, both antigen-expressing NIH:OVCAR-3 and antigen-negative SKOV3 cells were prepared in culture. For the assay, a 0.4 ng/μL solution of ^{89}Zr-DFO-MAb-B43.13 was prepared in PBS supplemented with 1% human serum albumin. Subsequently, 20 μL of this radioimmunoconjugate solution was added to a microcentrifuge tube containing 10 x 10^6 cells in 200 μL of culture media. The resulting solution was then thoroughly mixed using a micropipette and incubated for 1 h on ice. After 1 h, the cells were pelleted via centrifugation (600 × g for 5 min), and the supernatant was removed to another microcentrifuge tube. The cells were subsequently washed with 1 mL of ice-cold PBS and re-pelleted via centrifugation (600 × g for 5 min), and the supernatant was again removed to another centrifuge tube. This washing procedure was repeated two more times. Subsequently, the cell pellet, the media supernatant, and the three wash fractions were counted for radioactivity on a gamma counter calibrated for ^{89}Zr. Finally, the immunoreactive fraction of the radioimmunoconjugate was determined by the following formula:

$$\text{Immunoreactive Fraction} = [\text{Counts}_{\text{Cell Pellet}}]/[[\text{Counts}_{\text{Cell Pellet}} + \text{Counts}_{\text{Media Supernatant}} + \text{Counts}_{\text{Wash1}} + \text{Counts}_{\text{Wash2}} + \text{Counts}_{\text{Wash3}}]$$

No weighting was applied to the data, and the data were obtained in triplicate.

5.2.7 Radioimmunoconjugate stability: *In vitro* stability of ^{89}Zr-DFO-MAb-B43.13 radioimmunoconjugates with respect to radiochemical purity and loss of radioactivity from the antibody was investigated by incubation of the antibodies in human AB type serum for 7 d at 37 °C. The radiochemical purity of the antibodies was determined via radio-TLC with an eluent of 50 mM EDTA pH 5.0. All experiments were performed in triplicate.

5.2.8 Animal Xenografts: All animals were treated according to the guidelines set and approved by the Research Animal Resource Center and Institutional Animal Care and Use Committee at Memorial Sloan Kettering Cancer Center. Female athymic nude mice (01B74-Athymic NCr-nu/nu, 20-22 gm, 6-8 wk old) were obtained from National Cancer Institute and were allowed to acclimatize at the Memorial Sloan Kettering Cancer Center vivarium for 1 week before tumors were implanted. Mice were provided with food and water *ad libitum*. A total of 10 x 10^6 NIH:OVCAR-3 cells in 150 µL suspension of 1:1 media/Matrigel Basement Membrane Matrix (BD Biosciences) were injected subcutaneously on the right shoulder. Due to the slow *in vivo* tumorigenicity of NIH:OVCAR-3 cells and a tendency of the tumor to show regression after initial growth, a second xenograft inoculation of 10 x 10^6 NIH:OVCAR-3 cells (in 150µL suspension of 1:1 media/ Matrigel Basement Membrane Matrix (BD Biosciences) was made at the same site 10 days after the first xenograft inoculation. Tumor growth was monitored weekly. Tumor volume (V) was calculated using Vernier Calipers, where V = $\pi/6$ x length x width x height. Mice were used for imaging and acute biodistribution

studies after tumor volumes reached 150-300 mm^3. Separately, a cohort of mice were implanted with NIH:OVCAR-3 cells on the left shoulder and SKOV3 cells on the right in order to develop a bilateral tumor xenograft model for *in vivo* evaluation of the radioimmunoconjugates.

5.2.9 Acute Biodistribution: Acute *in vivo* biodistribution studies were performed in order to evaluate the uptake of ^{89}Zr-DFO-MAb-B43.13 and ^{89}Zr-DFO-IgG in mice bearing subcutaneous NIH:OVCAR-3 xenografts (right shoulder, 150-300 mm^3, 8-10 weeks post inoculation). Tumor-bearing mice were randomized before the study and were warmed gently with a heat lamp for 5 min before administration of the appropriate ^{89}Zr-DFO-antibody construct (0.55 – 0.75 MBq [15-20 μCi] in 200 μL 0.9% sterile saline, 4-6 μg) via intravenous tail vein injection (t = 0). Animals (n = 4 per group) were euthanized by CO_2(g) asphyxiation at 24, 48, 72, 96, and 120 h post-injection. To probe for target antigen saturation, an additional cohort of animals were administered ^{89}Zr-DFO-MAb-B43.13 with a dramatically lowered specific activity – achieved by co-injection of the standard dose of ^{89}Zr-DFO-MAb-B43.13 mixed with 480 μg of the cold, unlabeled DFO-MAb-B43.13 – and euthanized at 72 h post-injection. After asphyxiation, relevant tissues (including tumor) were removed, rinsed in water, dried in air for 5 min, weighed, and counted in a gamma counter calibrated for ^{89}Zr. Counts were converted into activity using a calibration curve generated from known standards. Count data were background- and decay-corrected to the

time of injection, and the %ID/g for each tissue sample was calculated by normalization to the total activity injected.

5.2.10 PET Imaging. PET imaging experiments were conducted on a microPET Focus rodent scanner (Concorde Microsystems). Mice bearing subcutaneous NIH:OVCAR-3 (right shoulder) xenografts (150-200 mm^3) were administered ^{89}Zr-DFO-MAb-B43.13 (10.2 – 12.0 MBq [275-325 μCi] in 200 μL 0.9% sterile saline) via intravenous tail vein injection (t = 0). Approximately 5 minutes prior to the PET images, mice were anesthetized by inhalation of 2% isoflurane (Baxter Healthcare, Deerfield, IL)/oxygen gas mixture and placed on the scanner bed; anesthesia was maintained using 1% isoflurane/gas mixture. PET data for each mouse were recorded via static scans at time points between 24 and 120 h. A minimum of 20 million coincident events were recorded for each scan, which lasted between 10-45 min. An energy window of 350-700 keV and a coincidence timing window of 6 ns were used. Data were sorted into 2-dimensional histograms by Fourier re-binning, and transverse images were reconstructed by filtered back-projection (FBP) into a 128 × 128 × 63 (0.72 × 0.72 × 1.3 mm) matrix. The image data were normalized to correct for non-uniformity of response of the PET, dead-time count losses, positron branching ratio, and physical decay to the time of injection but no attenuation, scatter, or partial-volume averaging correction was applied. The counting rates in the reconstructed images were converted to activity concentrations (percentage injected dose [% ID] per gram of tissue) by use of a system calibration factor derived from the imaging of a mouse-

sized water-equivalent phantom containing ^{89}Zr. Images were analyzed using ASIPro VMTM software (Concorde Microsystems).

5.2.11 *Ex vivo* analyses:

Ex vivo autoradiography and IHC

Immediately following sacrifice, tumors were excised and frozen. Cryosectioning and digital autoradiography was carried out as previously described[16] with the exception of the plate reader in this instance being a GE Typhoon 7000IP, with maximum pixel resolution of 25 μm.

Immediately following autoradiography exposure, sections were fixed in 10% buffered formalin, followed by blocking with 0.5% fish skin gelatin and immunostaining for CA125 using MAb-B43.13 at 1:100 dilution and secondary detection using goat anti-mouse Fab-Alexa 594 (Jackson Immuno Research) at 0.12 mg/ml. Immunofluorescence imaging of the entire specimen was carried out as previously described.[16] Sequential sections were used for H&E staining and images were acquired in a similar manner. Images were adjusted for visual quality and registered using ImageJ software.

Separately, fixed tissue slices of the tumor, ipsilateral and contralateral chain of brachial and axillary lymph nodes were submitted for analysis by histopathology to the laboratory for comparative pathology at the Memorial Sloan Kettering Cancer Center.

5.3 Results:

5.3.1 Preparation and functional characterization of anti-CA125 immunoconjugate:

MAb-B43.13 was obtained in high purity with yields of ~ 7 mg/L of hybridoma cell culture supernatant. Isothiocyanate-based bio-conjugation of desferrioxamine (Fig. 5.1) yielded ~ 4 molecules of DFO conjugated per molecule of MAb-B43.13, as determined via MALDI-ToF analysis (Fig. 5. 2).

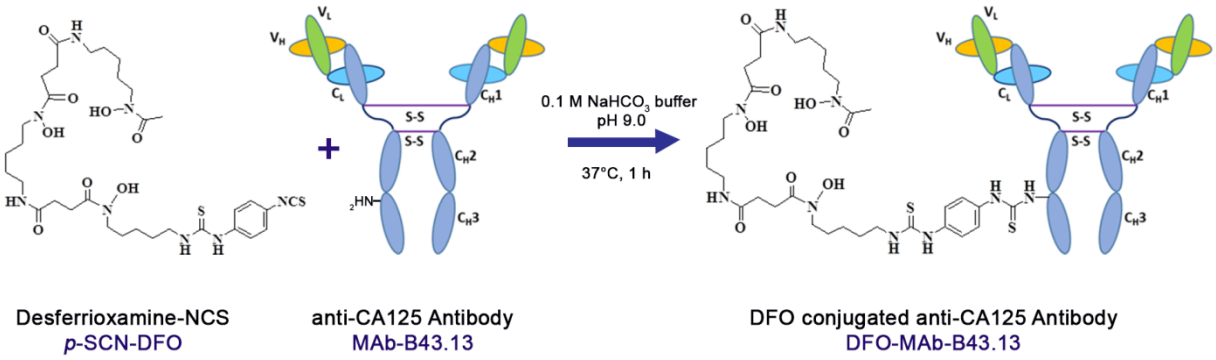

Figure 5.1: Diagrammatic representation for bioconjugation of DFO-NCS (Desferrioxamine-isothiocyanate) to anti-CA125 MAb-B43.13

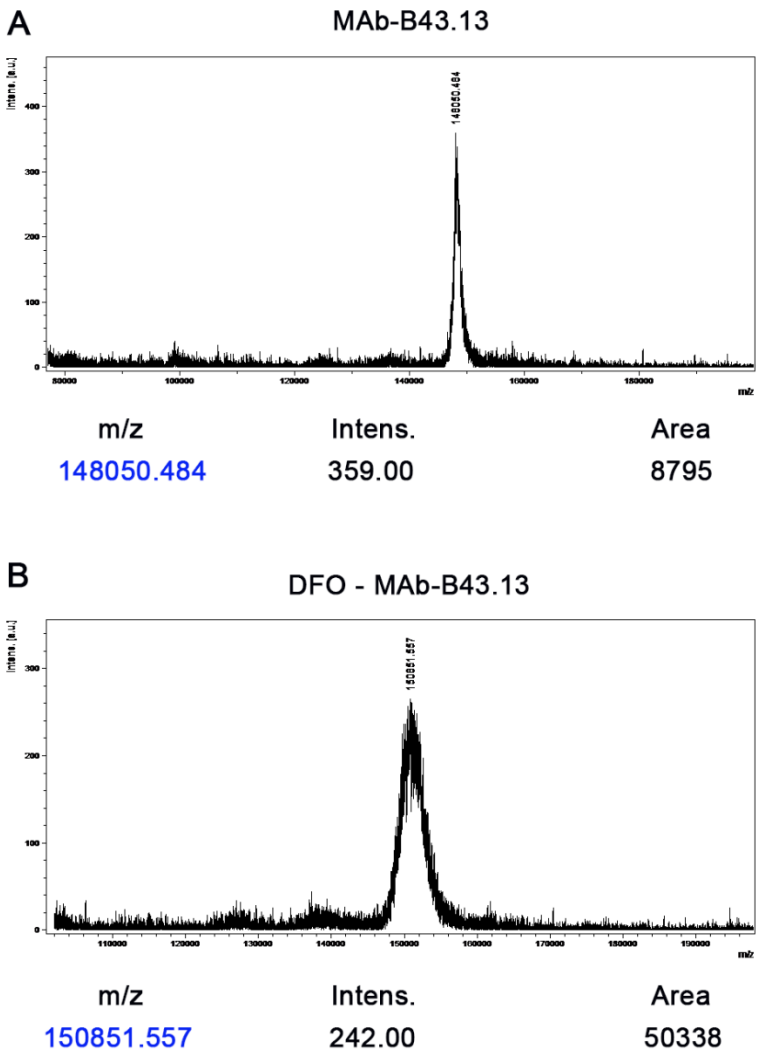

Figure 5.2: Characterization of number of bi-functional chelator (DFO) conjugated per MAb-B43.13. MALDI-ToF analysis of A) MAb-B43.13; B) DFO-MAb-B43.13. The masses (m/z) are highlighted in blue.

Functional characterization of the DFO-MAb-B43.13 revealed characteristic surface staining of CA125 as analyzed via immunofluorescence under the confocal microscope (Fig. 5.3A) and also by flow cytometry analysis of NIH:OVCAR-3 cells incubated with un-modified versions of this antibody and appropriate experimental controls (Fig. 5.3B).

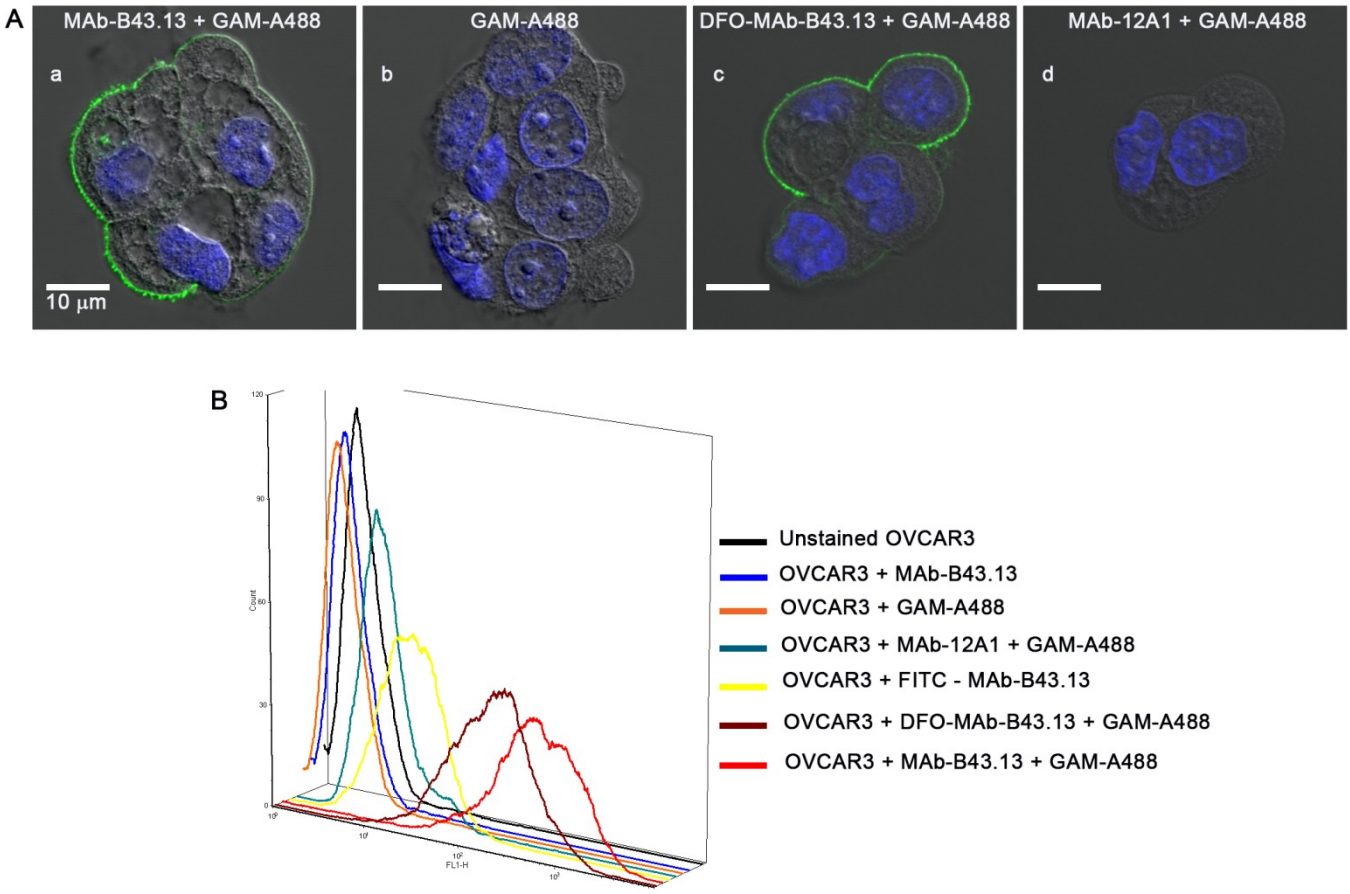

Figure 5.3: Functional characterization of DFO-MAb-B431.3. **A)** Immunofluorescence images of NIH:OVCAR-3 cells indirectly stained with **a)** MAb-B43.13 (positive control); **c)** DFO-MAb-B43.13; **d)** MAb-12A1 (isotype control); **b)** GAM-A488 (Goat anti-mouse Alexa Fluor 488 conjugated antibody) was used as a secondary antibody for immunostaining in all samples. **B)** 3D plot of histograms from flow cytometry analyses of DFO-MAb-B43.13 in comparison with control samples as indicated in the color code.

5.3.2 Preparation and functional characterization of ^{89}Zr-DFO-MAb-B43.13:

The DFO-MAb-B43.13 immunconjugate was radiolabeled with $^{89}Zr^{4+}$ via incubation of the antibody (300-400 μg) with ^{89}Zr (2.0-2.5 mCi, 74 – 92.5 MBq) in phosphate buffered saline at pH 7.0 – 7.5 for 1 h at room temperature (Fig. 5.4), followed by purification with size exclusion chromatography.

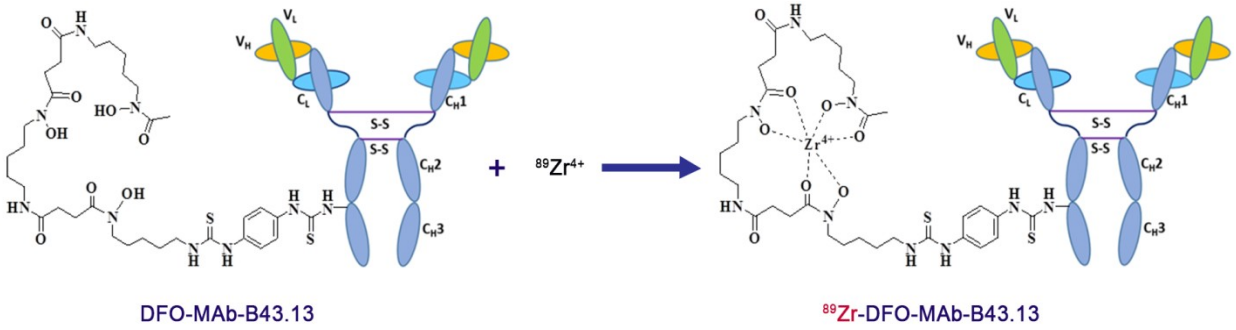

Figure 5.4: Diagrammatic representation for ^{89}Zr radiolabeling of DFO-MAb-B43.13

After purification, the final ^{89}Zr-DFO-MAb-B43.13 radioimmunoconjugate was isolated in > 99% radiochemical purity (Fig 5.5A, 5.5B) with a specific activity of 5.5 ± 0.8 mCi/mg (203.5 ± 29.6 MBq/mg). *In vitro* immunoreactivity experiments using the CA125-expressing NIH:OVCAR-3 cells revealed an average immunoreactive fraction of 93.4 ± 5.8% as determined by Lindmo assays (Fig 5.5C) and 0.91 ± 0.03 for ^{89}Zr-DFO-MAb-B43.13 as analyzed from antigen saturation binding assays. Conversely, *in vitro* analyses with the SKOV3 ovarian cancer cell line, which *does not* express the CA125 antigen, resulted in < 2% binding of the radioimmunoconjugate to the cells in question. Finally, to assay the stability of the radioimmunoconjugate to demetallation under biological conditions, ^{89}Zr-DFO-MAb-B43.13 was incubated in human AB type serum for 7

days at 37ºC. Radio-TLC analysis with an eluent of 50 mM EDTA (pH 5.0) performed over the course of the experiment demonstrated the radioimmunoconjugate to be > 96% stable in human serum.

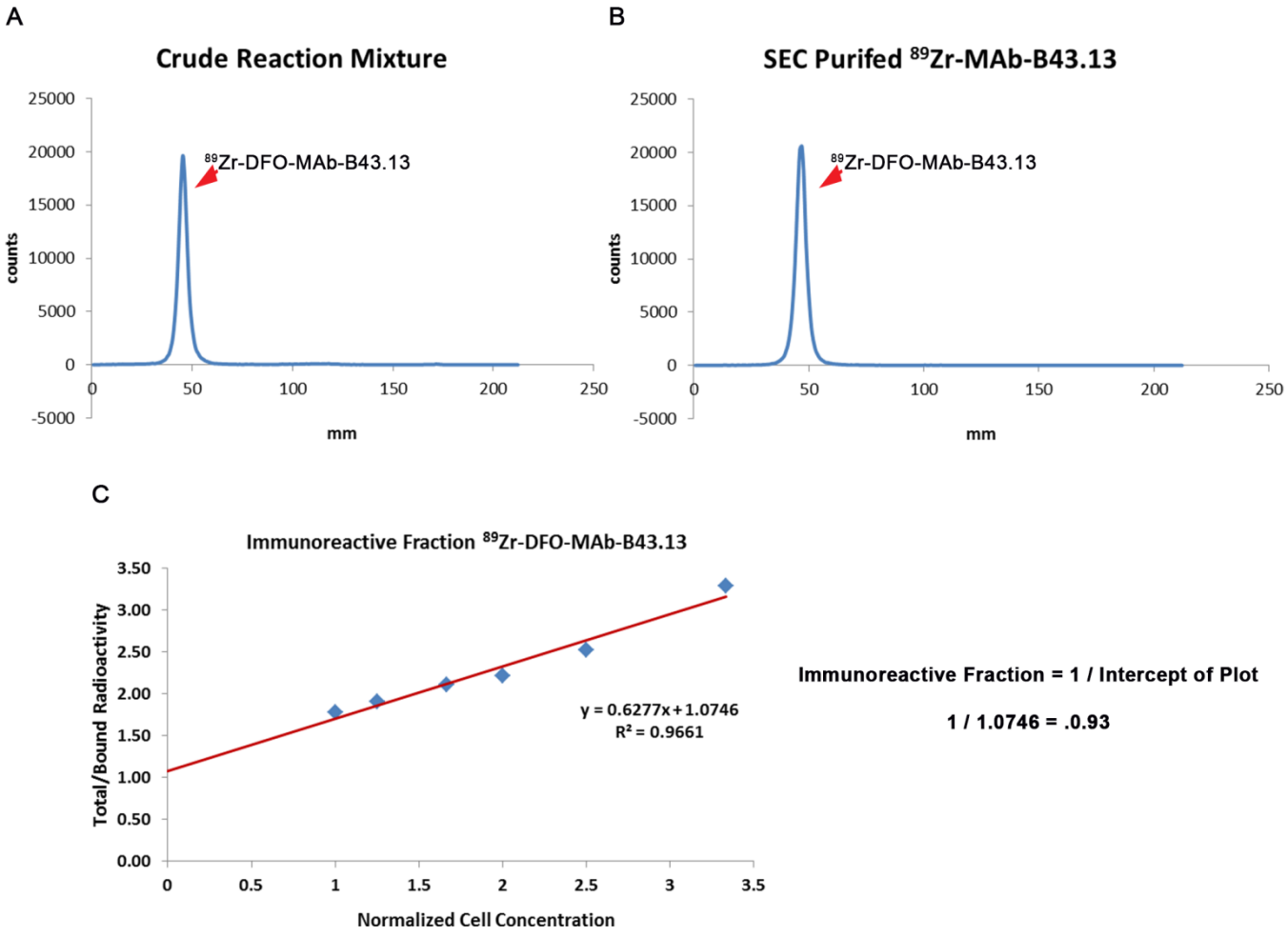

Fig 5.5: ^{89}Zr-DFO-MAb-B43.13 quality control and immunoreactivity test. **A)** Radio-TLC for the crude reaction mix of ^{89}Zr – labeling of DFO-MAb-B43.13; **B)** Radio-TLC of size exclusion PD-10 column purified ^{89}Zr-DFO-MAb-B43.13; **C)** Representative non-linear regression curve on a double inverse plot for measuring immunoreactive fraction of ^{89}Zr-DFO-MAb-B43.13 by Lindmo assay.

5.3.3 Acute Biodistribution:

In order to investigate the potential of ^{89}Zr-DFO-MAb-B43.13 for *in vivo* imaging, an acute biodistribution experiment was performed. To this end, mice bearing subcutaneous NIH:OVCAR-3 ovarian cancer xenografts (n = 4 per group) were injected via the tail vein with ^{89}Zr-DFO-MAb-B43.13 [15-20 μCi, (0.55 – 0.74 MBq), 4-6 μg] and euthanized at 24, 48, 72, 96, and 120 h post-injection, followed by the collection and weighing of tissues and an assay of the amount of ^{89}Zr activity in each tissue (Fig. 5.6, Tables 5.1 and 5.2). The amount of radioactivity in the tumor at 24 h was rather modest (7.2 ± 0.3 % ID/g) but increased significantly over the course of the experiment, reaching 22.3 ± 6.3 % ID/g at 72 h post-injection and a maximum of 24.7 ± 7.5 % ID/g at 120 h post-injection. As is typical for radioimmunoconjugates, a concomitant slow decrease in the amount of radioactivity in the blood was also observed, from 9.1 ± 0.6 % ID/g at 24 h to 4.0 ± 3.0 % ID/g at 120 h. The non-target organ with the highest activity concentration was the liver, with approximately ~15% ID/g at all time points in the experiment. All other organs including heart, lung, liver, spleen, stomach, large and small intestine, kidney, uterus/ovaries, muscle, and bone displayed activity concentrations often well below 5% ID/g. As a control, an additional cohort of mice (n=4) was co-injected 480 μg unlabeled DFO-MAb-B43.13 in order to saturate the antigen and thus illustrate selective blocking. Critically, the blocking experiment lowered the uptake of the radioimmunoconjugate in the tumor from 22.29 ± 6.3 % ID/g to 7.56 ± 3.2 %

ID/g at 72 h post-injection, clearly indicating that ^{89}Zr-DFO-MAb-B43.13 selectively targets the CA125 antigen.

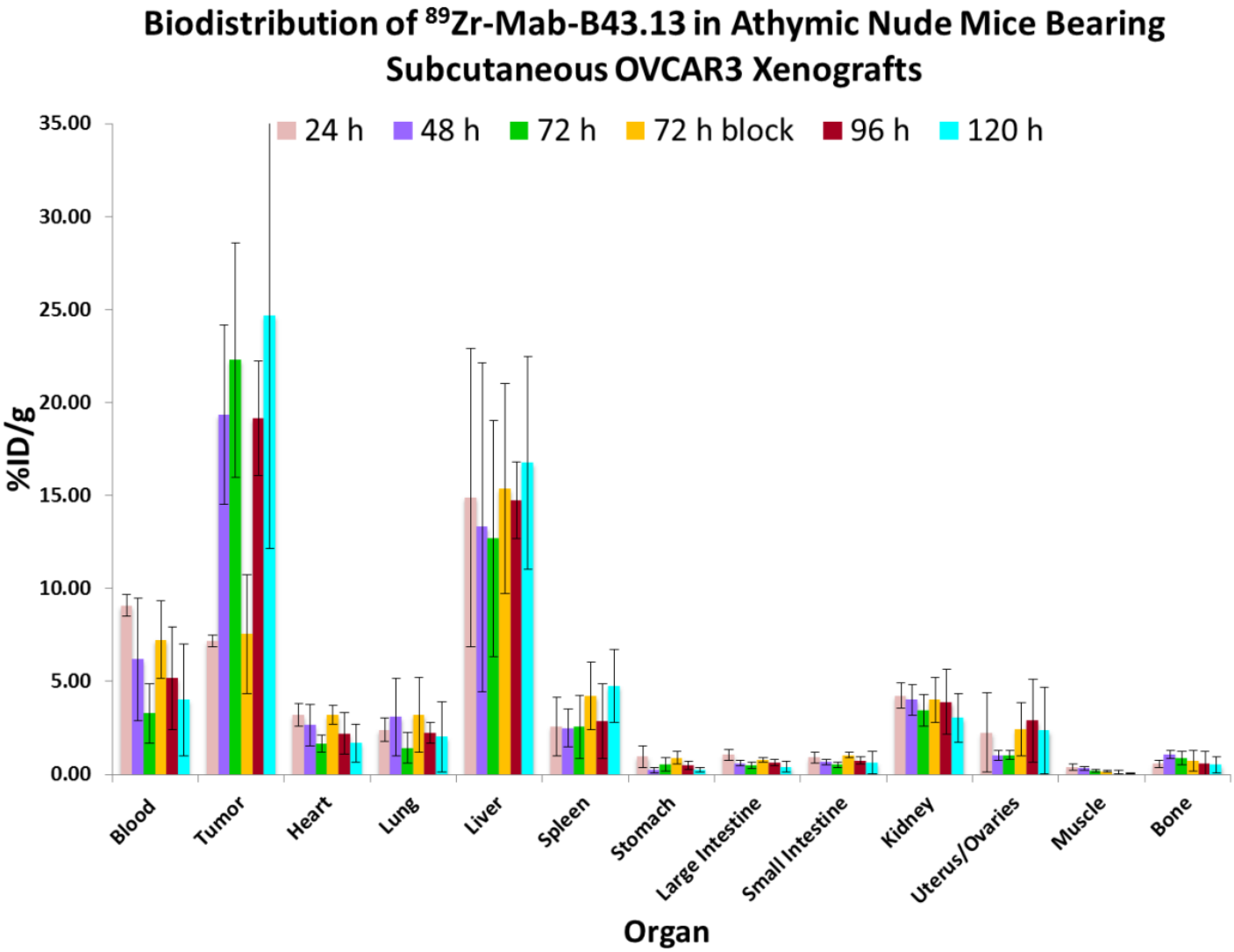

Figure 5.6: Biodistribution analysis. Bar diagram representation for *ex vivo* acute biodistribution data of the OVCAR3 tumors and various organs from xenograft mice injected with ^{89}Zr-DFO-MAb-B43.13 [15-20 μCi, (0.55 – 0.74 MBq), 4-6 μg] and euthanized at 24, 48, 72, 96, and 120 h post-injection. The Y axis represents ^{89}Zr radioactivity uptake represented as % injected dose per gram (% ID/g).

	24 h	48 h	72 h	72 h block	96 h	120 h
Blood	9.1 ± 0.6	6.2 ± 3.3	3.3 ± 1.6	7.2 ± 2.1	5.2 ± 2.8	4 ± 3
Tumor	7.2 ± 0.3	19.3 ± 4.8	22.3 ± 6.3	7.6 ± 3.2	19.2 ± 3.1	24.7 ± 7.5
Heart	3.2 ± 0.6	2.6 ± 1.1	1.6 ± 0.5	3.2 ± 0.5	2.2 ± 1.1	1.7 ± 1
Lung	2.4 ± 0.6	3.1 ± 2.1	1.4 ± 0.8	3.2 ± 2	2.2 ± 0.5	2 ± 1.9
Liver	14.9 ± 8	13.3 ± 8.8	12.7 ± 6.4	15.4 ± 5.6	14.7 ± 2.1	16.8 ± 5.7
Spleen	2.6 ± 1.6	2.5 ± 1	2.6 ± 1.7	4.2 ± 1.8	2.9 ± 2	4.8 ± 2
Stomach	1.0 ± 0.6	0.2 ± 0.1	0.5 ± 0.4	0.9 ± 0.3	0.5 ± 0.2	0.2 ± 0.1
Large Intestine	1.1 ± 0.3	0.6 ± 0.2	0.5 ± 0.2	0.8 ± 0.1	0.6 ± 0.2	0.4 ± 0.3
Small Intestine	0.9 ± 0.3	0.7 ± 0.1	0.5 ± 0.1	1 ± 0.1	0.7 ± 0.2	0.6 ± 0.6
Kidney	4.2 ± 0.7	4 ± 0.8	3.5 ± 0.9	4 ± 1.2	3.9 ± 1.7	3 ± 1.3
Uterus/Ovaries	2.2 ± 2.1	1.0 ± 0.3	1.0 ± 0.3	2.4 ± 1.4	2.9 ± 2.2	2.4 ± 2.3
Muscle	0.4 ± 0.2	0.3 ± 0.1	0.2 ± 0.1	0.2 ± 0.1	0.1 ± 0.1	0.1 ± 0.1
Bone	0.6 ± 0.2	1.1 ± 0.2	0.9 ± 0.4	0.7 ± 0.6	0.6 ± 0.6	0.5 ± 0.4

Table 5.1: *Ex vivo* biodistribution data for ^{89}Zr-DFO-MAb-B43.13 versus time in mice bearing subcutaneous OVCAR3 xenografts (n=4 for each time point). Mice were administered ^{89}Zr-DFO-MAb-B43.13 (0.55 – 0.75 MBq [15-20 μCi] in 200 μL 0.9% sterile saline) via tail vein injection (t = 0). For the 72 h time point, an additional cohort of animals were given ^{89}Zr-DFO-MAb-B43.13 with dramatically lowered specific activity (LSA), achieved by the coinjection of the standard dose of the ^{89}Zr-labeled construct mixed with 480 μg of cold, unlabeled DFO-MAb-B43.13.

	24 h	48 h	72 h	72 h block	96 h	120 h
Tumor/Blood	0.8 ± 0.1	3.1 ± 1.8	6.8 ± 3.8	1.0 ± 0.5	3.7 ± 2.1	6.2 ± 5.0
Tumor/Heart	2.2 ± 0.4	7.3 ± 3.6	13.5 ± 5.4	2.4 ± 1.1	8.7 ± 4.6	14.7 ± 10.0
Tumor/Lung	3 ± 0.8	6.3 ± 4.5	15.6 ± 10	2.4 ± 1.8	8.6 ± 2.5	12.2 ± 12.0
Tumor/Liver	0.5 ± 0.3	1.5 ± 1.0	1.8 ± 1.0	0.5 ± 0.3	1.3 ± 0.3	1.5 ± 0.7
Tumor/Spleen	2.8 ± 1.7	7.8 ± 3.7	8.7 ± 6.3	1.8 ± 1.1	6.7 ± 4.8	5.2 ± 2.7
Tumor/Stomach	7.4 ± 4.5	83.9 ± 55.7	41.8 ± 32.3	8.6 ± 4.9	38.5 ± 18.5	106.1 ± 65.4
Tumor/Large Intestine	6.8 ± 2	32.4 ± 11.5	45.9 ± 20.6	9.8 ± 4.3	30.9 ± 10.1	61.4 ± 49.7
Tumor/Small Intestine	7.9 ± 2.6	29.6 ± 9.6	43.4 ± 16.7	7.3 ± 3.3	25.6 ± 7.4	38.9 ± 38.1
Tumor/Kidney	1.7 ± 0.3	4.8 ± 1.6	6.5 ± 2.4	1.9 ± 1.0	4.9 ± 2.3	8.1 ± 4.3
Tumor/Uterus + Ovary	3.2 ± 3.1	19.3 ± 7.0	21.5 ± 8	3.1 ± 2.3	6.6 ± 5.3	10.5 ± 10.8
Tumor/Muscle	18.5 ± 8.5	60.4 ± 23.6	114.4 ± 46.6	47.5 ± 24.7	171.2 ± 144.9	565.4 ± 256.2
Tumor/Bone	12.6 ± 4.6	18.2 ± 6.1	25.7 ± 13.1	10.3 ± 9.3	32 ± 33.8	48.4 ± 44.3

Table 5.2: Tumor-to-tissue activity ratios for ^{89}Zr-DFO-MAb-B43.13 versus time in mice bearing subcutaneous NIH:OVCAR-3 xenografts (n = 4 for each time point).

5.3.4 Small animal imaging:

Small animal PET imaging experiments were employed to further investigate the *in vivo* behavior of ^{89}Zr-DFO-MAb-B43.13. Preliminary experiments with bilateral tumor xenograft mice revealed selective targeting of the ^{89}Zr-DFO-MAb-B43.13 in NIH:OVCAR-3 tumors and minimal non-specific uptake in SKOV3 tumors with major accumulation of the radioactivity in the liver as an organ of metabolism and clearance of antibody-based radioimmunoconjugates (Fig. 5.7).

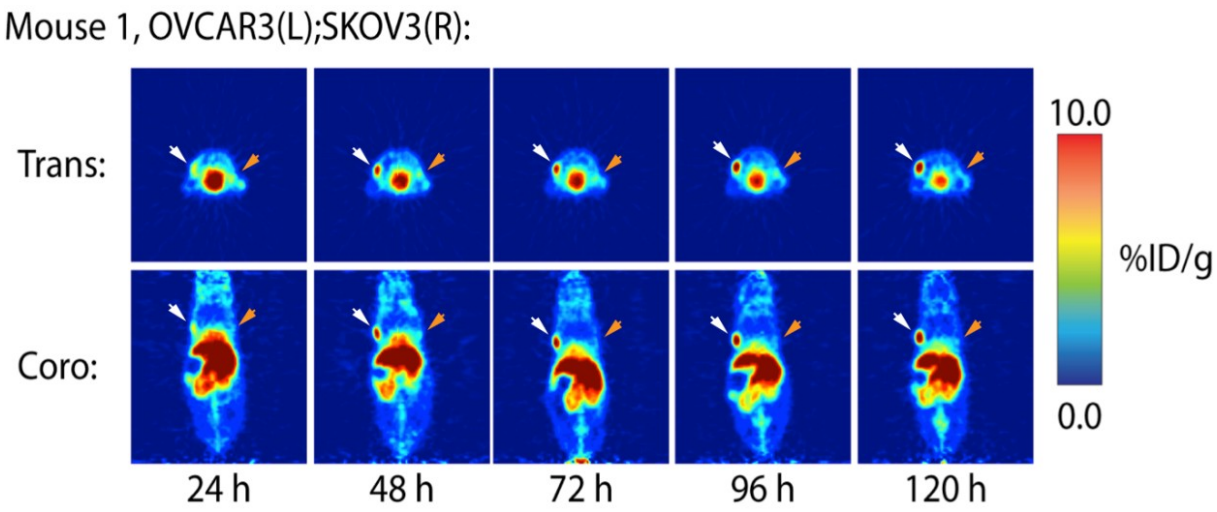

Figure 5.7: *In vivo* small animal PET imaging. Representative transverse and coronal PET images of ^{89}Zr-DFO-MAb-B43.13 (7 – 10 MBq [189-270 μCi] injected via tail vein in 200 μL 0.9 % sterile saline) in athymic nude mice bearing bilateral subcutaneous CA125-expressing NIH:OVCAR-3 xenografts on the left shoulder (indicated by white arrows) and CA125-negative SKOV3 on the right shoulder (indicated by orange arrows). Images were taken between 24 and 120 h post-injection.

In the experiments conducted with mice bearing subcutaneous NIH:OVCAR-3 tumor xenografts alone (n=4), ^{89}Zr-DFO-MAb-B43.13 (275-325 μCi; 10.2 – 12.0 MBq) was injected via the tail vein and the mice were imaged at 24, 48, 72, 96, and 120 h post-injection (Figs. 5.8 - 5.11).

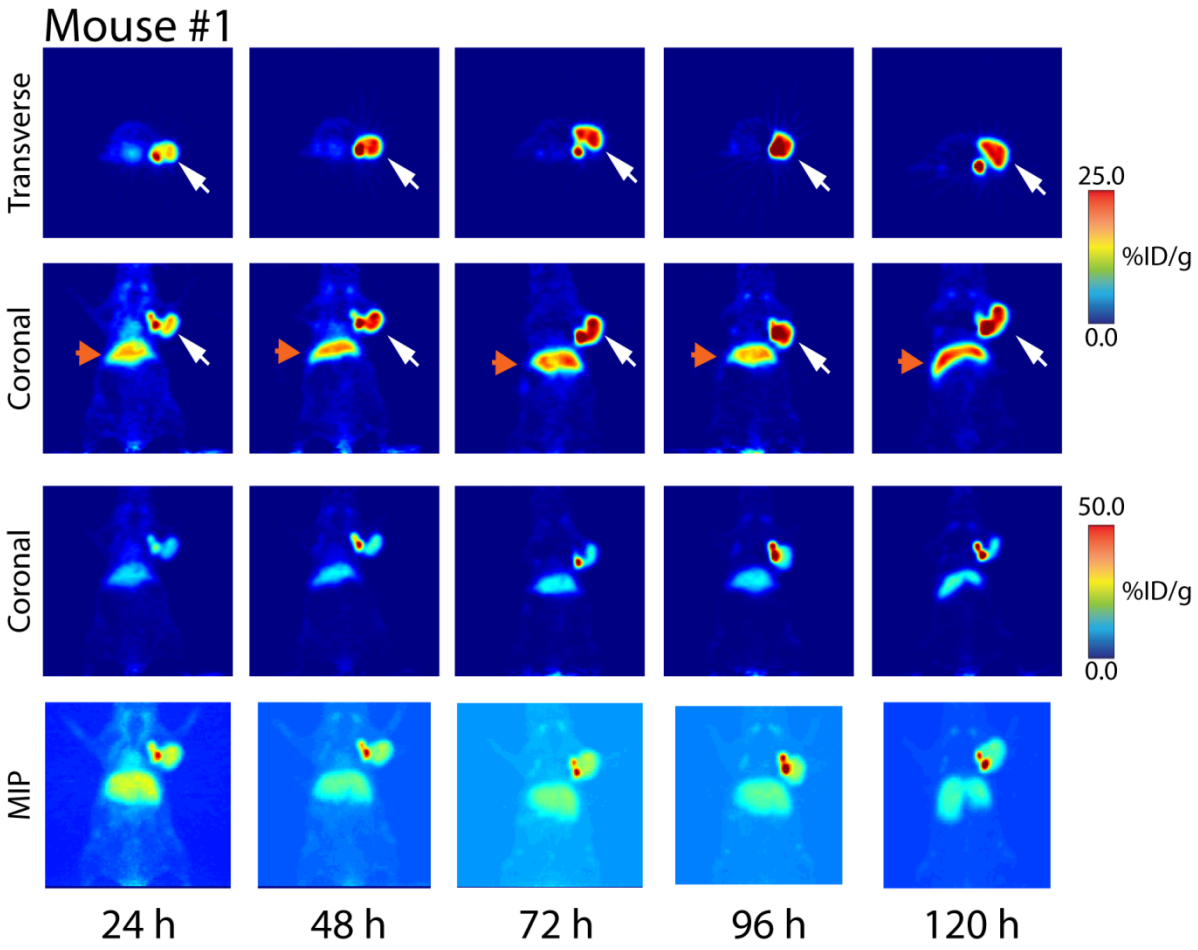

Figure 5.8: *In vivo* small animal PET imaging. Transverse and coronal PET images of ^{89}Zr-DFO-MAb-B43.13 (10.2 – 12.0 MBq [275-325 µCi] injected via tail vein in 200 µL 0.9 % sterile saline) in athymic nude mouse # 1 bearing subcutaneous CA125-expressing NIH:OVCAR-3 xenografts on the right shoulder. Images were taken between 24 and 120 h post-injection. Images in the top 2 panels are scaled with signal maxima set at 25 % ID/g, the middle set of coronal images are scaled with signal maxima set at 50 % ID/g. The bottom panel represents maximum intensity projection (MIP) images at all corresponding time points of evaluation. White arrow indicates the tumor, orange arrow indicates the liver.

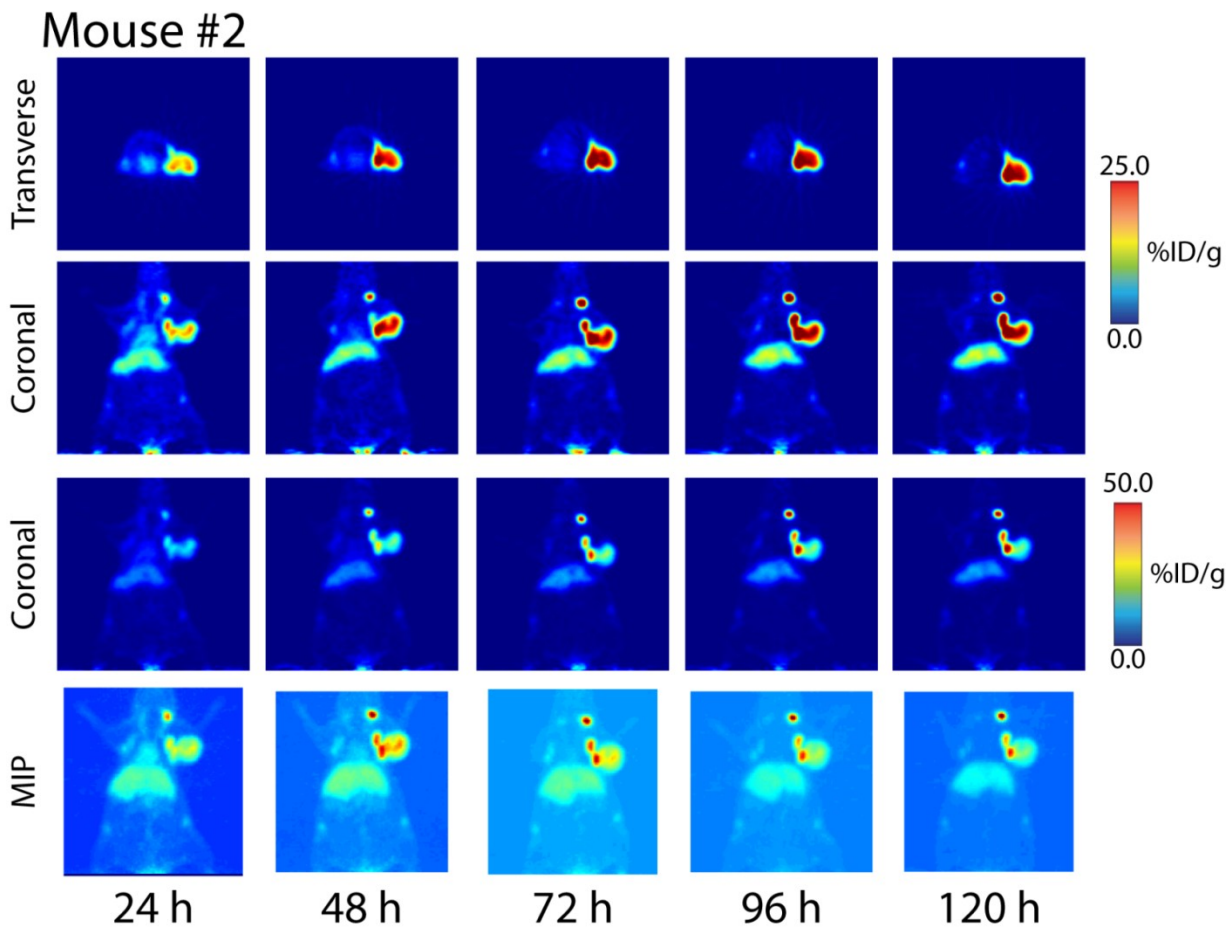

Figure 5.9: *In vivo* small animal PET imaging. Transverse and coronal PET images of ^{89}Zr-DFO-MAb-B43.13 (10.2 – 12.0 MBq [275-325 µCi] injected via tail vein in 200 µL 0.9 % sterile saline) in athymic nude mouse # 2 bearing subcutaneous CA125-expressing NIH:OVCAR-3 xenografts on the right shoulder. Images were taken between 24 and 120 h post-injection. Images in the top 2 panels are scaled with signal maxima set at 25 % ID/g, the middle set of coronal images are scaled with signal maxima set at 50 % ID/g. The bottom panel represents maximum intensity projection (MIP) images at all corresponding time points of evaluation.

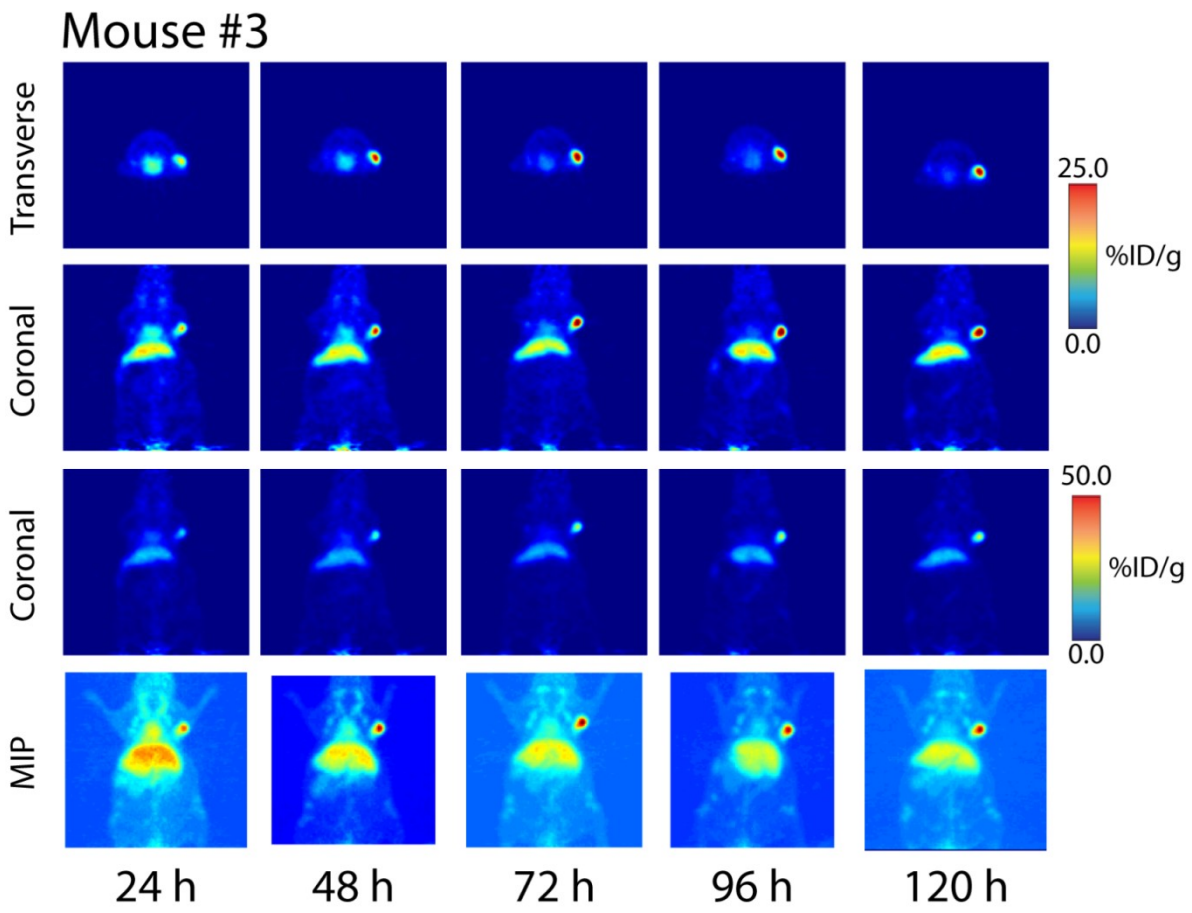

Figure 5.10: *In vivo* small animal PET imaging. Transverse and coronal PET images of ^{89}Zr-DFO-MAb-B43.13 (10.2 – 12.0 MBq [275-325 μCi] injected via tail vein in 200 μL 0.9 % sterile saline) in athymic nude mouse # 3 bearing subcutaneous CA125-expressing NIH:OVCAR-3 xenografts on the right shoulder. Images were taken between 24 and 120 h post-injection. Images in the top 2 panels are scaled with signal maxima set at 25 % ID/g, the middle set of coronal images are scaled with signal maxima set at 50 % ID/g. The bottom panel represents maximum intensity projection (MIP) images at all corresponding time points of evaluation.

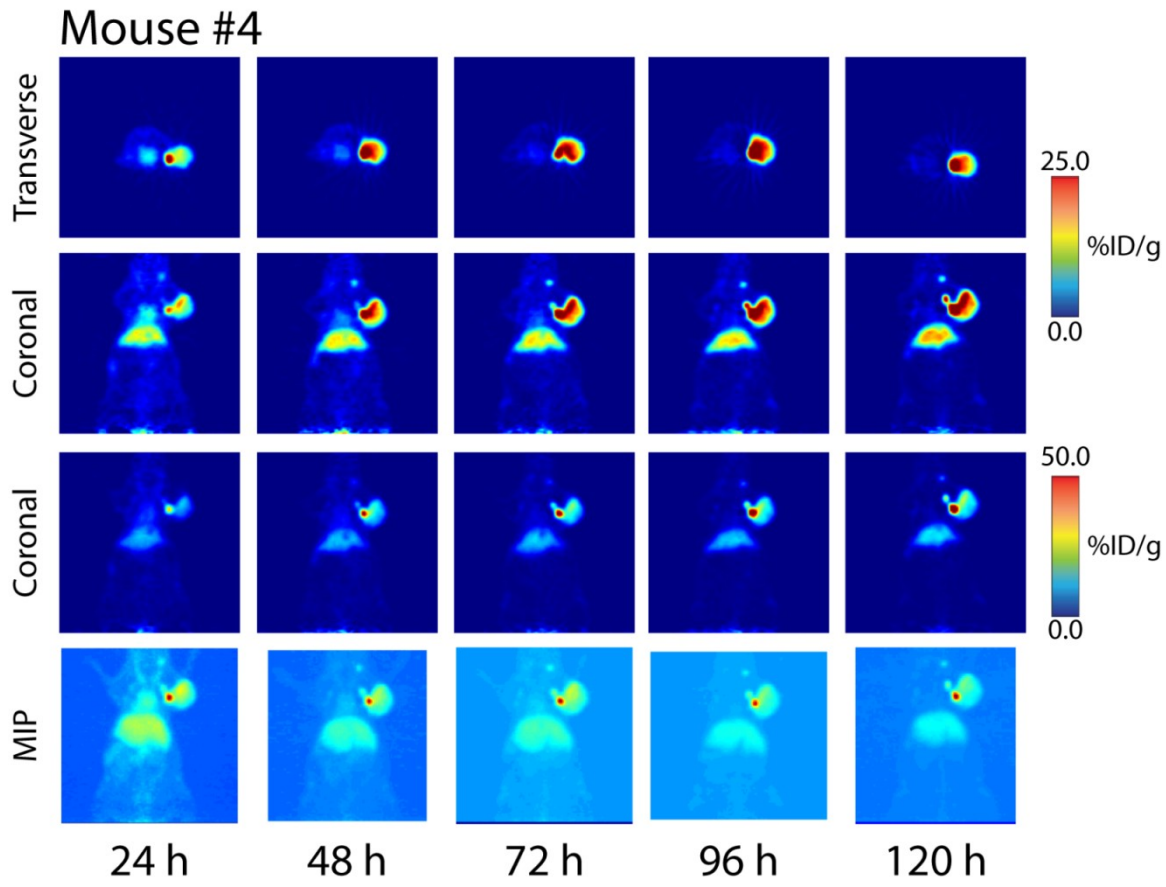

Figure 5.11: *In vivo* small animal PET imaging. Transverse and coronal PET images of ^{89}Zr-DFO-MAb-B43.13 (10.2 – 12.0 MBq [275-325 µCi] injected via tail vein in 200 µL 0.9 % sterile saline) in athymic nude mouse # 4 bearing subcutaneous CA125-expressing NIH:OVCAR-3 xenografts on the right shoulder. Images were taken between 24 and 120 h post-injection. Images in the top 2 panels are scaled with signal maxima set at 25 % ID/g, the middle set of coronal images are scaled with signal maxima set at 50 % ID/g. The bottom panel represents maximum intensity projection (MIP) images at all corresponding time points of evaluation.

The PET images from these animals largely confirm the data obtained from the acute biodistribution study. Even at early time points, the tumor can be clearly delineated from non-target tissue, and the amount of radiotracer in the tumor increases to a maximum of ~ 68.27 ± 17.26 %ID/g. Further, the organ with the highest amount of uptake was the liver, while all other non-target tissues displayed low levels of uptake. Time activity curves generated from the immuno-PET images at all the time points showing mean % ID/g and SUV_{max} from the tumor, muscle, heart, liver and kidneys of all animals (n=4) are presented in Fig. 5.12, Table 5.3 and Fig. 4.13, Table 5.4 respectively.

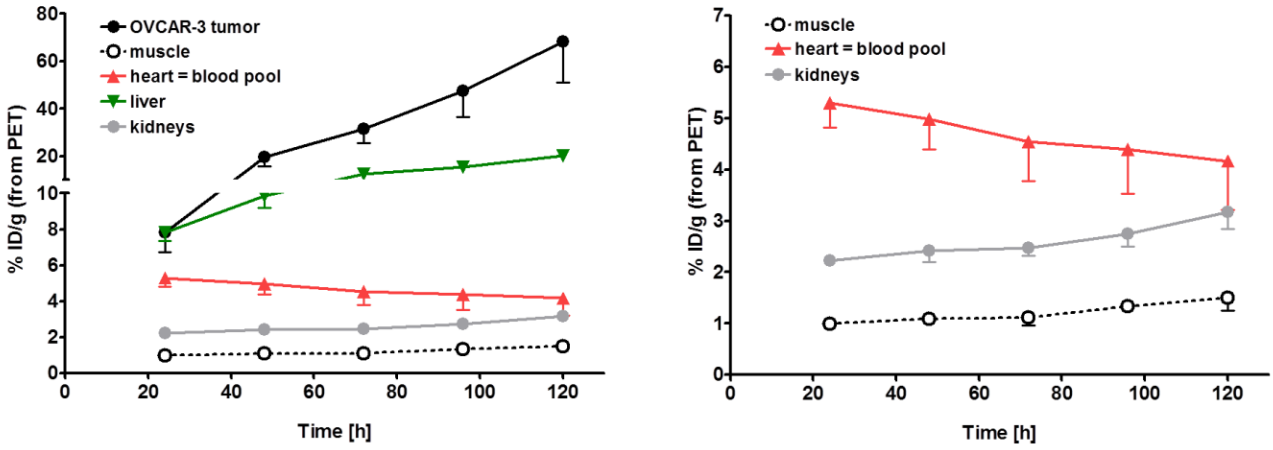

Figure 5.12: *In vivo* small animal PET imaging analysis. Time activity curves generated from immuno-PET images of athymic nude mice (n=4) bearing subcutaneous CA125-expressing NIH:OVCAR-3 ovarian cancer xenografts, injected with ^{89}Zr-DFO-MAb-B43.13 (10.2 – 12.0 MBq [275-325 µCi]). The data points represent uptake of radiotracer in various organs between 24 – 120 h post-injection. Data on X axis is represented in % ID/g.

	24 h	**48 h**	**72 h**	**96 h**	**120 h**
Tumor	7.83 ± 1.09	19.61 ± 3.72	31.58 ± 6.14	47.49 ± 10.92	68.27 ± 17.26
Muscle	1 ± 0.06	1.09 ± 0.07	1.12 ± 0.15	1.34 ± 0.11	1.50 ± 0.25
Heart	5.31 ± 0.49	4.98 ± 0.59	4.54 ± 0.76	4.39 ± 0.86	4.17 ± 0.95
Liver	7.84 ± 0.46	9.86 ± 0.67	12.96 ± 1.09	15.40 ± 0.81	20.20 ± 1.86
Kidney	2.23 ± 0.10	2.42 ± 0.23	2.47 ± 0.15	2.75 ± 0.24	3.17 ± 0.33

Table 5.3: *In vivo* biodistribution profile of ^{89}Zr-DFO-MAb-B43.13 in various organs as derived from immuno-PET images recorded between 24 – 120 h post-injection. All values are represented in % ID/g.

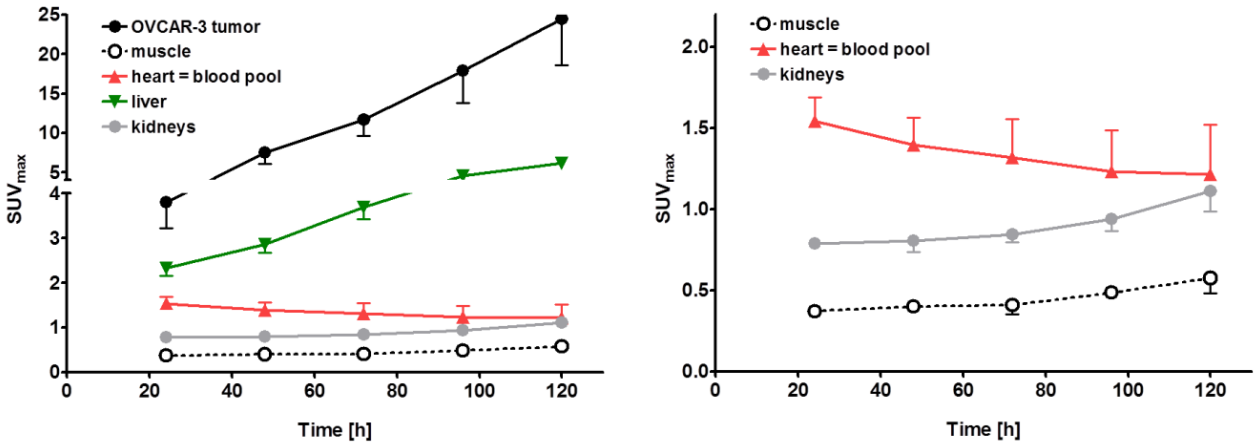

Figure 5.13: *In vivo* small animal PET imaging analysis. Time activity curves generated from immuno-PET images of athymic nude mice (n=4) bearing subcutaneous CA125-expressing NIH:OVCAR-3 xenografts, injected with ^{89}Zr-DFO-MAb-B43.13 (10.2 – 12.0 MBq [275-325 µCi]). The data points represent uptake of radiotracer in various organs between 24 – 120 h post-injection. Data on X axis is represented in SUV_{max}: Standardized Uptake Value.

	24 h	**48 h**	**72 h**	**96 h**	**120 h**
Tumor	3.81 ± 0.59	7.53 ± 1.42	11.72 ± 2.09	17.88 ± 4.05	24.48 ± 5.82
Muscle	0.37 ± 0.03	0.40 ± 0.03	0.41 ± 0.06	0.49 ± 0.04	0.58 ± 0.09
Heart	1.54 ± 0.15	1.40 ± 0.17	1.32 ± 0.24	1.23 ± 0. 25	1.22 ± 0.30
Liver	2.33 ± 0.16	2.87 ± 0.20	3.69 ± 0.27	4.54 ± 0.25	6.15 ± 0.61
Kidney	0.79 ± 0.03	0.81 ± 0.07	0.84 ± 0.05	0.94 ± 0.07	1.11 ± 0.12

Table 5.4: *In vivo* biodistribution profile of ^{89}Zr-DFO-MAb-B43.13 in various organs as derived from immuno-PET images recorded between 24 – 120 h post-injection. All values are represented in SUV_{max}.

The most intriguing aspect of the PET images, however, was the amount of uptake of the radiotracer observed in the lymph nodes proximal to the tumor. The brachial and axillary lymph nodes proximal to the tumor displayed activity concentrations ~ 50% ID/g, while the analogous distal lymph nodes displayed little to no uptake of the tracer (Fig. 5.14).

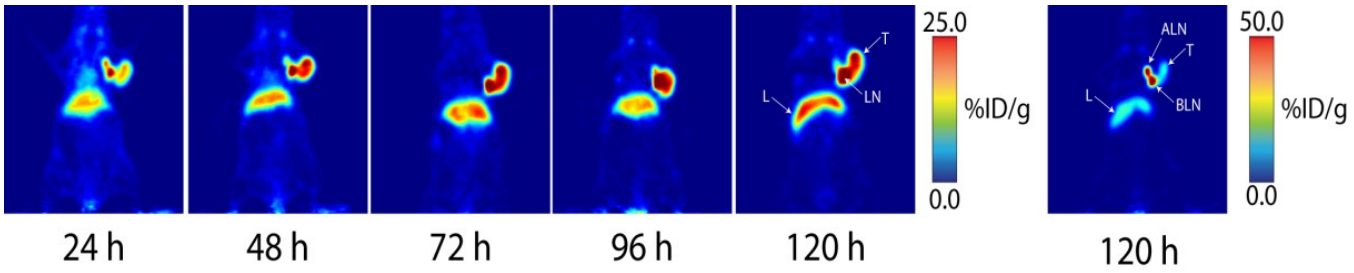

Figure 5.14: *In vivo* small animal PET imaging analysis. Coronal PET images of ^{89}Zr-DFO-MAb-B43.13 (10.2 – 12.0 MBq [275-325 μCi] injected via tail vein in 200 μL 0.9 % sterile saline) in athymic nude mice bearing subcutaneous, CA125-expressing NIH:OVCAR-3 ovarian cancer xenografts between 24 and 120 h post-injection. T = tumor; LN = lymph nodes; L = liver; ALN= axillary lymph node; BLN = brachial lymph node.

Interestingly, the uptake of the radiotracer in the proximal lymph nodes seemed to vary from animal to animal. In all cases, high levels of uptake were observed in the proximal brachial and axillary nodes, but in one case, high levels of uptake of the radiotracer were observed in the cervical lymph node proximal to the tumor (Fig. 5.15).

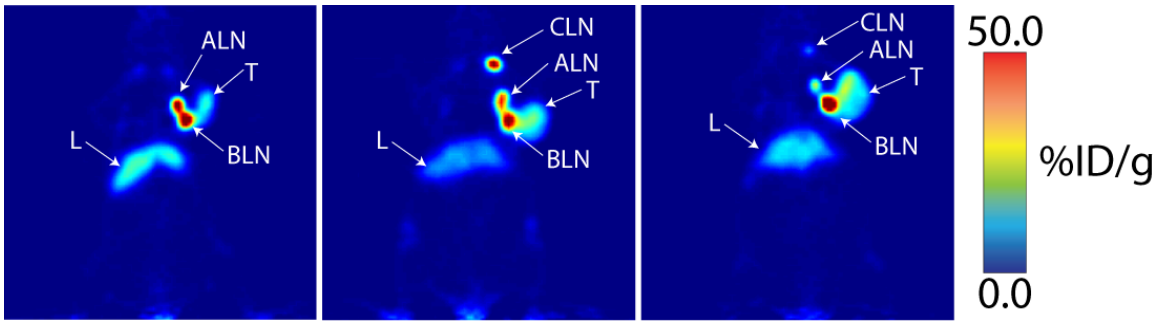

Figure 5.15: *In vivo* small animal PET imaging analysis. Coronal PET images of ^{89}Zr-DFO-MAb-B43.13 (10.2 – 12.0 MBq [275-325 µCi] injected via tail vein in 200 µL 0.9 % sterile saline) in three different athymic nude mice bearing subcutaneous CA125-expressing NIH:OVCAR-3 ovarian cancer xenografts at 120 h post-injection. T = tumor; LN = lymph nodes; L = liver; ALN= axillary lymph node; BLN = brachial lymph node; CLN = cervical lymph node.

5.3.5 Lymph node involvement:

In order to further investigate this phenomenon, an additional set of small animal PET imaging and acute biodistribution experiments were performed to compare the uptake of ^{89}Zr-DFO-MAb-B43.13 with that of a non-specific radioimmunoconjugate – ^{89}Zr-DFO-IgG. The DFO-IgG conjugate was prepared in a manner analogous to DFO-MAb-B43.13 and was labeled with ^{89}Zr via standard protocols to achieve high radiochemical purity (> 99 %) and specific activity (5.6 mCi/mg). For small animal imaging, 190 – 243 μCi (7 – 9 MBq) of ^{89}Zr-DFO-MAb-B43.13 or ^{89}Zr-DFO-IgG was injected into the tail vein of NIH:OVCAR-3 xenograft bearing mice (n=3 per group) and images were obtained at 24, 48, 72, 96, and 120 h post-injection (Figs. 5.16 and 5.17).

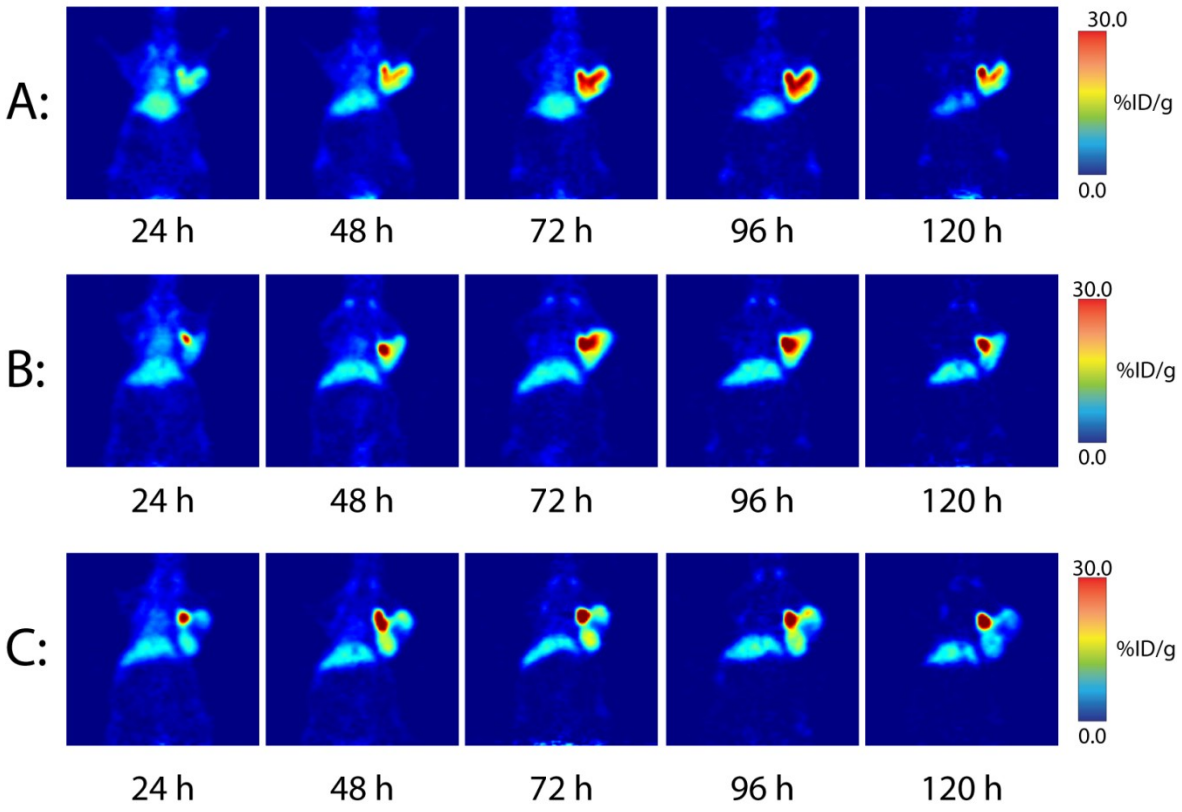

Figure 5.16: *In vivo* small animal PET imaging analysis. **A – C**) Coronal PET images of ^{89}Zr-DFO-MAb-B43.13 (7 – 9 MBq [190-243 µCi] injected via tail vein in 200 µL 0.9 % sterile saline) in athymic nude mice (n = 3) bearing subcutaneous CA125-expressing NIH:OVCAR-3 xenografts. Images were taken between 24 and 120 h post-injection and scaled using a signal maxima of 30 % ID/g.

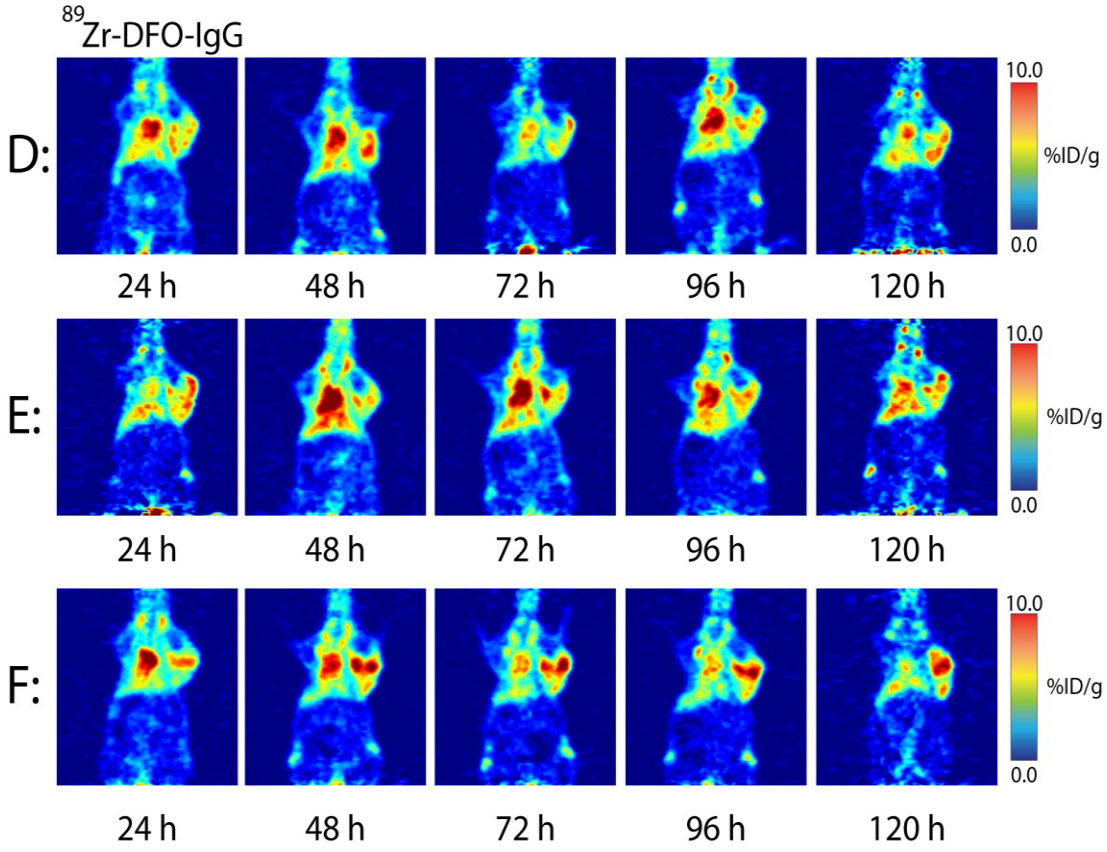

Fig 5.17: *In vivo* small animal PET imaging analysis. **D – F**) Coronal PET images of ^{89}Zr-DFO-IgG (7 – 9 MBq [190-243 μCi] injected via tail vein in 200 μL 0.9 % sterile saline) in athymic nude mice (n = 3) bearing subcutaneous CA125-expressing NIH:OVCAR-3 xenografts. Images taken between 24 and 120 h post-injection and scaled using a signal maxima of 10 % ID/g.

For acute biodistribution studies, mice bearing subcutaneous NIH:OVCAR-3 xenografts (n = 4 per group) were injected via the tail vein with either ^{89}Zr-DFO-MAb-B43.13 or ^{89}Zr-DFO-IgG [15-20 μCi, (0.5 – 0.7 MBq) 4 - 6 μg] and euthanized at 72 h post-injection, followed by the collection and weighing of tissues and an assay of the amount of ^{89}Zr activity in each tissue (Table 5.5).

	^{89}Zr-DFO-antiCA125	^{89}Zr-DFO-IgG
Blood	1.3 ± 1	9.9 ± 0.6
Tumor	18 ± 3.4	6.1 ± 0.4
Proximal Brachial Node	56.6 ± 39.4	6.1 ± 5
Proximal Axillary Node	104.8 ± 45.1	2.1 ± 0.9
Distal Brachial Node	6.4 ± 3.7	6 ± 2.7
Distal Axillary Node	3.7 ± 3.2	5.6 ± 4.5

Table 5.5: *Ex vivo* Biodistribution data for ^{89}Zr-DFO-antiCA125 and ^{89}Zr-DFO-IgG at 120 h post-injection in mice bearing subcutaneous NIH:OVCAR-3 xenografts (n=4). Mice were administered ^{89}Zr-DFO-antiCA125 or ^{89}Zr-DFO-IgG (0.55 – 0.75 MBq [15-20 μCi] in 200 μL 0.9 % sterile saline) via tail vein injection (t = 0).

Not surprisingly, the ^{89}Zr-DFO-MAb-B43.13 displayed higher levels of uptake in the tumor (18.1 ± 3.4 % ID/g) compared to ^{89}Zr-DFO-IgG (6.1 ± 0.4 % ID/g), while the amount of ^{89}Zr-DFO-IgG in the blood (9.9 ± 0.6 % ID/g) was far greater than that of ^{89}Zr-DFO-MAb-B43.13 (1.3 ± 1.0 % ID/g). This was consistent with observations from small animal PET images. Furthermore, acute biodistribution studies revealed that in the case of ^{89}Zr-DFO-MAb-B43.13, the ipsilateral axillary

and brachial nodes proximal to the tumor displayed uptake values of 56.6 ± 39.4 %ID/g and 104.8 ± 45.1 % ID/g, respectively. These uptake values were in stark contrast with the analogous contralateral nodes distal from the tumor, which had uptake values of 6.3 ± 3.7 % ID/g (brachial) and 3.7 ± 3.2 % ID/g (axillary). This is also represented in Fig 5.18.

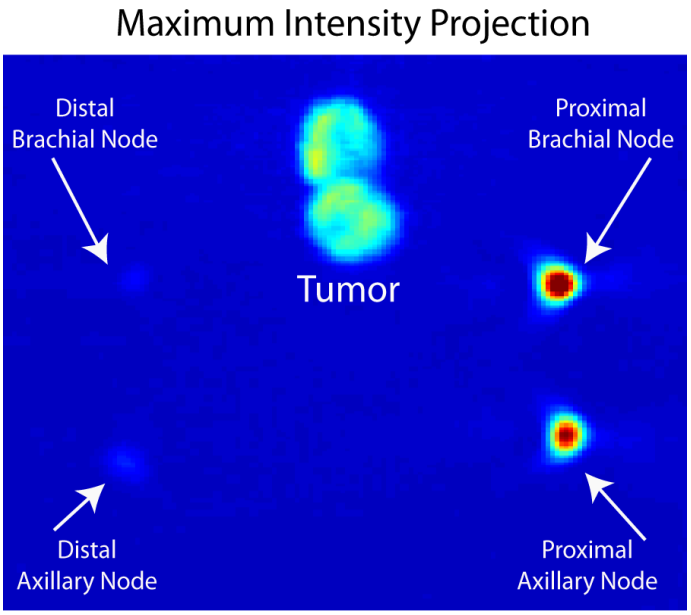

Figure 5.18: *Ex vivo* analysis. Digital autoradiograph of harvested tissues from NIH:OVCAR-3 bearing xenograft mouse injected with ^{89}Zr-DFO-MAb-B43.13 (7 – 9 MBq [190-243 μCi] injected via tail vein in 200 μL 0.9 % sterile saline) and sacrificed at 120 h p.i; tumor (top center), ipsilateral tumor proximal brachial lymph node (top right), ipsilateral tumor proximal axillary lymph node (bottom right), contralateral tumor distal brachial lymph node (top left) and contralateral tumor distal axillary lymph node (bottom left).

For the non-specific ^{89}Zr-DFO-IgG construct, these values were far lower and did not display significant differences between the proximal and distal lymph nodes. The proximal brachial and axillary nodes had activity concentrations of 6.1 ± 5.0 % ID/g and 2.1 ± 0.9 % ID/g, respectively, while the distal brachial and axillary nodes had activity concentrations of 5.9 ± 2.7 % ID/g and 5.6 ± 4.5 % ID/g, respectively.

5.3.6 *Ex vivo* analysis:

These observations led us to ask the question if this was a result of potential metastatic spread of epithelial ovarian cancer to these lymph nodes or a case of radioactive immunocomplexes of shed antigen draining into the ipsilateral proximal nodes. To this end, we performed *ex vivo* analysis after harvesting the relevant tissues – tumors, proximal and corresponding distal axillary and brachial lymph nodes from xenograft animals at the end of the experiments (120 h p.i).

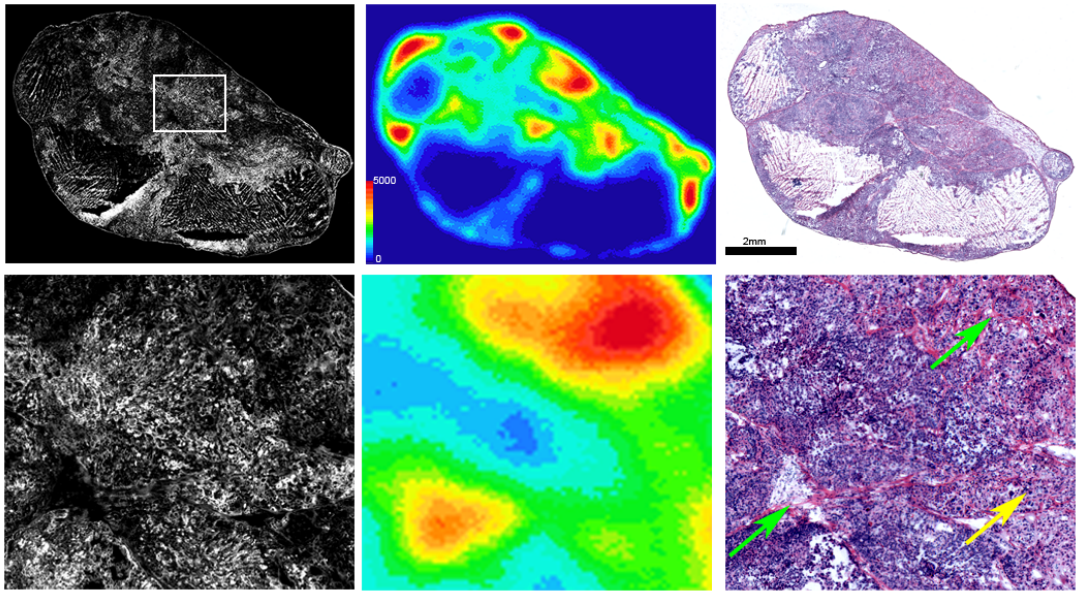

Figure 5.19: *Ex vivo* analysis of anti-CA125 MAb-targeted NIH:OVCAR-3 tumor using immunofluorescence (left panels), digital autoradiography (central panels) and immunohistochemistry (right panels). The images represent the relative distribution of ^{89}Zr-DFO-MAb-B43.13 and expression of CA125 in a human NIH:OVCAR-3 tumor xenografted in athymic nude mouse.

^{89}Zr-DFO-MAb-B43.13 distribution was heterogeneous, with regions of higher uptake in the periphery of the tumor, and less in the more central regions. There was very little activity associated with necrotic tumor regions. The high resolution images show ^{89}Zr-DFO-MAb-B43.13 uptake associated with areas of tumor stroma (green arrows), which are generally co-localized with tumor vasculature. Regions of CA125-positive tumor cells in close proximity to stromal regions (yellow arrow) also showed uptake of ^{89}Zr-DFO-MAb-B43.13.

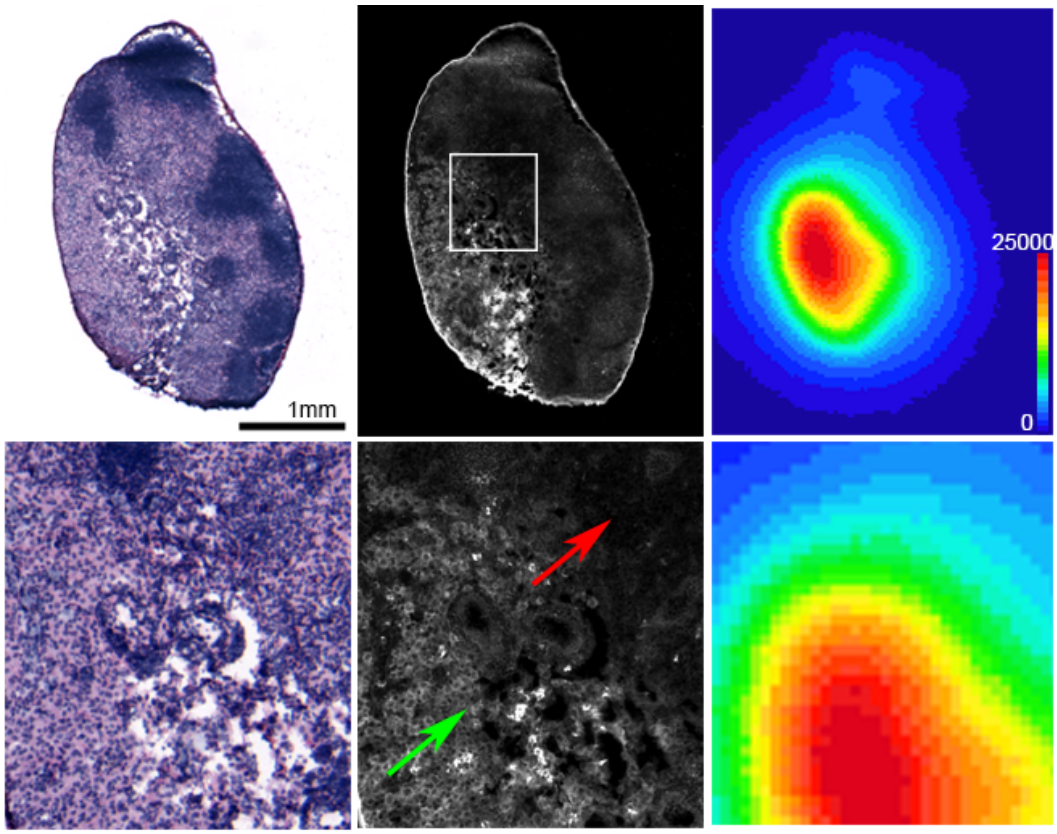

Figure 5.20: *Ex vivo* analysis of the tumor proximal brachial lymph node from an anti-CA125 MAb-targeted NIH:OVCAR-3 tumor xenograft mouse using immunofluorescence (left panels), digital autoradiography (central panels) and immunohistochemistry (right panels). The images represent the relative distribution of ^{89}Zr-DFO-MAb-B43.13 in the brachial lymph node in the ipsilateral chain proximal to the tumor.

CA125 staining was observed in discrete regions within the lymph node, but no tumor cells were observed. Uptake of ^{89}Zr-DFO-MAb-B43.13 was associated with regions of CA125 positivity (green arrow), but decreased in regions of low CA125 staining (red arrow).

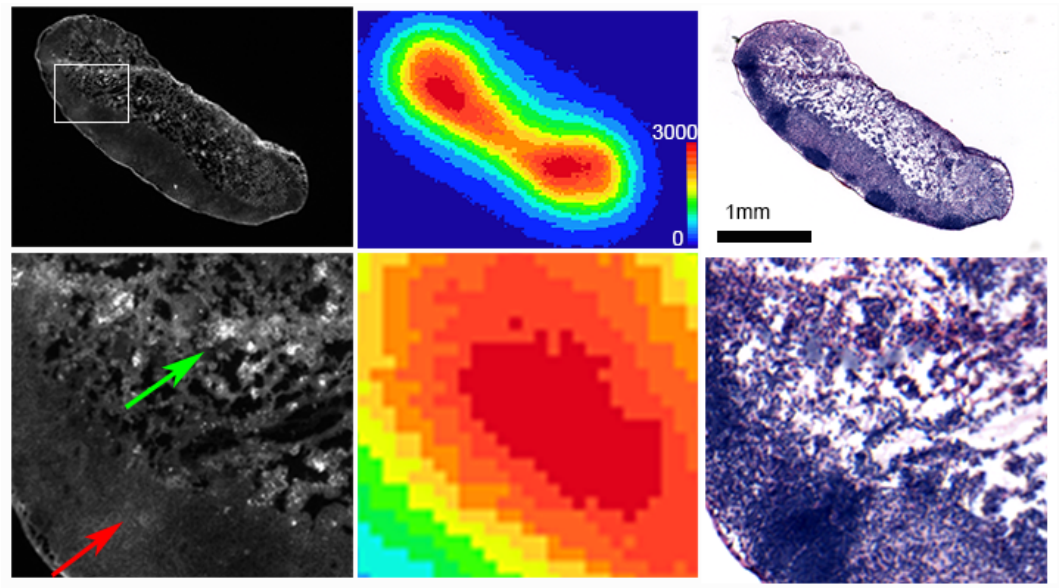

Figure 5.21: *Ex vivo* analysis of the non-tumor brachial lymph node from an anti-CA125 MAb-targeted NIH:OVCAR-3 tumor xenograft mouse using immunofluorescence(left panels), digital autoradiography (central panels) and immunohistochemistry (right panels). Uptake and relative distribution of ^{89}Zr-DFO-MAb-B43.13 in the brachial lymph node contralateral to the tumor location.

The appearance of this node was very similar to that of the ipsilateral tumor, with distinct heterogeneous staining of CA125, but no visible tumor cells. Again, uptake of ^{89}Zr-DFO-MAb-B43.13 was associated with regions of CA125 positivity (green arrow), but decreased in regions of low CA125 staining (red

arrow). However, it should be noted that the scale bar indicating the relative radioactive concentration on the autoradiographic images indicate that this lymph node contains a significantly lower ^{89}Zr-DFO-MAb-B43.13 concentration per unit area when compared to the ipsilateral node.

5.3.7 Histopathological Findings:

Histopathologic evaluation of the harvested and fixed tumor by a veterinarian pathologist at MSKCC, NY, revealed this tissue to be an ovoid neoplasm surrounded by a small amount of fibrous connective tissue, skeletal muscle, adipose tissue, and mammary glands. The neoplasm was composed of cells forming nests and papillary structures with lumens filled with proteinaceous fluid, and supported by a small to moderate amount of collagenous stroma. Cells were polygonal, with distinct borders, and a moderate amount of eosinophilic cytoplasm. The nuclei were oval, with finely stippled chromatin and one or two large prominent nucleoli. There was four fold anisokaryosis and multinucleated cells with an average of 55 mitoses per 400x fields. The tumor cells showed diffuse cytoplasmic staining upon performing immunohistochemical (IHC) staining for cytokeratin WSS.

Similar examination of the tumor proximal axillary lymph node revealed a lymphoid depletion of the paracortex, which is a normal finding in this strain. However, the paracortex had a focal area of coagulative necrosis. This area contained rare single polygonal cells with large nuclei, which resemble the cells described above in the tumor. However, upon immunohistochemical staining for

cytokeratin WSS, there were no positive cells and the area of necrosis was not present. On a deeper section stained with Haematoxylin and Eosin (H&E), the area of necrosis and atypical cells were absent. Histopathology performed on the the ipsilateral brachial and contralateral axillary and brachial showed no abnormal observations except for lymphoid depletion of the paracortex and cyst-like ectasia of some sinuses, which are normal findings in this strain.

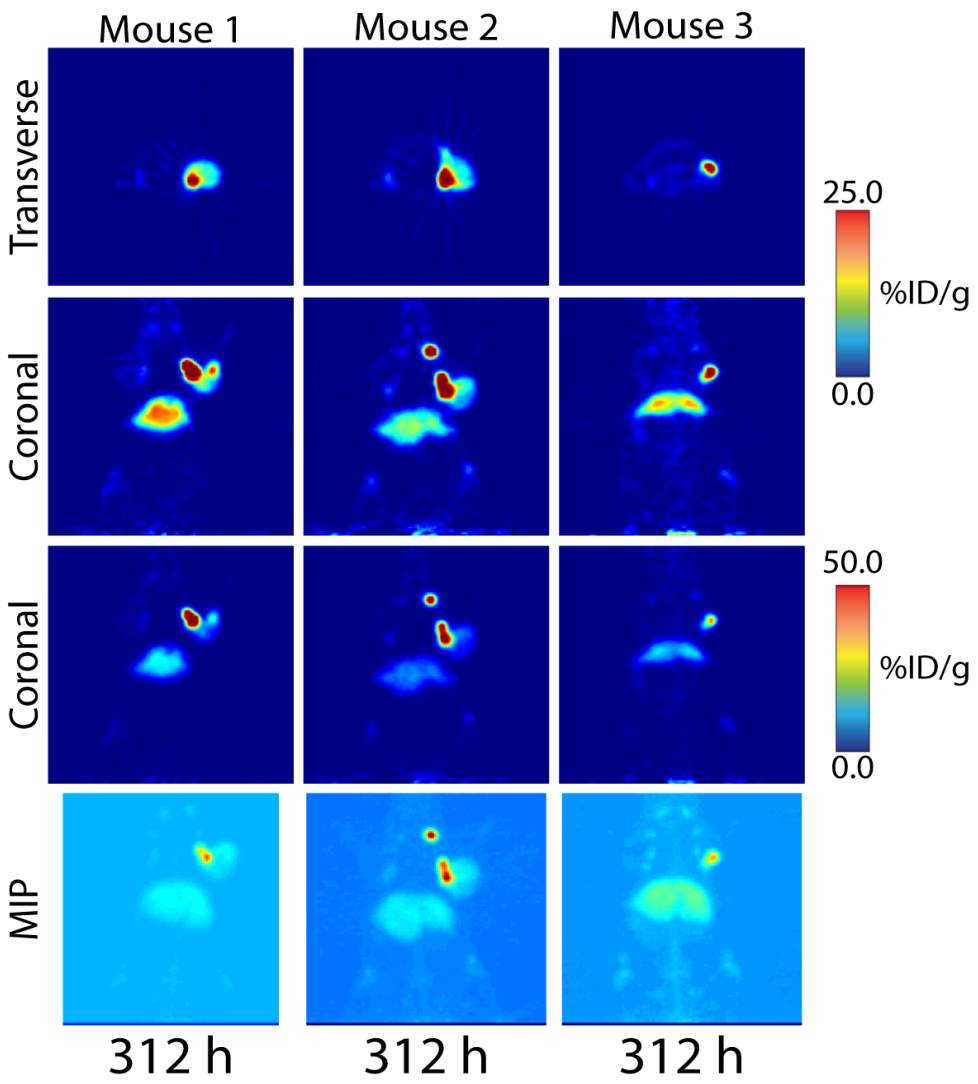

Figure 5.22: *In vivo* small animal PET imaging 312 h post-injection. Transverse and coronal PET images of ^{89}Zr-DFO-MAb-B43.13 (10.2 – 12.0 MBq [275-325 µCi] injected via tail vein in 200 µL 0.9% sterile saline) in athymic nude mice # 1, 2 and 3 bearing subcutaneous CA125-expressing OVCAR3 ovarian cancer xenografts at 312 h post-injection. Images in the top 2 panels are scaled with signal maxima set at 25 % ID/g, the middle set of coronal images are scaled with signal maxima set at 50 % ID/g. The bottom panel represents maximum intensity projection (MIP) images at all corresponding time points of evaluation.

5.4 Discussion:

Preparation of stable radioimmunoconjugates:

An impetus to generate novel antibodies and their derivatives for applications in targeted strategies such as immuno-PET for oncologic imaging has been accompanied by a need to use suitable radioisotopes that have a physical half-life compatible with the biological half-life of such antibody vectors. Despite its presence for decades, ^{89}Zr has recently gained popularity for its advantageous features[9] suited to immuno-PET strategies for imaging prostate specific membrane antigen,[17] and free prostate specific antigen,[18] in prostate cancer, Her2/neu in breast cancer,[19] CD8+ T cells in lymphomas,[20] CA19.9 in pancreatic cancer,[21] glypican3 in hepatocellular cancer,[22] L-type amino acid receptor in colorectal cancer[23] and many other neoplasms. In this chapter, we extended the potential for immuno-PET of epithelial ovarian cancer using the CA125 targeting MAb-B43.13 by radiolabeling it with ^{89}Zr. This enabled us to track the *in vivo* pharmacokinetic biodistribution of the full-length antibody radiotracer while allowing it to gain maximal tumor accretion up to 120 h post injection (p.i). This is a significant step forward in terms of the information we obtained from this study when compared with a ^{64}Cu-labeled version of the same antibody (presented in chapter 3 of this thesis), which was somewhat limited in its potential to deliver information only up to 48 h p.i due primarily to the physical half-life of the radioisotope.

Similar to the use of a tridentate azamacrocyclic chelator (NOTA) for ^{64}Cu-labeling of the MAb-B43.13 antibody, here we used desferrioxamine (DFO) – an

acyclic hexadentate siderophore with three hydroxamate groups for chelating radiometals such as $^{89}Zr^{4+}$. Owing to its ability for quantitative radiolabeling with ^{89}Zr in 1 hour at ambient room temperature and a demonstrated *in vitro* and *in vivo* stability with respect to demetallation, DFO has come to be the most widely used chelator for ^{89}Zr labeling of antibodies in immuno-PET.[12, 9, 24] In the present study, conjugation of an isothiocyanate-based bi-functional version of desferrioxamine (*p*-SCN-DFO) to the MAb-B43.13 in 10-fold molar excess resulted in ~ 4 molecules of DFO per MAb. Moreover, this did not compromise its immunoreactivity to the target antigen – CA125. This was reflected in the results from functional characterization of the DFO-MAb-B43.13 immunoconjugate via immunofluorescence and flow cytometry. Compared to the ^{64}Cu-NOTA-MAb-B43.13 study, the ratio of bifunctional chelator – to – MAb was increased in this study with intent to improve the specific activity of the resultant radioimmunoconjugate by virtue of having a reasonably higher number of DFOs conjugated per MAb without compromising its immunoreactivity. This objective was achieved upon obtaining high isolated radiochemical yields of purified and high specific activity ^{89}Zr-DFO-MAb-B43.13, which retained its immunoreactivity to CA125 expressed on NIH:OVCAR-3 cells as analyzed by two different methods. Furthermore, the stability of DFO chelated ^{89}Zr in biological medium such as serum was demonstrated by a less than 4% transmetallation from ^{89}Zr-DFO-MAb-B43.13 over 7 days. Even if this may not exactly be the case *in vivo* due to catabolism of the radioimmunoconjugate by

active cellular processes, it is a good indicator to suggest the use of such a chelator as far as resistance to transmetallation is concerned.

***In vivo* radiopharmacologic profile**:

The acute biodistribution experiments provided an *ex vivo* evaluation representative of the *in vivo* radiopharmacologic profile for ^{89}Zr-DFO-MAb-B43.13 in xenograft mice models. Except in the cohort used for the 72 h blocking experiment, ^{89}Zr-DFO-MAb-B43.13 showed a consistent trend for increasing tumor accretion over time up to 120 h, with a concomitantly decreasing activity in the blood pool of all animals. All other non-target organs maintained a baseline amount uptake of radioactivity which ultimately translates into a high tumor-to-non-tumor ratio with progression of time. The consistently high amount of radioactivity in the liver at all the time points evaluated in this study may be explained by more than one reason: a) the liver is a highly perfused organ and generally acts as the site of clearance for high molecular weight entities such as antibodies; b) immunocomplexes formed as a result of rapid sequestration of shed CA125 antigen by ^{89}Zr-DFO-MAb-B43.13 in the bloodstream of OVCAR-3 bearing xenograft mice potentially gets routed for clearance through the liver. The latter phenomenon has been reported to occur for CA125-MAb-B43.13 immunocomplexes formed within 2 h after injecting the antibody in a previous study by McQuarrie et al, using a ^{99m}Tc-labeled MAb-B43.13 for *in vivo* evaluation of its pharmacokinetics in human patients.[25, 26] However, in those reports, most of the immunocomplexes were cleared via the spleen due to an immunologic basis to this process. The possibility of an immunologic

involvement for clearance of such immunocomplexes in the present study seems negligible due to the relatively low level uptake of radioactivity found in the spleen of all animals at all times as compared to the heightened radioactivity levels in the liver. This observation for hepatic accumulation and clearance of potential immunocomplexes formed at early time points post-injection of the radiotracer is also supported by the differential clearance of an ^{18}F-labeled anti-CA125 scFv (Chapter 2) 1 h p.i through the hepatic route specifically in NIH:OVCAR-3 bearing xenograft mice, while owing to its molecular weight being below the renal threshold for clearance, the scFv by itself tends to be routed for clearance through the renal pathway. Furthermore, the specificity of CA125 targeting by ^{89}Zr-DFO-MAb-B43.13 was established by the blocking experiment which dramatically reduced the absolute tumor uptake by ~ 66% while demonstrating a concomitant increase of radioactivity uptake in most non-target organs possibly on account of achieving a high degree of saturation by un-labeled excess DFO-MAb-B43.13 at target sites in the tumor.

Small animal PET imaging:

The results from acute biodistribution studies corroborated well with our observations from small animal imaging studies, wherein the CA125 expressing tumors were delineated as early as 24 h p.i, albeit with modest uptake values that progressively increased during later time points of evaluation. This observation was consistent throughout the study and was also observed in the case of bi-lateral tumors, wherein CA125-positive NIH:OVCAR-3 tumors showed a modest uptake

of radiotracer at 24 h p.i but, progressively accumulated the radiotracer by 48 h and beyond, while the CA125-negative SKOV3 tumors showed a consistent non-specific tumor uptake by virtue of an enhanced permeability and retention effect.[27] Consistent with results from the acute biodistribution studies, the liver was the major non-target organ with progressive accumulation of radioactivity, possibly due to its physiological role as the organ of clearance for radioimunoconjugates and any associated immunocomplexes. Consequently, high contrast images were obtained at later time points (72 h and beyond) when maximum tumor accretion was achieved alongside minimal systemic background activity as a result of clearance. This aspect can be particularly interesting for the visualization of residual / recurring disease which tends to be present as small ovarian carcinomatous nodules within the peritoneum and may be confounded by background activity in scans performed at earlier time points. Such a non-invasive follow-up diagnosis via immuno-PET prior to second look surgery in patients who have already undergone surgical debulking and chemotherapy, could be of clinical benefit from the perspective of disease management. Nevertheless, a caveat to this approach is the persisting activity in the liver, which could potentially hinder the detection of epithelial ovarian tumors in this region of the peritoneum even at later time points, despite using ^{89}Zr immuno-PET. Although the tumor signals for radioactivity were strong until 312 h p.i, the liver continued to show persistent radioactivity even at this time point (Fig 22), plausibly attributed to its role as the organ of clearance.

Lymph node involvement and *Ex vivo* analysis:

An involvement of the tumor proximal lymph nodes as tissues with maximum uptake of the ^{89}Zr-DFO-MAb-B43.13 as demonstrated by small animal PET images and further verified through additional acute biodistribution studies including the use of a ^{89}Zr-DFO-IgG isotype control was the most stimulating part of this study. A completely different *in vivo* biodistribution profile between the CA125 targeted antibody and the isotype control in OVCAR3 xenograft mice, furthered by the selectively high uptake of ^{89}Zr-DFO-MAb-B43.13 in the harvested OVCAR3 tumor proximal lymph nodes ascertained this phenomenon beyond a sporadic occurrence of chance.

Ex vivo analyses of the ^{89}Zr-DFO-MAb-B43.13 distribution in OVCAR xenograft tumors was compared to both CA125 expression and the underlying tumor histology at 72 h p.i. The heterogeneous distribution of ^{89}Zr-DFO-MAb-B43.13 was consistent with our previous observations using ^{64}Cu-NOTA-MAb-B43.13, with generally higher uptake in the tumor periphery and reduced uptake in the central tumor regions (Fig. 5.19). This is not unusual since solid tumors have been described to have four distinct morphologic regions based on perfusion – an avascular necrotic region (usually at the center), a semi-necrotic region, a stabilized microcirculation region (at the periphery) and an advancing front (region with dense tumor nests surrounding the vasculature).[28] At higher magnification, we observed the uptake to be higher in stroma-dense tumor regions, suggesting a vascular component to the ^{89}Zr distribution of the radiotracer. Possible explanations for such localization include a limited tumor

penetration capability of full-length antibodies[29, 30, 31, 32] due primarily to their size that impedes extravasation across endothelial cells. Even after extravasation, the transport of antibodies within the tumor by diffusion has been noted to be as slow as 1 h to cover 100 μm.[28] This is exacerbated by the interstitial fluid pressure in solid tumors which prevents efficient transport of antibodies within the tumor.[33] Furthermore, it has also been demonstrated that perivascular distribution of antibodies in the tumor is dose – dependent, such that an injected dose below 50 μg would predominantly be localized to the perivascular space and not be able to penetrate the tumor as extensively as a 150 μg dose would. A contribution from the enhanced permeability and retention (EPR) effect[34] and / or binding-site barrier,[35] whereby high affinity of the antibody prevents complete antibody penetration into the tumor may be additional factors playing a role. However, regions of CA125-positive tumor cells in proximity to regions of stroma did show significant accumulation of ^{89}Zr-DFO-MAb-B43.13, implying that the clearance of unbound antibody from the tumor is not yet complete at this time-point.

On the other hand, the pattern of uptake in the brachial lymph nodes from the ipsilateral and contralateral chains to the tumor location shown as representative examples (Fig 5.20 and 5.21), revealed CA125 staining in both nodes, with no obvious difference in either the localization within the node, or the subjective intensity of the staining. ^{89}Zr distribution appeared to correspond to CA125 staining in both cases, but the fixed 25 μm resolution of the digital autoradiogram was clearly a limitation in this comparison. The use of appropriate photographic emulsions could potentially be used to further resolve the isotope distribution in

these tissues for future studies. Nonetheless, a major difference between the two representative lymph nodes shown was the relative ^{89}Zr radioactivity concentrations observed, with the ipsilateral node measuring over 8-fold higher average counts per unit area when compared with the contralateral node. This pattern was repeated in the axillary and inguinal nodes takes from both lymph node chains.

Such a pattern for uptake of ^{89}Zr-DFO-MAb-B43.13 in the lymph nodes may be suggestive of the presence of metastatic tumor deposits in the ipsilateral chain, absent in the contralateral chain. However, we were unable to detect tumor cells in any of the lymph nodes examined. The pattern of CA125 staining in the lymph nodes had the appearance of being cell-associated (Figs 5.20 and 5.21 green arrows), but this would also be consistent with the non-specific association of CA125 circulating with tumor infiltrating lymphocytes. The evaluation of the presence of tumor cells in these lymph nodes was a subjective assessment based on H&E staining and the possibility exists that small metastatic deposits are present. However, the CA125 staining and ^{89}Zr-DFO-MAb-B43.13 data point to the drainage of shed CA125 immunocomplexes from the tumor as being the most likely explanation of the lymph node observations presented thus far in this study.

Histopathologic findings confirmed the authenticity of the tumor to be an ovarian carcinoma and identified all lymph nodes as having some abnormalities that are expected as part of the nude mouse phenotype (lymphoid depletion of the paracortex and dilation of sinuses). However, the ipsilateral axillary lymph node had an area of necrosis, which was not an expected spontaneous finding in a nude

mouse lymph node. This area of necrosis contained rare large cells morphologically similar to the neoplastic cells that composed the tumor. However, a section from this lymph node stained negative for cytokeratin WSS – an epithelial marker that was positive on the tumor sample. A lack of further representation of such an area of necrosis with atypical cells in the ipsilateral axillary node in spite of cutting deeper into the block to obtain additional sections for analysis, left us to speculate if the abnormal area observed initially may have represented metastasis, even if very few cells were present. We were not able to confirm metastasis on additional sections due to the small size of the lesion while the three other lymph nodes did not have evidence of metastasis.

Metastasis or circulating immunocomplexes?

Along its course of disease progression, serous epithelial ovarian carcinoma has been reported as the most metastatic subtype of ovarian cancers which are generally known to be highly lymphophillic.[36] While a transcoelomic route[37] would be the most common mechanism for metastatic spread of ovarian cancers in their natural setting, they are also known to use the para-aortic and pelvic lymph nodes to metastasize within the body. Although rare, there have been a few reports of axillary lymph node metastasis of ovarian cancer.[38] Furthermore, increasing evidence for lymphangeogenesis promoted by growth factors (VEGF-C and D) secreted from solid tumors augment the possibilities for lymphatic spread of metastatic neoplasms.[39, 40] In epithelial ovarian cancers, high levels of pre-operative CA125 have clinically served as a prognostic indicator for

lymphatic metastasis in human patients in order to identify candidates for surgical lymphadenectomy.[41, 42] In the light of these facts and considering contemporary reports for immuno-PET imaging of tumor-induced lymphangeogenesis and metastasis,[43, 44, 45] alongwith a mathematically modeled proposition[46] to suggest that antibodies may find it easier to target micrometastasis than vascularized tumors encourages us to think that a case for metastasis should not be completely ruled out until further investigation.

Nevertheless, the presence of papillary structures filled with proteinaceous fluid interlacing the tumor nests in this study is consistent with our previous observations from the ^{64}Cu-NOTA-MAb-B43.13 study wherein tumor slices examined revealed dense CA125 staining in similar areas observed with H&E staining. These channels may be representative of lymphatics in the periphery of the tumor that potentially contribute to the draining of bound immunocomplexes or extravasated yet unbound ^{89}Zr-DFO-MAb-B43.13 that might find it easier to slip away into the proximal draining lymph nodes in the face of resistance to penetrate the tumor on account of interstitial fluid pressure and other factors mentioned previously. Lastly, given the immunotherapeutic aspect of MAb-B43.13 there could be a potential role for an immunologic basis to this observation or an interplay between one and more of these speculated factors leading to lymph node involvement. Further investigation of this phenomenon in a suitable disease model with inclusion of immunologic aspects is warranted.

5.5 Conclusion:

The present chapter is a leap forward in our approach to CA125 targeted immuno-PET for epithelial ovarian cancer. This study maximizes the potential of using the CA125 targeting antibody as a radiotracer for pre-clinical and clinical non-invasive imaging of EOC via immuno-PET. In the present work, we produced a ^{89}Zr-labeled version of MAb-B43.13 and performed preclinical evaluation of this radiotracer in sub-cutaneous xenograft mouse models for EOC. A wider window of opportunity was provided to trace the *in vivo* radiopharmacological fate of an antibody-based targeting vector to be applied beyond the 48 h window previously available to us using a ^{64}Cu-labeled version of the same antibody. Furthermore, this study imparted a translational relevance by knowing the destination and potential off-target effects of the radiopharmaceutical prior to designing potential clinical applications for imaging and therapy in future. In summary, this study demonstrated an amalgamation of the efficient *in vivo* tumor targeting capabilities of MAb-B43.13 and the favourable properties of ^{89}Zr towards developing a radiopharmaceutical for immuno-PET of epithelial ovarian tumors. Most importantly, it extended the scope of this technique and the radiotracer for the detection of potential metastasis and/or draining lymph nodes, which may be of clinical significance in the management of this disease.

5.6 References:

1. Wu AM, Senter PD. Arming antibodies: prospects and challenges for immunoconjugates. *Nat Biotechnol* 2005;**23**(9): 1137-46.
2. Sundaresan G, Yazaki PJ, Shively JE, et al. 124I-labeled engineered anti-CEA minibodies and diabodies allow high-contrast, antigen-specific small-animal PET imaging of xenografts in athymic mice. *J Nucl Med* 2003;**44**(12): 1962-9
3. O'Donoghue JA, Smith-Jones PM, Humm JL, et al. 124I-huA33 antibody uptake is driven by A33 antigen concentration in tissues from colorectal cancer patients imaged by immuno-PET. *J Nucl Med* 2011;**52**(12): 1878-85.
4. Knowles SM, Wu AM. Advances in immuno-positron emission tomography: antibodies for molecular imaging in oncology. *J Clin Oncol* 2012;**30**(31): 3884-92.
5. Holland JP, Williamson MJ, Lewis JS. Unconventional nuclides for radiopharmaceuticals. *Mol Imaging* 2010;**9**(1): 1-20.
6. Wright BD, Lapi SE. Designing the magic bullet? The advancement of immuno-PET into clinical use. *J Nucl Med* 2013;**54**(8): 1171-4.
7. Zhang Y, Hong H, Cai W. PET tracers based on Zirconium-89. *Curr Radioph*arm 2011;**4**(2): 131-9.
8. Holland JP, Sheh Y, Lewis JS. Standardized methods for the production of high specific-activity zirconium-89. *Nucl Med Biol* 2009;**36**(7): 729-39.
9. Deri MA, Zeglis BM, Francesconi LC, Lewis JS. PET imaging with (8)(9)Zr: from radiochemistry to the clinic. *Nucl Me*d Biol 2013;**40**(1): 3-14.
10. Fischer G, Seibold U, Schirrmacher R, Wangler B, Wangler C. (89)Zr, a radiometal nuclide with high potential for molecular imaging with PET: chemistry, applications and remaining challenges. *Molecules* 2013;**18**(6): 6469-90.
11. Perk LR, Visser GW, Vosjan MJ, et al. (89)Zr as a PET surrogate radioisotope for scouting biodistribution of the therapeutic radiometals (90)Y and (177)Lu in

tumor-bearing nude mice after coupling to the internalizing antibody cetuximab. *J Nucl Med* 2005;**46**(11): 1898-906.

12. Price EW, Zeglis BM, Lewis JS, Adam MJ, Orvig C. H6phospa-trastuzumab: bifunctional methylenephosphonate-based chelator with 89Zr, 111In and 177Lu. *Dalton Trans* 2014;**43**(1): 119-31.
13. Deri MA, Ponnala S, Zeglis BM, et al. Alternative Chelator for (89)Zr Radiopharmaceuticals: Radiolabeling and Evaluation of 3,4,3-(LI-1,2-HOPO). *J Med Chem* 2014;**57**(11): 4849-60.
14. Noujaim AA, Baum RP, Sykes TR, Sykes CJ, Hertel A, Niesen, A, et al. Monoclonal antibody B43.13 for immunoscintigraphy and immunotherapy of ovarian cancer. In Current Tumor Diagnosis: Applications, Clinical Relevance, Trends. Edited by Klapdor, R. Munich: W Zuckschwerdt Verlag; 1994; 823–829.
15. Lindmo T, Boven E, Cuttitta F, Fedorko J, Bunn PA, Jr. Determination of the immunoreactive fraction of radiolabeled monoclonal antibodies by linear extrapolation to binding at infinite antigen excess. *J Immunol Methods* 1984;**72**(1): 77-89.
16. Carlin S, Khan N, Ku T, Longo VA, Larson SM, Smith-Jones PM. Molecular targeting of carbonic anhydrase IX in mice with hypoxic HT29 colorectal tumor xenografts. *PLoS One* 2010;**5**(5): e10857
17. Holland JP, Divilov V, Bander NH, Smith-Jones PM, Larson SM, Lewis JS. 89Zr-DFO-J591 for immunoPET of prostate-specific membrane antigen expression in vivo. *J Nucl Med* 2010;**51**(8): 1293-300.
18. Ulmert D, Evans MJ, Holland JP, et al. Imaging androgen receptor signaling with a radiotracer targeting free prostate-specific antigen. *Cancer Discov* 2012;**2**(4): 320-7.

19. Holland JP, Caldas-Lopes E, Divilov V, et al. Measuring the pharmacodynamic effects of a novel Hsp90 inhibitor on HER2/neu expression in mice using Zr-DFO-trastuzumab. *PLoS One* 2010;**5**(1): e8859.

20. Tavare R, McCracken MN, Zettlitz KA, et al. Engineered antibody fragments for immuno-PET imaging of endogenous CD8+ T cells in vivo. *Proc Natl Acad Sci U S A* 2014;**111**(3): 1108-13.

21. Viola-Villegas NT, Rice SL, Carlin S, et al. Applying PET to broaden the diagnostic utility of the clinically validated CA19.9 serum biomarker for oncology. *J Nucl Med* 2013;**54**(11): 1876-82.

22. Sham JG, Kievit FM, Grierson JR, et al. Glypican-3-targeted 89Zr PET imaging of hepatocellular carcinoma. *J Nucl Med* 2014;**55**(5): 799-804.

23. Ikotun OF, Marquez BV, Huang C, et al. Imaging the L-type amino acid transporter-1 (LAT1) with Zr-89 immunoPET. *PLoS One* 2013;**8**(10): e77476

24. Tinianow JN, Gill HS, Ogasawara A, et al. Site-specifically ^{89}Zr-labeled monoclonal antibodies for ImmunoPET. *Nucl Med Biol* 2010;**37**(3): 289-97.

25. McQuarrie SA, Baum RP, Niesen A, et al. Pharmacokinetics and radiation dosimetry of ^{99}Tcm-labelled monoclonal antibody B43.13 in ovarian cancer patients. *Nucl Med Commun* 1997;**18**(9): 878-86.

26. McQuarrie SA, Riauka T, Baum RP, et al. The effects of circulating antigen on the pharmacokinetics and radioimmunoscintigraphic properties of ^{99m}Tc labelled monoclonal antibodies in cancer patients. *J Pharm Pharm Sci* 1998;**1**(3): 115-25.

27. Fang J, Nakamura H, Maeda H. The EPR effect: Unique features of tumor blood vessels for drug delivery, factors involved, and limitations and augmentation of the effect. *Adv Drug Deliv Rev* 2011;**63**(3): 136-51.

28. Jain RK. Transport of molecules, particles, and cells in solid tumors. *Annu Rev Biomed Eng* 1999;**1**: 241-63.

29. Buchegger F, Haskell CM, Schreyer M, et al. Radiolabeled fragments of monoclonal antibodies against carcinoembryonic antigen for localization of human colon carcinoma grafted into nude mice. *J Exp Med* 1983;**158**(2): 413-27.

30. Thurber GM, Schmidt MM, Wittrup KD. Factors determining antibody distribution in tumors. *Trends Pharmacol Sci* 2008;**29**(2): 57-61.

31. Rhoden JJ, Wittrup KD. Dose dependence of intratumoral perivascular distribution of monoclonal antibodies. *J Pharm Sci* 2012;**101**(2): 860-7.

32. Thurber GM, Schmidt MM, Wittrup KD. Antibody tumor penetration: transport opposed by systemic and antigen-mediated clearance. *Adv Drug Deliv Rev* 2008;**60**(12): 1421-34.

33. Heldin CH, Rubin K, Pietras K, Ostman A. High interstitial fluid pressure - an obstacle in cancer therapy. *Nat Rev Cancer* 2004;**4**(10): 806-13.

34. Heneweer C, Holland JP, Divilov V, Carlin S, Lewis JS. Magnitude of enhanced permeability and retention effect in tumors with different phenotypes: 89Zr-albumin as a model system. *J Nucl Med* 2011;**52**(4): 625-33.

35. Adams GP, Schier R, McCall AM, et al. High affinity restricts the localization and tumor penetration of single-chain fv antibody molecules. *Cancer Res* 2001;**61**(12): 4750-5.

36. Di Re F, Baiocchi G. Value of lymph node assessment in ovarian cancer: Status of the art at the end of the second millennium. *Int J Gynecol Cancer* 2000;**10**(6): 435-42.

37. Tan DS, Agarwal R, Kaye SB. Mechanisms of transcoelomic metastasis in ovarian cancer. *Lancet Oncol* 2006;**7**(11): 925-34.

38. Ceccarelli F, Barberi S, Pontesilli A, Zancla S, Ranieri E. Ovarian carcinoma presenting with axillary lymph node metastasis: a case report. *Eur J Gynaecol Oncol* 2011;**32**(2): 237-9.

39. Detmar M, Hirakawa S. The formation of lymphatic vessels and its importance in the setting of malignancy. *J Exp Med* 2002;**196**(6): 713-8.

40. Du LC, Chen XC, Wang D, et al. VEGF-D-induced draining lymphatic enlargement and tumor lymphangiogenesis promote lymph node metastasis in a xenograft model of ovarian carcinoma. *Reprod Biol Endocrinol* 2014;**12**: 14.

41. Ayhan A, Gultekin M, Dursun P, et al. Metastatic lymph node number in epithelial ovarian carcinoma: does it have any clinical significance? *Gynecol Onco*l 2008;**108**(2): 428-32.

42. Kim HS, Park NH, Chung HH, Kim JW, Song YS, Kang SB. Significance of preoperative serum CA-125 levels in the prediction of lymph node metastasis in epithelial ovarian cancer. *Acta Obstet Gynecol Scand* 2008;**87**(11): 1136-42.

43. Mumprecht V, Honer M, Vigl B, et al. In vivo imaging of inflammation- and tumor-induced lymph node lymphangiogenesis by immuno-positron emission tomography. *Cancer Res* 2010;**70**(21): 8842-51.

44. Mumprecht V, Detmar M. In vivo imaging of lymph node lymphangiogenesis by immuno-positron emission tomography. *Methods Mol Biol* 2013;**961**: 129-40.

45. Borjesson PK, Jauw YW, Boellaard R, et al. Performance of immuno-positron emission tomography with zirconium-89-labeled chimeric monoclonal antibody U36 in the detection of lymph node metastases in head and neck cancer patients. *Clin Cancer Res* 2006;**12**(7 Pt 1): 2133-40.

46. Thurber GM, Zajic SC, Wittrup KD. Theoretic criteria for antibody penetration into solid tumors and micrometastases. *J Nucl Med* 2007;**48**(6): 995-9.

6

Development of a CA125 targeting Diabody for application in same-day imaging of Epithelial Ovarian Cancer[5]

[5]*This is a work in progress. A version of this chapter will be submitted to the European Journal of Nuclear Medicine and Molecular Imaging Research:*
Sharma SK, Wuest M, Lapi SE, Wuest F.
CA125 Targeted Cys-Diabody for same day imaging of epithelial ovarian cancer

6.1 Introduction:

The *in vivo* pharmacokinetics of a molecular probe is central to its success as a radiotracer for application in PET imaging strategies. With recent advances and the promise of immuno-PET as a unique functional imaging strategy, a number of antibodies are being engineered for use in this technique.[1, 2] Nonetheless, despite excellent tumor targeting capabilities and ideal size for *in vivo* tumor targeting,[3] full-length antibodies are not the vectors of choice for translation as radiotracers for same-day or next-day imaging strategies. Their long residency in systemic circulation and slow clearance, which contribute to a tremendous therapeutic potential, paradoxically serve as a major disadvantage to application as radiotracers for molecular imaging. Consequently, they end up being incompatible for use with short-lived radioisotopes and when labeled with long-lived positron emitting radionuclides, they deliver a high systemic background to result in low tumor-to-normal tissue ratios at early time points. Furthermore, from a dosimetry perspective, they contribute to radioactivity burden in subjects over an extended period of time until sufficient tumor accumulation and systemic clearance of the radiotracer are achieved.

Considering these shortcomings, a pursuit to achieve high image quality as a consequence of high absolute tumor uptake values combined with high tumor-to-background ratios while simultaneously reducing the radiation burden in subjects, has propelled the development of a family of radiotracers based on engineered versions of the antibody. Recently, many such molecules have been deployed as vectors for molecular imaging of cancer via immuno-PET.[1,4] This paradigm is

based on the premise of an inverse correlation between size of the vector employed as a radiotracer and its *in vivo* pharmacokinetics.[2] Historically, F(ab) ~50 KDa and F(ab')$_2$ fragments (~ 110 KDa) had been used to achieve this goal. However, while the former showed low absolute tumor uptake values,[5, 6] the latter yielded high contrast at later time points (12-18 h) and does not qualify for use in same-day imaging strategies. On the other hand, single chain Fragment variable (scFv) formats considered as the smallest yet complete active binding unit of the antibody capable of binding to a target antigen become a victim of their own molecular weight, which ultimately manifests in anemic tumor uptake. This is primarily due to a combined effect of first-pass clearance and renal trapping that precludes tumor bioavailability of these targeting agents.[7, 8] Most importantly, despite retaining the specificity of the parental antibody for the target antigen, the scFv suffers from a lack of sufficient avidity to result in a short mean residency time within the tumor. However, the lack of Fc (Fragment crystallizable) region in this engineered format makes this class of engineered molecules immunologically inert for *in vivo* application in a variety of preclinical models and clinical subjects and contributes greatly towards achieving rapid systemic clearance as a desirable trait in an immuno-PET radiotracer for same-day imaging.

Collectively, these observations have prompted redesigning strategies to increase the avidity of such antibody fragments to render a bivalent binding capability comparable to that of the parent antibody molecule. Some such engineering approaches include: a) chemical cross-linking of two or more monomeric scFv units; b) tandem cloning of scFv units and its expression to yield dimers; c)

introduction of dimerization domains by recombinant methods; d) non-covalent dimerization to yield 'diabodies' as a result of shortening the length of inter-domain peptide linker.[9, 10, 11] More recently, the introduction of unpaired cysteine residues at the C-terminus of the scFv has led to the development of disulfide-linked dimers commonly referred to as Cys-Diabodies.[12, 13, 14, 15]

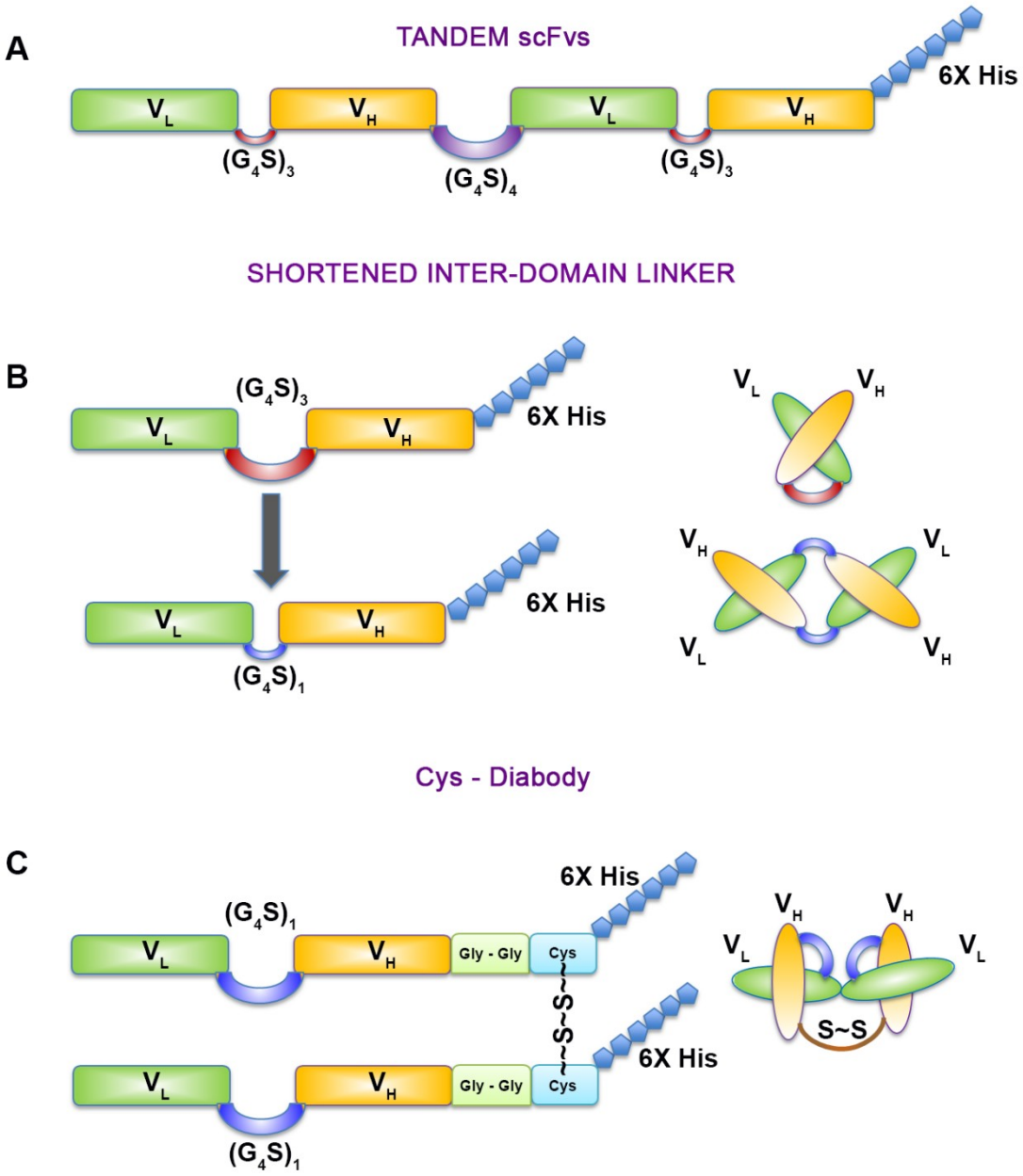

Figure 6.1: Diagrammatic representation of DNA constructs for the production of anti-CA125 diabodies: **A)** Two anti-CA125 scFvs cloned in tandem to form bivalent scFv; **B)** Shortening of inter-domain flexible peptide linker from $(G_4S)_3$ to $(G_4S)_1$ to form non-covalently-linked dimers (Diabodies); **C)** Introduction of unpaired cysteine residues at C-terminus of individual anti-CA125 scFv genes to form disulfide bonds upon periplasmic expression and *in vivo* folding in *E.coli* to form covalently-linked dimers (Cys-Diabodies). G: Glycine; S: Serine; 6X-His: hexa-histidine tag; S~S: disulfide bond.

The motivation for the generation of diabodies stems from the fact that this class of molecules would possess the best of all worlds in that they have a comparable functional avidity for binding to antigen as that of a complete antibody, yet they have a molecular weight (~ 55 KDa), which is intermediate to that of an scFv and a full-length antibody, and is well below the renal threshold for rapid systemic clearance. Diabodies targeting several tumor associated antigens have been proposed and demonstrated as suitable targeted radiotracers for same-day imaging strategies via immuno-PET.[16, 17, 18, 19]

In this chapter, we engineered the anti-CA125 scFv into a covalently linked dimer to develop it as a suitable immuno-PET radiotracer for same-day imaging of epithelial ovarian cancer. To this end, we introduced an unpaired cysteine at the C-terminus of the anti-CA125 scFv, such that recombinant expression and *in vivo* folding of this molecule within the periplasm of *E.coli* would result in a disulfide linked dimeric version of the scFv – the anti-CA125 Cys-Db. The immunoreactivity of the anti-CA125 Cys-Db was verified by biochemical assays such as immunoblotting, flow cytometry and immunofluorescence. Subsequently, the anti-CA125 Cys-Db was radiolabeled with ^{64}Cu ($t_{1/2}$ 12.7 h) and preliminary studies were performed using NIH:OVCAR-3 cells for *in vitro* analysis and corresponding xenograft bearing mice to evaluate its *in vivo* radiopharmacologic profiles and tumor targeting capabilities.

6.2 Materials and Methods:

6.2.1 Production of anti-CA125 Diabody:

A) **Cloning**: The genes for individual variable domains of the anti-CA125 scFv were amplified by polymerase chain reaction (PCR) from a previously reported plasmid construct pWET8.[20, 21] The plasmid encoding for anti-CA125 V_L-$(G_4S)_3$-V_H scFv reported in chapter 2 of this thesis was used as a template for splice overlap extension PCR in order to shorten the inter-domain peptide linker from the canonical $(Gly_4Ser)_3$ to $(Gly_4Ser)_1$. The anti-CA125 scFv was oriented as V_L-$(G_4S)_3$-V_H with the variable light chain domain at the N-terminus and variable heavy chain domain at the C-terminus. Furthermore, in a separate construct, a Gly-Gly-Cys tri-peptide was inserted between the last residue (Ser) at the end of the scFv heavy chain domain and the *Not* I cloning site by introducing the corresponding tri-peptide encoding oligonucleotide sequence into the antisense primer during PCR amplification of the anti-CA125 scFv. This construct is hereafter referred to as anti-CA125 Cys-Db in this thesis. Ultimately, both constructs were sub-cloned separately between *Nco* I and *Not* I restriction sites of pET-22b(+) vector (Novagen, 69744) for recombinant expression in *E.coli* Rosetta 2(DE3) (Novagen, 71400). The scFv DNA cloned in each recombinant construct was further verified by Sanger sequencing on a 3730 DNA analyzer (Applied Biosystems, Life Technologies) prior to transformation in the bacterial expression host.

B) **Expression and Purification**: Each recombinant plasmid coding for the two diabody constructs was transformed into chemically competent *E.coli* Rosetta 2(DE3) cells by heat-shock method and plated onto 1.5% 2x YT agar plates containing 100 µg/mL ampicillin and 34 µg/mL chloramphenicol. Single transformant colonies were picked for each construct and inoculated into 12.5 ml 2x YT medium (16 g/L tryptone, 10 g/L yeast extract and 5 g/L sodium chloride, pH 7.5) with 100 µg/ml ampicillin, 34 µg/mL chloramphenicol and cultured overnight by incubation at 37˚C with shaking at 200 rpm. 5 ml of the overnight grown cultures was added to 500 ml fresh 2x YT medium in the presence of antibiotics in 2 liter flasks and incubated at 37˚C with shaking at 220 rpm until an OD_{600} of 0.6 – 0.8 was achieved. The shake flask cultures were briefly placed in ice cold water for 15 minutes prior to induction with a final concentration of 0.8 mM IPTG. The induced cultures were incubated at 26˚C with shaking at 200 rpm overnight for 16 h. The bacteria were harvested by centrifugation at 7000 rpm for 30 minutes and the pellet obtained thereof was frozen by storage at -20˚C. Soluble diabodies were extracted from frozen cell pellets by lysis with BugBuster® Master Mix reagent as per the manufacturer's instructions. The cell lysate was cleared by centrifugation at 16,000 rpm for 30 minutes and the supernatant was collected for purification of soluble diabodies. C-terminal hexa-histidine tagged recombinant diabody was purified via immobilized metal affinity chromatography (IMAC) using a cobalt-based TALON® superflow metal affinity resin (Clontech, 635506). The cell lysate supernatant was passed over the resin at a flow rate of 1 mL/min to allow binding of the hexa-histidine tagged recombinant protein to the metal

affinity resin. Initial attempts to elute the captured protein from the column employed a step gradient of 10 mM, 20 mM, 40 mM, 80 mM, 120 mM and 150 mM of imidazole in 50 mM sodium di-hydrogen phosphate [$NaH_2PO_4.H_2O$] and 100 mM sodium chloride pH 7.0 used as the buffer solution. Later trials for purification were performed using a linear gradient of 10 mM – 150 mM imidazole as the eluant. 1 mL IMAC-eluted fractions were collected and analyzed by 12% SDS-PAGE under non-reducing conditions, followed by Coomassie staining and immunoblotting with 6X His MAb-HRP conjugate (Clontech, 631210). Eluted fractions containing high concentration of purified diabody were pooled together and dialyzed in phosphate buffered saline (pH 7.4) to remove excess imidazole and concentrated via centrifugation using Amicon Ultra-15, 10K MWCO filters (EMD Millipore, UFC901024). Anti-CA125 murine monoclonal antibody (MAb) was purified from MAb B43.13 hybridoma[22] cell culture supernatant by protein G affinity (Sigma, P-7700) on a BioLogic DuoFlow™ chromatography system (Bio-Rad, 760-0135). Final concentrations of the purified diabody and MAb were quantified using a Pierce™ BCA protein assay kit (Thermo Scientific, 23227) according to the manufacturer's recommendations.

6.2.2 Functional characterization of anti-CA125 Diabody:

6.2.2.1 Cell lines and culture conditions: Ovarian cancer cells NIH:OVCAR-3 (ATCC® HTB-161™) that overexpress CA125 were used for *in vitro* functional characterization studies. Cells were cultured in DMEM-F12 medium supplemented with 10% v/v fetal bovine serum (Life Technologies, 12483-020),

50 IU/mL penicillin, 50 μg/mL streptomycin (Life Technologies, 15140-122). NIH:OVCAR-3 cells were additionally supplemented with 7 μg/mL recombinant human insulin (SAFC Biosciences, 91077C). Cells were cultured using sterile techniques and grown in a 37°C incubator providing humidified atmosphere of 5% CO_2 in air.

6.2.2.2 Immunoblotting: 7.5 x 10^6 NIH:OVCAR-3 and SKOV3 cells were lysed with CelLytic™ M. Cell lysates were electrophoresed on a 4-15% Mini-PROTEAN® TGX™ precast gel (Bio-Rad) and transferred to a Trans-Blot nitrocellulose membrane (Bio-Rad). The membranes were probed separately to evaluate binding capabilities of the recombinant anti-CA125 targeting antibody-based constructs. The blots were blocked for 45 min with 5% non-fat dry milk (Carnation) in PBS having 0.1% Tween-20 (PBST). Anti-CA125 MAb (3 mg/mL), mouse anti-β actin IgG (Sigma, A1978), anti-CA125 scFv (~2 mg/mL) and anti-CA125 Cys-Db (~1 mg/mL) were used as primary antibodies (1: 5000 each) to probe the blots for 1 h at room temperature. Goat anti-mouse HRP conjugate (1: 5000) (Sigma, A4416), was used as secondary antibody to probe the blot against anti-CA125 MAb and mouse anti-β actin IgG for 1 h at room temperature. 6X His MAb-HRP conjugate (1:5000) (Clontech, 631210) was used as secondary antibody to probe against antigen-bound anti-CA125 scFv variants by incubating for 1 h at room temperature. Anti-CA125 targeting monoclonal antibody MAb B43.13 was used as a positive control. A hexa-histidine tagged anti-RANK receptor binding scFv[23] was used as an isotype control.

6.2.2.3 Flow Cytometry: 1.5 x 10^6 NIH:OVCAR-3 cells were harvested by trypsinization, rinsed twice with FACS buffer (PBS with 0.5% heat inactivated FBS, 2mM EDTA, 0.05% sodium azide) and resuspended by gentle tapping in ~100 µL of this buffer. 10 µg of anti-CA125 MAb B43.13, anti-CA125 scFv and anti-CA125 Cys-Db and a hexa-histidine tagged anti-RANK receptor binding scFv (isotype control), were incubated with the NIH:OVCAR-3 cell suspension for 30 min at room temperature. Cells were rinsed twice in FACS buffer and incubated for another 30 min with 2.4 µg of Penta·His Alexa Fluor 488 conjugate (Life Technologies, A-11001) for samples previously incubated with scFv/Db constructs. Cells were rinsed twice with FACS buffer and analyzed by flow cytometry on a BD FACS Calibur. Negative controls included unstained NIH:OVCAR-3 cells and cells incubated with Penta·His Alexa fluor 488 – conjugated antibody alone.

6.2.2.4 Immunofluorescence: NIH:OVCAR-3 cells were plated onto glass coverslips in 35-mm tissue culture dishes (100,000 cells/2 mL medium/dish) and incubated at 37°C for 48 h. The cells were rinsed with PBS and fixed in methanol for 30 min at -20°C. The fixed cells were incubated in 5% non-fat dry milk (Carnation) in PBS and immunostained separately for 1 h with anti-CA125 MAb-B43.13, anti-CA125 scFv, anti-CA125 Cys-Db (1:250). Alexa-fluor® 488 conjugated goat anti-mouse antibody and anti-Penta·His Alexa Fluor-488 conjugate were used as a secondary antibodies (1:500) in PBS containing 5% non-fat dry milk for samples previously incubated with MAb-B43.13 and anti-CA125

scFv/Cys-Db respectively. Appropriate control samples were included in the experiments. All antibody incubations were followed by three rinses with PBST for 10 min each. Coverslips were mounted on microscopy slides (Fisherbrand) using Mowiol® mounting medium (Calbiochem, 475904) supplemented with DAPI (50 µg/mL). Immunofluorescence was observed through a Zeiss Plan Apochromat 40X/1.3 Oil DIC M27 lens on a confocal laser scanning microscope (Zeiss LSM 710). The images were analyzed using Zen 2011 software and processed further using Adobe Photoshop CS6.

6.2.3 Radiolabeling of anti-CA125 Cys-Db:

6.2.3.1 General*:* All glassware was rinsed with ultra-pure HCl (Fisherbrand). Trace metals basis ultra-pure chemicals for buffer preparations were purchased from Sigma Aldrich. All buffer solutions were treated with biotechnology grade Chelex 100 (Bio-Rad, 143-2832).

6.2.3.2 NOTA Functionalization: p-SCN-Bn-NOTA [S-2-(4-Isothiocyanatobenzyl)-1,4,7-triazacyclononane-1,4,7-triacetic acid] (Macrocyclics Inc, B-605) was conjugated to anti-CA125 Cys-Db as a bi-functional chelator for ^{64}Cu radiolabeling. Briefly, a 6 molar excess of p-SCN-Bn-NOTA in DMSO was added to anti-CA125 Cys-Db in 0.1 M sodium bi-carbonate buffer pH 8.5 and allowed to react for 1 h at 37°C. NOTA-functionalized anti-CA125 Cys-Db was purified from un-conjugated NOTA while simultaneously achieving buffer

exchange into 0.25 M sodium acetate pH 5.5 by using an Econo-Pac® 10DG desalting column (Bio-Rad, 732-2010). Estimation of protein concentration of column eluted fractions was performed via bicinchoninic assay using a Pierce BCA Protein Assay Kit (Thermo, 23227) and A_{280} measurements on a nanodrop. Fractions with highest protein concentrations were identified and employed for further use in radiolabeling experiments.

6.2.3.3 ^{64}Cu labeling of NOTA-functionalized MAb/scFv: ^{64}Cu was produced via a ^{64}Ni(p,n)^{64}Cu nuclear reaction on a CS-15 biomedical cyclotron at Washington University, St. Louis, USA as described by Kume *et al*.[24] 85 MBq of ^{64}Cu-acetate was added to 100 µg NOTA-functionalized anti-CA125 Cys-Db and allowed to react at 30°C, 550 rpm for 1 h in a thermomixer. 1 mM EDTA was added to quench the reaction over 10 min. ^{64}Cu-labeled anti-CA125 Cys-Db radioimmunoconjugates were purified using an Econo-Pac® 10DG desalting column pre-equilibrated with 0.25 M sodium acetate, pH 5.5 used as the eluant. 350 µL elution fractions were collected from the column and radioactivity was measured on an Atomlab 400 dose calibrator (Biodex Inc). 15 µL of each elution fraction was electrophoresed on a 12% SDS-PAGE gel under non-reducing conditions and evaluated by autoradiography on a BAS-5000 phoshorimager (Fujifilm). Radiochemical yields and purity were determined by instant thin layer chromatography on ITLC-SG (Varian) using 10 mM EDTA pH 5.5 as the eluant. Fractions containing high specific activity radioimmunoconjugates were used for *in vitro* and *in vivo* radiopharmacological experiments.

6.2.4 *In vitro* immunoreactivity test:

The immunoreactive fraction of the prepared radioimmunoconjugate was determined as per the method of Lindmo et al.[25] Briefly, NIH:OVCAR-3 cells were aliquoted into microcentrifuge tubes at concentrations of 5, 4, 3, 2.5, 2, 1.5 and 0.5 x 10^6 cells in 500 μL PBS (pH 7.4). A stock solution of the radioimmunoconjugate (NOTA functinalized anti-CA125 Cys-Db) was prepared in PBS (pH 7.4) supplemented with 1% BSA such that 50 μL of this solution contained 20,000 cpm which was then uniformly aliquoted into individual tubes. This setup was allowed to incubate for 1 h at room temperature on a platform mixer. Thereafter, cells were pelleted by centrifugation (5,000 rpm for 3 mins), rinsed twice with ice cold PBS and the supernatant was aspirated prior to measuring cell-bound radioactivity on a γ-counter (Wizard$^{2®}$ 2480 Automatic Gamma Counter, Perkin-Elmer, Canada). Radioactivity data obtained thereof was background corrected and compared with counts from the total activity added control samples in the experiments. The immunoreactive fraction was determined by performing a linear regression analysis on a double-inverse plot of (total/bound) activity versus normalized cell concentration. All data was obtained in triplicates and no weighting was applied.

6.2.5 *In vivo* studies:

6.2.5.1 Xenograft models: All experiments were carried out according to guidelines of the Canadian Council on Animal Care (CCAC) and approved by the

local animal care committee of the Cross Cancer Institute, Edmonton. Six weeks old BALB/c nude female mice were obtained from Charles River labs (Quebec, Canada). The animals were housed in ventilated cages and provided food and water *ad libitum*. NIH:OVCAR-3 tumors were induced on the left shoulder by two subsequent subcutaneous injections of 15 x 10^6 and 10 x 10^6 cells in a 300 µL suspension of 1:1 mixture of PBS and matrigel (BD Biosciences). The second injection of cells was administered at the same site within 7-10 days. NIH:OVCAR-3 tumors grew for 6-8 weeks before reaching suitable tumor sizes of 150 – 200 mm^3.

6.2.5.2 Animal Imaging: Small animal PET experiments were performed on a MicroPET® R4 or INVEON PET scanner (Siemens Preclinical Solutions, Knoxville, TN, USA). Mice were anesthetized by inhalation of isoflurane in 40% oxygen/60% nitrogen, 1 L/min, while maintaining body temperature at 37°C throughout the experiment. 5 – 8 MBq of the radioimmunoconjugate (~30-40 µg) in 150 – 200 µL of 0.25M sodium acetate (pH 5.5) was administered intravenously via a tail vein catheter. Whole body PET data was acquired by performing static scans for each animal at 1 h p.i and 4 h p.i and 24 h p.i. Data acquisition continued for 60 min in 3D list mode. Standardized uptake values [SUV = (activity/ml tissue) / (injected activity/body weight), mlg^{-1}] were calculated for each ROI. Data are expressed as means ± SEM from n investigated animals. All PET image files were reconstructed using the maximum a posteriori (MAP) algorithm. The image files were further processed using the ROVER v

2.0.51 software (ABX GmbH, Radeberg, Germany). Masks for defining 3D regions of interest (ROI) were set and the ROIs were defined by thresholding.

6.3 Results:

6.3.1 Anti-CA125 Diabody production and characterization:

Two plasmid constructs, i) CA125 V_L-$(G_4S)_1$-V_H (with shortened inter-domain peptide linker) and ii) V_L-$(G_4S)_1$-V_H-GGC-6XHis (with C-terminal Cysteine) for the production of anti-CA125 diabodies were produced by recombinant methods and verified by Sanger's di-deoxy DNA sequencing (Fig. 6.2).

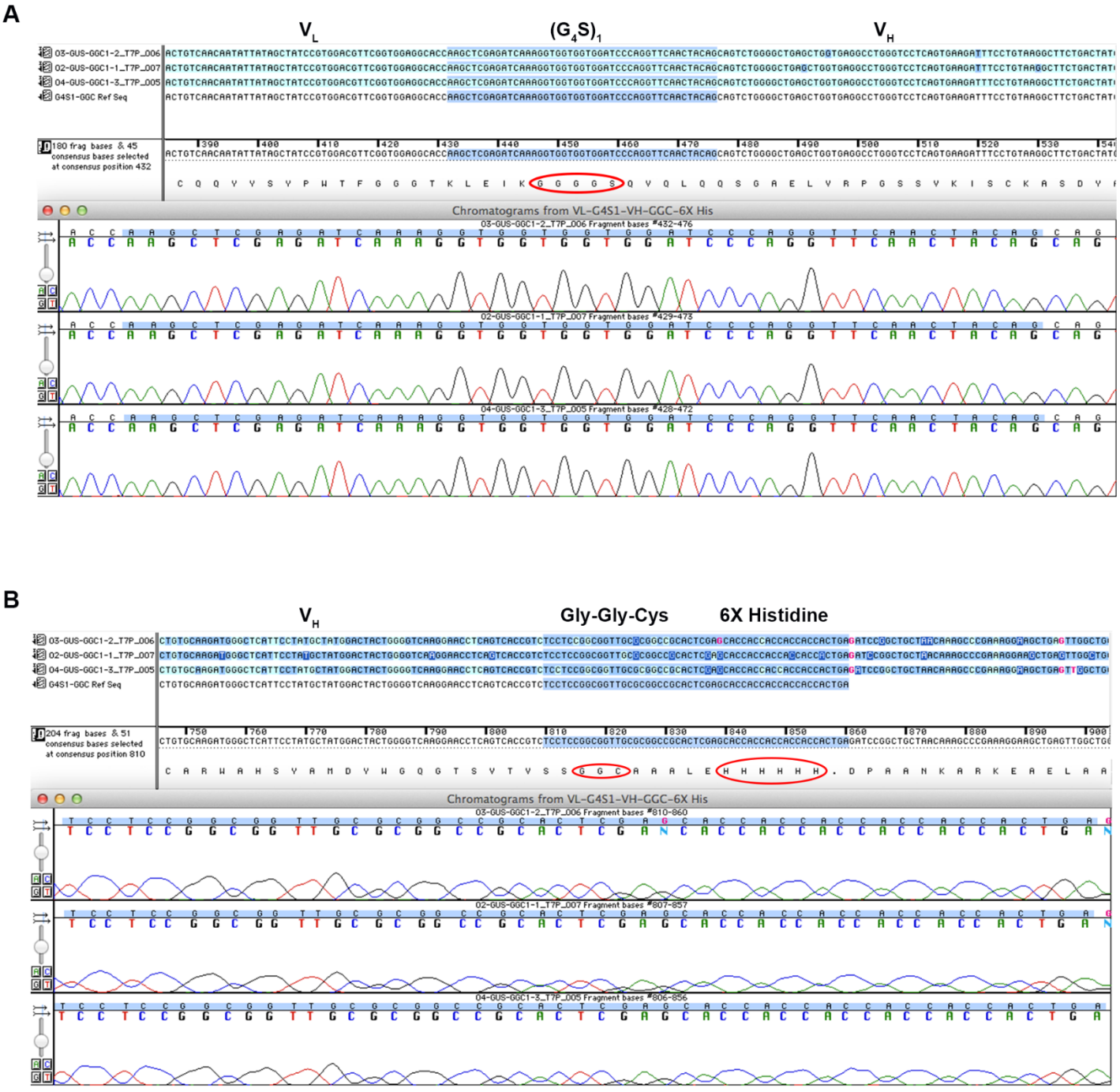

Figure 6.2: Representative segments of the sequence verified anti-CA125 V_L-$(G_4S)_1$-V_H and anti-CA125 Cys-Db DNA constructs: **A)** Highlighted inter-domain $(G_4S)_1$ linker of the anti-CA125 V_L-$(G_4S)_1$-V_H construct; **B)** C-terminus of the anti-CA125 Cys-Db construct highlighting the Gly-Gly-Cys tripeptide and hexa-histidine tag.

The anti-CA125 V_L-$(G_4S)_1$-V_H construct only yielded scFv monomers and did not show presence of diabodies (Fig. 3A). Anti-CA125 Cys-Db was purified in yields of 0.35 milligram per liter of recombinant bacterial culture using immobilized metal affinity chromatography (Fig. 3B and 3C). In a step gradient purification of the expressed protein using different concentrations of imidazole in the elution buffers, a mixture of monomeric anti-CA125 scFv and dimeric scFv (Cys-Db) were found. While lower imidazole concentrations up to 40 mM predominantly eluted monomeric scFv, later elution fractions containing higher concentrations of imidazole predominantly yielded the anti-CA125 Cys-Db (Fig. 6.3D).

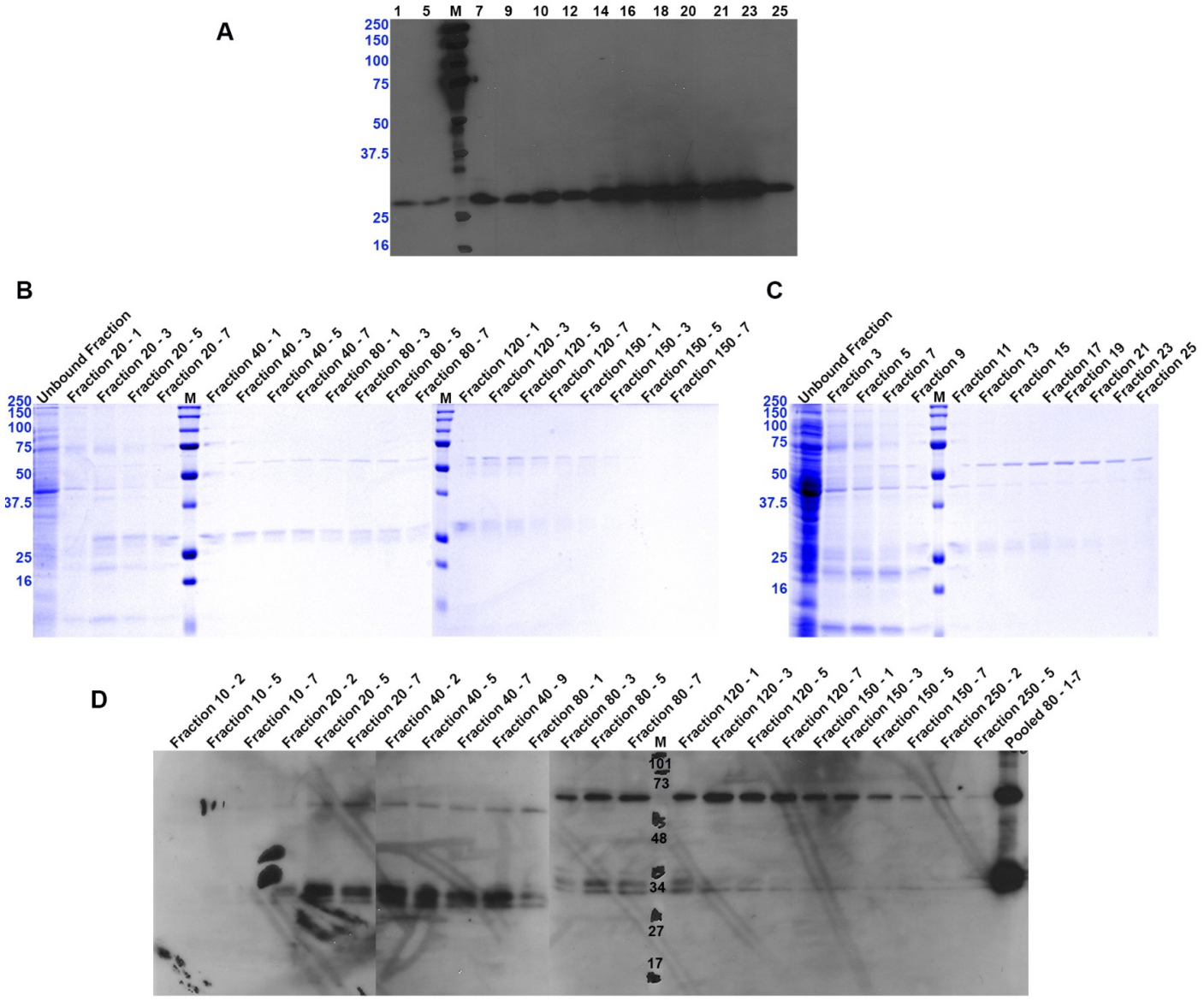

Figure 6.3: Analysis of recombinant anti-CA125 Cys-Db expression and purification. **A)** Representative immunoblot for IMAC-purified fractions of anti-CA125 V_L-$(G_4S)_1$-V_H diabody construct (fractions numbered in black) showing only scFv monomers under

non-reducing conditions; **B)** Coomassie-stained 12% non-reducing SDS-PAGE of anti-CA125 Cys-Db fractions purified by IMAC using a step – gradient of imidazole for elution of protein; **C)** Coomassie-stained 12% non-reducing SDS-PAGE of anti-CA125 Cys-Db fractions purified by IMAC using a linear gradient of imidazole for elution of protein; Migratory bands of pre-stained molecular weight markers are labeled in blue. MW is represented in KiloDaltons (KDa). **D)** Corresponding immunoblot of SDS-PAGE from B showing the presence of scFv monomers and anti-CA125 Cys-diabody.

The final preparation of a single-step IMAC-purified anti-CA125 Cys-Db in direct comparison with the monomeric anti-CA125 scFv is shown in Figs. 6.4A and 6.4B.

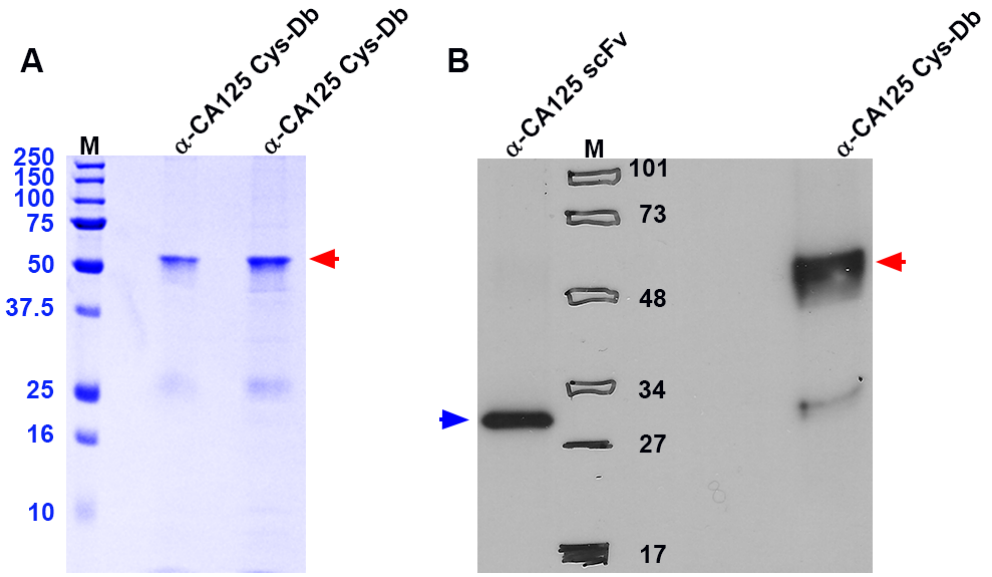

Figure 6.4: Gel analysis of anti-CA125 Cys-Db. **A)** Coomassie-stained 12% non-reducing SDS-PAGE of final preparations of purified anti-CA125 Cys-Db; **B)** Comparative immunoblot of purified anti-CA125 scFv and Cys-Db.

Immunoblotting to assess the biochemical activity of anti-CA125 Cys-Db as a specific targeting vector revealed its binding to high molecular weight CA125 antigen in NIH:OVCAR-3 cell lysate and absence of the corresponding band in SKOV3 cell lysates (Fig. 6.5A). Robust *in vitro* immunoreactivity was further demonstrated by flow cytometry experiments wherein a shift of forward scatter of fluorescence indicative of binding to CA125 on NIH:OVCAR-3 cells was observed in samples containing cells incubated with anti-CA125 scFv and Cys-Db whereas control samples revealed absence of a shift as seen in the histogram (Fig. 6.5B).

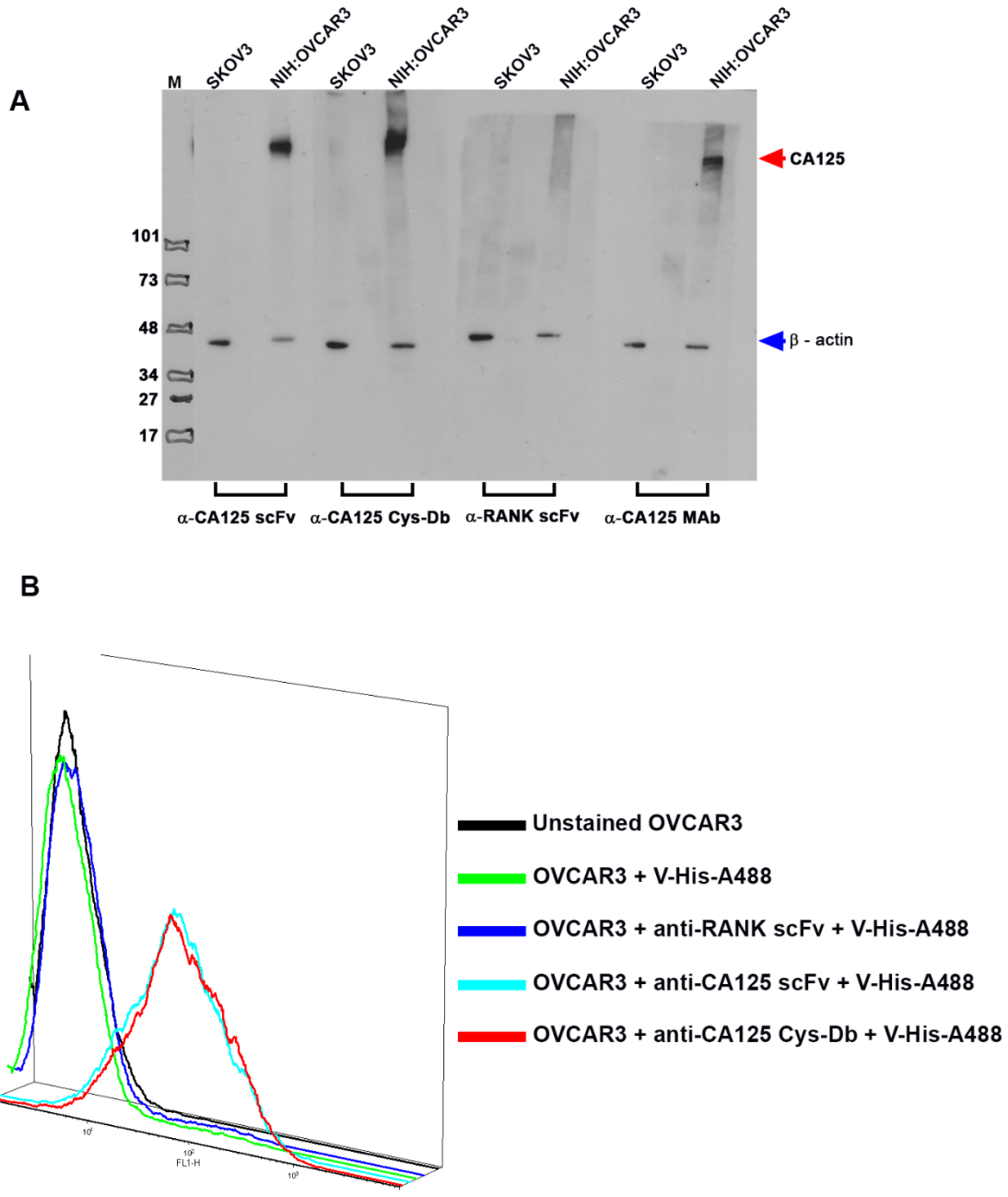

Figure 6.5: Functional characterization of anti-CA125 Cys-Db binding to CA125: **A)** Immuoblot of electrophoresed NIH:OVCAR-3 and SKOV3 cell lysates to verify biochemical binding activity of purified anti-CA125 Cys-Db; **B)** Flow cytometry analysis of NIH:OVCAR-3 cells indirectly stained with anti-CA125 scFv and anti-CA125 Cys-Db.

Furthermore, immunofluorescence experiments performed with anti-CA125 Cys-Db revealed membrane bound fluorescence in NIH:OVCAR-3 cells similar to the pattern demonstrated by anti-CA125 MAb-B43.13 and anti-CA125 scFv which were used as positive control samples as seen in Fig. 6.6.

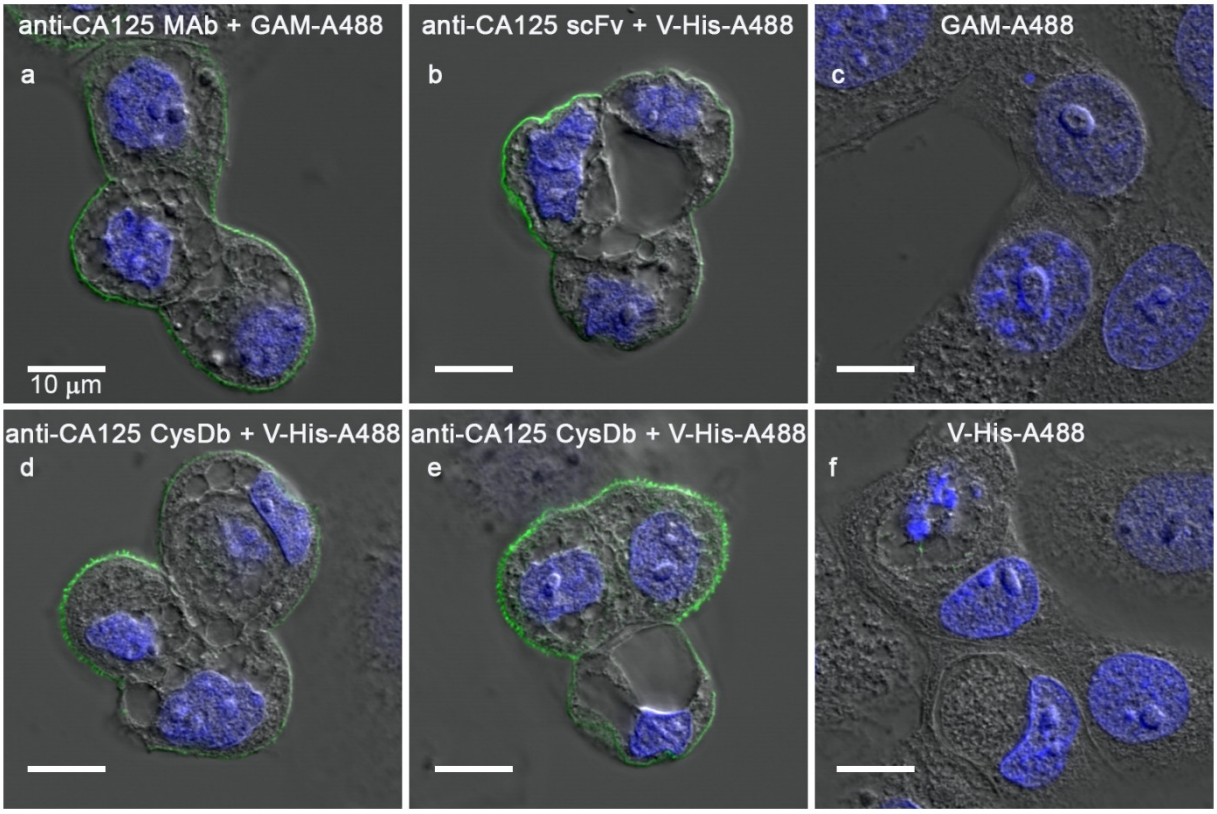

Figure 6.6: Functional characterization of anti-CA125 Cys-Db binding to CA125: Indirect immunostaining of NIH:OVCAR-3 cells with **a)** anti-CA125 MAb-B43.13 (positive control); **b)** anti-CA125 scFv; **c)** Goat Anti Mouse Alexa fluor-488 conjugated antibody (negative control); **d – e)** anti-CA125 Cys-Db; **f)** Anti – Penta His Alexa fluor-488 conjugated antibody (negative control). Scale bar represents 10 µm.

6.3.2 Production and *in vitro* characterization of ^{64}Cu-labeled anti-CA125 Cys-diabody:

^{64}Cu-labeling and purification of anti-CA125 Cys-Db provided the radioimmunoconjugate in isolated radiochemical yields of 35 ± 4 % (n=4) with specific activity of 54 MBq/mg.

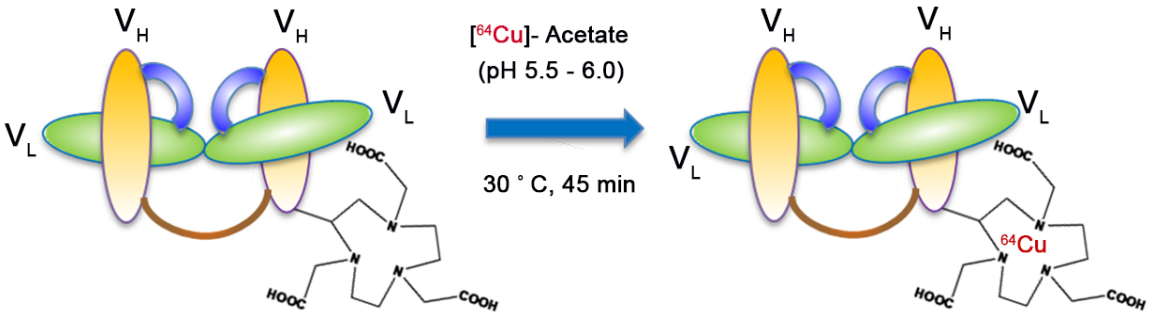

Figure 6.7: Diagrammatic representation of ^{64}Cu - radiolabeling scheme for anti-CA125 Cys-Db.

Assessment of the radiochemical purity of isolated radioimmunoconjugate fractions is shown as analyzed by ITLC in Figs. 6.8A and 6.9A-H and phosphorimages of electrophoresed fractions Figs. 6.8B and 6.8C.

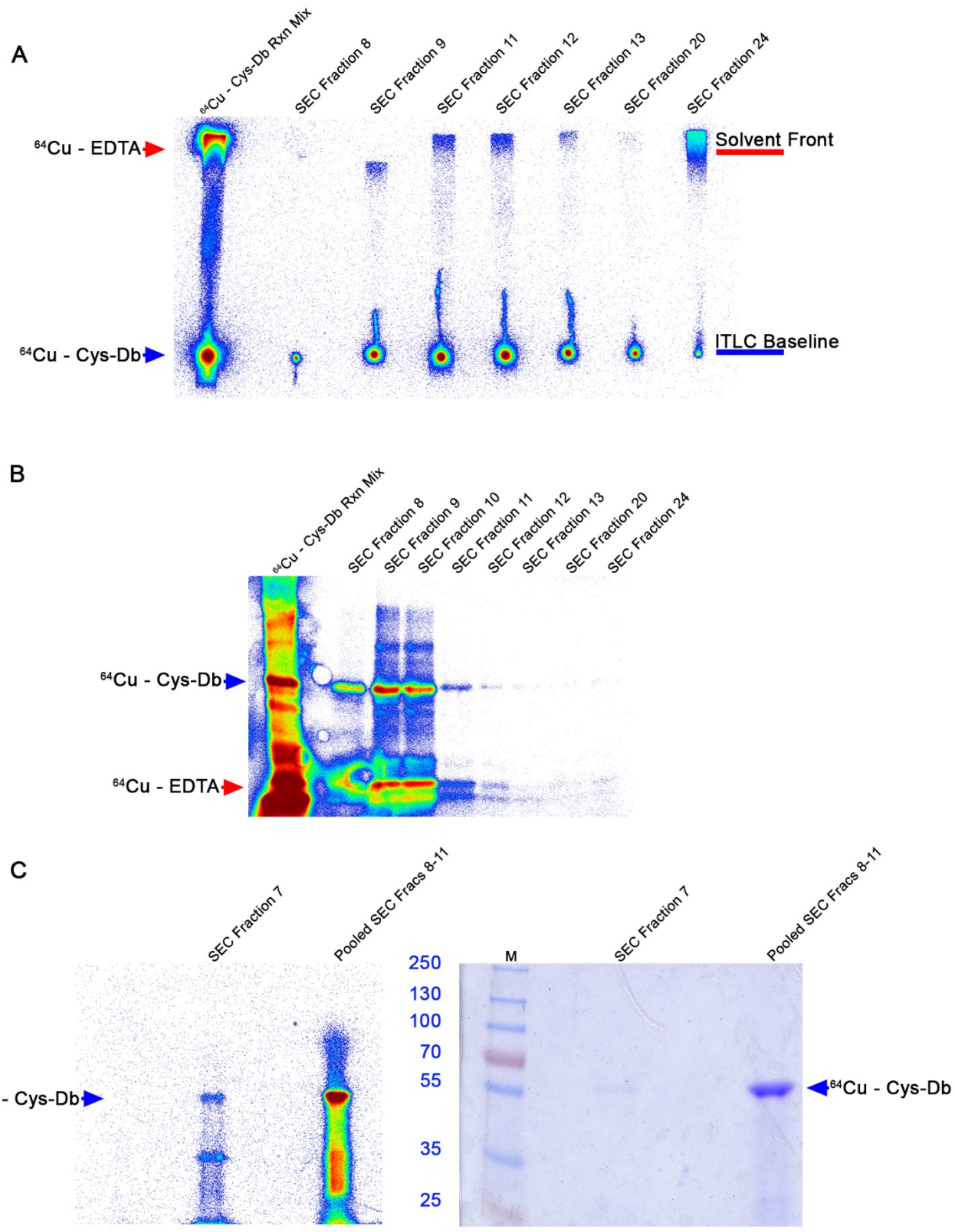
A
64Cu - Cys-Db Rxn Mix
SEC Fraction 8
SEC Fraction 9
SEC Fraction 11
SEC Fraction 12
SEC Fraction 13
SEC Fraction 20
SEC Fraction 24
64Cu - EDTA
Solvent Front
64Cu - Cys-Db
ITLC Baseline
B
64Cu - Cys-Db Rxn Mix
SEC Fraction 8
SEC Fraction 9
SEC Fraction 10
SEC Fraction 11
SEC Fraction 12
SEC Fraction 13
SEC Fraction 20
SEC Fraction 24
64Cu - Cys-Db
64Cu - EDTA
C
SEC Fraction 7
Pooled SEC Fracs 8-11
64Cu - Cys-Db
M
SEC Fraction 7
Pooled SEC Fracs 8-11
250
130
100
70
55
35
25
64Cu - Cys-Db

Figure 6.8: Quality control for SEC-purified anti-CA125 Cys-Db. **A)** Phosphorimage of radio-TLCs of size exclusion chromatography (SEC)-purified fractions of ^{64}Cu-labeled anti-CA125 Cys-Db; **B)** Phosphorimage of corresponding non-reducing SDS-PAGE of the same SEC-purified fractions of ^{64}Cu-labeled anti-CA125 Cys-Db; **C)** Corresponding phosphorimage and Coomassie-stained SDS-PAGE of ^{64}Cu-labeled anti-CA125 Cys-Db SEC-purified fractions. Blue arrows indicate ^{64}Cu-NOTA-anti-CA125 Cys-Db. Red arrows indicate un-conjugated ^{64}Cu chelated by EDTA.

Figure 6.9: Quality control of ^{64}Cu – anti-CA125 Cys-Db**. A)** Radio-TLC of crude reaction mixture at end of ^{64}Cu-labeling for anti-CA125 Cys-Db; **B – H)** Radio-TLCs of various SEC – purified fractions for ^{64}Cu – anti-CA125 Cys-Db.

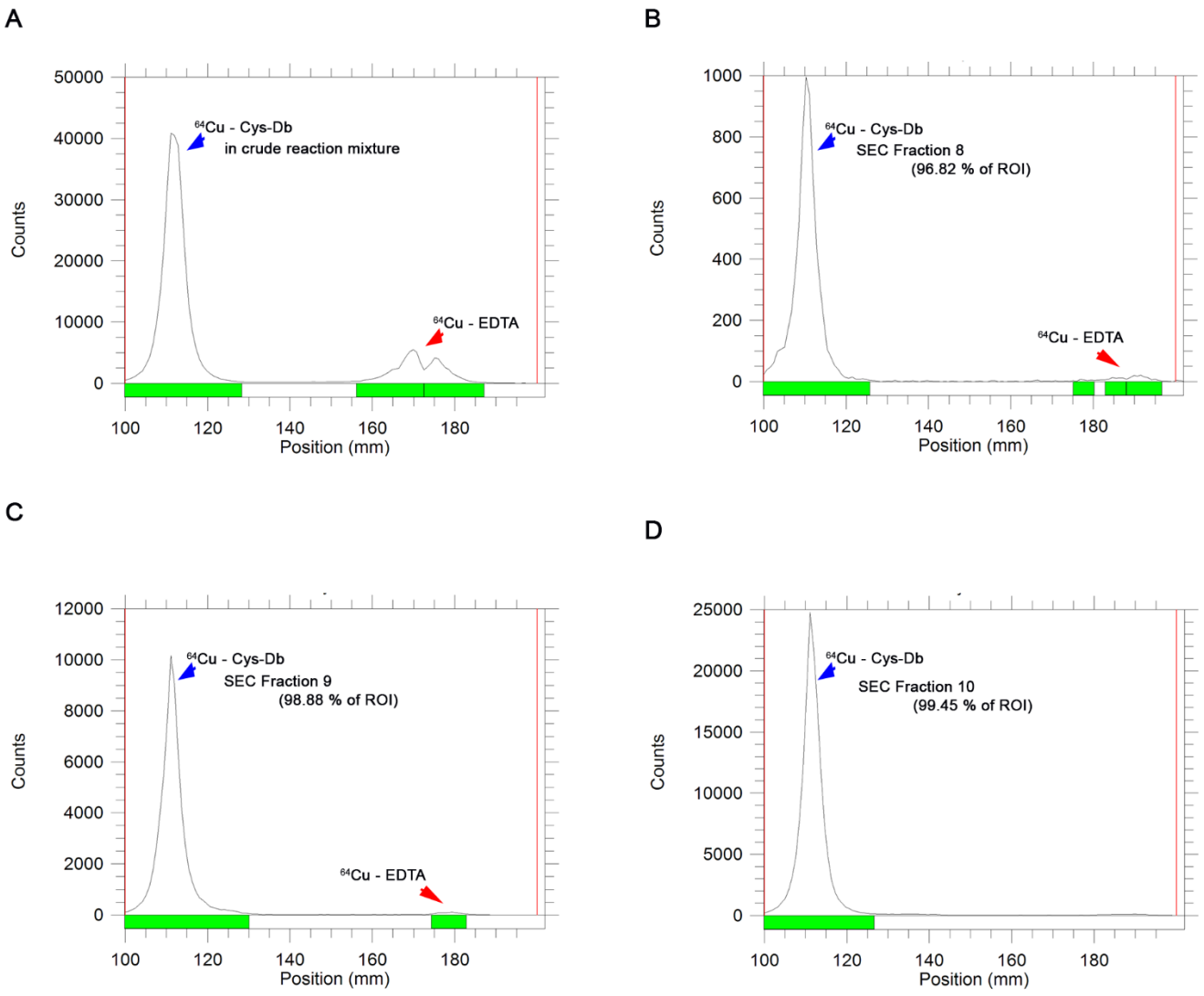

E

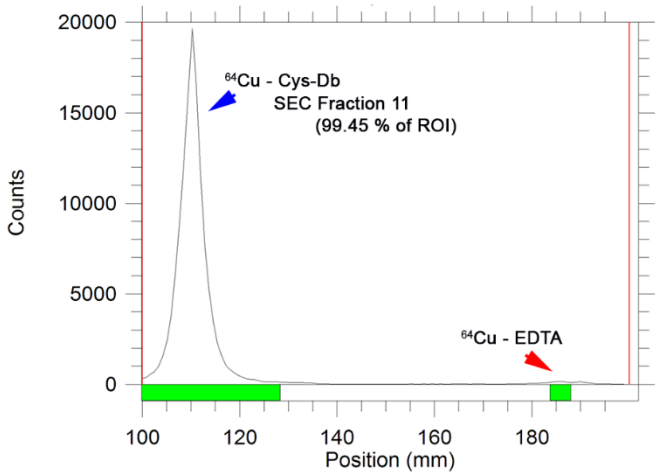
20000
15000
10000
5000
0
Counts
64Cu - Cys-Db
SEC Fraction 11
(99.45 % of ROI)
64Cu - EDTA
100
120
140
160
180
Position (mm)

F

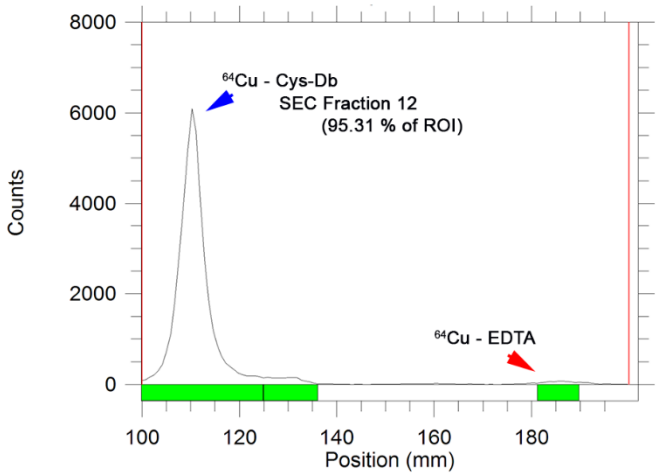
8000
6000
4000
2000
0
Counts
64Cu - Cys-Db
SEC Fraction 12
(95.31 % of ROI)
64Cu - EDTA
100
120
140
160
180
Position (mm)

G

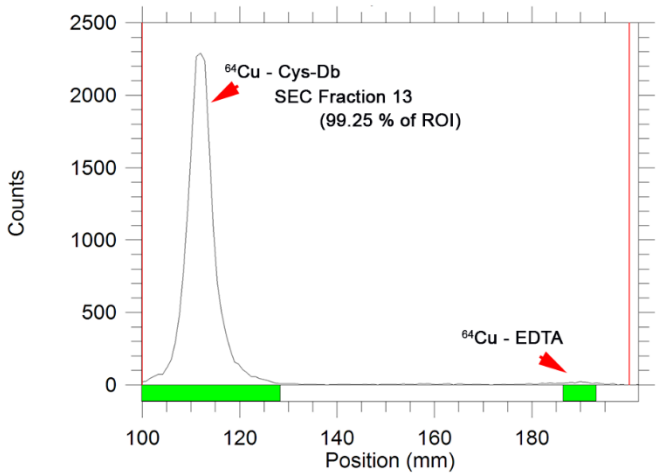
2500
2000
1500
1000
500
0
Counts
64Cu - Cys-Db
SEC Fraction 13
(99.25 % of ROI)
64Cu - EDTA
100
120
140
160
180
Position (mm)

H

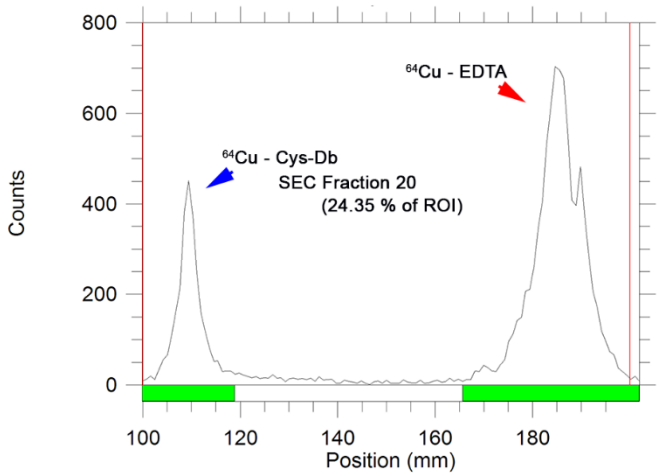
800
600
400
200
0
Counts
64Cu - EDTA
64Cu - Cys-Db
SEC Fraction 20
(24.35 % of ROI)
100
120
140
160
180
Position (mm)

The immunoreactivity of ^{64}Cu-labeled anti-CA125 Cys-Db preparations was found to be > 92% as obtained from the inverse of the intercept of plot seen in Fig. 6.10.

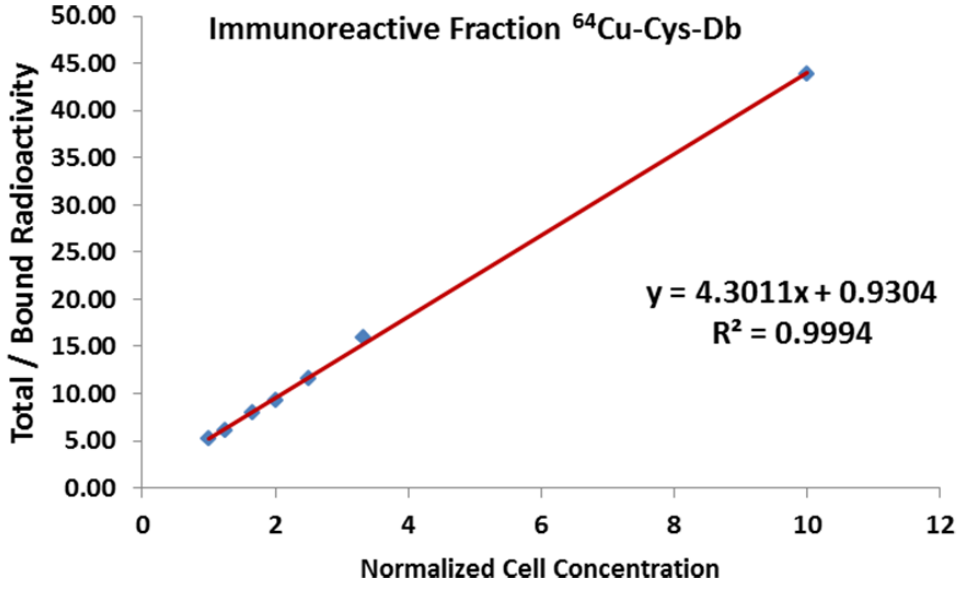

Figure 6.10: Immunoreactivity test: Representative double inverse plot from a Lindmo assay performed with ^{64}Cu-labeled anti-CA125 Cys-Db in NIH:OVCAR-3 cells. The intercept of the plot represents the immunoreactive fraction.

Purified radioimmunoconjugates were > 90% stable in human AB type serum over 48 h (Fig. 6.10A - F).

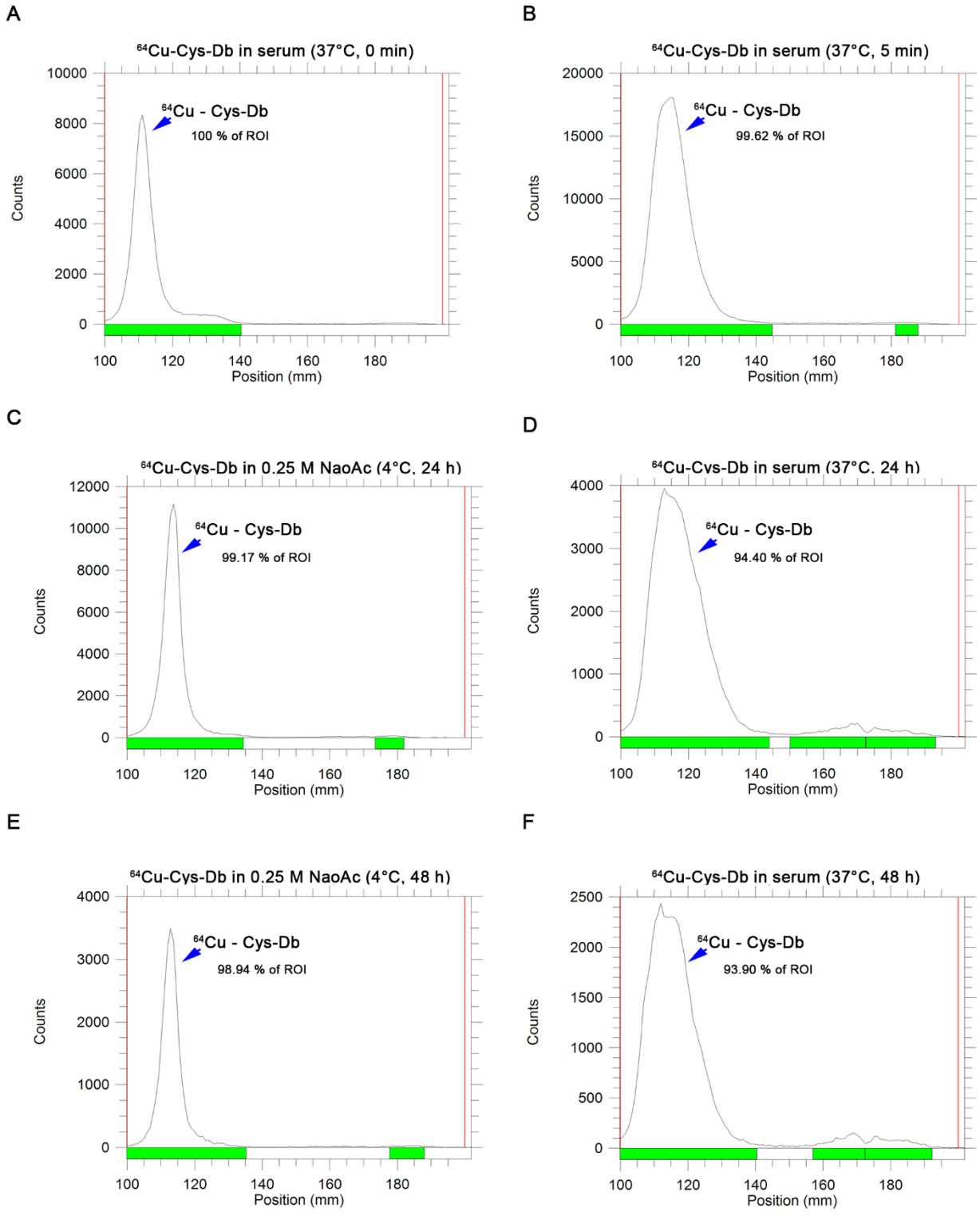

Figure 6.11: Quality Control for serum vs. buffer stability of the diabody. **A – F)** Radio-TLCs for *in vitro* stability of ^{64}Cu – anti-CA125 Cys-Db.

6.3.3 Small animal imaging:

In vivo analysis of ^{64}Cu-labeled anti-CA125 Cys-Db in BALB/c nude mice bearing NIH:OVCAR-3 xenografts as documented by micro-PET scans (Fig. 12) at three different time points post injection revealed the following:

A) at 1 h p.i, most of the radioactivity was seen circulating in the bloodstream, heart, liver, kidneys and bladder. At this time, the OVCAR3 tumor showed an accretion of the radiotracer equivalent to a SUV_{mean} of 0.41 ± 0.05 (n=4).

B) At 4 h p.i, there was a considerable reduction of circulating radiotracer and most of it was restricted to the kidneys with some of it present in the liver. At this time, the tumor showed an increase in accretion of ^{64}Cu-labeled anti-CA125 Cys-Db indicated by a SUV_{mean} of 0.60 (n=2).

C) At 24 h p.i, most of the radiotracer was restricted to the organs of clearance: kidneys, liver and bladder, while there was a relative decrease in tumor related activity to SUV_{mean} of 0.41 ± 0.07 (n=4).

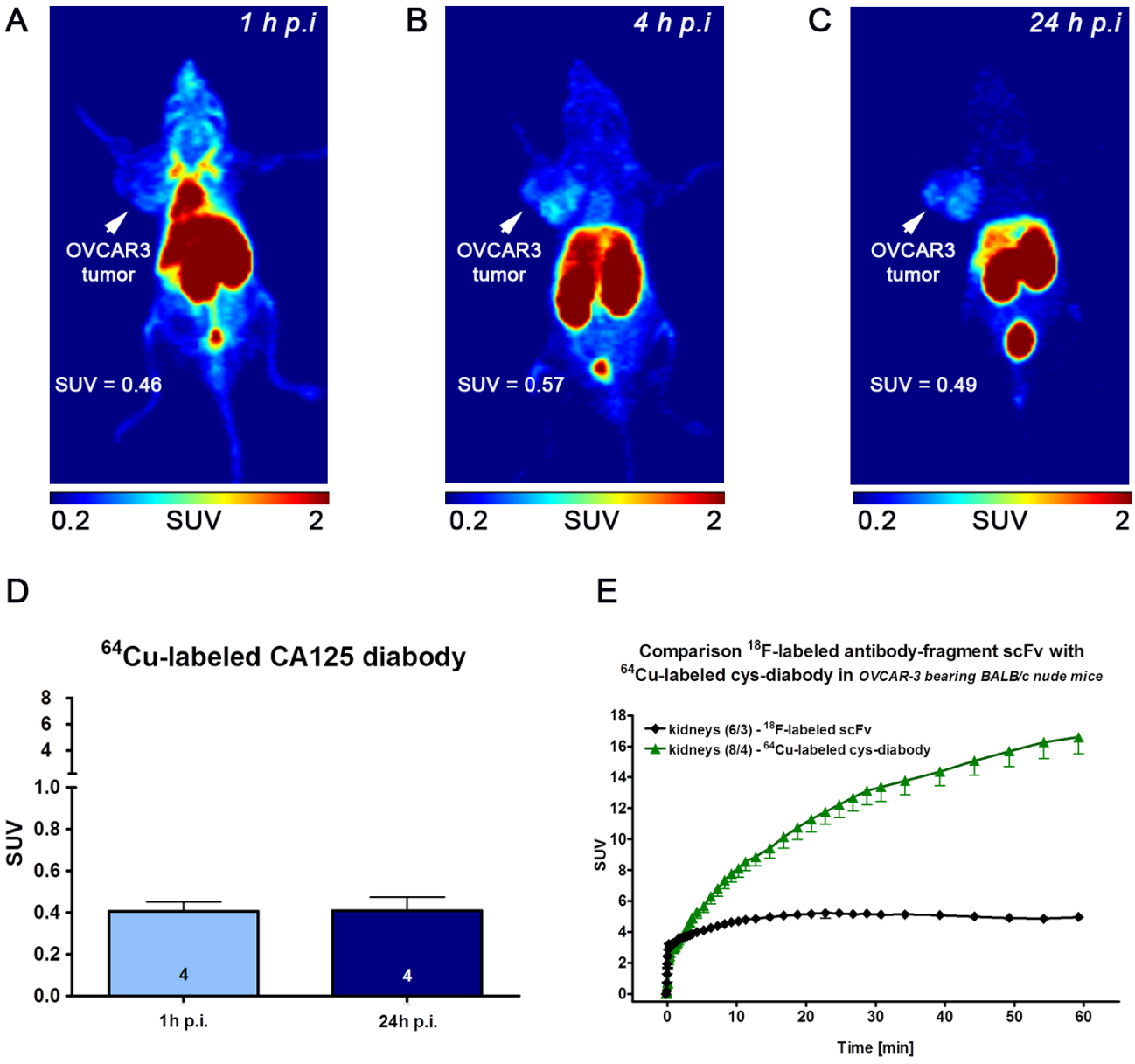

Figure 6.12*: In vivo* small animal PET imaging analysis. **A – C) S**mall animal-PET images of NIH:OVCAR-3 xenograft mice injected with ^{64}Cu-labeled anti-CA125 Cys-Db. Color intensity scale bars represent Standardized Uptake Value (SUV) of radiotracer in animals; **D)** Bar diagram representation of radiotracer SUV at 1 h p.i and 24 h p.i; **E)** Comparative Time Activity Curve for kidney uptake of ^{18}F-labeled anti-CA125 scFv and ^{64}Cu -anti-CA125 Cys-Db.

6.4 Discussion:

Given the practical limitations for *in vivo* tumor targeting by the anti-CA125 scFv format, here we produced an anti-CA125 diabody. The aim was to fulfill the unmet needs for avidity and increased molecular weight to synthesize a suitable molecular probe that can be used in an immuno-PET strategy for same-day imaging of epithelial ovarian cancer. Among the possibilities for recombinant engineering of the scFv into a diabody (Fig. 1), the option for tandem cloning of scFv subunits has been routinely used to produce bi-specific antibody fragments based on the scFv format. However, we refrained from using this strategy due to pre-existing low yields (~1 mg/L from shake flask cultures) of the monomeric anti-CA125 scFv, owing to its un-optimized codon sequence and generally hydrophobic nature of antibody fragments and their inherent tendency for aggregation as inclusion bodies in recombinant *E.coli*.[26, 27] Furthermore, given the limited translational capability of prokaryotic systems for recombinant synthesis of un-optimized eukaryotic genes[28], we considered that doubling the length and degree of hydrophobicity of such a protein encoded in a single plasmid construct could potentially be an inefficient strategy to obtain high enough yields of full-length protein.

Instead, we chose to adopt the simplest option to shorten the length of the inter-domain peptide linker. Ideally, this strategy is proposed to cause the non-covalent dimerization of two scFv molecules on account of limited steric flexibility due to a shortened linker that prevents interaction of variable domains within the monomeric scFv. This ultimately promotes hydrophobic interactions between the

variable light chain domain of one scFv molecule with the complementary heavy chain domain of the neighbouring scFv. However, in the case of anti-CA125 scFv, shortening of the inter-domain peptide linker from the canonical $(G_4S)_3$ to $(G_4S)_1$ did not result in dimerization. This may be explained by the fact that such a multimerization strategy that capitalizes on the length of the linker is also dependent on the variable domain orientation and amino acid composition of the scFv.[29]

Ultimately, we resorted to a more recently reported strategy for the production of diabodies that are covalently linked by intermolecular disulfide bonds formed between unpaired cysteine residues introduced at the C-terminus of monomeric scFv constructs. This strategy offers the benefits of producing *in vivo* folded diabodies with a potential for site specific radiolabeling for same-day imaging via immuno-PET. Nevertheless, we found a significant decrease in the overall yield of recombinant protein produced per litre and poor biochemical purity in the preparation of anti-CA125 Cys-Db produced from shake flask cultures. This could be an effect of the extra cysteine residue introduced into the scFv unit and has been previously reported to result in low yields, low purity and compromised antigen binding abilities upon periplasmic expression of recombinant scFv molecules similarly engineered to have unpaired cysteine residues.[30] Taking this into consideration, even though the cost of production may increase slightly, the gain in overall yields can be higher with alternative expression systems such as yeast, baculovirus or mammalian cells, engineered to preferentially secrete the recombinant protein into culture media, thus obviating the chances for *in vivo*

aggregation and non-specific interaction with other proteins as in the periplasmic space of *E.coli*.

Interestingly though, we found a mixed population of monomeric and dimeric scFv in our purification of the recombinant anti-CA125 Cys-Db. This may be explained by the dynamic equilibrium that tends to exist between these two protein forms of non-covalently associated scFv units in aqueous buffered environments. However, the selective elution of anti-CA125 Cys-Db under high imidazole concentrations in elution buffers used for step-gradient purification may plausibly be a result of stronger binding of this format with the metal affinity resin due to the doubled hexa-histidine tag per unit of covalently-linked recombinant protein (Cys-Db). Despite low yields, the purified anti-CA125 Cys-Db demonstrated CA125 targeting capabilities upon biochemical analysis via immunoblotting, flow cytometry and immunofluorescence. In particular, the immunofluorescence studies demonstrated characteristic membrane-bound signal for CA125 overexpressed by NIH:OVCAR-3 cells in comparison with anti-CA125 MAb-B43.13 used as a positive control and the monomeric anti-CA125 scFv molecule. This pattern of CA125 expression on NIH:OVCAR-3 cells has been observed in our own studies and demonstrated previously using an alternative FITC-labeled anti-CA125 antibody MAb B27.1.[31]

Furthermore, although the anti-CA125 Cys-Db was modified via conjugation to a bi-functional macrocyclic chelator and successfully radiolabeled with ^{64}Cu, we obtained low radiochemical yields and specific activity vis-à-vis previously reported (Chapter 3) values for the monomeric scFv radiolabeled in an identical

manner. This may have been due to the low overall recombinant yields obtained for this vector and subsequently low concentration of the diabody preparations, which may not have been ideal to allow conjugation of sufficient molecules of NOTA per diabody. Conversely, the yields for the the monomeric scFv were ~ 3 folds higher and yielded suitable concentration of this antibody fragment for downstream modifications such as NOTA conjugation and ^{64}Cu-labeling. Nevertheless, the purified radioimmunoconjugate demonstrated a high *in vitro* immunoreactive fraction when assayed with NIH:OVCAR-3 cells.

In vivo evaluation of the anti-CA125 Cys-Db demonstrated an expected radiopharmacologic profile which was suggestive of renal clearance for this molecule possessing a molecular weight of ~ 55 KDa. Furthermore, similar to the observations made in the case of ^{18}F-labeled anti-CA125 scFv (Chapter 3), the presence of a significant amount of radiotracer in the bloodstream 1 h p.i may be representative of circulating immunocomplexes (IC) between the ^{64}Cu-labeled anti-CA125 Cys-Db and CA125 antigen shed in the blood pool of the xenograft animals. Such high molecular weight ICs may eventually be cleared via the hepatic/splenic route and could plausibly account for the involvement of high liver signal until 4 h p.i. Although the increased avidity of diabodies was expected to yield a significantly improved absolute tumor accumulation, we found that the anti-CA125 Cys-Db did not perform any better than the monomeric scFv in the preliminary *in vivo* evaluations presented here.

In fact, a comparative analysis of the 1 h p.i time activity curves from dynamic micro-PET scans of ^{18}F-labeled anti-CA125 scFv and the ^{64}Cu-labeled anti-

CA125 Cys-Db revealed a significantly higher accumulation of Cys-Db radiotracer in the kidneys than with the monomeric scFv radiotracer (Fig. 12E). This may be attributed to the greater tendency of radio-metal chelated antibody fragments to be reabsorbed in the kidneys and a high retention of radiometabolites resulting from endocytosis in lysosomal compartments of renal cells.[32, 33, 34] However, a higher renal uptake of the diabody over the monomeric scFv has also been observed by Schneider *et al* [8] although they rationalized this to be a result of most of the scFv radiotracer being flushed out of the system within 1 h p.i. Nonetheless, existing evidence and results from various studies with other scFvs[35, 36] and nanobodies[37, 38] using hexa-histidine tagged recombinant molecules and comparing the effect of this polar group on the *in vivo* biodistribution of such molecules prompts us to speculate that besides being a radiometal immunoconjugate, the doubled hexa-histidine tags in the anti-CA125 Cys-Db molecule may be contributing greatly to an increased renal trapping of this radiotracer as observed in the kidneys of xenograft mice examined in this study. This aspect has been previously explained[37, 38] to occur as a result of the pH in the kidney cortex being lower than the pKa of imidazole rings in histidine residues of reabsorbed proteins/peptides in the renal tubules. Furthermore, a strong interaction between the protonated imidazole units of histidine residues and the negatively charged lumen of renal tubules rich in megalin and cubulin endocytic receptors[32] may preclude the anti-CA125 Cys-Db from attaining a desirable *in vivo* tumor uptake and realizing its proposed tumor targeting potential. Taken together, an evaluation of the *in vivo* radiopharmacologic profile and tumor

targeting capabilities of the anti-CA125 Cys-Db without the hexa-histidine tag and in the form of a radiofluorinated version is warranted to fully investigate the utility of this molecule for same-day imaging of epithelial ovarian cancer.

However, it is noteworthy that owing to their molecular weight and associated theoretical advantages thereof, diabodies would continue to be renally cleared even in the absence of the polar hexa-histidine tag. Nonetheless, substantial renal toxicity from the *in vivo* application of such radiotracers can be reduced while simultaneously achieving suitable tumor uptake values as demonstrated by further engineering the overall charge of the molecule by introducing negatively charged amino acids into the variable light chain domains of scFv units,[39] introducing cleavable linkers between radiometal chelate and antibody fragment to release the radiometabolites from lysosomal compartments of renal cells,[40] or site-specific PEGylation,[33] without significantly compromising the immunoreactivity of the targeting vector. Alternatively, administering a relatively excess dose of positively charged amino acids or succinylated gelatin to saturate the endocytic receptors on renal tubules[32, 38, 41] are options routinely exercised in the clinic for peptide receptor radionuclide therapy (PRRT).

6.5 Conclusion:

In the present chapter, we have demonstrated the development of a covalent dimer of an anti-CA125 scFv by engineering an additional unpaired cysteine at the C-terminus of the scFv construct. The recombinant expression and *in vivo* folding of such scFv molecules within the oxidizing periplasmic environment of recombinant *E.coli* promoted the production of anti-CA125 Cys-Db. Although recombinant yields of the anti-CA125 Cys-Db obtained in this study were relatively low, the construct demonstrated robust *in vitro* binding to target antigen CA125 overexpressed on NIH:OVCAR-3 cells. *In vivo* application of the anti-CA125 Cys-Db as a radiometal immunoconjugate in OVCAR3 xenograft mice was able to delineate the tumor as early as 1 h p.i albeit with low absolute tumor uptake values at this time point but a slight increase in tumor accretion up to 4 h p.i. The ^{64}Cu-labeled anti-CA125 Cys-Db continued to suffer from first pass clearance and high renal uptake attributed to its size, charge, presence of a doubled hexa-histidine tag and by virtue of being a radiometal immunoconjugate. Since these are preliminary analysis from a work in progress, further engineering and evaluation of the *in vivo* radiopharmacological profiles of this construct are warranted to make it a suitable radio-tracer for same-day imaging of epithelial ovarian cancer.

6.6 References:

1. Wu AM: Engineered antibodies for molecular imaging of cancer. *Methods* 2014, **65**(1):139-147.
2. Olafsen T, Wu AM: Antibody vectors for imaging. *Semin Nucl Med* 2010, **40**(3):167-181.
3. Wittrup KD, Thurber GM, Schmidt MM, Rhoden JJ: Practical theoretic guidance for the design of tumor-targeting agents. *Methods Enzymol* 2012, **503**:255-268.
4. Knowles SM, Wu AM: Advances in immuno-positron emission tomography: antibodies for molecular imaging in oncology. *J Clin Oncol* 2012, **30**(31):3884-3892.
5. Vogel CA, Bischof-Delaloye A, Mach JP, Pelegrin A, Hardman N, Delaloye B, Buchegger F: Direct comparison of a radioiodinated intact chimeric anti-CEA MAb with its F(ab')2 fragment in nude mice bearing different human colon cancer xenografts. *Br J Cancer* 1993, **68**(4):684-690.
6. Milenic DE, Yokota T, Filpula DR, Finkelman MA, Dodd SW, Wood JF, Whitlow M, Snoy P, Schlom J: Construction, binding properties, metabolism, and tumor targeting of a single-chain Fv derived from the pancarcinoma monoclonal antibody CC49. *Cancer Res* 1991, **51**(23 Pt 1):6363-6371.
7. Shively JE: ^{18}F labeling for immuno-PET: where speed and contrast meet. *J Nucl Med* 2007, **48**(2):170-172.
8. Schneider DW, Heitner T, Alicke B, Light DR, McLean K, Satozawa N, Parry G, Yoo J, Lewis JS, Parry R: In vivo biodistribution, PET imaging, and tumor accumulation of ^{86}Y- and ^{111}In-antimindin/RG-1, engineered antibody fragments in LNCaP tumor-bearing nude mice. *J Nucl Med* 2009, **50**(3):435-443.
9. Pluckthun A, Pack P: New protein engineering approaches to multivalent and bispecific antibody fragments. *Immunotechnology* 1997, **3**(2):83-105.

10. Kortt AA, Dolezal O, Power BE, Hudson PJ: Dimeric and trimeric antibodies: high avidity scFvs for cancer targeting. *Biomol Eng* 2001, **18**(3):95-108.

11. Le Gall F, Kipriyanov SM, Moldenhauer G, Little M: Di-, tri- and tetrameric single chain Fv antibody fragments against human CD19: effect of valency on cell binding. *FEBS Lett* 1999, **453**(1-2):164-168.

12. Olafsen T, Sirk SJ, Betting DJ, Kenanova VE, Bauer KB, Ladno W, Raubitschek AA, Timmerman JM, Wu AM: ImmunoPET imaging of B-cell lymphoma using 124I-anti-CD20 scFv dimers (diabodies). *Protein Eng Des Sel* 2010, **23**(4):243-249.

13. McCabe KE, Liu B, Marks JD, Tomlinson JS, Wu H, Wu AM: An engineered cysteine-modified diabody for imaging activated leukocyte cell adhesion molecule (ALCAM)-positive tumors. *Mol Imaging Biol* 2012, **14**(3):336-347.

14. Girgis MD, Federman N, Rochefort MM, McCabe KE, Wu AM, Nagy JO, Denny C, Tomlinson JS: An engineered anti-CA19-9 cys-diabody for positron emission tomography imaging of pancreatic cancer and targeting of polymerized liposomal nanoparticles. *J Surg Res* 2013, **185**(1):45-55.

15. Viola-Villegas NT, Sevak KK, Carlin SD, Doran MG, Evans HW, Bartlett DW, Wu AM, Lewis JS: Noninvasive Imaging of PSMA in Prostate Tumors with Zr-Labeled huJ591 Engineered Antibody Fragments: The Faster Alternatives. *Mol Pharm* 2014.

16. Williams LE, Wu AM, Yazaki PJ, Liu A, Raubitschek AA, Shively JE, Wong JY: Numerical selection of optimal tumor imaging agents with application to engineered antibodies. *Cancer Biother Radiophar* 2001, **16**(1):25-35.

17. Cai W, Olafsen T, Zhang X, Cao Q, Gambhir SS, Williams LE, Wu AM, Chen X: PET imaging of colorectal cancer in xenograft-bearing mice by use of an 18F-

labeled T84.66 anti-carcinoembryonic antigen diabody. *J Nucl Med* 2007, **48**(2):304-310.

18. Olafsen T, Sirk SJ, Olma S, Shen CK, Wu AM: ImmunoPET using engineered antibody fragments: fluorine-18 labeled diabodies for same-day imaging. *Tumour Biol* 2012, **33**(3):669-677.

19. Eder M, Knackmuss S, Le Gall F, Reusch U, Rybin V, Little M, Haberkorn U, Mier W, Eisenhut M: 68Ga-labelled recombinant antibody variants for immuno-PET imaging of solid tumours. *Eur J Nucl Med Mol Imaging* 2010, **37**(7):1397-1407.

20. Wang WW, Das D, McQuarrie SA, Suresh MR: Design of a bifunctional fusion protein for ovarian cancer drug delivery: single-chain anti-CA125 core-streptavidin fusion protein. *EurJ Pharm Biopharm* 2007, **65**(3):398-405.

21. Kriangkum J, Xu B, Gervais C, Paquette D, Jacobs FA, Martin L, Suresh MR: Development and characterization of a bispecific single-chain antibody directed against T cells and ovarian carcinoma. *Hybridoma* 2000, **19**(1):33-41.

22. Noujaim AA, Baum RP, Sykes TR, Sykes CJ, Hertel A, Niesen, A, et al. Monoclonal antibody B43.13 for immunoscintigraphy and immunotherapy of ovarian cancer. In Current Tumor Diagnosis: Applications, Clinical Relevance, Trends. Edited by Klapdor, R. Munich: W Zuckschwerdt Verlag; 1994; 823–829.

23. Newa M, Lam M, Bhandari KH, Xu B, Doschak MR: Expression, characterization, and evaluation of a RANK-binding single chain fraction variable: an osteoclast targeting drug delivery strategy. *Mol Pharm* 2014, **11**(1):81-89.

24. Kume M, Carey PC, Gaehle G, Madrid E, Voller T, Margenau W, Welch MJ, Lapi SE: A semi-automated system for the routine production of copper-64. *Appl Radiat Isot* 2012, **70**(8):1803-1806.

25. Lindmo T, Boven E, Cuttitta F, Fedorko J, Bunn PA, Jr.: Determination of the immunoreactive fraction of radiolabeled monoclonal antibodies by linear extrapolation to binding at infinite antigen excess. *J Immunol Methods* 1984, **72**(1):77-89.

26. Palomares LA, Estrada-Mondaca S, Ramirez OT: Production of recombinant proteins: challenges and solutions. *Methods Mol Biol* 2004, **267**:15-52.

27. Chowdhury PS, Vasmatzis G: Engineering scFvs for improved stability. *Methods Mol Biol* 2003, **207**:237-254.

28. Gustafsson C, Govindarajan S, Minshull J: Codon bias and heterologous protein expression. *Trends in biotechnology* 2004, **22**(7):346-353.

29. Lawrence LJ, Kortt AA, Iliades P, Tulloch PA, Hudson PJ: Orientation of antigen binding sites in dimeric and trimeric single chain Fv antibody fragments. *FEBS Lett* 1998, **425**(3):479-484.

30. Schmiedl A, Breitling F, Winter CH, Queitsch I, Dubel S: Effects of unpaired cysteines on yield, solubility and activity of different recombinant antibody constructs expressed in E. coli. *J Immunol Methods* 2000, **242**(1-2):101-114.

31. Xiao Z, McQuarrie SA, Suresh MR, Mercer JR, Gupta S, Miller GG: A three-step strategy for targeting drug carriers to human ovarian carcinoma cells in vitro. *J Biotechnol* 2002, **94**(2):171-184.

32. Vegt E, de Jong M, Wetzels JF, Masereeuw R, Melis M, Oyen WJ, Gotthardt M, Boerman OC: Renal toxicity of radiolabeled peptides and antibody fragments: mechanisms, impact on radionuclide therapy, and strategies for prevention. *J Nucl Med* 2010, **51**(7):1049-1058.

33. Li L, Crow D, Turatti F, Bading JR, Anderson AL, Poku E, Yazaki PJ, Carmichael J, Leong D, Wheatcroft D *et al*: Site-specific conjugation of monodispersed DOTA-PEGn to a thiolated diabody reveals the effect of increasing peg size on

kidney clearance and tumor uptake with improved 64-copper PET imaging. *Bioconjug Chem* 2011, **22**(4):709-716.

34. Yazaki PJ, Wu AM, Tsai SW, Williams LE, Ikler DN, Wong JY, Shively JE, Raubitschek AA: Tumor targeting of radiometal labeled anti-CEA recombinant T84.66 diabody and t84.66 minibody: comparison to radioiodinated fragments. *Bioconjug Chem* 2001, **12**(2):220-228.

35. Waibel R, Alberto R, Willuda J, Finnern R, Schibli R, Stichelberger A, Egli A, Abram U, Mach JP, Pluckthun A *et al*: Stable one-step technetium-99m labeling of His-tagged recombinant proteins with a novel Tc(I)-carbonyl complex. *Nat Biotechnol* 1999, **17**(9):897-901.

36. Kogelberg H, Miranda E, Burnet J, Ellison D, Tolner B, Foster J, Picon C, Thomas GJ, Meyer T, Marshall JF *et al*: Generation and characterization of a diabody targeting the alphavbeta6 integrin. *PloS One* 2013, **8**(9):e73260.

37. Xavier C, Vaneycken I, D'Huyvetter M, Heemskerk J, Keyaerts M, Vincke C, Devoogdt N, Muyldermans S, Lahoutte T, Caveliers V: Synthesis, preclinical validation, dosimetry, and toxicity of 68Ga-NOTA-anti-HER2 Nanobodies for iPET imaging of HER2 receptor expression in cancer. *J Nucl Med* 2013, **54**(5):776-784.

38. D'Huyvetter M, Vincke C, Xavier C, Aerts A, Impens N, Baatout S, De Raeve H, Muyldermans S, Caveliers V, Devoogdt N *et al*: Targeted Radionuclide Therapy with A (177)Lu-labeled Anti-HER2 Nanobody. *Theranostics* 2014, **4**(7):708-720.

39. Colcher D, Pavlinkova G, Beresford G, Booth BJ, Choudhury A, Batra SK: Pharmacokinetics and biodistribution of genetically-engineered antibodies. *Q J Nucl Med* 1998, **42**(4):225-241.

40. Arano Y: Strategies to reduce renal radioactivity levels of antibody fragments. *Q J Nucl Med* 1998, **42**(4):262-270.

41. Behr TM, Goldenberg DM, Becker W: Reducing the renal uptake of radiolabeled antibody fragments and peptides for diagnosis and therapy: present status, future prospects and limitations. *Eur J Nucl Med* 1998, **25**(2):201-212.

7

General Discussion and Conclusions

7.1 General Discussion and Conclusions:

7.1.1 Summary Discussion:

The work presented in this thesis focuses on the development of an immuno-PET strategy for the molecular imaging of epithelial ovarian cancer (EOC). The motivation for this work were the existing challenges for early detection of recurrent EOC and the glaring fact that elevation of CA125 levels occurs at least 3 months prior to recurrence and there is a median predicted lag time of 2 months between its detection by radiologic methods.[1, 2] This could be a good indication of recurrent disease brewing from post-treatment residual neoplasms in the peritoneum and conveniently escaping diagnostic surveillance from conventional radiologic imaging such as ultrasound, CT and MRI that deliver anatomical / morphologic information. Presently, PET is not used as a front-line imaging modality in the diagnosis of recurrent ovarian disease unless patients with rising CA125 levels show negative results with the aforementioned radiologic methods.[3] Although [^{18}F]FDG-PET has demonstrated higher sensitivity and accuracy for the detection of recurrent disease in such a scenario, it has its limitations with respect to uptake in the cystic ovarian tumors[4] and the small size of recurrent lesions, which may not have adequate [^{18}F]FDG uptake to be detected or resolved by clinical PET scanners.[3] With PET being the most functional imaging modality at hand, we devised a strategy to directly target CA125 and carry out non-invasive imaging of its expression in epithelial ovarian tumors, which were subcutaneously xenografted into immunocompromised mice. In doing

so, we enabled ourselves to test the hypothesis for *in vivo* targeting of CA125 and its utility for the imaging of EOC tumor burden in subjects.

The prospects of using a magic bullet:

Antibodies are naturally synonymous with the term 'targeting' owing to their primary affiliation with the immune system and their analogy as 'magic bullets'.[5] With several preclinical and clinical success stories[6, 7] for antibody-based tumor targeting, such a molecule was considered an ideal candidate as a targeting vector to be employed in our strategy.

Being a part of Dr. Suresh's research group provided a unique opportunity for access to prior research done by the groups of Noujaim, Schultes, Baum, Sykes, McQuarrie and Suresh et al.[8-10] They had developed and tested murine antibodies targeting various oncologic and infectious disease targets including CA125 in epithelial ovarian cancer.[11, 12] One of these antibodies – MAb-B43.13 had demonstrated immunotherapeutic potential early in the 1990s[13-17] and has only recently been through Phase III clinical trials with no significant effect as a maintenance monoimmunotherapeutic agent.[18] Interestingly though, it was initially intended for use as a ^{99m}Tc-labeled radioimmunoscintigraphic agent in SPECT imaging of human ovarian cancer patients.[19] More recent work from Dr. Suresh's group had demonstrated successful *in vitro* application of a bi-functional fusion protein[20] and a bi-specific single-chain antibody[21] targeting CA125 in EOC cells. The active CA125-targeting component in both these constructs was a single-chain Fragment variable (scFv) derivative of MAb-B43.13.

The recent surge of immuno-PET[22, 23] as a functional molecular imaging strategy has opened the doors to employ engineered antibodies[24] in conjunction with positron-emitting radionulcides for the synthesis and preclinical assessment of several molecular probes with potential clinical applications in oncologic imaging. Our access to a full-length antibody and its derivative fragment for CA125 targeting combined with a unique opportunity to perform radiochemistry and small animal PET imaging in the group of Dr. Wuest, set our goals towards the development of an immuno-PET strategy for imaging CA125 in EOC.

The promise, challenges and perils of using a fragment of the entire bullet: Where did the bullet's "magic" go?

Given the attractive propositions for retained immunoreactivity but better tumor penetration and faster *in vivo* clearance of single-chain Fragment variables (scFv) as compared with full-length antibodies; transforming an anti-CA125 scFv into a targeted molecular imaging probe by virtue of its radiolabeling with a relatively short-lived positron emitting radioisotope such as ^{18}F (Fluorine-18; $t_{1/2}$ 1.8 h) for same-day imaging of EOC was considered an ideal opportunity towards achieving high contrast PET images in a short duration of time.

This led us to our first objective (Chapter 2) – the synthesis of anti-CA125 scFv, which was sub-cloned from the previously reported bi-functional fusion construct.[20] This enabled its isolation from the potentially immunogenic 'core-streptavidin' segment in the parent construct while reducing the effective molecular weight (~28 KDa) of the resulting scFv-only construct in order to

achieve better tumor penetration and systemic clearance. In keeping with the simplicity and cost effectiveness of the procedure, we chose *E.coli* Rosetta 2(DE3) as a simple prokaryotic host system supplemented with rare codon tRNAs for the recombinant expression of anti-CA125 scFv. Nevertheless, such a simple expression host had its own challenges: a) expression of a murine sequence in a heterologous host; b) scFv molecules by themselves are hydrophobic in nature and tend to aggregate as inclusion bodies. This study further analyzed the effect of three factors that are known to impact recombinant soluble scFv expression in *E.coli* – a) variable domain orientation; b) inter-domain peptide linker sequence; c) codon optimization. Some of the salient findings of this study were a) recombinant soluble scFv expression was ~ 1.4 fold higher in the V_H-V_L orientation than the V_L-V_H orientation independent of the type of inter-domain peptide linker used; b) $(G_4S)_3$ inter-domain peptide linker yielded up to 2-fold higher expression of the scFv regardless of the domain orientation; c) up to 14-fold higher expression of recombinant soluble expression of the anti-CA125 scFv was achieved as a result of codon optimization. Most importantly, all the scFv constructs created and used in this study were found to be immunoreactive with the target – CA125 antigen as demonstrated by *in vitro* analysis. Thus, potential *in vivo* targeting could be attempted with either one of these constructs. It may be noteworthy to mention here that although there are reports of higher soluble recombinant expression[25, 26] of other scFvs using prokaryotic systems, this can be a subjective aspect since protein yields in such an exercise are dependent on several factors including but not limited to its sequence[27], inherent molecular

stability[28] owing to *in vivo* folding intermediates,[29] use of supplemental chaperone proteins,[30, 31] controlled induction procedures[32] etc.

Having achieved sufficient expression of the scFv, we set our hands onto fulfilling an objective as attractive as achieving same-day imaging of EOC in xenograft mice models. Moreover, the prospect of having a targeted ^{18}F-labeled scFv as a molecular probe for PET imaging of EOC would challenge the proposed limitation of [^{18}F]FDG uptake by ovarian tumors. In this study (Chapter 3), high specific activity *N*-succinimidyl-4-[^{18}F]fluorobenzoate ([^{18}F]SFB) was used as a prosthetic group to create [^{18}F]FBz-anti-CA125 scFv for use as a radiotracer, although in very modest radiochemical yields.[33]

At this point, it may be worth mentioning that even though radiofluorination using prosthetic groups such as [^{18}F]SFB is a useful technique, there is a specific need for speed in this process attributed not to the decay of ^{18}F itself, but to a relatively rapid degradation of [^{18}F]SFB in the slightly alkaline (pH 8.3) environment in borate buffer which is used to provide a conducive opportunity for acylation reactions to occur on primary amines in biomolecules. In a more dramatic sense, this is akin to a question of 'to-be' or 'not-to-be' for [^{18}F]SFB, while radiolabeling is ultimately achieved through a tug-of-war between the two processes – acylation on primary amines versus degradation of the prosthetic group. Furthermore, even though high radiochemical yields have been obtained in our research team over the last hundreds of routine automated syntheses of this prosthetic group; this procedure has been a subject to few

failures invariably attributed to its sensitivity for the shelf-life of critical reagents used in the reaction scheme (example TSTU).

Alternatively, given the relatively short biological half-lives of antibody fragments and the aforementioned minor limitations with using [^{18}F]SFB in developing radiotracers for same-day imaging, it might be prudent to employ ^{68}Ga for such objectives. A growing rate of acceptance and use of this PET-radionuclide in the clinic, an ability to produce it literally from a bench-top generator instead of the dependency on a cyclotron for ^{18}F production, combined with the ease for radiolabeling biomolecules via functionalization with readily available azamacrocyclic chelators such as NOTA and ultimately the prospects to achieve very high specific activity radiotracer are just some of the excellent advantages to consider using this isotope for future applications with antibody fragments.

Our experience demonstrated that despite excellent *in vitro* immunoreactivity with the target antigen on NIH:OVCAR-3 cells, the [^{18}F]FBz-anti-CA125 scFv radiotracer demonstrated poor *in vivo* tumor uptake. Such a result is in agreement with other reports and is largely attributed to the limitations of monomeric scFv-based radiotracers that lack the avidity required for sufficient tumor retention and tend to be victims of first-pass renal clearance, which is compounded further by massive renal retention owing to the hydrophobic nature and positive charge of scFv molecules and the presence of a polar C-terminal hexa-histidine tag in such fusion proteins that collectively precludes its *in vivo* tumor bioavailability.[34, 35] Thus, as evaluated from relative tumor uptake of the

two radiotracers in CA125-positive NIH:OVCAR-3 tumors in xenograft mouse models, the ^{18}F-labeled anti-CA125 scFv could not outperform [^{18}F]FDG in its anticipated function as a radiotracer within this study.

Nevertheless, an interesting observation was the differential *in vivo* radiopharmacological profile as analyzed from the time activity curves of ^{18}F-labeled anti-CA125 scFv between the CA125-positive versus CA125-negative tumor bearing animals. This was indicative of a potential immunocomplex formation of the ^{18}F-labeled anti-CA125 scFv with shed CA125 antigen circulating in the bloodstream of NIH:OVCAR-3 bearing mice. This could be yet another factor to preclude tumor bioavailability of scFv-based radiotracers used under an *in vivo* setting with shed antigens such as CA125. While this is an interesting feature, presence of shed antigens in previous studies[36, 37] employing full-length antibodies as immuno-PET radiotracers, have not significantly affected their tumor targeting capabilities.

Here it is: Using the full-length antibody to harness the potential of CA125 for non-invasive molecular imaging of Epithelial Ovarian Cancer:

Thus, we considered it worthwhile to employ the full-length anti-CA125 antibody – MAb-B43.13 as an immuno-PET tracer for CA125 imaging. In doing so, we would not only overcome the limitation for avidity, but also circumvent the problem of kidney retention as was observed with the scFv format. However, using the full-length antibody would prevent us from performing a same-day imaging procedure which would be an ideal approach for potential clinical

translation. This also meant using a relatively longer-lived PET radionuclide in order to fulfill the prerequisite for a favourable match between the biological (serum) half-life of the targeting vector and the physical (radioactive decay) half-life of the radioisotope.

To this end, we conducted our next study (Chapter 4) choosing ^{64}Cu ($t_{1/2}$ 12.7 h) to radiolabel the anti-CA125 MAb-B43.13 and its derivative scFv, that were both functionalized with *p*-SCN-Bn-NOTA [S-2-(4-Isothiocyanatobenzyl)-1,4,7-triazacyclononane-1,4,7-triacetic acid], which served as a bi-functional chelator to indirectly label the CA125 targeting vectors. Some of the salient features of this study were – a) detailed functional characterization of the CA125 antibody and scFv was demonstrated prior to modifications for use in immuno-PET; b) ideal antibody functionalization strategy with consistent yields for bioconjugation of radiometal chelator was achieved; b) high specific activity ^{64}Cu-labeled CA125 antibody-based radiotracers were obtained; c) consistent *in vitro* immunoreactivity was demonstrated; d) a detailed analysis of uptake of the radiotracers in CA125-positive versus CA125-negative tumors was performed via small animal PET imaging studies; e) *in vivo* imaging studies could conveniently be performed up to 48 h post injection (p.i); f) specificity of antibody-based radiotracer uptake was demonstrated through competition studies analyzed via small animal PET; g) the quantitative nature of PET was highlighted by an ability to account for non-specific tumor uptake of the radiotracer by virtue of enhanced permeability and retention effect; h) both anti-CA125 targeting vectors demonstrated expected radiopharmacologic profiles, especially with respect to

clearance; i) *ex vivo* analysis of harvested tumor samples was performed via digital autoradiography, immunofluorescence and immunohistochemistry to demonstrate the extent of CA125 expression and localization of ^{64}Cu-anti-CA125 MAb-B43.13 based targeting of CA125 in the NIH:OVCAR-3 tumor.

Most importantly, this study demonstrated a superiority of the full-length antibody over its derivative single-chain antibody counterpart for *in vivo* tumor targeting. This is in agreement with several other reports in literature and has been attributed not only to the bivalent nature of the antibody to render it with an increased avidity as compared to the scFv, but mainly to a much higher tumor bioavailability of the full-length antibody owing to a longer residency in circulation on account of its regeneration by neonatal Fc receptors (FcRn) expressed in most cells of the body. Furthermore, the ^{64}Cu-labeled MAb-B43.13 clearly outperformed [^{18}F]FDG in its absolute tumor uptake, although these may not ideally be compared due to a fundamental difference in the radioisotopes used and the respective time points for performing small animal PET imaging. Nevertheless, it was indicative enough to demonstrate the utility of a targeted radiotracer such as ^{64}Cu-labeled anti-CA125 MAb B43.13 over a metabolic radiotracer such as [^{18}F]FDG.

Although the use of an ^{18}F-labeled scFv in chapter 3 indicated the possible presence of circulating CA125 antigen, the results from a 24 h p.i scan with ^{64}Cu-labeled MAb-B43.13 did not indicate for as much shed CA125 antigen in the bloodstream of xenograft mice bearing NIH:OVCAR-3 tumors as assayed by a Human CA125 ELISA kit with 5 U/mL as its limit of detection for CA125 in

serum samples. This finding could be indicative for a prospective utility of CA125 targeted immuno-PET in the absence of any detectable levels of shed CA125. However, such a direct interpretation of the results is being used with caution considering that MAb-B43.13 has a high affinity for CA125 and may have sequestered whatever little was present in the circulation at early time points post-injection of the tracer to form immunocomplexes leading to the liver and spleen for clearance by the reticuloendothelial system. This could be an additional explanation for the radioactivity observed in these organs.

Furthermore, the sensitivity of immuno-PET to deliver such strong signals despite relatively low physical quantity of radiotracer uptake is reflected by the *ex vivo* autoradiography analysis in this study, wherein out of 4.55 MBq of ^{64}Cu-labeled MAb-B43.13 (30-40 μg) injected into the NIH:OVCAR-3 xenograft mouse, only 0.08 MBq of radioactivity was measured in the tumor at the time of harvest from this animal for digital autoradiography and immunohistochemistry.

Maximizing the potential: Can we do better?

In order to maximize the tumor targeting ability of anti-CA125 MAb-B43.13 and study its *in vivo* radiopharmacologic profile beyond the limits decipherable with ^{64}Cu, we chose to step up to the next level. An increasing clinical acceptance and use of ^{89}Zr ($t_{1/2}$ 78.4 h) prompted us to use this PET radionuclide in order to fulfill this objective (Chapter 5) and deliver a potentially translational benefit to the use of this antibody as a molecular imaging probe for immuno-PET of epithelial ovarian cancer.

Some of the salient features of this study were: a) synthesis of biochemically-active immunoconjugate with higher number of radiometal chelator (Desferrioxamine – DFO) conjugated per MAb-B43.13 molecule; b) consistent yields of high specific activity ^{89}Zr-DFO-MAb-B43.13 were obtained; c) ^{89}Zr-DFO-MAb-B43.13 demonstrated a high degree of *in vitro* serum stability up to 7 days; d) the radiotracer was immunoreactive when tested post-synthesis; e) this strategy extended the ability to perform CA125 targeted functional imaging and tracking of the radiopharmacological profile up to 120 h p.i; f) specificity of tumor targeting by ^{89}Zr-DFO-MAb-B43.13 was demonstrated via competition blocking experiments; g) acute *ex vivo* biodistribution studies provided further information to corroborate findings from small animal PET imaging studies; h) *ex vivo* analysis of harvested tumors via digital autoradiography, immunofluorescence and immunohistochemistry allowed investigation into the extent of CA125 expression in the NIH:OVCAR-3 tumors and pattern of its targeting by ^{89}Zr-DFO-MAb-B43.13.

While the extended time window to perform functional imaging provided a great opportunity to observe a gradually increasing uptake of ^{89}Zr-DFO-MAb-B43.13 in the tumor with a concomitantly decreasing background, it also allowed an evaluation of radioactivity in potential off-target sites such as the liver – attributed to its function as an organ of metabolism and clearance of antibodies and potential immunocomplexes of radiotracers with circulating shed antigens *in vivo*. Nevertheless, the most exciting outcome of this study was the observation for radioactivity localized in the lymph nodes of the ipsilateral chain proximal to

the xenografted tumors. We speculate that this may be a result of immunocomplexes of the radiotracer and shed antigen draining into these lymph nodes or a consequence of metastatic occurrence in these organs. Despite a confirmation for this observation through repeated small animal PET and *ex vivo* acute biodistribution and digital autoradiography studies, there is indeterminate evidence from histopathological analysis of the effected lymph nodes to claim metastasis as the cause for lymph node involvement. Thus, a further investigation of this phenomenon is warranted in an intraperitoneal xenograft mouse model that can more closely represent the natural mode of lymph node metastasis of ovarian neoplasms. Furthermore, although the chances for an immunological basis to this observation in immunocompromised mice are fairly low, these cannot be completely ruled out, given the premise for a previously demonstrated immunotherapeutic role of MAb-B43.13 in humans. Overall, the observations of lymph node involvement in this study are unique and promising for potential clinical use; either to identify draining lymph nodes or sites of potential metastasis in epithelial ovarian cancer.

Re-(kindling) the magic in it by Re-(engineering) the antibody fragment!

Having maximized on the potential of MAb-B43.13 through ^{89}Zr-immuno-PET of EOC, we revisited the prospect for same-day imaging with antibody fragments. To this end, we chose to design and synthesize a CA125-targeting diabody (Chapter 6), in conformity with the best format reported in the literature for the purposes of same-day imaging via immuno-PET.[38-41] Unlike

other reports for the generation of non-covalently-linked diabodies and scFv multimers[42, 43] by virtue of shortening of the inter-domain peptide linker, we observed no such effect on the anti-CA125 B43.13 scFv. Instead, we produced a covalently-linked diabody (Cys-Db) by introducing an unpaired cysteine residue into the scFv molecule at its C-terminus and just upstream of the hexa-histidine tag with the aim to facilitate disulfide bond formation between such cysteine residues from adjacent scFv molecules during *in vivo* folding within the oxidative environment of the bacterial periplasm. The anti-CA125 Cys-Db provided low soluble expression of this construct plausibly attributed to an inherent *in vitro* and *in vivo* instability of proteins with unpaired cysteine residues.[44, 45] Although this is presented here as a work in progress, there are a few demonstrated aspects including recombinant expression, purification, bioconjugation of radiometal chelator and subsequent radiolabeling with ^{64}Cu – all of which were low in comparison to the scFv monomer reported in chapter 2 of this thesis. Small animal PET imaging performed with ^{64}Cu-anti-CA125 Cys-Db revealed no improvement in absolute NIH:OVCAR-3 tumor uptake values in comparison with the ^{64}Cu-anti-CA125 scFv. Instead, we observed a higher degree of renal trapping of radioactivity plausibly due to an effect of the doubled hexa-histidine tag and its associated polarity on this construct resulting in enhanced re-absorption and retention in the negatively charged renal tubules. Overall, in its present format, the anti-CA125 Cys-Db may not be suitable for transformation and use as a molecular imaging probe for immuno-PET of epithelial ovarian cancer.

In summary, this thesis provides variations on a central theme of molecular imaging of epithelial ovarian cancer that was achieved through the use of a variety of antibody-based targeting vectors, radioisotopes, *in vitro*, *in vivo* and *ex vivo* methods of analysis. The various chapters in this thesis provide a proof-of-concept to affirm the feasibility for using CA125 as a target and the concomitant development of radiotracers for the immuno-PET of epithelial ovarian cancer.

7.2 Conclusions:

- scFv molecules are the simplest and most attractive units for the creation of engineered antibodies, however, their expression in heterologous host systems may demand a degree of optimization in order to reap the maximum benefits of recombinant yield and biochemical activity.
- Monomeric scFv molecules can be good *in vitro* diagnostic and research tools, but are not suitable for use as *in vivo* molecular imaging probes in immuno-PET of solid tumors.
- Full-length antibodies clearly outperform smaller fragments such as scFv for the purpose of *in vivo* tumor targeting in an immuno-PET setting.
- ^{64}Cu-NOTA-MAb-B43.13 provides excellent tumor-to-background ratios as early as 24 h p.i and demonstrates minimal trans-metallation and degradation as a radioimmunoconjugate in serum.
- ^{89}Zr-DFO-MAb-B43.13 extends the performance window for immuno-PET of EOC. It also provides an opportunity to achieve high contrast PET

images at later time points with an extended possibility to detect lymph node involvement or small metastatic lesions.

- Creation of Cys-Diabodies increases the avidity of the monomeric scFv, but is limited in its performance as an *in vivo* molecular imaging probe, especially when used as a hexa-histidine fusion tagged protein.
- With a successful demonstration for *in vivo* targeting of EOC using antibody formats that target CA125, we fulfilled our hypothesis to affirm that CA125 is indeed a useful target for molecular imaging of EOC.

7.3 Limitations:

- No gene knock outs or knock downs have been used to silence CA125 expression and demonstrate a lack of *in vitro* or *in vivo* targeting. Instead we used a SKOV3 ovarian cancer cell line as a negative control at all levels of analysis (*in vitro*, *in vivo* and *ex vivo*) presented in this thesis.
- Although full-length antibodies deliver the best performance amongst the antibody formats tested as part of the works presented in this thesis and elsewhere in literature, these targeting agents concomitantly deliver an unnecessary radiation burden that can result in off-target effects in patient subjects.
- The effect of reasonably high uptake of radioactivity in the organs of clearance – the liver for the full-length antibody and the kidneys for the antibody fragments, may confound the ability to detect tumors in the

vicinity of these organs in a natural setting of ovarian cancer within the peritoneum.

7.4 FUTURE DIRECTIONS:

- Further improve the soluble expression of anti-CA125 scFv and Cys-Db by using solubility enhancing tags and/or alternative expression systems.
- Production of a stable and high expressing Cys-Diabody bereft of the polar hexa-histidine tag.
- Develop a pre-targeting approach to achieve high contrast PET images with significantly minimized radiation burden to subjects.
- Develop alternative animal xenograft models such as orthotopic, intraperitoneal or transgenic mice to reflect a closer to natural site and mode of occurrence/spread of ovarian neoplasms.
- Perform small animal imaging and analysis of tumor burden in the aforementioned disease models to evaluate the capability of MAb-B43.13-based immuno-PET tracers to detect small volume disease and/or metastatic spread.

7.5 References:

1. Marcus CS, Maxwell GL, Darcy KM, Hamilton CA, McGuire WP. Current approaches and challenges in managing and monitoring treatment response in ovarian cancer. *J Cancer* 2014;**5**(1): 25-30.
2. Gadducci A, Sartori E, Zola P, et al. Serum CA125 assay in the early diagnosis of recurrent epithelial ovarian cancer. *Oncol Rep* 1996;**3**(2): 301-3.
3. Testa AC, Di Legge A, Virgilio B, et al. Which imaging technique should we use in the follow up of gynaecological cancer? *Best Pract Res Clin Obstet Gynaecol* 2014;**28**(5): 769-91.
4. Lutz AM, Willmann JK, Drescher CW, et al. Early diagnosis of ovarian carcinoma: is a solution in sight? *Radiology* 2011;259(2): 329-45.
5. Strebhardt K, Ullrich A. Paul Ehrlich's magic bullet concept: 100 years of progress. *Nat Rev Cancer* 2008;**8**(6): 473-80.
6. Weiner LM. Building better magic bullets--improving unconjugated monoclonal antibody therapy for cancer. *Nat Rev Cancer* 2007;**7**(9): 701-6.
7. O'Shea JJ, Kanno Y, Chan AC. In search of magic bullets: the golden age of immunotherapeutics. *Cell* 2014;**157**(1): 227-40.
8. Noujaim AA, Schultes BC, Baum RP, Madiyalakan R. Induction of CA125-specific B and T cell responses in patients injected with MAb-B43.13--evidence for antibody-mediated antigen-processing and presentation of CA125 in vivo. *Cancer Biother Radiopharm* 2001;**16**(3): 187-203.
9. Schultes BC, Zhang C, Xue LY, Noujaim AA, Madiyalakan R. Immunotherapy of human ovarian carcinoma with OvaRex MAb-B43.13 in a human-PBL-SCID/BG mouse model. *Hybridoma* 1999;**18**(1): 47-55.

10. Sykes TR, Somayaji VV, Bier S, et al. Radiolabeling of monoclonal antibody B43.13 with rhenium-188 for immunoradiotherapy. *Appl Radiat Isot* 1997;**48**(7): 899-906.

11. Nap M, Vitali A, Nustad K, et al. Immunohistochemical characterization of 22 monoclonal antibodies against the CA125 antigen: 2nd report from the ISOBM TD-1 Workshop. *Tumour Biol* 1996;**17**(6): 325-31.

12. Nustad K, Bast RC, Jr., Brien TJ, et al. Specificity and affinity of 26 monoclonal antibodies against the CA 125 antigen: first report from the ISOBM TD-1 workshop. International Society for Oncodevelopmental Biology and Medicine. *Tumour Biol* 1996;**17**(4): 196-219.

13. Schultes BC, Baum RP, Niesen A, Noujaim AA, Madiyalakan R. Anti-idiotype induction therapy: anti-CA125 antibodies (Ab3) mediated tumor killing in patients treated with Ovarex mAb B43.13 (Ab1). *Cancer Immunol Immunother* 1998;**46**(4): 201-12.

14. Baum RP, Noujaim AA, Nanci A, et al. Clinical course of ovarian cancer patients under repeated stimulation of HAMA using MAb OC125 and B43.13. *Hybridom*a 1993;**12**(5): 583-9.

15. Madiyalakan R, Sykes TR, Dharampaul S, et al. Antiidiotype induction therapy: evidence for the induction of immune response through the idiotype network in patients with ovarian cancer after administration of anti-CA125 murine monoclonal antibody B43.13. *Hybridoma* 1995;**14**(2): 199-203.

16. Madiyalakan R, Kuzma M, Noujaim AA, Suresh MR. An antibody-lectin sandwich assay for the determination of CA125 antigen in ovarian cancer patients. *Glycoconj J* 1996;**13**(4): 513-7.

17. Madiyalakan R, Yang R, Schultes BC, Baum RP, Noujaim AA. OVAREX MAb-B43.13:IFN-gamma could improve the ovarian tumor cell sensitivity to CA125-specific allogenic cytotoxic T cells. *Hybridoma* 1997;**16**(1): 41-5.

18. Berek J, Taylor P, McGuire W, Smith LM, Schultes B, Nicodemus CF. Oregovomab maintenance monoimmunotherapy does not improve outcomes in advanced ovarian cancer. *J Clin Onco*l 2009;**27**(3): 418-25.

19. McQuarrie SA, Baum RP, Niesen A, et al. Pharmacokinetics and radiation dosimetry of 99Tcm-labelled monoclonal antibody B43.13 in ovarian cancer patients. *Nucl Med Commun* 1997;**18**(9): 878-86.

20. Wang WW, Das D, McQuarrie SA, Suresh MR. Design of a bifunctional fusion protein for ovarian cancer drug delivery: single-chain anti-CA125 core-streptavidin fusion protein. *Eur J Pharm Biopharm* 2007;**65**(3): 398-405.

21. Kriangkum J, Xu B, Gervais C, et al. Development and characterization of a bispecific single-chain antibody directed against T cells and ovarian carcinoma. *Hybridoma* 2000;**19**(1): 33-41.

22. Wu AM. Antibodies and antimatter: the resurgence of immuno-PET. *J Nucl Med* 2009;**50**(1): 2-5.

23. Wright BD, Lapi SE. Designing the magic bullet? The advancement of immuno-PET into clinical use. *J Nucl Med* 2013;**54**(8): 1171-4.

24. Wu AM. Engineered antibodies for molecular imaging of cancer. *Methods* 2014;**65**(1): 139-47.

25. Yang T, Yang L, Chai W, Li R, Xie J, Niu B. A strategy for high-level expression of a single-chain variable fragment against TNFalpha by subcloning antibody variable regions from the phage display vector pCANTAB 5E into pBV220. *Protein Expr Purif* 2011;**76**(1): 109-14.

26. Kipriyanov SM. High-level periplasmic expression and purification of scFvs. *Methods Mol Biol* 2009;**562**: 205-14.

27. Jung S, Pluckthun A. Improving in vivo folding and stability of a single-chain Fv antibody fragment by loop grafting. *Protein Eng* 1997;**10**(8): 959-66.

28. Vaks L, Benhar I. Production of stabilized scFv antibody fragments in the E. coli bacterial cytoplasm. *Methods Mol Biol* 2014;**1060**: 171-84.

29. Nieba L, Honegger A, Krebber C, Pluckthun A. Disrupting the hydrophobic patches at the antibody variable/constant domain interface: improved in vivo folding and physical characterization of an engineered scFv fragment. *Protein Eng* 1997;**10**(4): 435-44

30. Entzminger KC, Chang C, Myhre RO, McCallum KC, Maynard JA. The Skp chaperone helps fold soluble proteins in vitro by inhibiting aggregation. *Biochemistry* 2012;**51**(24): 4822-34.

31. Zhang X, Xie J, Sun Y, et al. High-level expression, purification, and characterization of bifunctional ScFv-9R fusion protein. *Appl Microbiol Biotechnol* 2014;**98**(12): 5499-506.

32. Sawyer JR, Schlom J, Kashmiri SV. The effects of induction conditions on production of a soluble anti-tumor sFv in Escherichia coli. *Protein Eng* 1994;**7**(11): 1401-6.

33. Wester HJ, Hamacher K, Stocklin G. A comparative study of N.C.A. fluorine-18 labeling of proteins via acylation and photochemical conjugation. *Nucl Med Biol* 1996;**23**(3): 365-72.

34. Vegt E, de Jong M, Wetzels JF, et al. Renal toxicity of radiolabeled peptides and antibody fragments: mechanisms, impact on radionuclide therapy, and strategies for prevention. *J Nucl Med* 2010;**51**(7): 1049-58.

35. D'Huyvetter M, Vincke C, Xavier C, et al. Targeted Radionuclide Therapy with A (177)Lu-labeled Anti-HER2 Nanobody. *Theranostics* 2014;**4**(7): 708-20.

36. McQuarrie SA, Riauka T, Baum RP, et al. The effects of circulating antigen on the pharmacokinetics and radioimmunoscintigraphic properties of 99m Tc labelled monoclonal antibodies in cancer patients. *J Pharm Pharm Sci* 1998;**1**(3): 115-25.

37. Viola-Villegas NT, Rice SL, Carlin S, et al. Applying PET to broaden the diagnostic utility of the clinically validated CA19.9 serum biomarker for oncology. *J Nucl Med* 2013;**54**(11): 1876-82.

38. Shively JE. 18F labeling for immuno-PET: where speed and contrast meet. *J Nucl Med* 2007;**48**(2): 170-2.

39. Cai W, Olafsen T, Zhang X, et al. PET imaging of colorectal cancer in xenograft-bearing mice by use of an 18F-labeled T84.66 anti-carcinoembryonic antigen diabody. *J Nucl* Med 2007;**48**(2): 304-10.

40. McCabe KE, Liu B, Marks JD, Tomlinson JS, Wu H, Wu AM. An engineered cysteine-modified diabody for imaging activated leukocyte cell adhesion molecule (ALCAM)-positive tumors. *Mol Imaging Biol* 2012;**14**(3): 336-47.

41. Olafsen T, Sirk SJ, Betting DJ, et al. ImmunoPET imaging of B-cell lymphoma using 124I-anti-CD20 scFv dimers (diabodies). *Protein Eng Des Sel* 2010;**23**(4): 243-9.

42. Kortt AA, Dolezal O, Power BE, Hudson PJ. Dimeric and trimeric antibodies: high avidity scFvs for cancer targeting. *Biomol Eng* 2001;**18**(3): 95-108.

43. Pluckthun A, Pack P. New protein engineering approaches to multivalent and bispecific antibody fragments. *Immunotechnology* 1997;**3**(2): 83-105.

44. Schmiedl A, Breitling F, Winter CH, Queitsch I, Dubel S. Effects of unpaired cysteines on yield, solubility and activity of different recombinant antibody constructs expressed in E. coli. *J Immunol Method*s 2000;**242**(1-2): 101-14.

45. Kipriyanov SM, Moldenhauer G, Martin AC, Kupriyanova OA, Little M. Two amino acid mutations in an anti-human CD3 single chain Fv antibody fragment that affect the yield on bacterial secretion but not the affinity. *Protein Eng* 1997;**10**(4): 445-53.

Bibliography

1. National Cancer Institute, SEER Training Modules http://training.seer.cancer.gov/anatomy/reproductive/female/ovaries.html
2. Oktem O, Oktay K. The ovary: anatomy and function throughout human life. *Ann N Y Acad Sci* 2008;**1127**: 1-9.
3. Erickson BK, Conner MG, Landen CN, Jr. The role of the fallopian tube in the origin of ovarian cancer. *Am J Obstet Gynecol* 2013;**209**(5): 409-14.
4. Prat J. Ovarian carcinomas: five distinct diseases with different origins, genetic alterations, and clinicopathological features. *Virchows Arch* 2012;**460**(3): 237-49.
5. Mutch DG, Prat J. 2014 FIGO staging for ovarian, fallopian tube and peritoneal cancer. *Gynecol Oncol* 2014;**133**(3): 401-4.
6. Holschneider CH, Berek JS. Ovarian cancer: epidemiology, biology, and prognostic factors. *Semin Surg Oncol* 2000;**19**(1): 3-10.
7. Cho KR, Shih Ie M. Ovarian cancer. *Annu Rev Pathol* 2009;4: 287-313.
8. Jones PM, Drapkin R. Modeling High-Grade Serous Carcinoma: How Converging Insights into Pathogenesis and Genetics are Driving Better Experimental Platforms. *Front Oncol* 2013;**3**: 217.
9. Cho KR. Ovarian cancer update: lessons from morphology, molecules, and mice. *Arch Pathol Lab Med* 2009;**133**(11): 1775-81.
10. Rescigno P, Cerillo I, Ruocco R, Condello C, De Placido S, Pensabene M. New hypothesis on pathogenesis of ovarian cancer lead to future tailored approaches. *Biomed Res Int* 2013;**2013**: 852839.
11. Ahmed AA, Etemadmoghadam D, Temple J, et al. Driver mutations in TP53 are ubiquitous in high grade serous carcinoma of the ovary. *J Pathol* 2010;**221**(1): 49-56.

12. Gubbels JA, Claussen N, Kapur AK, Connor JP, Patankar MS. The detection, treatment, and biology of epithelial ovarian cancer. *J Ovarian Res* 2010;**3**: 8.

13. Fathalla MF. Incessant ovulation--a factor in ovarian neoplasia? *Lancet* 1971;**2**(7716): 163.

14. Espey LL. Ovulation as an inflammatory reaction--a hypothesis. *Biol Reprod* 1980;**22**(1): 73-106.

15. Zhu Y, Nilsson M, Sundfeldt K. Phenotypic plasticity of the ovarian surface epithelium: TGF-beta 1 induction of epithelial to mesenchymal transition (EMT) in vitro. *Endocrinology* 2010;**151**(11): 5497-505.

16. Murdoch WJ, Murphy CJ, Van Kirk EA, Shen Y. Mechanisms and pathobiology of ovulation. *Soc Reprod Fertil Suppl* 2010;**67**: 189-201.

17. Kurman RJ, Shih Ie M. The origin and pathogenesis of epithelial ovarian cancer: a proposed unifying theory. *Am J Surg Pathol* 2010;**34**(3): 433-43.

18. Piek JM, van Diest PJ, Zweemer RP, et al. Dysplastic changes in prophylactically removed Fallopian tubes of women predisposed to developing ovarian cancer. *J Pathol* 2001;**195**(4): 451-6.

19. Lee Y, Miron A, Drapkin R, et al. A candidate precursor to serous carcinoma that originates in the distal fallopian tube. *J Pathol* 2007;**211**(1): 26-35.

20. Kindelberger DW, Lee Y, Miron A, et al. Intraepithelial carcinoma of the fimbria and pelvic serous carcinoma: Evidence for a causal relationship. *Am J Surg Pathol* 2007;**31**(2): 161-9.

21. Soussi T, Ishioka C, Claustres M, Beroud C. Locus-specific mutation databases: pitfalls and good practice based on the p53 experience. *Nat Rev Cancer* 2006;**6**(1): 83-90.

22. Przybycin CG, Kurman RJ, Ronnett BM, Shih Ie M, Vang R. Are all pelvic (nonuterine) serous carcinomas of tubal origin? *Am J Surg Pathol* 2010;**34**(10): 1407-16.

23. Folkins AK, Jarboe EA, Saleemuddin A, et al. A candidate precursor to pelvic serous cancer (p53 signature) and its prevalence in ovaries and fallopian tubes from women with BRCA mutations. *Gynecol Oncol* 2008;**109**(2): 168-73.

24. Karst AM, Drapkin R. The new face of ovarian cancer modeling: better prospects for detection and treatment. *F1000 Med Rep* 2011;**3**: 22.

25. Levanon K, Ng V, Piao HY, et al. Primary ex vivo cultures of human fallopian tube epithelium as a model for serous ovarian carcinogenesis. *Oncogene* 2010;**29**(8): 1103-13.

26. Karst AM, Levanon K, Drapkin R. Modeling high-grade serous ovarian carcinogenesis from the fallopian tube. *Proc Natl Acad Sci U S A* 2011;**108**(18): 7547-52.

27. Graziano DF, Finn OJ. Tumor antigens and tumor antigen discovery. *Cancer Treat Res* 2005;**123**: 89-111.

28. Bast RC, Jr. Status of tumor markers in ovarian cancer screening. *J Clin Oncol* 2003;**21**(10 Suppl): 200s-05s.

29. Husseinzadeh N. Status of tumor markers in epithelial ovarian cancer has there been any progress? A review. *Gynecol Oncol* 2011;**120**(1): 152-7.

30. Su Z, Graybill WS, Zhu Y. Detection and monitoring of ovarian cancer. *Clin Chim Acta* 2013;**415**: 341-5.

31. Bast RC, Jr., Feeney M, Lazarus H, Nadler LM, Colvin RB, Knapp RC. Reactivity of a monoclonal antibody with human ovarian carcinoma. *J Clin Invest* 1981;**68**(5): 1331-7.

32. Gupta D, Lis CG. Role of CA125 in predicting ovarian cancer survival - a review of the epidemiological literature. *J Ovarian Res* 2009;**2:** 13.

33. Yin BW, Dnistrian A, Lloyd KO. Ovarian cancer antigen CA125 is encoded by the MUC16 mucin gene. *Int J Cancer* 2002;**98**(5): 737-40.

34. Madiyalakan R, Kuzma M, Noujaim AA, Suresh MR. An antibody-lectin sandwich assay for the determination of CA125 antigen in ovarian cancer patients. *Glycoconj J* 1996;**13**(4): 513-7.

35. O'Brien TJ, Raymond LM, Bannon GA, et al. New monoclonal antibodies identify the glycoprotein carrying the CA 125 epitope. *Am J Obstet Gynecol* 1991;**165**(6 Pt 1): 1857-64.

36. Lloyd KO, Yin BW, Kudryashov V. Isolation and characterization of ovarian cancer antigen CA 125 using a new monoclonal antibody (VK-8): identification as a mucin-type molecule. *Int J Cancer* 1997;**71**(5): 842-50.

37. Nap M, Vitali A, Nustad K, et al. Immunohistochemical characterization of 22 monoclonal antibodies against the CA125 antigen: 2nd report from the ISOBM TD-1 Workshop. *Tumour Biol* 1996;**17**(6): 325-31.

38. Nustad K, Bast RC, Jr., Brien TJ, et al. Specificity and affinity of 26 monoclonal antibodies against the CA 125 antigen: first report from the ISOBM TD-1 workshop. International Society for Oncodevelopmental Biology and Medicine. *Tumour Biol* 1996;**17**(4): 196-219.

39. Nustad K, Lebedin Y, Lloyd KO, et al. Epitopes on CA 125 from cervical mucus and ascites fluid and characterization of six new antibodies. Third report from the ISOBM TD-1 workshop. *Tumour Biol* 2002;**23**(5): 303-14.

40. Warren DJ, Nustad K, Beard JB, O'Brien TJ. Expression and epitope characterization of a recombinant CA 125 repeat: fourth report from the ISOBM TD-1 workshop. *Tumour Biol* 2009;**30**(2): 51-60.

41. Perez BH, Gipson IK. Focus on Molecules: human mucin MUC16. *Exp Eye Res* 2008;**87**(5): 400-1.

42. Bressan A, Bozzo F, Maggi CA, Binaschi M. OC125, M11 and OV197 epitopes are not uniformly distributed in the tandem-repeat region of CA125 and require the entire SEA domain. *Dis Markers* 2013;**34**(4): 257-67.

43. Davis HM, Zurawski VR, Jr., Bast RC, Jr., Klug TL. Characterization of the CA 125 antigen associated with human epithelial ovarian carcinomas. *Cancer Res* 1986;**46**(12 Pt 1): 6143-8.

44. Hattrup CL, Gendler SJ. Structure and function of the cell surface (tethered) mucins. *Annu Rev Physiol* 2008;**70**: 431-57.

45. O'Brien TJ, Beard JB, Underwood LJ, Dennis RA, Santin AD, York L. The CA 125 gene: an extracellular superstructure dominated by repeat sequences. *Tumour Biol* 2001;**22**(6): 348-66.

46. Weiland F, Martin K, Oehler MK, Hoffmann P. Deciphering the Molecular Nature of Ovarian Cancer Biomarker CA125. *Int J Mol Sci* 2012;**13**(8): 10568-82.

47. Berman ZT, Moore LJ, Knudson KE, Whelan RJ. Synthesis and structural characterization of the peptide epitope of the ovarian cancer biomarker CA125 (MUC16). *Tumour Biol* 2010;**31**(5): 495-502.

48. Patankar MS, Jing Y, Morrison JC, et al. Potent suppression of natural killer cell response mediated by the ovarian tumor marker CA125. *Gynecol Oncol* 2005;**99**(3): 704-13.

49. Baalbergen A, Janssen JW, van der Weiden RM. CA-125 levels are related to the likelihood of pregnancy after in vitro fertilization and embryo transfer. *Am J Reprod Immunol* 2000;**43**(1): 21-4.

50. Miller KA, Deaton JL, Pittaway DE. Evaluation of serum CA 125 concentrations as predictors of pregnancy with human in vitro fertilization. *Fertil Steril* 1996;**65**(6): 1184-9.

51. Mazor M, Bashiri A, Ghezzi F, et al. Maternal serum CA 125 is of prognostic value in patients with uterine bleeding in the detection of small-for-gestational-age neonates. *Eur J Obstet Gynecol Reprod Biol* 1996;**67**(2): 143-7.

52. Spitzer M, Kaushal N, Benjamin F. Maternal CA-125 levels in pregnancy and the puerperium. *J Reprod Med* 1998;**43**(4): 387-92.

53. Argueso P, Tisdale A, Spurr-Michaud S, Sumiyoshi M, Gipson IK. Mucin characteristics of human corneal-limbal epithelial cells that exclude the rose bengal anionic dye. *Invest Ophthalmol Vis Sci* 2006;**47**(1): 113-9.

54. Argueso P, Guzman-Aranguez A, Mantelli F, Cao Z, Ricciuto J, Panjwani N. Association of cell surface mucins with galectin-3 contributes to the ocular surface epithelial barrier. *J Biol Chem* 2009;**284**(34): 23037-45.

55. Durak-Nalbantic A, Resic N, Kulic M, et al. Serum level of tumor marker carbohydrate antigen-CA125 in heart failure. *Med Arh* 2013;**67**(4): 241-4.

56. Yilmaz MB, Nikolaou M, Cohen Solal A. Tumour biomarkers in heart failure: is there a role for CA-125? *Eur J Heart Fail* 2011;**13**(6): 579-83.

57. Cheon DJ, Wang Y, Deng JM, et al. CA125/MUC16 is dispensable for mouse development and reproduction. *PLoS One* 2009;**4**(3): e4675.

58. Gubbels JA, Felder M, Horibata S, et al. MUC16 provides immune protection by inhibiting synapse formation between NK and ovarian tumor cells. *Mol Cancer* 2010;**9**: 11.

59. Belisle JA, Horibata S, Jennifer GA, et al. Identification of Siglec-9 as the receptor for MUC16 on human NK cells, B cells, and monocytes. *Mol Cancer* 2010;**9**: 118.

60. Avril T, Floyd H, Lopez F, Vivier E, Crocker PR. The membrane-proximal immunoreceptor tyrosine-based inhibitory motif is critical for the inhibitory signaling mediated by Siglecs-7 and -9, CD33-related Siglecs expressed on human monocytes and NK cells. *J Immunol* 2004;**173**(11): 6841-9.

61. Dunn GP, Bruce AT, Ikeda H, Old LJ, Schreiber RD. Cancer immunoediting: from immunosurveillance to tumor escape. *Nat Immunol* 2002;**3**(11): 991-8.

62. Rump A, Morikawa Y, Tanaka M, et al. Binding of ovarian cancer antigen CA125/MUC16 to mesothelin mediates cell adhesion. *J Biol Chem* 2004;**279**(10): 9190-8.

63. Gubbels JA, Belisle J, Onda M, et al. Mesothelin-MUC16 binding is a high affinity, N-glycan dependent interaction that facilitates peritoneal metastasis of ovarian tumors. *Mol Cancer* 2006;**5**(1): 50.

64. Sathyanarayana BK, Hahn Y, Patankar MS, Pastan I, Lee B. Mesothelin, Stereocilin, and Otoancorin are predicted to have superhelical structures with ARM-type repeats. *BMC Struct Biol* 2009;**9**: 1.

65. Felder M, Kapur A, Gonzalez-Bosquet J, et al. MUC16 (CA125): tumor biomarker to cancer therapy, a work in progress. *Mol Cancer* 2014;**13**(1): 129.

66. van der Burg ME, Lammes FB, Verweij J. The role of CA 125 in the early diagnosis of progressive disease in ovarian cancer. *Ann Oncol* 1990;**1**(4): 301-2.

67. Niloff JM, Bast RC, Jr., Schaetzl EM, Knapp RC. Predictive value of CA 125 antigen levels in second-look procedures for ovarian cancer. *Am J Obstet Gynecol* 1985;**151**(7): 981-6.

68. Trape J, Filella X, Alsina-Donadeu M, Juan-Pereira L, Bosch-Ferrer A, Rigo-Bonnin R. Increased plasma concentrations of tumour markers in the absence of neoplasia. *Clin Chem Lab Med* 2011;**49**(10): 1605-20.

69. Menon U, Gentry-Maharaj A, Ryan A, et al. Recruitment to multicentre trials--lessons from UKCTOCS: descriptive study. *BMJ* 2008;**337**: a2079.

70. Menon U, Gentry-Maharaj A, Hallett R, et al. Sensitivity and specificity of multimodal and ultrasound screening for ovarian cancer, and stage distribution of detected cancers: results of the prevalence screen of the UK Collaborative Trial of Ovarian Cancer Screening (UKCTOCS). *Lancet Oncol* 2009;**10**(4): 327-40.

71. Gadducci A, Cosio S, Zola P, Landoni F, Maggino T, Sartori E. Surveillance procedures for patients treated for epithelial ovarian cancer: a review of the literature. *Int J Gynecol Cancer* 2007;**17**(1): 21-31.

72. Niloff JM, Knapp RC, Lavin PT, et al. The CA 125 assay as a predictor of clinical recurrence in epithelial ovarian cancer. *Am J Obstet Gynecol* 1986;**155**(1): 56-60.

73. McQuarrie SA, Baum RP, Niesen A, et al. Pharmacokinetics and radiation dosimetry of 99Tcm-labelled monoclonal antibody B43.13 in ovarian cancer patients. *Nucl Med Commun* 1997;**18**(9): 878-86.

74. Berek JS. Immunotherapy of ovarian cancer with antibodies: a focus on oregovomab. *Expert Opin Biol Ther* 2004;**4**(7): 1159-65.

75. Schultes BC, Baum RP, Niesen A, Noujaim AA, Madiyalakan R. Anti-idiotype induction therapy: anti-CA125 antibodies (Ab3) mediated tumor killing in patients treated with Ovarex mAb B43.13 (Ab1). *Cancer Immunol Immunother* 1998;**46**(4): 201-12.

76. Berek J, Taylor P, McGuire W, Smith LM, Schultes B, Nicodemus CF. Oregovomab maintenance monoimmunotherapy does not improve outcomes in advanced ovarian cancer. *J Clin Oncol* 2009;**27**(3): 418-25.

77. Reinartz S, Kohler S, Schlebusch H, et al. Vaccination of patients with advanced ovarian carcinoma with the anti-idiotype ACA125: immunological response and survival (phase Ib/II). *Clin Cancer Res* 2004;**10**(5): 1580-7.

78. Reinartz S, Hombach A, Kohler S, et al. Interleukin-6 fused to an anti-idiotype antibody in a vaccine increases the specific humoral immune response against CA125+ (MUC-16) ovarian cancer. *Cancer Res* 2003;**63**(12): 3234-40.

79. Sabbatini P, Dupont J, Aghajanian C, et al. Phase I study of abagovomab in patients with epithelial ovarian, fallopian tube, or primary peritoneal cancer. *Clin Cancer Res* 2006;**12**(18): 5503-10.

80. Pfisterer J, Harter P, Simonelli C, et al. Abagovomab for ovarian cancer. *Expert Opin Biol Ther* 2011;**11**(3): 395-403.

81. Hassan R, Ho M. Mesothelin targeted cancer immunotherapy. *Eur J Cancer* 2008;**44**(1): 46-53.

82. Xiang X, Feng M, Felder M, et al. HN125: A Novel Immunoadhesin Targeting MUC16 with Potential for Cancer Therapy. *J Cancer* 2011;**2**: 280-91.

83. Chen Y, Clark S, Wong T, et al. Armed antibodies targeting the mucin repeats of the ovarian cancer antigen, MUC16, are highly efficacious in animal tumor models. *Cancer Res* 2007;**67**(10): 4924-32.

84. Pastuskovas CV, Mallet W, Clark S, et al. Effect of immune complex formation on the distribution of a novel antibody to the ovarian tumor antigen CA125. *Drug Metab Dispos* 2010;**38**(12): 2309-19.

85. Goff BA, Mandel LS, Drescher CW, et al. Development of an ovarian cancer symptom index: possibilities for earlier detection. *Cancer* 2007;**109**(2): 221-7.

86. Andersen MR, Goff BA, Lowe KA, et al. Combining a symptoms index with CA 125 to improve detection of ovarian cancer. *Cancer* 2008;**113**(3): 484-9.

87. Andersen MR, Goff BA, Lowe KA, et al. Use of a Symptom Index, CA125, and HE4 to predict ovarian cancer. *Gynecol Oncol* 2010;**116**(3): 378-83.

88. Lutz AM, Willmann JK, Drescher CW, et al. Early diagnosis of ovarian carcinoma: is a solution in sight? *Radiology* 2011;**259**(2): 329-45.

89. McDonald JM, Doran S, DeSimone CP, et al. Predicting risk of malignancy in adnexal masses. *Obstet Gynecol* 2010;**115**(4): 687-94

90. Testa AC, Di Legge A, Virgilio B, et al. Which imaging technique should we use in the follow up of gynaecological cancer? *Best Pract Res Clin Obstet Gynaecol* 2014;**28**(5): 769-91.

91. Pannu HK, Bristow RE, Montz FJ, Fishman EK. Multidetector CT of peritoneal carcinomatosis from ovarian cancer. *Radiographics* 2003;**23**(3): 687-701.

92. Murakami M, Miyamoto T, Iida T, et al. Whole-body positron emission tomography and tumor marker CA125 for detection of recurrence in epithelial ovarian cancer. *Int J Gynecol Cancer* 2006;**16** Suppl 1: 99-107.

93. Zimny M, Siggelkow W, Schroder W, et al. 2-[Fluorine-18]-fluoro-2-deoxy-d-glucose positron emission tomography in the diagnosis of recurrent ovarian cancer. *Gynecol Oncol* 2001;**83**(2): 310-5.

94. Muramatsu T, Yamashita E, Takahashi K, et al. Usefulness of combined PET/CT for patient with epithelial ovarian cancer showing recurrence based on tumor marker CA125. *Tokai J Exp Clin Med* 2007;**32**(1): 23-7.

95. Soussan M, Wartski M, Cherel P, et al. Impact of FDG PET-CT imaging on the decision making in the biologic suspicion of ovarian carcinoma recurrence. *Gynecol Oncol* 2008;**108**(1): 160-5.

96. Risum S, Hogdall C, Loft A, et al. The diagnostic value of PET/CT for primary ovarian cancer--a prospective study. *Gynecol Oncol* 2007;**105**(1): 145-9.

97. Risum S, Loft A, Engelholm SA, et al. Positron emission tomography/computed tomography predictors of overall survival in stage IIIC/IV ovarian cancer. *Int J Gynecol Cancer* 2012;**22**(7): 1163-9.

98. Fuccio C, Castellucci P, Marzola MC, Al-Nahhas A, Fanti S, Rubello D. Noninvasive and invasive staging of ovarian cancer: review of the literature. *Clin Nucl Med* 2011;**36**(10): 889-93.

99. Antunovic L, Cimitan M, Borsatti E, et al. Revisiting the clinical value of 18F-FDG PET/CT in detection of recurrent epithelial ovarian carcinomas: correlation with histology, serum CA-125 assay, and conventional radiological modalities. *Clin Nucl Med* 2012;**37**(8): e184-8.

100. Bristow RE, del Carmen MG, Pannu HK, et al. Clinically occult recurrent ovarian cancer: patient selection for secondary cytoreductive surgery using combined PET/CT. *Gynecol Oncol* 2003;**90**(3): 519-28.

101. Makhija S, Howden N, Edwards R, Kelley J, Townsend DW, Meltzer CC. Positron emission tomography/computed tomography imaging for the detection of recurrent ovarian and fallopian tube carcinoma: a retrospective review. *Gynecol Oncol* 2002;**85**(1): 53-8.

102. Garcia Velloso MJ, Boan Garcia JF, Villar Luque LM, Aramendia Beitia JM, Lopez Garcia G, Richter Echeverria JA. [F-18-FDG positron emission tomography in the diagnosis of ovarian recurrence. Comparison with CT scan and CA 125]. *Rev Esp Med Nucl* 2003;**22**(4): 217-23.

103. Kurokawa T, Yoshida Y, Kawahara K, et al. Whole-body PET with FDG is useful for following up an ovarian cancer patient with only rising CA-125 levels within the normal range. *Ann Nucl Med* 2002;**16**(7): 491-3.

104. Simcock B, Neesham D, Quinn M, Drummond E, Milner A, Hicks RJ. The impact of PET/CT in the management of recurrent ovarian cancer. *Gynecol Oncol* 2006;**103**(1): 271-6.

105. Ebina Y, Watari H, Kaneuchi M, et al. Impact of FDG PET in optimizing patient selection for cytoreductive surgery in recurrent ovarian cancer. *Eur J Nucl Med Mol Imaging* 2014;**41**(3): 446-51.

106. Gu P, Pan LL, Wu SQ, Sun L, Huang G. CA 125, PET alone, PET-CT, CT and MRI in diagnosing recurrent ovarian carcinoma: a systematic review and meta-analysis. *Eur J Radiol* 2009;**71**(1): 164-74.

107. Thrall MM, DeLoia JA, Gallion H, Avril N. Clinical use of combined positron emission tomography and computed tomography (FDG-PET/CT) in recurrent ovarian cancer. *Gynecol Oncol* 2007;**105**(1): 17-22.

108. Iyer RB, Balachandran A, Devine CE. PET/CT and cross sectional imaging of gynecologic malignancy. *Cancer Imaging* 2007;**7** Spec No A: S130-8.

109. Lai CH, Yen TC, Chang TC. Positron emission tomography imaging for gynecologic malignancy. *Curr Opin Obstet Gynecol* 2007;**19**(1): 37-41.

110. Kalli KR, Oberg AL, Keeney GL, et al. Folate receptor alpha as a tumor target in epithelial ovarian cancer. *Gynecol Oncol* 2008;**108**(3): 619-26.

111. Guo W, Hinkle GH, Lee RJ. 99mTc-HYNIC-folate: a novel receptor-based targeted radiopharmaceutical for tumor imaging. *J Nucl Med* 1999;**40**(9): 1563-9.

112. Mathias CJ, Hubers D, Low PS, Green MA. Synthesis of [(99m)Tc]DTPA-folate and its evaluation as a folate-receptor-targeted radiopharmaceutical. *Bioconjug Chem* 2000;**11**(2): 253-7.

113. Leamon CP, Parker MA, Vlahov IR, et al. Synthesis and biological evaluation of EC20: a new folate-derived, (99m)Tc-based radiopharmaceutical. *Bioconjug Chem* 2002;**13**(6): 1200-10.

114. Okarvi SM, Jammaz IA. Preparation and in vitro and in vivo evaluation of technetium-99m-labeled folate and methotrexate conjugates as tumor imaging agents. *Cancer Biother Radiopharm* 2006;**21**(1): 49-60

115. Maurer AH, Elsinga P, Fanti S, Nguyen B, Oyen WJ, Weber WA. Imaging the folate receptor on cancer cells with 99mTc-etarfolatide: properties, clinical use, and future potential of folate receptor imaging. *J Nucl Med* 2014;**55**(5): 701-4.

116. Siegel BA, Dehdashti F, Mutch DG, et al. Evaluation of 111In-DTPA-folate as a receptor-targeted diagnostic agent for ovarian cancer: initial clinical results. *J Nucl Med* 2003;**44**(5): 700-7.

117. Muller C. Folate-based radiotracers for PET imaging--update and perspectives. *Molecules* 2013;**18**(5): 5005-31.

118. AlJammaz I, Al-Otaibi B, Al-Rumayan F, Al-Yanbawi S, Amer S, Okarvi SM. Development and preclinical evaluation of new (124)I-folate conjugates for PET imaging of folate receptor-positive tumors. *Nucl Med Biol* 2014;**41**(6): 457-63.

119. Perrone MG, Malerba P, Uddin MJ, et al. PET radiotracer [(18)F]-P6 selectively targeting COX-1 as a novel biomarker in ovarian cancer: Preliminary investigation. *Eur J Med Chem* 2014;**80**: 562-8.

120. van Dam GM, Themelis G, Crane LM, et al. Intraoperative tumor-specific fluorescence imaging in ovarian cancer by folate receptor-alpha targeting: first in-human results. *Nat Med* 2011;**17**(10): 1315-9.

121. Wang Y, Miao Z, Ren G, Xu Y, Cheng Z. A novel Affibody bioconjugate for dual-modality imaging of ovarian cancer. *Chem Commun* (Camb) 2014.

122. Liu TW, Stewart JM, Macdonald TD, et al. Biologically-targeted detection of primary and micro-metastatic ovarian cancer. *Theranostics* 2013;**3**(6): 420-7.

123. Lee H, Kim J, Kim H, Kim Y, Choi Y. A folate receptor-specific activatable probe for near-infrared fluorescence imaging of ovarian cancer. *Chem Commun* (Camb) 2014;**50**(56): 7507-10.

124. Buist MR, Kenemans P, den Hollander W, et al. Kinetics and tissue distribution of the radiolabeled chimeric monoclonal antibody MOv18 IgG and F(ab')2 fragments in ovarian carcinoma patients. *Cancer Res* 1993;**53**(22): 5413-8.

125. Zalutsky MR, Knapp RC, Bast RC, Jr. Influence of circulating antigen on blood pool activity of a radioiodinated monoclonal antibody. *Int J Rad Appl Instrum B* 1988;**15**(4): 431-7.

126. Chatal JF, Saccavini JC, Gestin JF, et al. Biodistribution of indium-111-labeled OC 125 monoclonal antibody intraperitoneally injected into patients operated on for ovarian carcinomas. *Cancer Res* 1989;**49**(11): 3087-94.

127. Rubin SC, Kairemo KJ, Brownell AL, et al. High-resolution positron emission tomography of human ovarian cancer in nude rats using 124I-labeled monoclonal antibodies. *Gynecol Oncol* 1993;**48**(1): 61-7.

128. van Dongen GA, Visser GW, Lub-de Hooge MN, de Vries EG, Perk LR. Immuno-PET: a navigator in monoclonal antibody development and applications. *Oncologist* 2007;**12**(12): 1379-89.

129. Wu AM. Antibodies and antimatter: the resurgence of immuno-PET. *J Nucl Med* 2009;**50**(1): 2-5.

130. McCabe KE, Wu AM. Positive progress in immunoPET--not just a coincidence. *Cancer Biother Radiopharm* 2010;**25**(3): 253-61.

131. Cai W, Olafsen T, Zhang X, et al. PET imaging of colorectal cancer in xenograft-bearing mice by use of an 18F-labeled T84.66 anti-carcinoembryonic antigen diabody. *J Nucl Med* 2007;**48**(2): 304-10.

132. Olafsen T, Sirk SJ, Olma S, Shen CK, Wu AM. ImmunoPET using engineered antibody fragments: fluorine-18 labeled diabodies for same-day imaging. *Tumour Biol* 2012;**33**(3): 669-77.

133. Hong H, Zhang Y, Orbay H, et al. Positron emission tomography imaging of tumor angiogenesis with a (61/64)Cu-labeled F(ab')(2) antibody fragment. *Mol Pharm* 2013;**10**(2): 709-16.

134. Zhang Y, Hong H, Orbay H, et al. PET imaging of CD105/endoglin expression with a (6)(1)/(6)(4)Cu-labeled Fab antibody fragment. *Eur J Nucl Med Mol Imaging* 2013;**40**(5): 759-67.

135. Lepin EJ, Leyton JV, Zhou Y, et al. An affinity matured minibody for PET imaging of prostate stem cell antigen (PSCA)-expressing tumors. *Eur J Nucl Med Mol Imaging* 2010;**37**(8): 1529-38.

136. Olafsen T, Sirk SJ, Betting DJ, et al. ImmunoPET imaging of B-cell lymphoma using 124I-anti-CD20 scFv dimers (diabodies). *Protein Eng Des Sel* 2010;**23**(4): 243-9.

137. Olafsen T, Betting D, Kenanova VE, et al. Recombinant anti-CD20 antibody fragments for small-animal PET imaging of B-cell lymphomas. *J Nucl Med* 2009;**50**(9): 1500-8.

138. Fu M, Brewer S, Olafsen T, et al. Positron emission tomography imaging of endometrial cancer using engineered anti-EMP2 antibody fragments. *Mol Imaging Biol* 2013;**15**(1): 68-78.

139. Lutje S, Franssen GM, Sharkey RM, et al. Anti-CEA antibody fragments labeled with [(18)F]AlF for PET imaging of CEA-expressing tumors. *Bioconjug Chem* 2014;**25**(2): 335-41.

140. Fonge H, Leyton JV. Positron emission tomographic imaging of iodine 124 anti-prostate stem cell antigen-engineered antibody fragments in LAPC-9 tumor-bearing severe combined immunodeficiency mice. *Mol Imaging* 2013;**12**(3): 191-202.

141. McCabe KE, Liu B, Marks JD, Tomlinson JS, Wu H, Wu AM. An engineered cysteine-modified diabody for imaging activated leukocyte cell adhesion molecule (ALCAM)-positive tumors. *Mol Imaging Biol* 2012;**14**(3): 336-47

142. Girgis MD, Kenanova V, Olafsen T, McCabe KE, Wu AM, Tomlinson JS. Anti-CA19-9 diabody as a PET imaging probe for pancreas cancer. *J Surg Res* 2011;**170**(2): 169-78.

143. Li L, Crow D, Turatti F, et al. Site-specific conjugation of monodispersed DOTA-PEGn to a thiolated diabody reveals the effect of increasing peg size on kidney clearance and tumor uptake with improved 64-copper PET imaging. *Bioconjug Chem* 2011;**22**(4): 709-16.

144. Natarajan A, Habte F, Gambhir SS. Development of a novel long-lived immunoPET tracer for monitoring lymphoma therapy in a humanized transgenic mouse model. *Bioconjug Chem* 2012;**23**(6): 1221-9.

145. Zhang Y, Hong H, Severin GW, et al. ImmunoPET and near-infrared fluorescence imaging of CD105 expression using a monoclonal antibody dual-labeled with (89)Zr and IRDye 800CW. *Am J Transl Res* 2012;**4**(3): 333-46.

146. Ogasawara A, Tinianow JN, Vanderbilt AN, et al. ImmunoPET imaging of phosphatidylserine in pro-apoptotic therapy treated tumor models. *Nucl Med Biol* 2013;**40**(1): 15-22

147. Viola-Villegas NT, Rice SL, Carlin S, et al. Applying PET to broaden the diagnostic utility of the clinically validated CA19.9 serum biomarker for oncology. *J Nucl Med* 2013;**54**(11): 1876-82.

148. Stillebroer AB, Franssen GM, Mulders PF, et al. ImmunoPET imaging of renal cell carcinoma with (124)I- and (89)Zr-labeled anti-CAIX monoclonal antibody cG250 in mice. *Cancer Biother Radiopharm* 2013;**28**(7): 510-5.

149. Ikotun OF, Marquez BV, Huang C, et al. Imaging the L-type amino acid transporter-1 (LAT1) with Zr-89 immunoPET. PLoS One 2013;**8**(10): e77476.

150. Holland JP, Divilov V, Bander NH, Smith-Jones PM, Larson SM, Lewis JS. 89Zr-DFO-J591 for immunoPET of prostate-specific membrane antigen expression in vivo. J Nucl Med 2010;**51**(8): 1293-300.

151. Sham JG, Kievit FM, Grierson JR, et al. Glypican-3-targeted 89Zr PET imaging of hepatocellular carcinoma. *J Nucl Med* 2014;**55**(5): 799-804.

152. Wu AM. Engineered antibodies for molecular imaging of cancer. *Methods* 2014;**65**(1): 139-47.

153. Knowles SM, Wu AM. Advances in immuno-positron emission tomography: antibodies for molecular imaging in oncology. *J Clin Oncol* 2012;**30**(31): 3884-92.

154. Wu AM, Olafsen T. Antibodies for molecular imaging of cancer. *Cancer* J 2008;**14**(3): 191-7.

155. Chakravarty R, Goel S, Cai W. Nanobody: the "magic bullet" for molecular imaging? *Theranostics* 2014;**4**(4): 386-98.

156. Marcus CS, Maxwell GL, Darcy KM, Hamilton CA, McGuire WP. Current approaches and challenges in managing and monitoring treatment response in ovarian cancer. *J Cancer* 2014;5(1): 25-30.

157. Gadducci A, Sartori E, Zola P, et al. Serum CA125 assay in the early diagnosis of recurrent epithelial ovarian cancer. *Oncol Rep* 1996;3(2): 301-3.

158. Hori SS, Gambhir SS. Mathematical model identifies blood biomarker-based early cancer detection strategies and limitations. *Sci Transl Med* 2011;3(109): 109ra16.

159. Torizuka T, Nobezawa S, Kanno T, et al. Ovarian cancer recurrence: role of whole-body positron emission tomography using 2-[fluorine-18]-fluoro-2-deoxy- D-glucose. *Eur J Nucl Med Mol Imaging* 2002;29(6): 797-803.

160. Holliger P, Hudson PJ. Engineered antibody fragments and the rise of single domains. *Nat Biotechnol* 2005;**23**(9): 1126-36.

161. Bird RE, Hardman KD, Jacobson JW, et al. Single-chain antigen-binding proteins. *Science* 1988;**242**(4877): 423-6.

162. Kipriyanov SM. High-level periplasmic expression and purification of scFvs. *Methods Mol Biol* 2009;**562**: 205-14.

163. Clackson T, Hoogenboom HR, Griffiths AD, Winter G. Making antibody fragments using phage display libraries. *Nature* 1991;**352**(6336): 624-8.

164. Schaffitzel C, Hanes J, Jermutus L, Pluckthun A. Ribosome display: an in vitro method for selection and evolution of antibodies from libraries. *J Immunol Methods* 1999;**231**(1-2): 119-35.

165. Feldhaus MJ, Siegel RW. Yeast display of antibody fragments: a discovery and characterization platform. *J Immunol Methods* 2004;**290**(1-2): 69-80.

166. J.V. Schaefer, A. Honneger, A. Pluckthun, Construction of scFv fragments from hybridoma or spleen cells by PCR assembly, in: R. Kontermann, S. Dubel (Eds.), Antibody Engineering, Vol 1, Springer-Verlag, Berlin, Heidelberg, 2010, pp. 21-44.

167. Toleikis L, Frenzel A. Cloning single-chain antibody fragments (ScFv) from hyrbidoma cells. *Methods Mol Biol* 2012;**907**: 59-71.

168. Fields C, O'Connell D, Xiao S, Lee GU, Billiald P, Muzard J. Creation of recombinant antigen-binding molecules derived from hybridomas secreting specific antibodies. *Nat Protoc* 2013;**8**(6): 1125-48.

169. Scholler N, Urban N. CA125 in ovarian cancer. *Biomark Med* 2007;**1**(4): 513-23.

170. Capstick V, Maclean GD, Suresh MR, et al. Clinical evaluation of a new two-site assay for CA125 antigen. *Int J Biol Markers* 1991;**6**(2): 129-35.

171. Singleton J, Guillen DE, Scully MS, et al. Characterization of antibodies to CA 125 that bind preferentially to the cell-associated form of the antigen. *Tumour Biol* 2006;**27**(3): 122-32.

172. Luo D, Geng M, Schultes B, et al. Expression of a fusion protein of scFv-biotin mimetic peptide for immunoassay. *J Biotechnol* 1998;**65**(2-3): 225-8.

173. Hashimoto Y, Tanigawa K, Nakashima M, et al. Construction of the single-chain Fv from 196-14 antibody toward ovarian cancer-associated antigen CA125. *Biol Pharm Bull* 1999;**22**(10): 1068-72.

174. Kriangkum J, Xu B, Gervais C, et al. Development and characterization of a bispecific single-chain antibody directed against T cells and ovarian carcinoma. *Hybridoma* 2000;**19**(1): 33-41.

175. Wang WW, Das D, McQuarrie SA, Suresh MR. Design of a bifunctional fusion protein for ovarian cancer drug delivery: single-chain anti-CA125 core-streptavidin fusion protein. *Eur J Pharm Biopharm* 2007;**65**(3): 398-405.

176. Boivin M, Lane D, Piche A, Rancourt C. CA125 (MUC16) tumor antigen selectively modulates the sensitivity of ovarian cancer cells to genotoxic drug-induced apoptosis. *Gynecol Oncol* 2009;**115**(3): 407-13.

177. Ma J, Luo D, Kwon GS, Samuel J, Noujaim AA, Madiyalakan R. Use of encapsulated single chain antibodies for induction of anti-idiotypic humoral and cellular immune responses. *J Pharm Sci* 1998;**87**(11): 1375-8.

178. Accardi L, Di Bonito P. Antibodies in single-chain format against tumour-associated antigens: present and future applications. *Curr Med Chem* 2010;**17**(17): 1730-55.

179. Burgess-Brown NA, Sharma S, Sobott F, Loenarz C, Oppermann U, Gileadi O. Codon optimization can improve expression of human genes in Escherichia coli: A multi-gene study. *Protein Expr Purif* 2008;**59**(1): 94-102.

180. Tiwari A, Sankhyan A, Khanna N, Sinha S. Enhanced periplasmic expression of high affinity humanized scFv against Hepatitis B surface antigen by codon optimization. *Protein Expr Purif* 2010;**74**(2): 272-9.

181. Gustafsson C, Govindarajan S, Minshull J. Codon bias and heterologous protein expression. *Trends Biotechnol* 2004;**22**(7): 346-53.

182. Noujaim AA, Baum RP, Sykes TR, Sykes CJ, Hertel A, Niesen, A, et al. Monoclonal antibody B43.13 for immunoscintigraphy and immunotherapy of ovarian cancer, in: Klapdor, R. (Ed.), Current Tumor Diagnosis: Applications, Clinical Relevance, Trends. W Zuckschwerdt Verlag, Munich, 1994, pp. 823–829.

183. Newa M, Lam M, Bhandari KH, Xu B, Doschak MR. Expression, characterization, and evaluation of a RANK-binding single chain fraction variable: an osteoclast targeting drug delivery strategy. *Mol Pharm* 2014;**11**(1): 81-9.

184. Mobus VJ, Baum RP, Bolle M, et al. Immune responses to murine monoclonal antibody-B43.13 correlate with prolonged survival of women with recurrent ovarian cancer. *Am J Obstet Gynecol* 2003;**189**(1): 28-36.

185. Noujaim AA, Schultes BC, Baum RP, Madiyalakan R. Induction of CA125-specific B and T cell responses in patients injected with MAb-B43.13--evidence for antibody-mediated antigen-processing and presentation of CA125 in vivo. *Cancer Biother Radiopharm* 2001;**16**(3): 187-203.

186. Kortt AA, Dolezal O, Power BE, Hudson PJ. Dimeric and trimeric antibodies: high avidity scFvs for cancer targeting. *Biomol Eng* 2001;**18**(3): 95-108.

187. Whitlow M, Bell BA, Feng SL, et al. An improved linker for single-chain Fv with reduced aggregation and enhanced proteolytic stability. *Protein Eng* 1993;**6**(8): 989-95.

188. Palomares LA, Estrada-Mondaca S, Ramirez OT. Production of recombinant proteins: challenges and solutions. *Methods Mol Biol* 2004;**267**: 15-52.

189. Carrio MM, Villaverde A. Construction and deconstruction of bacterial inclusion bodies. *J Biotechnol* 2002;**96**(1): 3-12.

190. Nieba L, Honegger A, Krebber C, Pluckthun A. Disrupting the hydrophobic patches at the antibody variable/constant domain interface: improved in vivo folding and physical characterization of an engineered scFv fragment. *Protein Eng* 1997;**10**(4): 435-44.

191. Chowdhury PS, Vasmatzis G. Engineering scFvs for improved stability. *Methods Mol Biol* 2003;**207**: 237-54.

192. Tsumoto K, Nakaoki Y, Ueda Y, et al. Effect of the order of antibody variable regions on the expression of the single-chain HyHEL10 Fv fragment in E. coli and the thermodynamic analysis of its antigen-binding properties. *Biochem Biophys Res Commun* 1994;**201**(2): 546-51.

193. Hamilton S, Odili J, Gundogdu O, Wilson GD, Kupsch JM. Improved production by domain inversion of single-chain Fv antibody fragment against high molecular weight proteoglycan for the radioimmunotargeting of melanoma. *Hybrid Hybridomics* 2001;**20**(5-6): 351-60.

194. Kane JF. Effects of rare codon clusters on high-level expression of heterologous proteins in Escherichia coli. Curr Opin Biotechnol 1995;6(5): 494-500.

195. Knappik A, Pluckthun A. Engineered turns of a recombinant antibody improve its in vivo folding. *Protein Eng* 1995;**8**(1): 81-9.

196. Xiao Z, McQuarrie SA, Suresh MR, Mercer JR, Gupta S, Miller GG. A three-step strategy for targeting drug carriers to human ovarian carcinoma cells in vitro. *J Biotechnol* 2002;**94**(2): 171-84.

197. Wu AM, Yazaki PJ: Designer genes: recombinant antibody fragments for biological imaging. *Q J Nucl Med* 2000, **44**:268-283.

198. Iagaru AH, Mittra ES, McDougall IR, Quon A, Gambhir SS: 18F-FDG PET/CT evaluation of patients with ovarian carcinoma. *Nucl Med Commun* 2008, **29**:1046-1051.

199. Mading P, Fuchtner F, Wust F: Module-assisted synthesis of the bifunctional labelling agent N-succinimidyl 4-[(18)F]fluorobenzoate ([(18)F]SFB). *Appl Radiat Isot* 2005, **63**:329-332.

200. Olafsen T, Wu AM: Antibody vectors for imaging. *Semin Nucl Med* 2010, **40**(3):167-181.

201. Wester HJ, Hamacher K, Stocklin G: A comparative study of N.C.A. fluorine-18 labeling of proteins via acylation and photochemical conjugation. *Nucl Med Biol* 1996, **23**:365-372.

202. Vaidyanathan G, Zalutsky MR: Improved synthesis of *N*-succinimidyl 4-[^{18}F]fluorobenzoate and its application to the labeling of a monoclonal antibody fragment. *Bioconjug Chem* 1994, **5**:352-356.

203. Garg PK, Garg S, Zalutsky MR: Fluorine-18 labeling of monoclonal antibodies and fragments with preservation of immunoreactivity. *Bioconjug Chem* 1991, **2**:44-49.

204. McQuarrie SA, Riauka T, Baum RP, et al. The effects of circulating antigen on the pharmacokinetics and radioimmunoscintigraphic properties of 99m Tc labelled monoclonal antibodies in cancer patients. *J Pharm Pharm Sci* 1998;**1**(3): 115-25.

205. Williams LE, Wu AM, Yazaki PJ, et al. Numerical selection of optimal tumor imaging agents with application to engineered antibodies. *Cancer Biother Radiopharm* 2001;**16**(1): 25-35.

206. Wittrup KD, Thurber GM, Schmidt MM, Rhoden JJ: Practical theoretic guidance for the design of tumor-targeting agents. *Methods enzymol* 2012, **503**:255-268.

207. Schneider DW, Heitner T, Alicke B, Light DR, McLean K, Satozawa N, Parry G, Yoo J, Lewis JS, Parry R: In vivo biodistribution, PET imaging, and tumor

accumulation of 86Y- and 111In-antimindin/RG-1, engineered antibody fragments in LNCaP tumor-bearing nude mice. *J Nucl Med* 2009, **50**:435-443.

208. Eder M, Knackmuss S, Le Gall F, et al. 68Ga-labelled recombinant antibody variants for immuno-PET imaging of solid tumours. *Eur J Nucl Med Mol Imaging* 2010;**37**(7): 1397-407.

209. Vegt E, de Jong M, Wetzels JF, Masereeuw R, Melis M, Oyen WJ, Gotthardt M, Boerman OC: Renal toxicity of radiolabeled peptides and antibody fragments: mechanisms, impact on radionuclide therapy, and strategies for prevention. *J Nucl Med* 2010, **51**:1049-1058.

210. D'Huyvetter M, Vincke C, Xavier C, Aerts A, Impens N, Baatout S, De Raeve H, Muyldermans S, Caveliers V, Devoogdt N *et al*: Targeted Radionuclide Therapy with a ^{177}Lu-labeled Anti-HER2 Nanobody. *Theranostics* 2014, **4**:708-720.

211. Howlader N, Noone AM, Krapcho M, et al. SEER Cancer Statistics Review, 1975-2010, National Cancer Institute. Bethesda, MD, http://seer.cancer.gov/csr/1975_2010/, based on November 2012 SEER data submission, posted to the SEER web site, April 2013.

212. Bast RC, Jr., Xu FJ, Yu YH, Barnhill S, Zhang Z, Mills GB. CA 125: the past and the future. *Int J Biol Markers* 1998;**13**(4): 179-87.

213. Pignata S, Cannella L, Leopardo D, Bruni GS, Facchini G, Pisano C. Follow-up with CA125 after primary therapy of advanced ovarian cancer: in favor of continuing to prescribe CA125 during follow-up. *Ann Oncol* 2011;**22** Suppl 8: viii40-viii44.

214. Son H, Khan SM, Rahaman J, et al. Role of FDG PET/CT in staging of recurrent ovarian cancer. *Radiographics* 2011;**31**(2): 569-83.

215. Murakami M, Miyamoto T, Iida T, et al. Whole-body positron emission tomography and tumor marker CA125 for detection of recurrence in epithelial ovarian cancer. *Int J Gynecol Cancer* 2006;**16** Suppl 1: 99-107.

216. Zimny M, Siggelkow W, Schroder W, et al. 2-[Fluorine-18]-fluoro-2-deoxy-d-glucose positron emission tomography in the diagnosis of recurrent ovarian cancer. *Gynecol Oncol* 2001;**83**(2): 310-5.

217. Gadducci A, Cosio S. Surveillance of patients after initial treatment of ovarian cancer. *Crit Rev Oncol Hematol* 2009;**71**(1): 43-52.

218. Baum RP, Noujaim AA, Nanci A, et al. Clinical course of ovarian cancer patients under repeated stimulation of HAMA using MAb OC125 and B43.13. *Hybridoma* 1993;**12**(5): 583-9.

219. Schultes BC, Zhang C, Xue LY, Noujaim AA, Madiyalakan R. Immunotherapy of human ovarian carcinoma with OvaRex MAb-B43.13 in a human-PBL-SCID/BG mouse model. *Hybridoma* 1999;**18**(1): 47-55.

220. Cooper MS, Ma MT, Sunassee K, et al. Comparison of (64)Cu-complexing bifunctional chelators for radioimmunoconjugation: labeling efficiency, specific activity, and in vitro/in vivo stability. *Bioconjug Chem* 2012;**23**(5): 1029-39.

221. Kume M, Carey PC, Gaehle G, et al. A semi-automated system for the routine production of copper-64. *Appl Radiat Isot* 2012;**70**(8): 1803-6.

222. Lindmo T, Boven E, Cuttitta F, Fedorko J, Bunn PA, Jr. Determination of the immunoreactive fraction of radiolabeled monoclonal antibodies by linear extrapolation to binding at infinite antigen excess. *J Immunol Methods* 1984;**72**(1): 77-89.

223. Prat J. New insights into ovarian cancer pathology. *Ann Oncol* 2012;**23** Suppl 10: x111-7.

224. Lutz AM, Ray P, Willmann JK, Drescher C, Gambhir SS. 2-deoxy-2-[F-18]fluoro-D-glucose accumulation in ovarian carcinoma cell lines. *Mol Imaging Biol* 2007;**9**(5): 260-6.

225. Fang J, Nakamura H, Maeda H. The EPR effect: Unique features of tumor blood vessels for drug delivery, factors involved, and limitations and augmentation of the effect. *Adv Drug Deliv Rev* 2011;**63**(3): 136-51.

226. Dearling JL, Voss SD, Dunning P, et al. Imaging cancer using PET--the effect of the bifunctional chelator on the biodistribution of a (64)Cu-labeled antibody. *Nucl Med Biol* 2011;**38**(1): 29-38.

227. Masuho Y, Zalutsky M, Knapp RC, Bast RC, Jr. Interaction of monoclonal antibodies with cell surface antigens of human ovarian carcinomas. *Cancer Res* 1984;**44**(7): 2813-9.

228. Marth C, Zeimet AG, Widschwendter M, Daxenbichler G. Regulation of CA 125 expression in cultured human carcinoma cells. *Int J Biol Markers* 1998;**13**(4): 207-9

229. Wu AM, Senter PD. Arming antibodies: prospects and challenges for immunoconjugates. *Nat Biotechnol* 2005;**23**(9): 1137-46.

230. Sundaresan G, Yazaki PJ, Shively JE, et al. 124I-labeled engineered anti-CEA minibodies and diabodies allow high-contrast, antigen-specific small-animal PET imaging of xenografts in athymic mice. *J Nucl Med* 2003;**44**(12): 1962-9

231. O'Donoghue JA, Smith-Jones PM, Humm JL, et al. 124I-huA33 antibody uptake is driven by A33 antigen concentration in tissues from colorectal cancer patients imaged by immuno-PET. *J Nucl Med* 2011;**52**(12): 1878-85.

232. Holland JP, Williamson MJ, Lewis JS. Unconventional nuclides for radiopharmaceuticals. *Mol Imaging* 2010;**9**(1): 1-20.

233. Wright BD, Lapi SE. Designing the magic bullet? The advancement of immuno-PET into clinical use. *J Nucl Med* 2013;**54**(8): 1171-4.

234. Zhang Y, Hong H, Cai W. PET tracers based on Zirconium-89. *Curr Radioph*arm 2011;**4**(2): 131-9.

235. Holland JP, Sheh Y, Lewis JS. Standardized methods for the production of high specific-activity zirconium-89. *Nucl Med Biol* 2009;**36**(7): 729-39.

236. Deri MA, Zeglis BM, Francesconi LC, Lewis JS. PET imaging with (8)(9)Zr: from radiochemistry to the clinic. *Nucl Me*d Biol 2013;**40**(1): 3-14.

237. Fischer G, Seibold U, Schirrmacher R, Wangler B, Wangler C. (89)Zr, a radiometal nuclide with high potential for molecular imaging with PET: chemistry, applications and remaining challenges. *Molecules* 2013;**18**(6): 6469-90.

238. Perk LR, Visser GW, Vosjan MJ, et al. (89)Zr as a PET surrogate radioisotope for scouting biodistribution of the therapeutic radiometals (90)Y and (177)Lu in tumor-bearing nude mice after coupling to the internalizing antibody cetuximab. *J Nucl Med* 2005;**46**(11): 1898-906.

239. Price EW, Zeglis BM, Lewis JS, Adam MJ, Orvig C. H6phospa-trastuzumab: bifunctional methylenephosphonate-based chelator with 89Zr, 111In and 177Lu. *Dalton Trans* 2014;**43**(1): 119-31.

240. Deri MA, Ponnala S, Zeglis BM, et al. Alternative Chelator for (89)Zr Radiopharmaceuticals: Radiolabeling and Evaluation of 3,4,3-(LI-1,2-HOPO). *J Med Chem* 2014;**57**(11): 4849-60.

241. Carlin S, Khan N, Ku T, Longo VA, Larson SM, Smith-Jones PM. Molecular targeting of carbonic anhydrase IX in mice with hypoxic HT29 colorectal tumor xenografts. *PLoS One* 2010;**5**(5): e10857

242. Ulmert D, Evans MJ, Holland JP, et al. Imaging androgen receptor signaling with a radiotracer targeting free prostate-specific antigen. *Cancer Discov* 2012;**2**(4): 320-7.

243. Holland JP, Caldas-Lopes E, Divilov V, et al. Measuring the pharmacodynamic effects of a novel Hsp90 inhibitor on HER2/neu expression in mice using Zr-DFO-trastuzumab. *PLoS One* 2010;**5**(1): e8859.

244. Tavare R, McCracken MN, Zettlitz KA, et al. Engineered antibody fragments for immuno-PET imaging of endogenous CD8+ T cells in vivo. *Proc Natl Acad Sci U S A* 2014;**111**(3): 1108-13.

245. Sham JG, Kievit FM, Grierson JR, et al. Glypican-3-targeted 89Zr PET imaging of hepatocellular carcinoma. *J Nucl Med* 2014;**55**(5): 799-804.

246. Ikotun OF, Marquez BV, Huang C, et al. Imaging the L-type amino acid transporter-1 (LAT1) with Zr-89 immunoPET. *PLoS One* 2013;**8**(10): e77476

247. Tinianow JN, Gill HS, Ogasawara A, et al. Site-specifically ^{89}Zr-labeled monoclonal antibodies for ImmunoPET. *Nucl Med Biol* 2010;**37**(3): 289-97.

248. Jain RK. Transport of molecules, particles, and cells in solid tumors. *Annu Rev Biomed Eng* 1999;**1**: 241-63.

249. Buchegger F, Haskell CM, Schreyer M, et al. Radiolabeled fragments of monoclonal antibodies against carcinoembryonic antigen for localization of human colon carcinoma grafted into nude mice. *J Exp Med* 1983;**158**(2): 413-27.

250. Thurber GM, Schmidt MM, Wittrup KD. Factors determining antibody distribution in tumors. *Trends Pharmacol Sci* 2008;**29**(2): 57-61.

251. Rhoden JJ, Wittrup KD. Dose dependence of intratumoral perivascular distribution of monoclonal antibodies. *J Pharm Sci* 2012;**101**(2): 860-7.

252. Thurber GM, Schmidt MM, Wittrup KD. Antibody tumor penetration: transport opposed by systemic and antigen-mediated clearance. *Adv Drug Deliv Rev* 2008;**60**(12): 1421-34.

253. Heldin CH, Rubin K, Pietras K, Ostman A. High interstitial fluid pressure - an obstacle in cancer therapy. *Nat Rev Cancer* 2004;**4**(10): 806-13.

254. Heneweer C, Holland JP, Divilov V, Carlin S, Lewis JS. Magnitude of enhanced permeability and retention effect in tumors with different phenotypes: 89Zr-albumin as a model system. *J Nucl Med* 2011;**52**(4): 625-33.

255. Adams GP, Schier R, McCall AM, et al. High affinity restricts the localization and tumor penetration of single-chain fv antibody molecules. *Cancer Res* 2001;**61**(12): 4750-5.

256. Di Re F, Baiocchi G. Value of lymph node assessment in ovarian cancer: Status of the art at the end of the second millennium. *Int J Gynecol Cancer* 2000;**10**(6): 435-42.

257. Tan DS, Agarwal R, Kaye SB. Mechanisms of transcoelomic metastasis in ovarian cancer. *Lancet Oncol* 2006;**7**(11): 925-34.

258. Ceccarelli F, Barberi S, Pontesilli A, Zancla S, Ranieri E. Ovarian carcinoma presenting with axillary lymph node metastasis: a case report. *Eur J Gynaecol Oncol* 2011;**32**(2): 237-9.

259. Detmar M, Hirakawa S. The formation of lymphatic vessels and its importance in the setting of malignancy. *J Exp Med* 2002;**196**(6): 713-8.

260. Du LC, Chen XC, Wang D, et al. VEGF-D-induced draining lymphatic enlargement and tumor lymphangiogenesis promote lymph node metastasis in a xenograft model of ovarian carcinoma. *Reprod Biol Endocrinol* 2014;**12**: 14.

261. Ayhan A, Gultekin M, Dursun P, et al. Metastatic lymph node number in epithelial ovarian carcinoma: does it have any clinical significance? *Gynecol Onco*l 2008;**108**(2): 428-32.

262. Kim HS, Park NH, Chung HH, Kim JW, Song YS, Kang SB. Significance of preoperative serum CA-125 levels in the prediction of lymph node metastasis in epithelial ovarian cancer. *Acta Obstet Gynecol Scand* 2008;**87**(11): 1136-42.

263. Mumprecht V, Honer M, Vigl B, et al. In vivo imaging of inflammation- and tumor-induced lymph node lymphangiogenesis by immuno-positron emission tomography. *Cancer Res* 2010;**70**(21): 8842-51.

264. Mumprecht V, Detmar M. In vivo imaging of lymph node lymphangiogenesis by immuno-positron emission tomography. *Methods Mol Biol* 2013;**961**: 129-40.

265. Borjesson PK, Jauw YW, Boellaard R, et al. Performance of immuno-positron emission tomography with zirconium-89-labeled chimeric monoclonal antibody U36 in the detection of lymph node metastases in head and neck cancer patients. *Clin Cancer Res* 2006;**12**(7 Pt 1): 2133-40.

266. Thurber GM, Zajic SC, Wittrup KD. Theoretic criteria for antibody penetration into solid tumors and micrometastases. *J Nucl Med* 2007;**48**(6): 995-9.

267. Vogel CA, Bischof-Delaloye A, Mach JP, Pelegrin A, Hardman N, Delaloye B, Buchegger F: Direct comparison of a radioiodinated intact chimeric anti-CEA MAb with its F(ab')2 fragment in nude mice bearing different human colon cancer xenografts. *Br J Cancer* 1993, **68**(4):684-690.

268. Milenic DE, Yokota T, Filpula DR, Finkelman MA, Dodd SW, Wood JF, Whitlow M, Snoy P, Schlom J: Construction, binding properties, metabolism, and tumor targeting of a single-chain Fv derived from the pancarcinoma monoclonal antibody CC49. *Cancer Res* 1991, **51**(23 Pt 1):6363-6371.

269. Shively JE: ^{18}F labeling for immuno-PET: where speed and contrast meet. *J Nucl Med* 2007, **48**(2):170-172.

270. Pluckthun A, Pack P: New protein engineering approaches to multivalent and bispecific antibody fragments. *Immunotechnology* 1997, **3**(2):83-105.

271. Le Gall F, Kipriyanov SM, Moldenhauer G, Little M: Di-, tri- and tetrameric single chain Fv antibody fragments against human CD19: effect of valency on cell binding. *FEBS Lett* 1999, **453**(1-2):164-168.

272. Girgis MD, Federman N, Rochefort MM, et al.: An engineered anti-CA19-9 cys-diabody for positron emission tomography imaging of pancreatic cancer and targeting of polymerized liposomal nanoparticles. *J Surg Res* 2013, **185**(1):45-55.

273. Viola-Villegas NT, Sevak KK, Carlin SD, Doran MG, Evans HW, Bartlett DW, Wu AM, Lewis JS: Noninvasive Imaging of PSMA in Prostate Tumors with Zr-Labeled huJ591 Engineered Antibody Fragments: The Faster Alternatives. *Mol Pharm* 2014.

274. Eder M, Knackmuss S, Le Gall F, Reusch U, Rybin V, Little M, Haberkorn U, Mier W, Eisenhut M: 68Ga-labelled recombinant antibody variants for immuno-PET imaging of solid tumours. *Eur J Nucl Med Mol Imaging* 2010, **37**(7):1397-1407.

275. Lawrence LJ, Kortt AA, Iliades P, Tulloch PA, Hudson PJ: Orientation of antigen binding sites in dimeric and trimeric single chain Fv antibody fragments. *FEBS Lett* 1998, **425**(3):479-484.

276. Schmiedl A, Breitling F, Winter CH, Queitsch I, Dubel S: Effects of unpaired cysteines on yield, solubility and activity of different recombinant antibody constructs expressed in E. coli. *J Immunol Methods* 2000, **242**(1-2):101-114.

277. Yazaki PJ, Wu AM, Tsai SW, Williams LE, Ikler DN, Wong JY, Shively JE, Raubitschek AA: Tumor targeting of radiometal labeled anti-CEA recombinant

T84.66 diabody and t84.66 minibody: comparison to radioiodinated fragments. *Bioconjug Chem* 2001, **12**(2):220-228.

278. Waibel R, Alberto R, Willuda J, Finnern R, Schibli R, Stichelberger A, Egli A, Abram U, Mach JP, Pluckthun A *et al*: Stable one-step technetium-99m labeling of His-tagged recombinant proteins with a novel Tc(I)-carbonyl complex. *Nat Biotechnol* 1999, **17**(9):897-901.

279. Kogelberg H, Miranda E, Burnet J, Ellison D, Tolner B, Foster J, Picon C, Thomas GJ, Meyer T, Marshall JF *et al*: Generation and characterization of a diabody targeting the alphavbeta6 integrin. *PloS One* 2013, **8**(9):e73260.

280. Xavier C, Vaneycken I, D'Huyvetter M, Heemskerk J, Keyaerts M, Vincke C, Devoogdt N, Muyldermans S, Lahoutte T, Caveliers V: Synthesis, preclinical validation, dosimetry, and toxicity of ^{68}Ga-NOTA-anti-HER2 Nanobodies for iPET imaging of HER2 receptor expression in cancer. *J Nucl Med* 2013, **54**(5):776-784.

281. D'Huyvetter M, Vincke C, Xavier C, Aerts A, Impens N, Baatout S, De Raeve H, Muyldermans S, Caveliers V, Devoogdt N *et al*: Targeted Radionuclide Therapy with A (177)Lu-labeled Anti-HER2 Nanobody. *Theranostics* 2014, **4**(7):708-720.

282. Colcher D, Pavlinkova G, Beresford G, Booth BJ, Choudhury A, Batra SK: Pharmacokinetics and biodistribution of genetically-engineered antibodies. *Q J Nucl Med* 1998, **42**(4):225-241.

283. Arano Y: Strategies to reduce renal radioactivity levels of antibody fragments. *Q J Nucl Med* 1998, **42**(4):262-270.

284. Behr TM, Goldenberg DM, Becker W: Reducing the renal uptake of radiolabeled antibody fragments and peptides for diagnosis and therapy: present status, future prospects and limitations. *Eur J Nucl Med* 1998, **25**(2):201-212.

285. Marcus CS, Maxwell GL, Darcy KM, Hamilton CA, McGuire WP. Current approaches and challenges in managing and monitoring treatment response in ovarian cancer. *J Cancer* 2014;**5**(1): 25-30.

286. Strebhardt K, Ullrich A. Paul Ehrlich's magic bullet concept: 100 years of progress. *Nat Rev Cancer* 2008;**8**(6): 473-80.

287. Weiner LM. Building better magic bullets--improving unconjugated monoclonal antibody therapy for cancer. *Nat Rev Cancer* 2007;**7**(9): 701-6.

288. O'Shea JJ, Kanno Y, Chan AC. In search of magic bullets: the golden age of immunotherapeutics. *Cell* 2014;**157**(1): 227-40.

289. Sykes TR, Somayaji VV, Bier S, et al. Radiolabeling of monoclonal antibody B43.13 with rhenium-188 for immunoradiotherapy. *Appl Radiat Isot* 1997;**48**(7): 899-906.

290. Madiyalakan R, Sykes TR, Dharampaul S, et al. Antiidiotype induction therapy: evidence for the induction of immune response through the idiotype network in patients with ovarian cancer after administration of anti-CA125 murine monoclonal antibody B43.13. *Hybridoma* 1995;**14**(2): 199-203.

291. Madiyalakan R, Yang R, Schultes BC, Baum RP, Noujaim AA. OVAREX MAb-B43.13:IFN-gamma could improve the ovarian tumor cell sensitivity to CA125-specific allogenic cytotoxic T cells. *Hybridoma* 1997;**16**(1): 41-5.

292. Yang T, Yang L, Chai W, Li R, Xie J, Niu B. A strategy for high-level expression of a single-chain variable fragment against TNF-alpha by subcloning antibody variable regions from the phage display vector pCANTAB 5E into pBV220. *Protein Expr Purif* 2011;**76**(1): 109-14.

293. Jung S, Pluckthun A. Improving in vivo folding and stability of a single-chain Fv antibody fragment by loop grafting. *Protein Eng* 1997;**10**(8): 959-66.

294. Vaks L, Benhar I. Production of stabilized scFv antibody fragments in the E. coli bacterial cytoplasm. *Methods Mol Biol* 2014;**1060**: 171-84.

295. Entzminger KC, Chang C, Myhre RO, McCallum KC, Maynard JA. The Skp chaperone helps fold soluble proteins in vitro by inhibiting aggregation. *Biochemistry* 2012;**51**(24): 4822-34.

296. Zhang X, Xie J, Sun Y, et al. High-level expression, purification, and characterization of bifunctional ScFv-9R fusion protein. *Appl Microbiol Biotechnol* 2014;**98**(12): 5499-506.

297. Sawyer JR, Schlom J, Kashmiri SV. The effects of induction conditions on production of a soluble anti-tumor sFv in Escherichia coli. *Protein Eng* 1994;**7**(11): 1401-6.

298. Kipriyanov SM, Moldenhauer G, Martin AC, Kupriyanova OA, Little M. Two amino acid mutations in an anti-human CD3 single chain Fv antibody fragment that affect the yield on bacterial secretion but not the affinity. *Protein Eng* 1997;**10**(4): 445-53.